Fatigue Damage Evaluation in Thin-Walled Structures Using Guided Waves

By

Hankai Zhu

A Thesis by Publication Submitted for the degree of

Doctor of Philosophy

School of Architecture and Civil Engineering

The University of Adelaide

November 2023

Abstract

Thin-walled structural components are common in engineering design across many industries and applications. These components are often subjected to cyclic loading, which can lead to fatigue damage accumulation, nucleation and propagation of defects and, finally, to structural failures. The use of damage detection techniques as a part of safety inspections allows to monitor defects and prevent structural failures. However, damage evaluation in thin-walled structures can be challenging with the traditional non-destructive evaluation (NDE) techniques. Therefore, development of new NDE techniques is important to maintain structural integrity and safe operation of infrastructure.

The overall aim of this thesis is to develop new NDE techniques, specifically for thin-walled structures and non-ideal geometries, for the detection and evaluation of early-stage fatigue damage. These new techniques are based on fundamental modes of Lamb and edge waves, which are the most suitable for thin-walled structural components, as these modes disperse rapidly over propagation distance in thick structures.

In Chapter 2, the accumulation of low-cycle fatigue damage is investigated using the low-frequency Lamb wave mixing method combined with phase-reversal approach. Chapter 3 proposes a new approach for the frequency selection and a time-shifting technique to improve the efficiency of wave mixing method for the fatigue damage evaluation.

Detection and evaluation techniques for fatigue edge cracks in realistic structures are developed in Chapters 4, 5 and 6. Chapter 4 investigates the propagation of edge waves along corners of thin-walled structures for the detection of edge cracks. Chapter 5 explores the propagation of the fundamental quasi-edge wave modes in thin-walled structures with non-ideal (curved) edges and the use of these modes for defect evaluation. In Chapter 6, the edge crack length is evaluated using the fundamental mode of edge waves. Moreover, a new Finite Element (FE) model is proposed to simulate the interactions of elastic waves with fatigue cracks, which also accounts for the plasticity-induced closure phenomena.

The main outcomes of the thesis are briefly summarised below,

(1) Development of a new technique for the evaluation of early-stage fatigue damage using the fundamental mode of Lamb waves and wave mixing method;

(2) Development of a new approach for the frequency selection and a time-shifting method, which can improve the efficiency of wave mixing method for damage evaluation;

(3) Investigation of the propagation of edge waves in plates with sharp and rounded corners, which supports the further development of a NDE technique to evaluate damage in inaccessible locations;

(4) Investigation of the quasi-edge wave modes and the development of a Semi-Analytical Finite Element (SAFE) model to characterise the wave propagation properties;

(5) Development of a new technique for the evaluation of the edge crack length based on the fundamental mode of edge waves, and

(6) Development of an advanced FE model to simulate the interaction of elastic waves with cracks considering the plasticity-induced closure phenomena.

Overall, the findings of this thesis provide knowledge and deeper understanding of fatigue damage evaluation using guided waves. The outcomes will help apply guided wave based NDE techniques to real structures.

Declaration

I, Hankai Zhu, certify that this work contains no material which has been accepted for the award of any other degree or diploma in my name in any university or other tertiary institution and, to the best of my knowledge and belief, contains no material previously published or written by another person, except where due reference has been made in the text. In addition, I certify that no part of this work will, in the future, be used in a submission in my name for any other degree or diploma in any university or other tertiary institution without the prior approval of the University of Adelaide and where applicable, any partner institution responsible for the joint award of this degree.

The author acknowledges that copyright of published works contained within this thesis resides with the copyright holder(s) of those works.

I give permission for the digital version of my thesis to be made available on the web, via the University's digital research repository, the Library Search and also through web search engines, unless permission has been granted by the University to restrict access for a period of time.

I acknowledge the support I have received for my research through the provision of an Australian Government Research Training Program Scholarship.

Signature: Date: 27/10/2023

Acknowledgement

The PhD journey is one of the most important milestones in my life. There are many people have supported me during my PhD candidature, and I would like to appreciate their help below.

Firstly, I would like to express my gratitude to my supervisors, Professor Alex Ching-Tai Ng, and Professor Andrei Kotousov. I could not be able to achieve such exceptional productivity without their support and encouragement. Andrei can always provide constructive suggestions, and his knowledge of fatigue cracks is critical for my studies. I would greatly appreciate the time and effort that he put into my research. Alex encouraged me to overcome all the challenges that I face throughout the journey. His advice on the finite element simulation of wave propagation have been of great help. Special appreciation to Dr Francis Rose for his technical advice and notes.

Moreover, I would like to thank my colleagues, and we had a lot of insightful discussions on the feasibility of research ideas. Special thanks to John (Jinghang) Wu, for the long-lasting friendship, and for the moment of joy and sadness we have shared together. I would like to acknowledge the support from the technicians of Chapman laboratory, especially for the help from Mr Ian Ogier. His expertise in machining metals greatly improved the quality of the experiments. I am also grateful for the scholarship and the financial support provided by the University of Adelaide and the Australian Research Council.

I would like to thank the love and support from my family, in particularly, my parents, Ning Xu and Xiang Zhu. Their support is undeniably critical for me to pursue and complete this challenging journey. Their unconditional support gave me the courage and the strength to push forward what is possible. Their encouragement helped me to go through my darkest hours, and now, I would like to share and celebrate this moment with them, which I am so proud of.

Overall, I believe that my PhD journey was challenging and rewarding. I thank myself to complete this challenging journey, which makes me feel a strong sense of achievement. I dedicated all my time during the past few years to the research. This journey gives me an opportunity to prove myself and to explore my horizons.

List of Publications

This thesis consists of a combination of published and submitted for publication journal articles. The main body of the thesis is based on the following journal articles and submitted manuscripts:

Journal papers (Published)

1. **H. Zhu**, C.T. Ng, and A. Kotousov, Low-frequency Lamb wave mixing for fatigue damage evaluation using phase-reversal approach, *Ultrasonics*, 124 (2022), 106768.
2. **H. Zhu**, C.T. Ng, and A. Kotousov, Frequency selection and time shifting for maximizing the performance of low-frequency guided wave mixing, *Ndt & E International*, 133 (2023), 102735.
3. **H. Zhu**, C.T. Ng, and A. Kotousov, Fatigue crack detection in edges of thin-walled structures with corners using the fundamental mode of edge waves, *Ultrasonics*, 132 (2023), 106995.
4. **H. Zhu**, A. Kotousov, and C.T. Ng, Defects evaluation near edges of structural elements using the fundamental mode of edge waves, *Journal of Sound and Vibration*, 557 (2023), 117753.

Journal papers (Manuscript)

5. **H. Zhu**, A. Kotousov, and C.T. Ng, Evaluation of fatigue cracks using the fundamental mode of edge waves (Submitted)

The following articles are of close relevance to the proposed research topic but exclude in this thesis:

Journal papers

1. X. Hu, T. Yin, **H. Zhu**, C.T. Ng, and A. Kotousov, Structural health monitoring of partially immersed metallic plates using nonlinear guided wave mixing, *Construction and Building Materials* 346 (2022), 128381.

Conference papers

1. **H. Zhu**, C.T. Ng, and A. Kotousov, The use of phase-reversal approach for extraction of second order harmonics of mixing waves, in: *ACAM10: 10th Australasian Congress on Applied Mechanics*, 1, 1, 2021, 184-192, Engineers Australia, 2021.
2. **H. Zhu**, C.T. Ng, and A. Kotousov, The performance optimization of combinational harmonic generation for quasi-synchronous Lamb wave mixing, in: *Sensors and Smart Structures Technologies for Civil, Mechanical, and Aerospace Systems 2022*, SPIE, 2022, pp. 293-300.

The following award presented to the author during the candidature:

1. *Best postgraduate student paper award-Highly commenced*, in 10th Australasian Congress on Applied Mechanics (ACAM10).

Table of Contents

Chapter 1

Introduction

Chapter 1: Introduction

The thesis represents a compendium of a published and submitted research articles, which united by the same topic and methodology. Each article has been published in a leading international journal related to the broader research area of guided waves and NDE. Every article has a proper literature review section. In order to avoid the repetition, this current Introductory Section provide a brief summary of the most significant developments in the area, states the aims and objectives of this thesis.

1.1. Background

The thin-walled structures are widely used in the civil and mechanical engineering, some examples including plate, frames of ship and aircraft structures, I-beam, and angle stiffeners. Integrity of these common structural components are of critical importance in engineering design. Almost all these components, to some extent, are subjected to cyclic loading. This loading can often first result in fatigue damage at micro-scale level (so called, early fatigue damage), which is difficult to detect and evaluate.

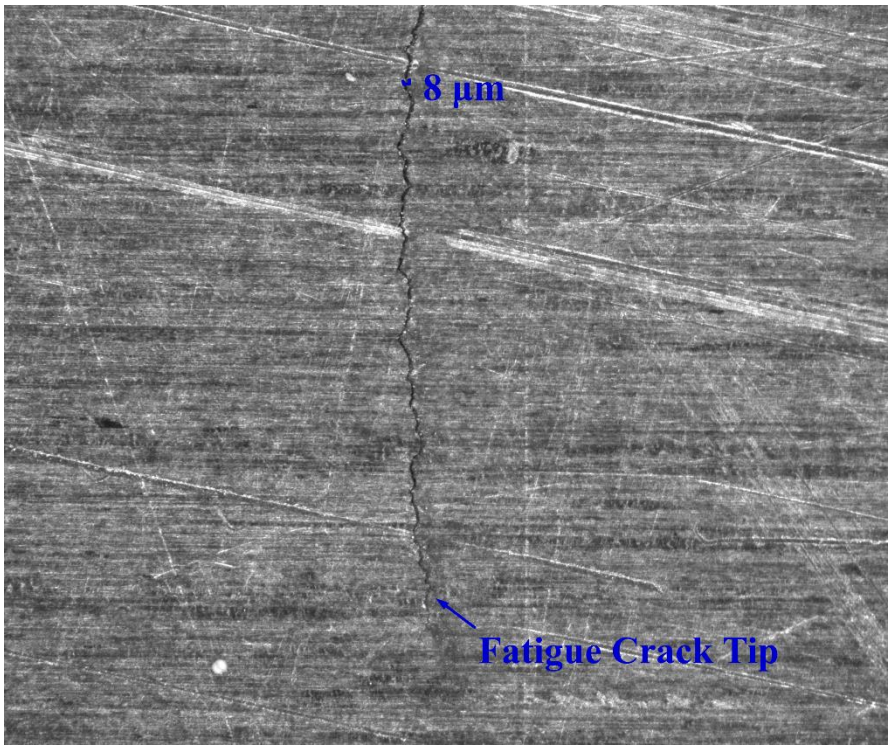

Figure 1.1. Microscope image of a fatigue crack in an aluminium plate

Early fatigue damage, which is associated with microstructural changes of the material, can accumulate and progress rapidly to the next stage – fatigue cracks, see Figure 1.1, and, finally, result in a structural failure. Therefore, non-destructive evaluation (NDE) and Structural Health Monitoring (SHM) for the purpose of fatigue damage evaluation have attracted significant attention during the recent decade.

With advance of manufacturing techniques over the past twenty years the early-stage fatigue damage, or damage accumulated before formation of macro- crack, can now dominate the total fatigue life of structural components. Therefore, the evaluation of both stages of the damage progression is critical in order to maintain safe and efficient operation of high-values assets and infrastructure.

1.2. NDE with guide waves

Different techniques have been developed in the past to detect fatigue damage, including digital image correlation [1], high-density electro-pulsing [2], ultrasonic modulation [3, 4]. These techniques have their own advantages and limitations. Among the aforementioned techniques, techniques based on ultrasonic guided waves, are considered as one of the most promising for non-destructive defect inspections and future SHM systems [5-8].

Table 1.1. NDE with nonlinear guided waves

Damage type	Thin-walled structures	Pipes	Composite plates
Material nonlinearity	Material imperfection [9-12] Cyclic fatigue damage [13-15] Thermal damage [16-18] Corrosion and pitting [19, 20]	Fatigue damage [21-23]	Material imperfection [24, 25] Thermal and impact damage [26-28]
CAN	Fatigue crack [29-34]	Fatigue crack [35, 36]	Delamination [37, 38]

The effects of micro-structural damage (or early fatigue damage) on wave propagation are mainly considered within two aspects: changes of material nonlinearity and generation of

contact acoustic nonlinearity (CAN). The change of material nonlinearity can be associated with accumulation of micro-structural defects or localised plastic deformations. The generation of CAN is typically due to the interaction between the guided waves and the micro-cracks (i.e., fatigue crack or delamination). In the previous studies, the guided waves have shown a good sensitivity to different types of micro-scaled damage in different types of structures made of different materials, and the details of some of the past studies are summarised in Table. 1.1.

1.3. Fundamental modes of guided waves

The past studies have also demonstrated that the nonlinear guided waves are sensitive to the microstructural damage, and some of the examples have been summarized in Table 1.1 in the previous sub-section. The existing nonlinear guided wave NDE techniques rely on the generation of second harmonic. The generation process requires meeting the synchronism condition (i.e., the phase velocity matching of the f_a and $2f_a$), as well as the non-zero power flux condition [7, 39, 40]. The common approach to achieve the synchronism is the use of cross-modes or the higher-order Lamb wave mode pairs (S_1-S_2). However, the higher-order Lamb waves are normally highly dispersive and energy decaying, which limits the propagation as well as detection and analysis of the generated second harmonic. In addition, there are limited wave mode pairs, which can be selected to achieve the aforementioned conditions required for the second harmonic generation. Another constraint of the cross-mode method is the multi-mode generation, which can make the signal analysis difficult. These constraints limit the practical application of cross-modes in NDE techniques.

Recently, the fundamental modes of guided waves have attracted a lot of attention for the purpose of the evaluation of the distributed damage, namely, the fundamental symmetric mode of Lamb waves (S_0), and the fundamental symmetric mode of edge waves (ES_0). The S_0 mode is a dispersive and can propagate for a long distance without energy decay in plate-like structures guided by the free surfaces. The propagation of ES_0 mode is concentrated and localized near the free edge of plate and shell structures. This feature-guided wave mode has also zero energy decay and, in addition, it is only slightly dispersive. The latter property is very attractive for NDE applications. In Figure 1.2, illustrates the propagation of these two wave modes. The propagation characteristics of these two wave modes are complementary for the fatigue damage and defect evaluation, specifically, Lamb wave modes can be applied to

evaluate material degradation due to early fatigue damage while the edge wave mode can target fatigue cracks, which normally initiate from free surface.

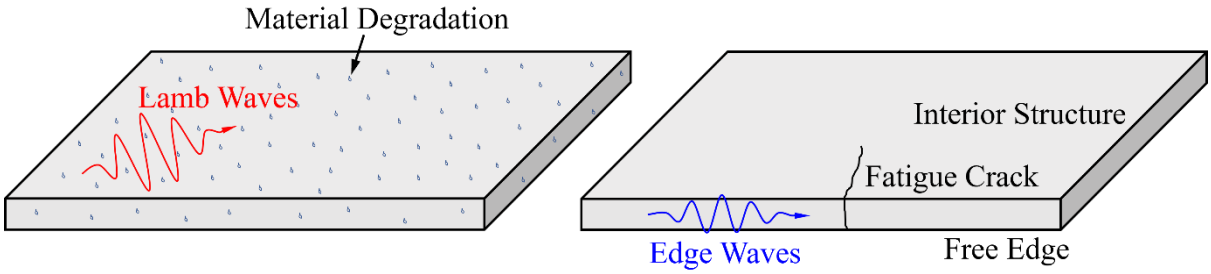

Figure 1.2. Schematic illustration of the propagation of S_0 and ES_0 modes in an ideal thin-walled structure

With the S_0 and ES_0 wave modes it is possible to the achieve quasi-synchronism in order to generate high-order harmonics, and the theoretical framework of the quasi-phase velocity matching for the purpose of the second harmonic generation has been developed by Muller *et al.* [41]. Several previous studies have investigated the propagation of these modes experimentally [15, 42, 43] and numerically [44-46]. These studies have demonstrated that the second harmonic increases with the accumulation of the material nonlinearity. In addition, the S_0 mode have been employed to detect the CAN generation due to fatigue crack in a metallic plate [34, 47, 48] and due to the loosening of bolted joint [49]. Therefore, the nonlinear fundamental guided waves have demonstrated a good sensitive to the micro-scaled damage.

In general, the fundamental modes of guided waves have a number of advantages compared with the higher-order modes of guided waves. These advantages include (1) long wave propagation distance and long accumulative distance of second harmonic; (2) avoidance of multi-modes generation; (3) flexibility of frequency selection; and (4) less demanding on instrumentation.

The fundamental modes of guided waves are in low-frequency range below the cut-off frequency, and these wave modes are only weakly dispersive across the entire low-frequency range. There are only very limited wave modes coupling in the low frequency range, and the generation of these fundamental wave modes can be relatively simple. The fundamental wave modes can be generated by using a piezoelectric transducer (PZT), which can be bonded on the engineering structures and is more suitable for the practical application. Therefore, the

fundamental wave modes are also very promising for the long distant inspection of fatigue damage across a wide range of practical situations.

1.4. Wave mixing method

Many recent studies focused on the utilization of the combinational harmonic generation to evaluate microstructural damage. The generation of the combinational harmonics using the wave mixing method is similar with the generation of the second harmonic, which requires the synchronism/quasi-synchronism condition, and the non-zero power flux condition. In addition, the second harmonics (at $2f_a$ and $2f_b$) and the combinational harmonics (at f_a+f_b and f_b-f_a) can be generated simultaneously using the wave mixing method. The main reason of the utilization of the wave mixing method is that the combinational harmonic generation can avoid the nonlinearity due to the instrumentation [13, 50]. The latter was reported as the main challenge for the development of nonlinear wave approaches for NDE application.

From the literature, the wave mixing can be achieved with (1) codirectional collinear waves, (2) contour-propagating collinear waves, and (3) non-collinear waves. A secondary wave can be generated in the wave mixing zone in addition to the two excited waves. In the codirectional collinear wave mixing method, two incident waves propagate in the same direction, and the wave mixing area is directly associated with the dispersion properties between the two emitting waves. Generally, the wave mixing zone of this method is rather large, which enables the evaluation of the distributed nonlinearity cumulation [10, 11, 51, 52]. In contrast, the contour-propagating collinear wave mixing and non-collinear wave mixing have a confined wave mixing zone. Two waves are excited in the opposite direction or in certain angles to generate a secondary wave, and these wave mixing methods are suitable for locating the localized damage (i.e., fatigue crack) [53, 54], and the characterization of the localised material damage [17, 50]. It should be noted that the codirectional collinear wave mixing has less restrictions than the other two methods (i.e., excitation frequencies or wave propagation angle), which makes this method particularly suitable for the practical application. As aforementioned, the combinational harmonic generation is similar to the second harmonic generation. However, the wave mode pairs are limited to a few combinations only [17, 55, 56]. In contrast, the collinear wave mixing based on the quasi-synchronism has a significant flexibility with the frequency selection. Therefore, the present research mainly focuses on the codirectional collinear wave mixing method.

1.5. Feature guided waves

Over the past few years, many research efforts have been directed to the investigation of guided wave propagation in realistic engineering structures, instead of ideal geometries such as plate with ideal sharp edges or a circular pipe. The interior geometry of the realistic engineering structures can be complex, which leads to significant dispersion and multi-mode generation during inspections with guided waves. However, these complex geometry features of structural components can also serve as a waveguide, which permit propagation of specific wave modes at certain frequencies. These waves are, so called, feature guided waves. In the literature, various feature guided wave modes have been investigated, including in rail web [57, 58], bonded stiffeners [59, 60], fastener hole [61], transverse bends [62-64], and fuel weep hole [65, 66]. Other investigations focused on defect detection using these feature guided waves, some examples including defects in steel rebar [67-69], L-joints [70], T-joint stiffeners [71], I-beams [72-74], square tubes [75], and pipe bend and supports [76-78].

One of the main challenges of the utilisation of the feature guided waves for development of practical NDE techniques is the evaluation of wave dispersive characteristics. Semi-analytical finite element (SAFE) method is considered as one of the most promising method to calculate the dispersion properties [79, 80]. This method is applicable to arbitrary wave guide cross-sections. It allows to analyse the wave properties by considering the propagation of harmonic waves. This method has been proven to be a powerful tool for investigating the feature guided waves, especially for structural elements with complex shapes [59, 63, 81]. SAFE-PML is the modification of the SAFE method, using the perfectly matched layer (PML), which serves as an absorbing layer and the leaking waves propagating far away the waveguide can be absorbed [68, 82]. The complex-valued eigenvalues can be obtained after solving the eigen-value problem modelled by the SAFE-PML method. Infinite number of eigenvalues can be obtained for a certain frequency, however, the wave modes unable to be determined directly. Hence, a wave mode filtering algorithm is needed to link the eigenvalues and the wave modes [68, 82]. The real part of the eigenvalue represents the wavenumber, while the complex part can be used to calculate the attenuation of the corresponding wave mode.

Edge waves can also be considered as a type of feature guided wave, which propagate along the free edges of thin-walled structures. The wave properties of the fundamental edge waves converge to the wedge wave in the high frequency range, and this wave mode approaches to the Rayleigh wave in the long-wavelength limit (in the very low frequency, $f << 50$ kHz). In

addition, the fundamental edge waves are weakly dispersive, while the higher order edge waves are strongly dispersive. Generally, the fundamental edge waves are coupled with different wave modes across the entire frequency, in specific, SH_0 in the low frequency range, and S_0 and higher order Lamb wave in the high frequency range.

Structural elements with free edges are widely used in the engineering application, and fatigue cracks often initiate from these edges. As aforementioned, the conventional Lamb and shear waves are strongly dispersive considering a complex interior structure. However, the fundamental edge waves have shown small decay over long wave propagation distance [83], which makes this wave mode a promising candidate for the long distant inspection. This wave mode showed a good sensitive to the corrosion damage [84] and material imperfection [43].

In the literature, the analytical/semi-analytical approaches were generally utilised for the calculation of the dispersion properties of edge waves, by enforcing the boundary conditions and applying the boundary collocation method [85, 86] or reciprocity theorem [87]. However, the mode decomposition of edge waves requires solving 3D equilibrium equations, instead of the 2D framework for the plane theory of elasticity [86, 88]. Therefore, the calculation of the dispersion properties of edge waves is complex, especially for the edge wave properties in non-ideal edges. This leads to the need of further development of a method, which can calculate the wave properties of edge waves in the realistic geometries, instead of the sharp edge.

1.6. Aim and objectives

The overall aim of the present research is to advance and develop NDE techniques for the purpose of fatigue damage evaluation in thin-walled structures, using the fundamental modes of guided waves including feature guided waves. In particular, this thesis is focused on the development of wave mixing method for the material degradation evaluation, and the fatigue crack evaluation using edge waves. In addition, the new developments are aimed to be applicable to practical applications, which can be of non-ideal geometries. Therefore, this overall aim of the present research can be achieved by addressing the following objectives:

i. To evaluate the combinational harmonic generation due to the progressive fatigue damage, using wave mixing of fundamental mode of Lamb waves with the incorporation of the phase-reversal approach;

ii. To develop a method which can be utilised for the frequency pair selection and performance optimization of the wave mixing method, using the fundamental modes of guided waves;
iii. To investigate the fundamental mode of edge waves propagating through the corners of thin-walled structures, and to locate fatigue cracks in hidden or inaccessible locations;
iv. To investigate the defect evaluation in non-ideal edges of thin-walled structures using the fundamental modes of edge waves, and to provide a comprehensive method for the calculation of wave properties of edge waves in non-ideal edges.
v. To evaluate the length of fatigue cracks using the fundamental mode of edge waves, and to develop an advanced FE model to simulate the closure behaviour of the fatigue crack;

1.7. Outlines of thesis

This thesis comprises of five journal articles closely related to the proposed objectives, four of which are published in the leading international journals, and one manuscript has been submitted for the publication. The thesis consists of seven chapters, which are

Chapter 1 provides a general introduction to the NDE and guided waves for the purpose of fatigue damage and defect evaluation. It discusses the advantages of fundamental modes of guided waves and wave mixing method, and provides overview of feature guided waves.

Chapter 2 investigates the generation of the combinational harmonic due to material imperfections and low-cycle fatigue damage, using the wave mixing method for the fundamental mode of Lamb waves. The experimental and numerical studies demonstrate that the combinational harmonics show a good sensitivity to the accumulation and progression of fatigue damage fatigue. Different effects of the incident wave on wave mixing properties are investigated. It is also found that the implementation of the phase-reversal approach in the wave mixing can improve considerably the quality of experimental results related to the fatigue damage evaluation.

Chapter 3 proposes a new technique for the frequency pair selection of the wave mixing using fundamental modes of guided waves. The quasi-synchronised wave modes have a significant flexibility for the frequency pair selection. The trial-and-error method was generally used for the frequency pair selection in the past. The developed technique provides an improved understanding on the frequency pair selection for the quasi-synchronised wave modes.

Moreover, a new time shifting method is suggested to enhance and facilitate the generation of the second and combinational harmonic generation due to the collinear wave mixing. In addition, this method can be very useful when various limitations exist on the frequency selection, which can avoid the overlapping and optimize the performance of the generated harmonics.

Chapter 4 investigates the propagation of the fundamental mode of edge waves (ES_0) along sharp and curved corners of thin-walled structures. The experimental studies demonstrate the ability of the ES_0 propagating through multiple sharp corners. Further numerical studies show that the rounded corners, with radius-to-wavelength above 3, have no significant impact on the displacement amplitude of edge waves. The numerical simulations also show that the second harmonic generated due to the interaction between fatigue crack and the edge waves can propagate through corners as well. This finding is used in a feasibility study focusing on detection and localisation of fatigue cracks in the inaccessible locations.

Chapter 5 further explores the fundamental mode of edge wave propagation in the non-ideal (curved) edges of thin-walled structures. The SAFE method is implemented, and the comparison between the calculated wave properties and the theoretical results shows an excellent agreement. This agreement provides the confidence to investigate the wave properties of edge waves by the application of the SAFE method. Previously, the wave properties of edge waves were obtained largely based on the derived theoretical solutions. In addition, the quasi-fundamental antisymmetric mode of edge wave (QEA_0), which is an analogue of the fundamental mode of edge wave for non-ideal geometries, demonstrates a low energy decay and can propagate for long distances, while its symmetric counterpart (QES_0) exhibits strong dispersion. The QEA_0 is further studied for the purpose of defect inspections. The conducted studies indicate a good sensitive to crack-like defects with the characteristic length of more than 0.1 wavelength.

Chapter 6 focuses on the evaluation of the length of high-cycle fatigue crack, which is partially closed due to the plasticity-induced crack closure phenomenon. The experimental studies have demonstrated that the reflected and transmitted signals at different frequencies of the incident ES_0 waves correlate very well with the length of the opened region of fatigue cracks. An advanced FE model has been developed to simulate the wave interactions associated with plasticity-induced closure of fatigue cracks. In addition, the numerical results show that

the increase of tensile pre-stress levels leads to the reduction of crack closure near the crack tip, which allows the fatigue crack length to be evaluated more accurately.

Chapter 7 summarizes findings of the present research and outlines the recommendations for the future studies.

References

[1] Carroll J D, Abuzaid W, Lambros J and Sehitoglu H 2013 High resolution digital image correlation measurements of strain accumulation in fatigue crack growth *International Journal of Fatigue* **57** 140-50

[2] Hosoi A, Kishi T and Ju Y 2013 Healing of fatigue crack by high-density electropulsing in austenitic stainless steel treated with the surface-activated pre-coating *Materials* **6** 4213-25

[3] Kim Y, Lim H J and Sohn H 2018 Nonlinear ultrasonic modulation based failure warning for aluminum plates subject to fatigue loading *International Journal of Fatigue* **114** 130-7

[4] Lim H J, Sohn H, DeSimio M P and Brown K 2014 Reference-free fatigue crack detection using nonlinear ultrasonic modulation under various temperature and loading conditions *Mech. Syst. Signal. Process.* **45** 468-78

[5] Mitra M and Gopalakrishnan S 2016 Guided wave based structural health monitoring: A review *Smart. Mater. Struct.* **25** 053001

[6] Su Z, Ye L and Lu Y 2006 Guided Lamb waves for identification of damage in composite structures: A review *J. Sound Vib.* **295** 753-80

[7] Su Z, Zhou C, Hong M, Cheng L, Wang Q and Qing X 2014 Acousto-ultrasonics-based fatigue damage characterization: Linear versus nonlinear signal features *Mech. Syst. Signal. Process.* **45** 225-39

[8] Lissenden C J 2021 Nonlinear ultrasonic guided waves—Principles for nondestructive evaluation *J. Appl. Phys.* **129** 021101

[9] Bermes C, Kim J-Y, Qu J and Jacobs L J 2007 Experimental characterization of material nonlinearity using Lamb waves *Appl. Phys. Lett.* **90** 021901

[10] Sampath S and Sohn H 2022 Cubic nonlinearity parameter measurement and material degradation detection using nonlinear ultrasonic three-wave mixing *Ultrasonics* **121** 106670

[11] Shan S, Hasanian M, Cho H, Lissenden C J and Cheng L 2019 New nonlinear ultrasonic method for material characterization: Codirectional shear horizontal guided wave mixing in plate *Ultrasonics* **96** 64-74

[12] Yang Y, Ng C-T and Kotousov A 2019 Second-order harmonic generation of Lamb wave in prestressed plates *J. Sound Vib.* **460** 114903

[13] Croxford A J, Wilcox P D, Drinkwater B W and Nagy P B 2009 The use of non-collinear mixing for nonlinear ultrasonic detection of plasticity and fatigue *J. Acoust. Soc. Am.* **126** EL117-EL22

[14] Pruell C, Kim J-Y, Qu J and Jacobs L 2009 A nonlinear-guided wave technique for evaluating plasticity-driven material damage in a metal plate *NDT&E Int.* **42** 199-203

[15] Zhu W, Xiang Y, Liu C-j, Deng M, Ma C and Xuan F-z 2018 Fatigue damage evaluation using nonlinear Lamb Waves with Quasi phase-velocity matching at low frequency *Materials* **11** 1920

[16] Wang K, Cao W, Liu M, Li Y, Zhou P and Su Z 2020 Advancing elastic wave imaging using thermal susceptibility of acoustic nonlinearity *International Journal of Mechanical Sciences* **175** 105509
[17] Hasanian M and Lissenden C J 2017 Second order harmonic guided wave mutual interactions in plate: Vector analysis, numerical simulation, and experimental results *J. Appl. Phys.* **122** 084901
[18] Wen F, Shan S and Cheng L 2021 Third harmonic shear horizontal waves for material degradation monitoring *Struct. Health Monitor.* **20** 475-83
[19] Cao W X, Xu L, Su Z Q, Pang B J, Chi R Q, Wang L and Wang X Y 2021 Modeling of pitting damage-induced ultrasonic nonlinearity in AL-Whipple shields of spacecraft: Theory, simulation, and experimental validation *International Journal of Mechanical Sciences* **207** 106659
[20] Ding X, Xu C, Deng M, Zhao Y, Bi X and Hu N 2021 Experimental investigation of the surface corrosion damage in plates based on nonlinear Lamb wave methods *NDT&E Int.* **121** 102466
[21] Li W, Lan Z, Hu N and Deng M 2021 Modeling and simulation of backward combined harmonic generation induced by one-way mixing of longitudinal ultrasonic guided waves in a circular pipe *Ultrasonics* **113** 106356
[22] Yeung C and Ng C T 2020 Nonlinear guided wave mixing in pipes for detection of material nonlinearity *J. Sound Vib.* **485** 115541
[23] Liu Y, Khajeh E, Lissenden C J and Rose J L 2014 Higher order interaction of elastic waves in weakly nonlinear hollow circular cylinders. II. Physical interpretation and numerical results *J. Appl. Phys.* **115** 214902
[24] Jiang C, Li W, Deng M and Ng C-T 2022 Quasistatic pulse generation of ultrasonic guided waves propagation in composites *J. Sound Vib.* 116764
[25] Jiang C, Li W, Deng M and Ng C-T 2022 Quasistatic pulse generation of ultrasonic guided waves propagation in composites *J. Sound Vib.* **524** 116764
[26] Andreades C, Fierro G P M and Meo M 2020 A nonlinear ultrasonic SHM method for impact damage localisation in composite panels using a sparse array of piezoelectric PZT transducers *Ultrasonics* **108** 106181
[27] Hong M, Mao Z, Todd M D and Su Z 2017 Uncertainty quantification for acoustic nonlinearity parameter in Lamb wave-based prediction of barely visible impact damage in composites *Mech. Syst. Signal. Process.* **82** 448-60
[28] Li W, Cho Y and Achenbach J D 2012 Detection of thermal fatigue in composites by second harmonic Lamb waves *Smart. Mater. Struct.* **21** 085019
[29] Cho H and Lissenden C J 2012 Structural health monitoring of fatigue crack growth in plate structures with ultrasonic guided waves *Struct. Health Monitor.* **11** 393-404
[30] Jingpin J, Xiangji M, Cunfu H and Bin W 2017 Nonlinear Lamb wave-mixing technique for micro-crack detection in plates *NDT&E Int.* **85** 63-71
[31] Wang K, Li Y, Su Z, Guan R, Lu Y and Yuan S 2019 Nonlinear aspects of "breathing" crack-disturbed plate waves: 3-D analytical modeling with experimental validation *International Journal of Mechanical Sciences* **159** 140-50
[32] Wang K, Liu M, Su Z, Yuan S and Fan Z 2018 Analytical insight into "breathing" crack-induced acoustic nonlinearity with an application to quantitative evaluation of contact cracks *Ultrasonics* **88** 157-67
[33] Xu L, Su Y, Wang K, Yang X, Yuan S and Su Z 2021 An elastodynamic reciprocity theorem-based closed-form solution to second harmonic generation of lamb waves by a fatigue crack: Theory & experimental validation *J. Sound Vib.* **509** 116226

[34] Yang Y, Ng C-T, Kotousov A, Sohn H and Lim H J 2018 Second harmonic generation at fatigue cracks by low-frequency Lamb waves: Experimental and numerical studies *Mech. Syst. Signal. Process.* **99** 760-73
[35] Guan R, Lu Y, Wang K and Su Z 2019 Fatigue crack detection in pipes with multiple mode nonlinear guided waves *Struct. Health Monitor.* **18** 180-92
[36] Guo X, Zhang D and Zhang J 2012 Detection of fatigue-induced micro-cracks in a pipe by using time-reversed nonlinear guided waves: A three-dimensional model study *Ultrasonics* **52** 912-9
[37] Soleimanpour R and Ng C-T 2017 Locating delaminations in laminated composite beams using nonlinear guided waves *Engineering Structures* **131** 207-19
[38] Soleimanpour R, Ng C-T and Wang C H 2017 Higher harmonic generation of guided waves at delaminations in laminated composite beams *Struct. Health Monitor.* **16** 400-17
[39] Deng M and Pei J 2007 Assessment of accumulated fatigue damage in solid plates using nonlinear Lamb wave approach *Appl. Phys. Lett.* **90** 121902
[40] Hong M, Su Z, Lu Y, Sohn H and Qing X 2015 Locating fatigue damage using temporal signal features of nonlinear Lamb waves *Mech. Syst. Signal. Process.* **60** 182-97
[41] Müller M F, Kim J-Y, Qu J and Jacobs L J 2010 Characteristics of second harmonic generation of Lamb waves in nonlinear elastic plates *J. Acoust. Soc. Am.* **127** 2141-52
[42] Hu X, Ng C-T and Kotousov A 2022 Early damage detection of metallic plates with one side exposed to water using the second harmonic generation of ultrasonic guided waves *Thin-Walled Structures* **176** 109284
[43] Hughes J M, Kotousov A and Ng C-T 2020 Generation of higher harmonics with the fundamental edge wave mode *Appl. Phys. Lett.* **116** 101904
[44] Chillara V K and Lissenden C J 2014 Nonlinear guided waves in plates: A numerical perspective *Ultrasonics* **54** 1553-8
[45] Wan X, Tse P, Xu G, Tao T and Zhang Q 2016 Analytical and numerical studies of approximate phase velocity matching based nonlinear S0 mode Lamb waves for the detection of evenly distributed microstructural changes *Smart. Mater. Struct.* **25** 045023
[46] Zuo P, Zhou Y and Fan Z 2016 Numerical and experimental investigation of nonlinear ultrasonic Lamb waves at low frequency *Appl. Phys. Lett.* **109** 021902
[47] Yang Y, Ng C-T and Kotousov A 2018 Influence of crack opening and incident wave angle on second harmonic generation of Lamb waves *Smart. Mater. Struct.* **27** 055013
[48] Yang Y, Ng C T, Mohabuth M and Kotousov A 2019 Finite element prediction of acoustoelastic effect associated with Lamb wave propagation in pre-stressed plates *Smart. Mater. Struct.* **28** 095007
[49] Yang Y, Ng C-T and Kotousov A 2019 Bolted joint integrity monitoring with second harmonic generated by guided waves *Struct. Health Monitor.* **18** 193-204
[50] Sun M and Qu J 2020 Analytical and numerical investigations of one-way mixing of Lamb waves in a thin plate *Ultrasonics* **108** 106180
[51] Li W, Deng M, Hu N and Xiang Y 2018 Theoretical analysis and experimental observation of frequency mixing response of ultrasonic Lamb waves *J. Appl. Phys.* **124** 044901
[52] Hu X, Yin T, Zhu H, Ng C-T and Kotousov A 2022 Structural health monitoring of partially immersed metallic plates using nonlinear guided wave mixing *Construction and Building Materials* **346** 128381
[53] Blanloeuil P, Rose L, Veidt M and Wang C 2021 Nonlinear mixing of non-collinear guided waves at a contact interface *Ultrasonics* **110** 106222

[54] Sampath S and Sohn H 2022 Detection and localization of fatigue crack using nonlinear ultrasonic three-wave mixing technique *International Journal of Fatigue* **155** 106582
[55] Hasanian M and Lissenden C J 2018 Second order ultrasonic guided wave mutual interactions in plate: Arbitrary angles, internal resonance, and finite interaction region *J. Appl. Phys.* **124** 164904
[56] Matsuda N and Biwa S 2011 Phase and group velocity matching for cumulative harmonic generation in Lamb waves *J. Appl. Phys.* **109** 094903
[57] Ramatlo D A, Wilke D N and Loveday P W 2018 Development of an optimal piezoelectric transducer to excite guided waves in a rail web *NDT&E Int.* **95** 72-81
[58] Hakoda C and Lissenden C J 2020 Application of a general expression for the group velocity vector of elastodynamic guided waves *J. Sound Vib.* **469** 115165
[59] Fan Z, Castaings M, Lowe M J, Biateau C and Fromme P 2013 Feature-guided waves for monitoring adhesive shear modulus in bonded stiffeners *NDT&E Int.* **54** 96-102
[60] Yu X, Fan Z, Castaings M and Biateau C 2017 Feature guided wave inspection of bond line defects between a stiffener and a composite plate *NDT&E Int.* **89** 44-55
[61] Masserey B and Fromme P 2017 Analysis of high frequency guided wave scattering at a fastener hole with a view to fatigue crack detection *Ultrasonics* **76** 78-86
[62] Ramdhas A, Pattanayak R K, Balasubramaniam K and Rajagopal P 2015 Symmetric low-frequency feature-guided ultrasonic waves in thin plates with transverse bends *Ultrasonics* **56** 232-42
[63] Yu X, Manogharan P, Fan Z and Rajagopal P 2016 Shear horizontal feature guided ultrasonic waves in plate structures with 90 transverse bends *Ultrasonics* **65** 370-9
[64] Yu X, Ratassepp M and Fan Z 2017 Damage detection in quasi-isotropic composite bends using ultrasonic feature guided waves *Composites Science and Technology* **141** 120-9
[65] Vien B S, Rose L R F and Chiu W K 2017 Experimental and Computational Studies on the Scattering of an Edge-Guided Wave by a Hidden Crack on a Racecourse Shaped Hole *Materials* **10** 732
[66] Doherty C C and Chiu W K 2012 Three-dimensional finite element modelling of ultrasonic-guided wave scattering from fuel weep holes *Struct Health Monit* **11** 442-51
[67] Aseem A and Ng C T 2021 Debonding detection in rebar-reinforced concrete structures using second harmonic generation of longitudinal guided wave *NDT&E Int.* **122** 102496
[68] Zuo P, Yu X and Fan Z 2017 Numerical modeling of embedded solid waveguides using SAFE-PML approach using a commercially available finite element package *NDT&E Int.* **90** 11-23
[69] Sriramadasu R C, Banerjee S and Lu Y 2019 Detection and assessment of pitting corrosion in rebars using scattering of ultrasonic guided waves *NDT&E Int.* **101** 53-61
[70] Rucka M 2010 Experimental and numerical study on damage detection in an L-joint using guided wave propagation *J. Sound Vib.* **329** 1760-79
[71] Doherty C and Chiu W K 2012 Scattering of ultrasonic-guided waves for health monitoring of fuel weep holes *Struct Health Monit* **11** 27-42
[72] Masurkar F and Tse P 2020 Theoretical and experimental evaluation of the health status of a 1018 steel I-beam using nonlinear Rayleigh waves: Application to evaluating localized plastic damage due to impact loading *Ultrasonics* **108** 106036
[73] Zhu H, Ng C-T and Kotousov A 2022 The performance optimization of combinational harmonic generation for quasi-synchronous Lamb wave mixing. In: *Sensors and Smart Structures Technologies for Civil, Mechanical, and Aerospace Systems 2022*: SPIE) pp 293-300

[74] Cheng L, Xin H, Groves R M and Veljkovic M 2021 Acoustic emission source location using Lamb wave propagation simulation and artificial neural network for I-shaped steel girder *Construction and Building Materials* **273** 121706
[75] Wan X, Liu M, Zhang X, Fan H, Tse P W, Dong M, Wang X, Wei H, Xu C and Ma H 2021 The use of ultrasonic guided waves for the inspection of square tube structures: Dispersion analysis and numerical and experimental studies *Struct. Health Monitor.* **20** 58-73
[76] Heinlein S, Cawley P and Vogt T 2018 Reflection of torsional T (0, 1) guided waves from defects in pipe bends *NDT&E Int.* **93** 57-63
[77] Verma B, Mishra T K, Balasubramaniam K and Rajagopal P 2014 Interaction of low-frequency axisymmetric ultrasonic guided waves with bends in pipes of arbitrary bend angle and general bend radius *Ultrasonics* **54** 801-8
[78] Khalili P and Cawley P 2018 The choice of ultrasonic inspection method for the detection of corrosion at inaccessible locations *NDT&E Int.* **99** 80-92
[79] Bartoli I, Marzani A, Di Scalea F L and Viola E 2006 Modeling wave propagation in damped waveguides of arbitrary cross-section *J. Sound Vib.* **295** 685-707
[80] Predoi M V, Castaings M, Hosten B and Bacon C 2007 Wave propagation along transversely periodic structures *J. Acoust. Soc. Am.* **121** 1935-44
[81] Chen R, Hu C, Xu J, Gong Z, Liu L, Wang P and Chen X 2021 Research on guided wave propagation characteristics in turnout rails with variable cross-section *J. Sound Vib.* **494** 115853
[82] Zuo P and Fan Z 2017 SAFE-PML approach for modal study of waveguides with arbitrary cross sections immersed in inviscid fluid *J. Sound Vib.* **406** 181-96
[83] Hughes J M, Mohabuth M, Kotousov A and Ng C-T 2021 The fundamental ultrasonic edge wave mode: Propagation characteristics and potential for distant damage detection *Ultrasonics* **114** 106369
[84] Hughes J M, Mohabuth M, Khanna A, Vidler J, Kotousov A and Ng C-T 2021 Damage detection with the fundamental mode of edge waves *Struct. Health Monitor.* **20** 74-83
[85] Wilde M V, Golub M V and Eremin A A 2019 Experimental and theoretical investigation of transient edge waves excited by a piezoelectric transducer bonded to the edge of a thick elastic plate *J. Sound Vib.* **441** 26-49
[86] Feng F, Shen Z and Shen J 2017 Edge waves in a 3D plate: two solutions based on plate mode matching *Mathematics and Mechanics of Solids* **22** 2065-74
[87] Wilde M V, Golub M V and Eremin A A 2019 Experimental observation of theoretically predicted spectrum of edge waves in a thick elastic plate with facets *Ultrasonics* **98** 88-93
[88] Zernov V and Kaplunov J 2008 Three-dimensional edge waves in plates *Proceedings of the Royal Society A: Mathematical, Physical and Engineering Sciences* **464** 301-18

Chapter 2

Low-frequency Lamb wave mixing for fatigue damage evaluation using phase-reversal approach

Publication:

H. Zhu, C.T. Ng, and A. Kotousov, Low-frequency Lamb wave mixing for fatigue damage evaluation using phase-reversal approach, *Ultrasonics*, 124 (2022), 106768.

Statement of Authorship

Title of Paper	Low-frequency Lamb wave mixing for fatigue damage evaluation using phase-reversal approach
Publication Status	☑ Published ☐ Accepted for Publication ☐ Submitted for Publication ☐ Unpublished and Unsubmitted work written in manuscript style
Publication Details	H. Zhu, C.T. Ng, and A. Kotousov, Low-frequency Lamb wave mixing for fatigue damage evaluation using phase-reversal approach, Ultrasonics, 124 (2022), 106768.

Principal Author

Name of Principal Author (Candidate)	Hankai Zhu		
Contribution to the Paper	Conceptualization, Methodology, Experiment, Finite Element simulation, Validation, Formal analysis, Writing – original draft and editing.		
Overall percentage (%)	75%		
Certification:	This paper reports on original research I conducted during the period of my Higher Degree by Research candidature and is not subject to any obligations or contractual agreements with a third party that would constrain its inclusion in this thesis. I am the primary author of this paper.		
Signature		Date	23/10/2023

Co-Author Contributions

By signing the Statement of Authorship, each author certifies that:

i. the candidate's stated contribution to the publication is accurate (as detailed above);

ii. permission is granted for the candidate in include the publication in the thesis; and

iii. the sum of all co-author contributions is equal to 100% less the candidate's stated contribution.

Name of Co-Author	Ching-Tai Ng		
Contribution to the Paper	Supervision, Advising, Writing – review and editing.		
Signature		Date	6 Nov 2023

Name of Co-Author	Andrei Kotousov		
Contribution to the Paper	Supervision, Advising, Writing – review and editing.		
Signature		Date	7 Nov 2023

Chapter 2: Low-frequency Lamb wave mixing for fatigue damage evaluation using phase-reversal approach

Hankai Zhu[1], Ching Tai Ng[1], Andrei Kotousov[2]

[1] School of Civil, Environmental and Mining Engineering, The University of Adelaide, Adelaide, SA 5005, Australia

[2] School of Mechanical Engineering, The University of Adelaide, Adelaide, SA 5005, Australia

Abstract

Fatigue damage is difficult to detect and evaluate non-destructively, specifically at its early stages (before the macro-crack formation). In this study, fatigue damage is evaluated based on the growth rate of the combinational harmonics generated by mixing of two fundamental symmetric mode (S_0) of Lamb waves in the low frequency range. The incorporation of the phase reversal approach to the wave mixing method could potentially improve the evaluation of the combinational and second harmonics and avoid the influence of other undesirable harmonics. A series of parametric case studies are carried out using the three-dimensional (3D) finite element (FE) method to investigate the effects of the excitation frequencies and time delay of the incident waves in wave mixing on the transient response of a weakly-nonlinear material. The numerical results and experimental results show that the sum combinational harmonic and second harmonics are sensitive to weak material nonlinearities. Further experiments on damaged samples by cyclic loading demonstrate that the sum combinational harmonic has much better sensitivity to the progressive fatigue damage than the the second harmonics. In general, the outcomes of this study indicate that the damage evaluation of early stage fatigue damage is feasible and effective with the wave mixing method using the S_0 waves generated at low frequency, and the phase-reversal approach improves considerably the quality of experimental results in the fatigue damage evaluation.

Keywords: Nonlinear Lamb wave mixing, phase-reversal approach, material nonlinearity, fatigue damage, structural health monitoring

2.1. Introduction

Non-destructive evaluation (NDE) and structural health monitoring (SHM) are undisputedly important for maintaining structural integrity, specifically for structures working under cyclic loading. It is well recognized that progressive material degradation due to fatigue can lead to structural failures. Fatigue damage is difficult to evaluate at the early stage (before the formation of the macro crack) using the traditional NDE, which have been developed for evaluation of isolated material defects, discontinuities and inhomogeneities [1]. Relatively recently, nonlinear guided waves have attracted significant attention. In particular, these waves exhibit a good sensitivity to contact acoustic nonlinearities (CAN) [2-4] as well as to material nonlinearities [5-7]. The conventional approach relies on the second harmonic generation by using the cross-mode method, from the first order symmetric mode to the second order symmetric mode (S_1-S_2) [8, 9]. However, the cross-mode method requires a certain wave mode pair to achieve the synchronism and non-zero power flux conditions [10, 11], which are limited to few pairs in the high frequency range only [12]. Moreover, the main constraints of the cross-mode method are the influence of multi-modal and highly dispersive waves in the high frequency range (in the frequency range of MHz) on the accuracy of the experimental results. Hence, the detected signal can be severely distorted due to the coupling of the multiple modes [13]. In addition, the wave propagation distance, which is suitable for experimental measurements can be quite short due to the wave dispersion.

2.1.1. Combinational harmonic generation

The theoretical framework for describing the generation and propagation of the second harmonic using fundamental symmetric mode (S_0) of guided wave at low frequency have been provided by Muller et al. [14]. In this work, the conditions of the internal resonance for S_0 wave were derived. Wan et al. [15] suggested that S_0 wave is suitable for characterising weak material nonlinearities using the second harmonic. The maximum cumulative propagation distance of S_0 wave was examined numerically [15, 16], and these studies showed that S_0 wave in the lower frequency range can have a rather long propagation distance where the accumulation rate of the second harmonics is linear.

The utilisation of combinational harmonics can provide more information of the damage if compared with the conventional second harmonic [17, 18]. The wave mixing method can be used to generate second harmonics at the double of the fundamental frequencies at $2f_a$ and $2f_b$,

as well as combinational harmonics at $f_a + f_b$ and $f_b - f_a$, simultaneously. Ishii et al. [19] and Hasanian and Lissenden [20] conducted a study on the selection of wave mode pairs in wave mixing. Several studies demonstrated that the combinational harmonics may be more sensitive to micro-scale damage or defects than the second harmonics in the low frequency range [21-23]. However, this conclusion still requires further studies. The third order harmonics can also be generated using the wave mixing method. Li et al. [24] assessed the generation of the third order harmonics using the cross-mode method. It is also generally agreed that one of the main advantages of the wave mixing method is the minimisation of the nonlinearities associated with the instrumentation [25, 26]. The quasi-synchronised wave provides a better flexibility in the selection of the excitation frequency. It was demonstrated that quasi-synchronised waves can be used for the collinear wave mixing [26-28], which is the focus of the current study. Meanwhile, the noncollinear wave mixing and counter-propagating wave mixing methods are more suitable for the localised defect evaluation [29-31].

2.1.2. Extraction of harmonics using phase reversal approach

The phase reversal approach can be applied to enhance the characterisation of weak material nonlinearities. Kim et al. [32] showed that the phase reversal approach can be used to extract and characterise the second harmonic, while the fundamental harmonics and the third order harmonic can be supressed. Some studies focusing on metallic structures applied this approach for bulk waves [33, 34]. Li et al. [35] applied the phase reversal approach to extract the second harmonic using cross-mode method for the evaluation of low-velocity impact damage in composite plates, and the phase velocity matching and group velocity matching conditions should be satisfied [36]. Shan et al. [37] investigated the adhesive nonlinearity of a bonding layer using the low-frequency Lamb wave. The second harmonic due to the adhesive nonlinearity was extracted using the phase reversal approach. Their study suggested that the phase reversal approach may have an excellent performance if applied to the evaluation of the weak material nonlinearity. In this case the magnitudes of the amplitudes of the generated harmonics are usually much smaller than the corresponding harmonic amplitudes due to CAN [38, 39]. The second harmonic due to the CAN in a pipe was extracted using phase-reversal approach [40], and the envelop of the extracted signal in the time-domain was used for the quantitative evaluation of damage.

The studies focused on investigating the wave mixing of S_0 Lamb waves were limited, especially for the low frequency range. In the low frequency range, the synchronism and non-power flux conditions are achieved approximately, as the phase velocities of the fundamental frequency and the sum of the fundamental frequencies, and the mode shapes in the thickness direction are almost identical. In addition, the group velocities of S_0 waves are also very close at low frequency, the latter has been identified as an additional condition for wave mixing [17, 41], specifically for the co-directional collinear wave mixing [20]. The time delay of the incident wave may be applied if the two incident waves have matched group velocities, which allows that the incident waves to be generated by different excitation sources [42].

In this study, the phase reversal approach is incorporated into the wave mixing method. Further, the sensitivity of the combinational harmonics to weak material nonlinearities is investigated experimentally and numerically for the case of the wave mixing of two low-frequency S_0 waves. We also address the feasibility of the implementation of the phase-reversal approach using the collinear wave mixing to evaluate the second and combinational harmonics. The outcomes of this study provide basic knowledge and preliminary results, which can be implemented in the development of new damage detection techniques.

This paper is organised as follow. Section 2.2 introduces the phase reversal approach and wave mixing method. It also provides the theoretical background for mathematical modelling of the effects of material nonlinearities on wave generation. Section 2.3 presents a three-dimensional (3D) finite element (FE) model for simulating the nonlinear wave mixing. Parametric studies are performed to investigate the performance of different excitation frequency pairs in response to the weak material nonlinearities. It also investigates the effect of time delay of the incident waves on the harmonic wave generation. Then, Section 2.4 presents experimental results on wave mixing obtained using one-dimensional (1D) laser vibrometer. The effect of fatigue damage on wave generation is investigated using the wave mixing method and phase reversal approach. The experimental results also support the outcomes of the FE modelling provided in the previous section. Finally, the conclusions from the present study are drawn in Section 2.5.

2.2. Theoretical background

2.2.1. Nonlinear response of wave mixing

Assuming the nonlinearity is considerably small compared with the linear wave components, and therefore the perturbation method can be applied [43, 44]. Using the superposition of the homogeneous solution and the nonhomogeneous solution, and this leads to the final solution which represents the original displacement field of mixing wave,

$$\begin{aligned} u\,(x,t)^{(0°)} &= A_a\,sin(k_a x-\omega_a t)+A_b\,sin(k_b x-\omega_b t) \\ -\frac{\beta x}{8c^2}\{&{A_a}^2{\omega_a}^2\,cos2(k_a x-\omega_a t)+{A_b}^2{\omega_b}^2\,cos2(k_b x-\omega_b t) \\ &+2A_aA_b\omega_a\omega_b\,cos[(k_a+k_b)x-(\omega_a+\omega_b)t] \\ &+2A_aA_b\omega_a\omega_b\,cos[(k_b-k_a)x-(\omega_b-\omega_a)t]\} \end{aligned} \tag{2.1}$$

where A_a, A_b, ω_a, ω_b, k_a and k_b are amplitude, angular frequencies, and wavenumber of waves *a* and *b*. c is the wave velocity. β is the relative nonlinear parameters. Based on the Equation (2.1), the phase-reversed displacement field (with 180° phase shift) of the wave mixing can be determined. The phase reversal approach is carried out through superposition of the original displacement field and phase-reversed displacement field as shown in Equation (2.2).

$$\begin{aligned} u\,(x,t)^{(0°+180°)} = -\frac{\beta x}{8c^2}\{&2{A_a}^2{\omega_a}^2\,cos2(k_a x-\omega_a t)+2{A_b}^2{\omega_b}^2\,cos2(k_b x-\omega_b t) \\ &+4A_aA_b\omega_a\omega_b\,cos[(k_a+k_b)x-(\omega_a+\omega_b)t] \\ &+4A_aA_b\omega_a\omega_b\cos\,[(k_b-k_a)x-(\omega_b-\omega_a)t]\} \end{aligned} \tag{2.2}$$

The relative nonlinear parameters of second harmonic (β') and combinational harmonics ($\beta_{\pm}{}'$) are defined in Equations (2.3a) and (2.3b), respectively.

$$\beta' = \frac{A_2}{{A_1}^2} \tag{2.3a}$$

$$\beta_{\pm}{}' = \frac{A_{b\pm a}}{A_aA_b} \tag{2.3b}$$

where A_1 is the amplitude of the linear wave response, A_2 is the amplitude of second harmonic, and $A_{b\pm a}$ represent the amplitude of combinational harmonics.

The amplitudes of the displacements in the nonlinear wave components in Equation (2.2) are doubled in comparison with the classical solution, Equation (2.1), due to the application of the phase-reversed approach. The corresponding frequency spectrum can be

obtained using the Fourier transform, and it is schematically illustrated in Figure 2.1, where f_a and f_b are the frequencies of waves *a* and *b*, respectively.

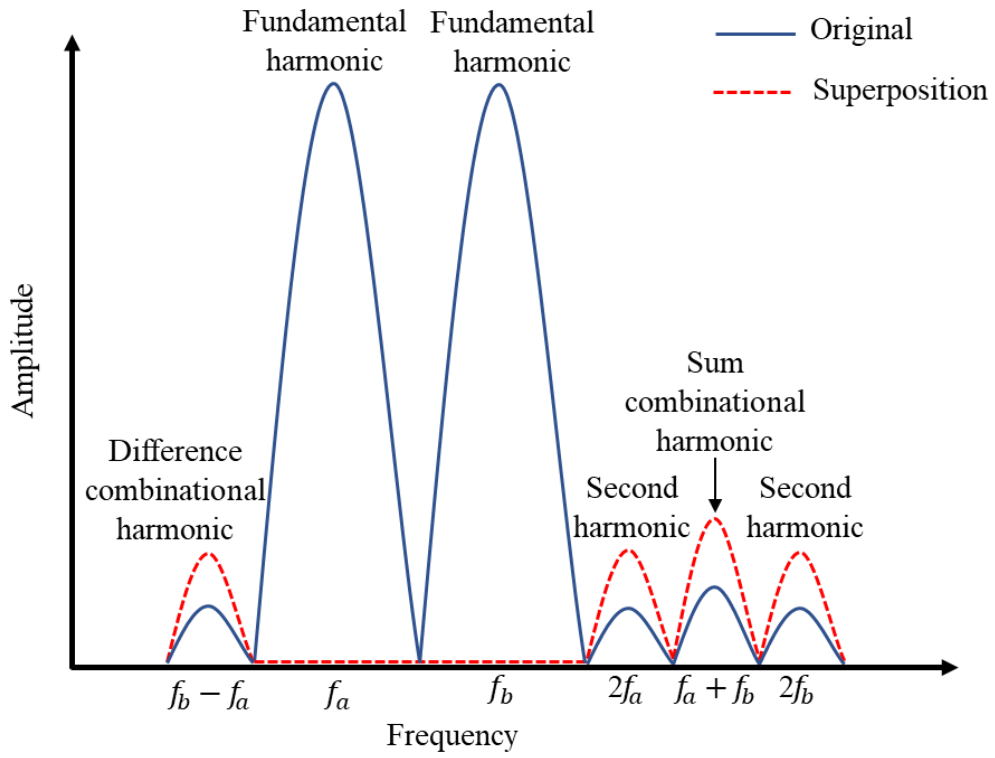

Figure 2.1. Schematic diagram of phase-reversal approach incorporated into wave mixing method in frequency spectrum

As shown in Figure 2.1, the generation of the linear response corresponding to the fundamental frequencies is supressed with the phase reversal approach, and only the second harmonics and combinational harmonics remained. In addition to the elimination of the fundamental harmonics, the phase reversal approach also supresses the third order harmonics [38]. All these features can be considered as a significant advantage of the present approach.

It can be noted that the phase reversal approach can also be applied for enhancing the evaluation of the third order harmonics by subtracting the original and phased-reversed displacement fields. However, the enhancement of the third order harmonic results in the cancellation of the second order harmonics. The present study focuses on the sum combinational harmonic (f_a + f_b), and therefore, the fundamental harmonics at excitation frequencies and the third order harmonics are minimized after the superposition of the original

and phased-reversed displacement fields. In the present study, a circular PZT is utilised to generate the incident waves, which may be considered as a source of circular-crested waves. The phase reversal approach is still applicable in this case, and the circular-crested waves asymptotically approach the straight-crested waves, which can be considered as the plane waves at long propagation distances, from the transient FE studies, say longer than three wavelengths.

2.2.2. Modelling of material nonlinearity

The material nonlinearities and field equations can be incorporated into the FE modelling. Below we briefly overview the basic equations and procedure. The classical infinitesimal theory only considers the second order terms, and therefore the theory is limited to linear materials. The third order terms of the Murnaghan's strain energy function can also be incorporated into FE for the simulation of material nonlinearities as demonstrated in the previous studies [45, 46].

Using the reference configuration $\boldsymbol{X}$ to describe the current configuration of material $\boldsymbol{x}$ [11], the displacement vector $\boldsymbol{u}$ and displacement gradient tensor $\boldsymbol{F}$ are expressed as

$$\boldsymbol{u} = \boldsymbol{x} - \boldsymbol{X} \tag{2.7a}$$

$$\boldsymbol{F} = \frac{\partial \boldsymbol{x}}{\partial \boldsymbol{X}} = \boldsymbol{I} + \boldsymbol{H} \tag{2.7b}$$

where $\boldsymbol{I}$ denotes identity tensor, and $\boldsymbol{H}$ denotes the displacement gradient, which can be further expressed as $\boldsymbol{H} = \partial \boldsymbol{u}/\partial \boldsymbol{X}$. The second Piola-Kirchhoff stress for an isotropic medium can be expressed in terms of Murnaghn's strain energy function W in respect of the Green-Lagrange strain tensor $\boldsymbol{E}$ [47].

$$\boldsymbol{T}_{\boldsymbol{pk2}} = \frac{\partial W(\boldsymbol{E})}{\partial \boldsymbol{E}} \tag{2.8a}$$

$$\boldsymbol{E} = \frac{1}{2}(\boldsymbol{H} + \boldsymbol{H}^T + \boldsymbol{H}^T\boldsymbol{H}) \tag{2.8b}$$

The Murnaghn's strain energy function [48] can be expressed using principal invariants i_1, i_2 and i_3,

$$W(\boldsymbol{E}) = \frac{1}{2}(\lambda + 2\mu){i_1}^2 + \frac{1}{3}(l + 2m){i_1}^3 - 2\mu i_2 - 2m i_1 i_2 + n i_3 \tag{2.9}$$

where λ and μ are Lame's elastic constants. l, m and n are third order elastic constants. The principal invariants can be expressed as $i_1 = tr(\boldsymbol{E}), i_2 = \frac{1}{2}\left[{i_1}^2 - tr(\boldsymbol{E})^2\right], i_3 = det(\boldsymbol{E})$.

Hence, the Cauchy stress can be obtained in terms of the second Piola-Kirchhoff stress $\boldsymbol{T_{pk2}}$ and deformation gradient $\boldsymbol{F}$ as

$$\sigma = \boldsymbol{J}^{-1}\boldsymbol{F}\frac{\partial W(\boldsymbol{E})}{\partial \boldsymbol{E}}\boldsymbol{F}^T \tag{2.10}$$

where $\boldsymbol{J}^{-1}$ is the Jacobian determinant of deformation gradient $\boldsymbol{F}$, and the Equation (2.10) is applicable for the formulation of the constitutive behaviour of material in the VUMAT subroutine [16], which can be implemented in ABAQUS/Explicit for modelling the weak material nonlinearity.

2.3. Numerical case studies

2.3.1. 3D finite element model

The wave propagation behaviour was simulated in ABAQUS/Explicit using a 3D FE model. The material properties of 6061-T651 aluminium plate are listed in Table 2.1 [49], which are consistent with the material properties utilised in the experimental study (in the experimental studies section).

Table 2.1. Material properties of 6061-T651 aluminium at intact conditions [49]

ρ (kg·m^{-3})	λ (GPa)	μ (GPa)	l (GPa)	m (GPa)	n (GPa)
2704	54.3	27.2	-281.5	-339.0	-416.0

The thickness of the plate is 1.6 mm and the reduced dimension of plate was modelled to reduce the computational cost. Hence, the symmetric boundary conditions were applied, and the width of the plate is 400 mm with the length of 800 mm as shown in Figure 2.2. The highest excitation frequency was 200 kHz because of the quasi-synchronism and group velocity matching based on the dispersion curve (Figure 2.8a shown in the experimental validation of 3D FE model section). Therefore the element size of 0.4 mm was selected in the FE simulation to ensure more than 20 elements per wavelength [50]. Eight layers of element are applied in

the thickness direction, and eight-node linear brick element with reduced integration (C3D8R) was used in the FE model.

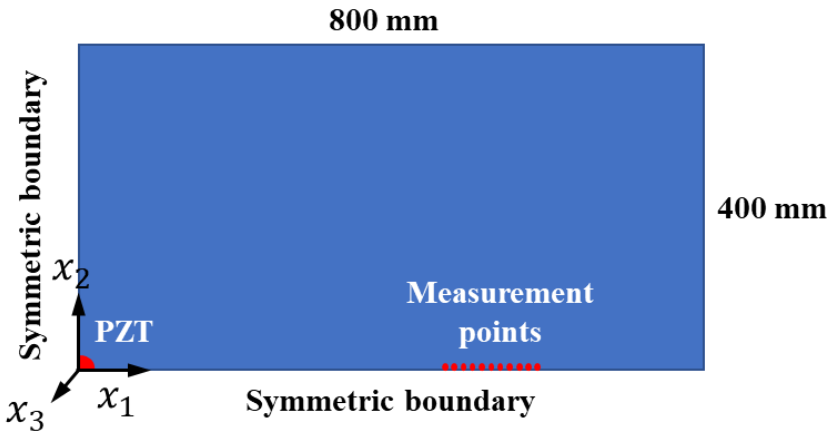

Figure 2.2. 3D FE model

A quarter of circular PZT was simulated using the problem symmetry, and the fundamental Lamb wave mode was excited by applying vertical nodal displacement with 7 µm amplitude on the nodes of the quarter of circular PZT. A cyclindrical coordinate was used for the PZT to simulate the generation of circular-crested waves. The symmetric boundary conditions can also prevent the generation of edge waves and ensure the measured waves are Lamb waves. The first measurement point is set at 400 mm from the centre of the PZT and the remaining measurement points were calculated with an interval of 10 mm, which ensure the S_0 wave and A_0 wave are completely separated since the S_0 wave propagates much faster than the A_0 wave mode in the low frequency range. Therefore, the undisturbed S_0 wave can be measured at the selected points. The vertical nodal displacement was calculated at the top surface of the plate (in the x_3 direction), which is cosnsistent with the experimental measurements in the next section. A small value of damping was added in the FE model to ensure the computational stability. The Hann window was employed on the carrier frequencies, and two fundamental waves were pre-mixed to generate the excitation signal. The sensitivity of varying frequency pairs for wave mixing in response to weak material nonlinearites and the effect of time delay on the incident waves are studied using numerical parametric studies as discussed in the following sections.

2.3.2. Effect of varying excitation frequencies on wave mixing

In Table 2.2, four cases of frequency pairs for wave mixing are considered to investigate the sensitivity of varying excitation frequencies on weak material nonlinearity. The frequency pairs of wave mixing are selected based of quasi-synchronous phase velocity in the low frequency range from 100 kHz to 200 kHz as shown in the dispersion curve (Figure 2.8a in the experimental studies section). Different numbers of cycles are used for the higher frequency wave *b*, to pair with the time duration of the lower frequency wave *a*.

Table 2.2. Different cases of wave mixing frequency pairs with varying excitation frequencies

Case	Fundamental frequency (f_a)	Number of cycles (N_a)	Fundamental frequency (f_b)	Number of cycles (N_b)
1	125 kHz	8 cycles	175 kHz	8 cycles
2	130 kHz	8 cycles	170 kHz	9 cycles
3	135 kHz	8 cycles	185 kHz	10 cycles
4	145 kHz	8 cycles	185 kHz	9 cycles

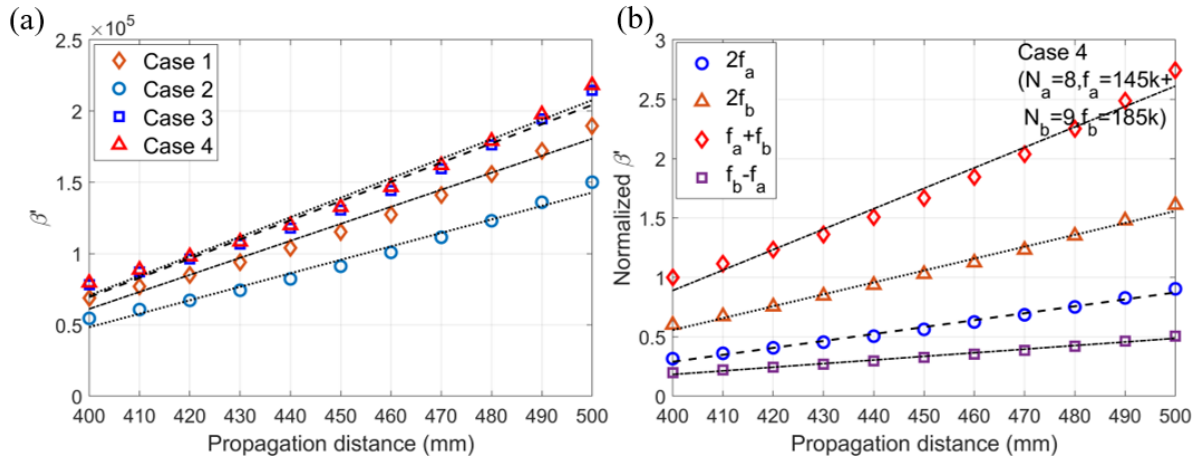

Figure 2.3. FE simulated relative nonlinear parameter of (a) sum combinational harmonic of different excitation frequencies in wave mixing and (b) comparison with second harmonics and combinational harmonics in Case 4

The second harmonics and combinational harmonics are extracted by the superposition of the original signal and the phase-reversed signal in the time-domain, and the measured time-domain signals are analysed using fast Fourier transform (FFT). The amplitude of the fundamental harmonics and second order harmonics of original signal in frequency spectrum is nearly identical to the amplitude of the phase-reversed signal. The relative nonlinear parameter of superposed signal showed approximately doubled amplitude compared with that of the original signal. The phenomenon agrees well with the Equation (9a). Figure 2.3a shows the relative nonlinear parameters of sum combinational harmonic of varying excitation frequencies after using phase reversal approach. The linearly proportional increase of relative nonlinear parameters with propagation distance is observed in all four cases, which indicates the cumulative effect due to the weak material nonlinearities. In particular, Case 4 shows higher amplitude of sum combinational harmonic generation, which can be considered as better performance to weak material nonlinearities than other frequency pairs of wave mixing. The second and combinational harmonics of Case 4 are compared in Figure 2.3b, and the relative nonlinear parameters are normalized about the value of sum combinational harmonic at the first measurement point since one of the main focus of this study is on the performance of sum combinational harmonic. The results suggest that the sum combinational harmonic ($f_a + f_b$) has better performance compared with the second harmonics ($2f_a$ and $2f_b$). The difference combinational harmonic ($f_b - f_a$) in Figure 2.3b shows negligible harmonic cumulation, which is likely due to the normal excitability of the low-frequency S_0 wave [51]. The out-of-plane displacement is received, and the sensing sensitivity of S_0 wave is lower at the low frequency ($f_b - f_a$) compared with the high frequency ($f_a + f_b$). Hence, the second harmonics ($2f_a$ and $2f_b$) and sum combinational harmonic ($f_a + f_b$) are the focus of the experimental studies.

2.3.3. Effect of time delay on the incident waves

The time delay can be applied for S_0 wave mixing in the low frequency range. In this section, the effect of the time delay on the generation of combinational harmonic is investigated, and due to space limitations only the results of Case 4 are shown in Figure 2.4. The varying time delays were applied on the higher frequency wave *b*, from 0 μs to 6.6 μs, and the peaks of two fundamental waves in time domain are matched when the time delay is 3.3 μs.

Figure 2.4 shows the frequency spectrum of the original signal with varying time delay in wave mixing. In Figure 2.4a, the second harmonics ($2f_a$ and $2f_b$) are coupled with the sum

combinational harmonic (f_a + f_b), which is very difficult for the harmonic analysis of combinational harmonics and second harmonics. The second harmonics and the sum combinational harmonic are separated asymptotically with the increase of the time delay from 0 µs to 3.3 µs, and reached the minimum overlapping at time delay of 3.3 µs (as shown in Figures 2.4b and 2.4c). The overlapping between second harmonics and sum combinational harmonic increased from time delay of 3.3 µs to 6.6 µs (in Figure 2.4d). Hence, the time delay of 3.3 µs is used for wave mixing of Case 4, considering that the second harmonics and the sum combinational harmonic need to be analysed for comparison.

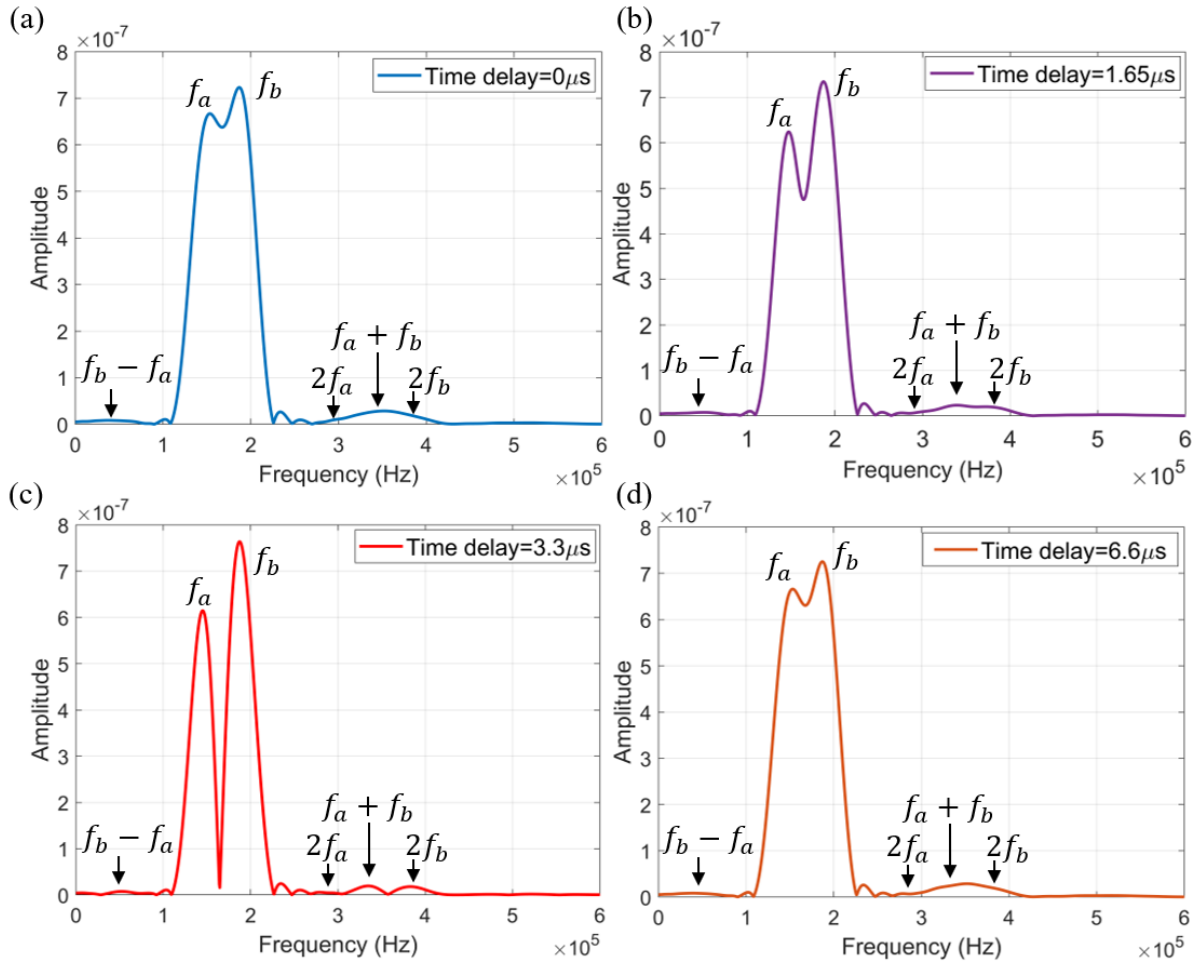

Figure 2.4. FE simulated effect of time delay on the incident waves (a) 0 µs; (b) 1.65 µs; (c) 3.3 µs and (d) 6.6 µs in Case 4

2.4. Experimental Studies

2.4.1. Experimental setup

The experimental setup for guided wave testing is shown in Figure 2.5. The pre-mixing tone-burst pulse was generated using a NI PXIE-5122 signal generation module, which was amplified by the Ciprian high-voltage power amplifier using peak-to-peak voltage of 160V. The amplified excitation signal was passed through a 10mm diameter and 0.5mm thickness of circular PZT, and was then applied to an intact plate specimen (length=1100 mm, width=508 mm, thickness=1.6 mm). The PZT was bonded on the specimen using thin layer of conductive epoxy, and the nonlinearity of which is trivial [37], and therefore, it is neglected in this study. The specimen was fixed on a frame, and placed perpendicular to the 1D laser head. Reflective painting was applied over the scanning area to enhance the signal reflection for 1D laser vibrometer. The same four cases (see Table 2.2) as in the numerical case studies were reproduced in the present experiments.

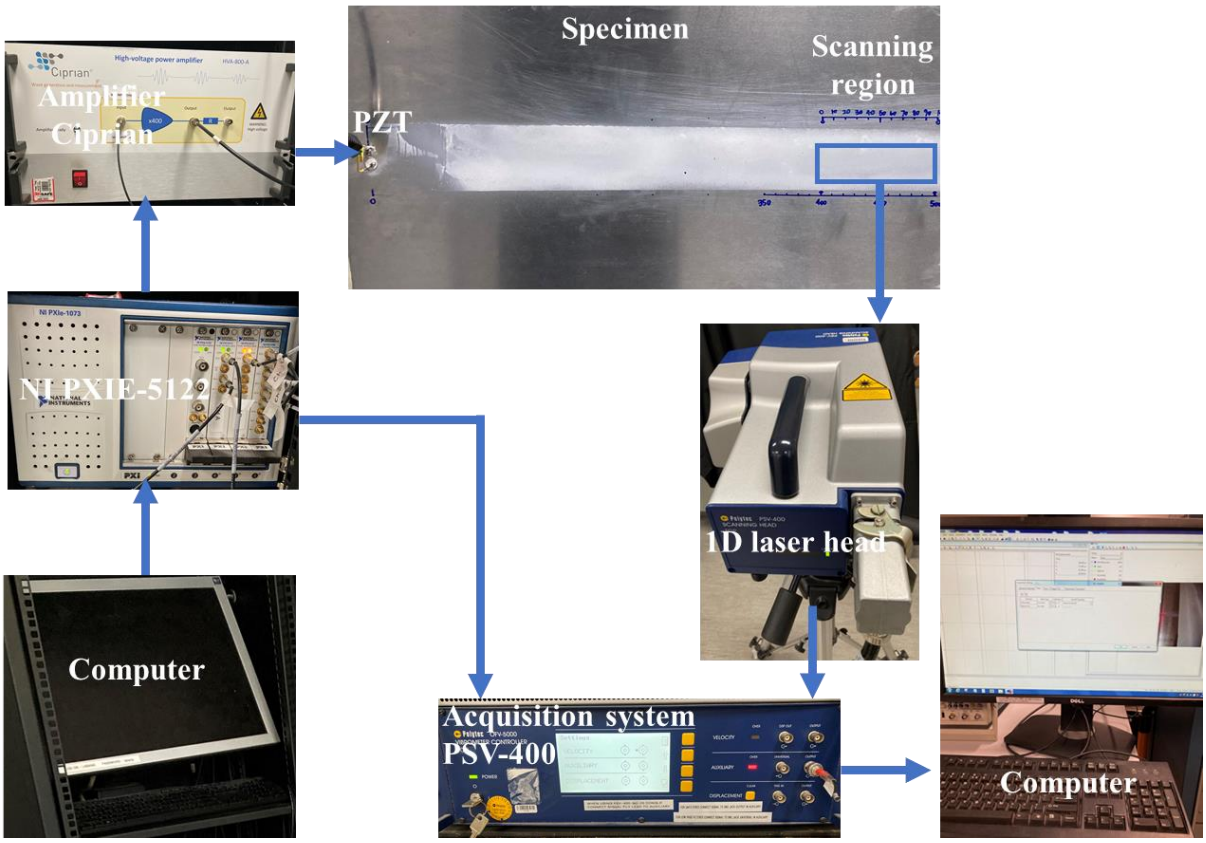

Figure 2.5. Experimental setup for guided wave testing using 1D laser vibrometer

The first measurement point is located 400 mm from the excitation source, and the interval between remaining measurement points is 10 mm, which is identical to the numerical case studies described in the numerical case studies section. The out-of-plane displacement

field was measured using by 1D laser vibrometer [52], and the data was acquired by the PSV-400 acquisition system, which was connected to the computer. The acquisition system was also connected to the NI PXIE-5122 signal generation module to synchronize the excitation signal. The sampling frequency was set at 25.6 MHz with 39.06 nanosecond sampling resolution. Each measurement was obtained by averaging of 1200 signal acquisition to improve the signal-to-noise ratio. Low pass filter form 0 kHz to 800 kHz was applied as the low frequency range is the focus of this study. The measurement for each frequency pair was repeated four times with room temperature of approximately 20 °C, and the time interval between each group of measurement was around 4 hours with all instruments reconnected and calibrated.

2.4.2. Weak material nonlinearity

The S_0 waves are extracted from the obtained time-domain displacement signals (see Figure 2.8b). The phase-reversal approach is then applied by superposition of the original signals and the phase-reversed signals in the time-domain. Figure 2.6b indicates that the phase-reversal approach provides an excellent improvement to the quality of experimental data. In particular, it minimises the fundamental harmonics, and hence, the second harmonics and combinational harmonics can be evaluated more efficiently. The third order harmonics are also suppressed, which also reduces the overlapping of harmonics and improves the overall quality of the signal processing. It can be noted that the original signal and the phase-reversed signal have a small discrepancy as shown in Figure 2.6a, which are identical in the FE simulations. The small discrepancy in the frequency-domain may be caused by a minor amplitude difference between the original signal and the phase-reversed signal in the time-domain. The asymptotic expression of the zeroth order Bessel function of the first kind is related to the phase lag, in the case when the circular-crested waves are generated using circular PZT [53]. The vertical displacement field of the circular-crested waves are directly associated with the zeroth order Bessel function of the first kind. Hence, the amplitude difference in displacement field may be associated with the phase difference between the original signal and the phase-reversed signal, which introduces additional phase shift of π. In addition, there are measurement noise in experiment [54], and the displacement amplitude is relatively small in out-of-plane direction. Since the small discrepancy of second and combinational harmonics in original signal and the phase-reversed signal, the second and combinational harmonics of superposed signal are

considered as the superposition of that of the original signal and that of the phase-reversed signal, which agrees well with the results shown in Figure 2.6b.

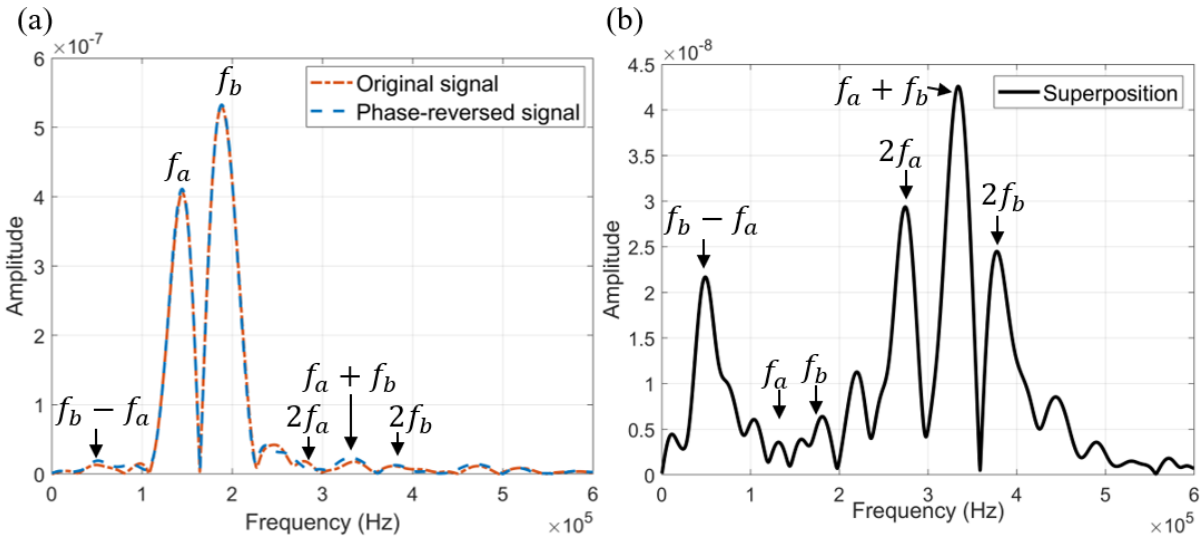

Figure 2.6. Experimentally measured weak material nonlinearity using phase reversal approach in frequency spectrum at the first measurement point of Case 4. (a) Original signal and phase-reversed signal, and (b) signal obtained after superposition

In Figure 2.7, the sum combinational harmonic (f_a + f_b) for varying wave mixing frequency pairs is plotted against the wave propagation distance. The relative nonlinear parameters of the original signal, phase-reversed signal and the superposed signal are analysed for each frequency pair of wave mixing. The results of Figure 2.7 show that the relative nonlinear parameter is linearly proportional with the propagation distance for all four considered cases. The best fit functions are shown with the error bars, and the results show linear increasing trend. The R-square value indicates the level of difference between the observed data and the fitted function. The higher value of R-square indicates a better performance on the accumulation of material nonlinearity. The sum combinational harmonic shows better performance with improved R-square value after the phase-reversal approach was applied compared with that of the original signal and the phased-reversed signal. This phenomenon is observed in all four cases of wave mixing frequency pairs, and this could be considered as the improved quality of experiments due to the extraction of sum combinational harmonic.

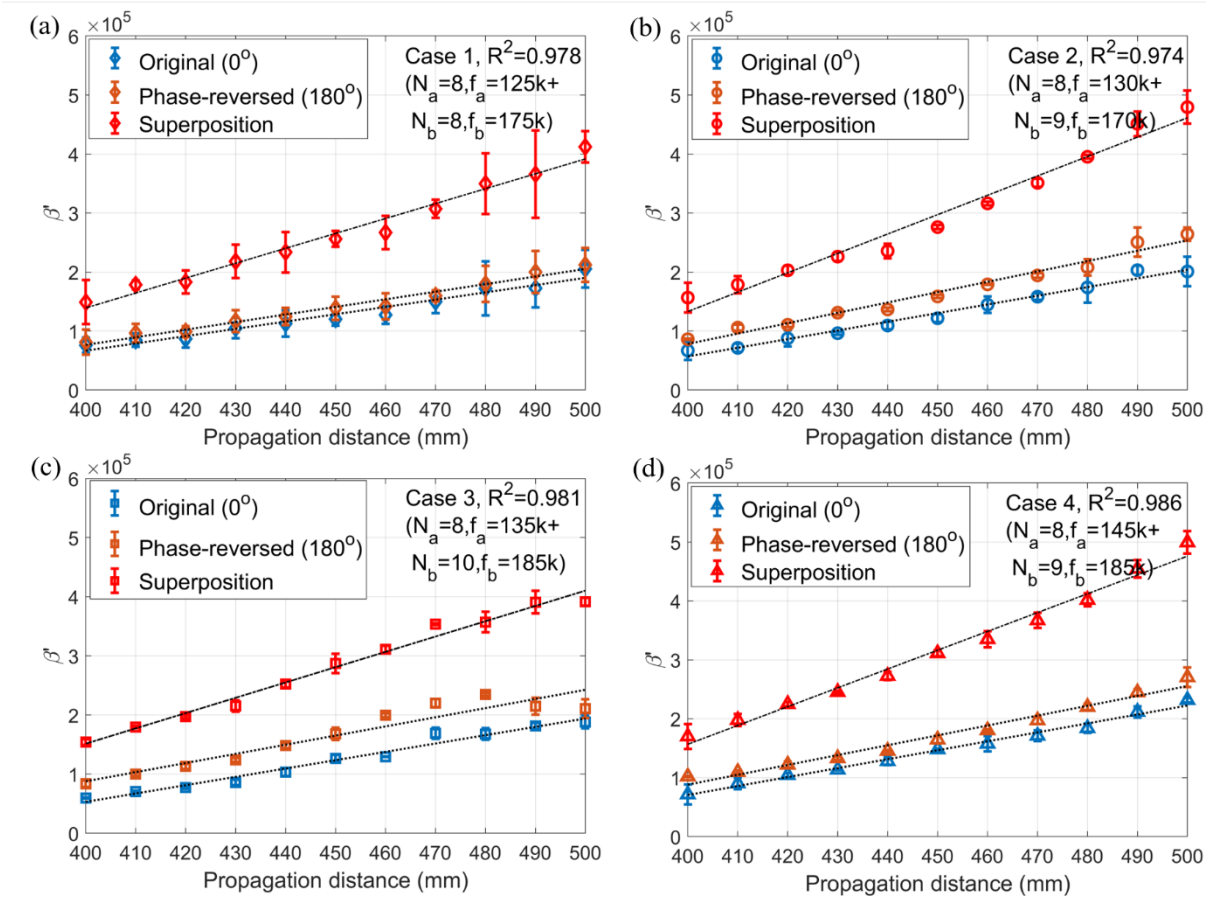

Figure 2.7. Experimentally measured relative nonlinear parameters of sum combinational harmonic generation on weak material nonlinearity, (a) Case 1, (b) Case 2, (c) Case 3, and (d) Case 4

The second order harmonics and third order harmonics show overlapping in the frequency spectrum of Case 1 and Case 3 before phase-reversal approach is applied. This could be one of the reasons of the relative nonlinear parameter discrepancy in Case 1 and Case 3 (see Figures 2.7a and 2.7c). The second harmonics and combinational harmonics are extracted efficiently using phase-reversal approach, which reduces the overlapping significantly, and therefore the phase-reversal approach could provide additional advantage on wave mixing in the low frequency range. In Figure 2.7d, Case 4 has a better performance with respect to the harmonic accumulation with a higher value of R-square, and the error bars are typically smaller, which are consistent with the results in the numerical case studies. The frequency pair of wave mixing corresponding to Case 4 is also applied to fatigue samples, the outcomes will be discussed in the progressive fatigue damage section.

2.4.3. Experimental validation of 3D finite element model

The linear features of guided waves include the group velocity, phase velocity, and the waveform of mixing waves in time-domain. The group velocity and phase velocity of S_0 waves are measured in numerical simulations and experiments. The frequency is measured from 100 kHz to 200 kHz with 10 kHz interval. In the numerical simulations, the group velocity and phase velocity are measured up to 400 kHz to ensure that the FE model can accurately capture the second harmonic of the highest fundamental frequency. DISPERSE software is a commercial package, which utilises global matrix to calculate the phase velocity and the group velocity [55].

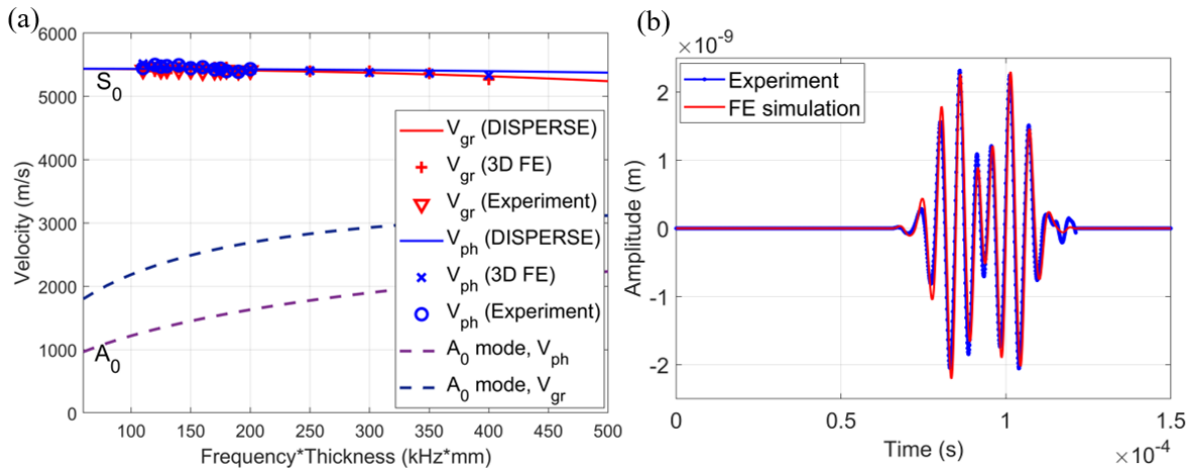

Figure 2.8. Linear features of guided wave validation (a) dispersion curve and (b) time-domain displacement signals of mixing wave at the first measurement point in Case 4

Figure 2.8a shows a very good agreement between the DISPERSE results, FE simulation and experimental data. Staszewski et al. [52] argued that the peak amplitude of 1D laser-based measurement could be compared with the numerical simulation after normalization. The time domain signals of numerical simulations also matches well with the experimental data for all measurement points, when the numerical results are normalized by the peak displacement amplitude in experiment at the first measurement point for all the measurement points in numerical simulation. The comparison of time-domain displacement signals at the

first measurement point is shown in Figure 2.8b. The well-matched linear features of the S_0 waves suggest that the FE model provides a good prediction of linear guided wave propagation.

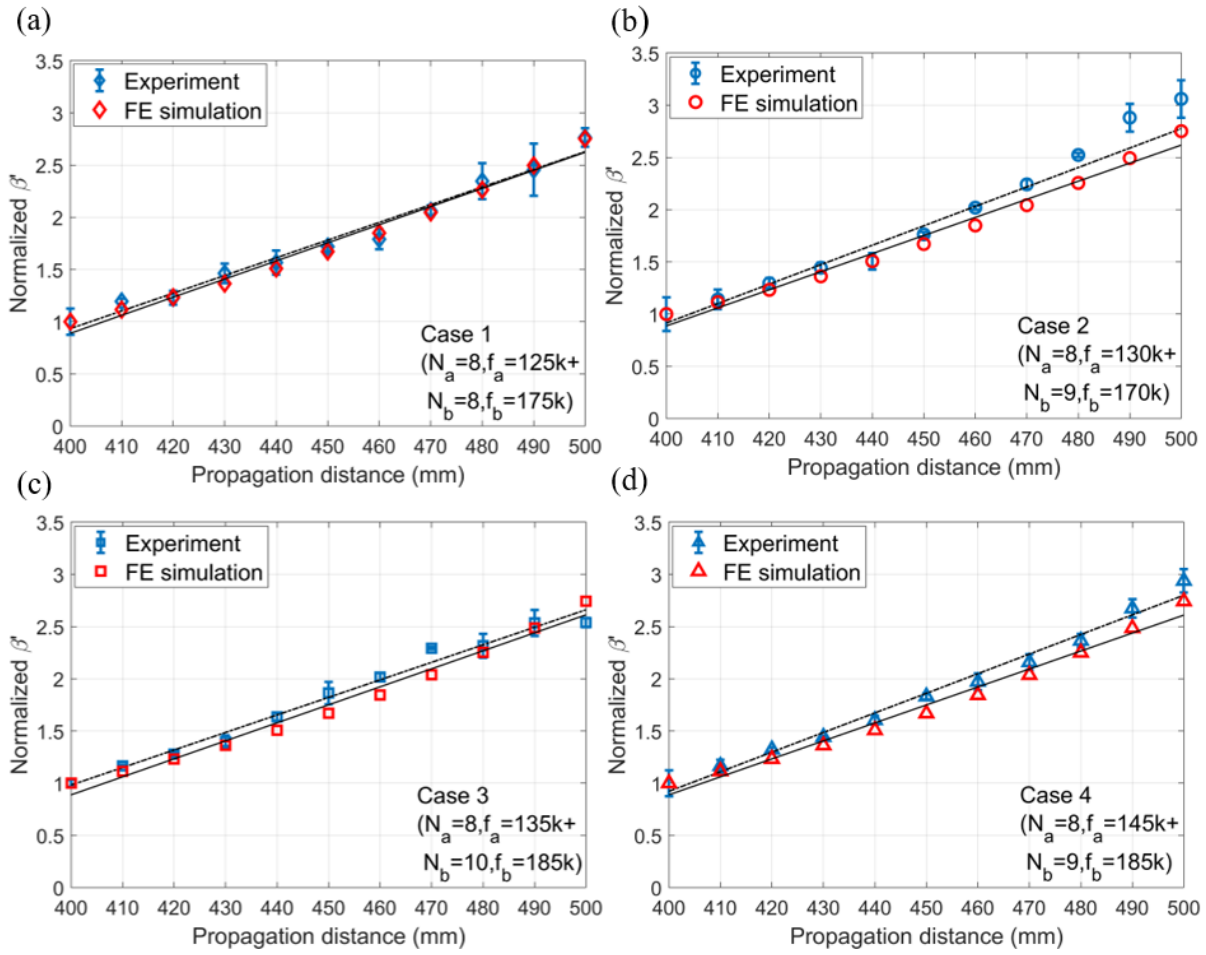

Figure 2.9. Validation of relative nonlinear parameters of sum combinational harmonic against wave propagation distance in (a) Case 1, (b) Case 2, (c) Case 3 and (d) Case 4

There are four wave mixing frequency pairs, which were simulated numerically and reproduced experimentally. The nonlinear response of wave mixing obtained numerically is validated experimentally after the normalization of the relative nonlinear parameters. The numerical results and the experimental results are normalized by the relative nonlinear parameter value at the first measurement point. The results show linear increasing trend due to the accumulation of material nonlinearity response over the propagation distance. The sum combinational harmonics of superposed signals are compared in Figure 2.9, and the results show very good agreement between numerical simulation and experimental results. In Figure 2.9b, the last two points are considered as the outliers of the best fitted line for Case 2. The

relatively large error bar at these two points may be caused by the small out-of-plane displacements after a long propagation distance [52]. However, the good prediction of the accumulation effect can be observed in this case since the increasing trends of the numerical simulations and experimental results are approximately identical.

2.4.4. Progressive fatigue damage

The aluminium specimen had length of 850 mm and width of 508 mm to meet the size constraints of the testing machine (INSTRON 1242). The specimen was connected with the testing machine with steel grips and 26 bolts, which were evenly distributed at the two sides of the specimen to improve the connection with the testing machine and distribute the cyclic loading evenly. The fatigue damage is introduced by applying the maximum tensile loading of 90 kN (at R = 0.1) with loading frequency of 1.5 Hz to prevent the buckling of a slender specimen during the cyclic testing. The measurement is carried out with 5,000 fatigue cycles interval, and the specimen finally fails after 12,417 fatigue cycles in the bolting region, where material strength is weakened by the stress concentration due to the holes. The guided wave testing uses identical setup as shown in the experimental setup section, and the position of laser vibrometer and supporting frame of specimen remains unchanged to ensure the cumulative effect is measured consistently. However, the measurement points are moved forward to avoid boundary reflection of incident waves, and the first measurement point is at 190 mm from the excitation location, which is more than five wavelengths of the wave with lower excitation frequency.

The results in Figure 2.10a show excellent sensitivity of the sum combinational harmonic ($f_a + f_b$) to the fatigue damage. The slope of linear trend obviously increases with the cumulation of fatigue damage. The results agree well with the previous study [32]. The R-square value increases with the level of the fatigue damage. The reduced R-square value in intact plate compared with the same case in Figure 2.7d may be due to the reduced propagation distance. In Figure 2.10b, the sum combinational harmonic at the first measurement point rapidly increases from intact condition to the fatigue damage of 5000 cycles, and has slower increase from 5000 cycles to 10000 cycles. The results show that the sum combinational harmonic generation has a good sensitivity to the progressive fatigue damage, and the phase reversal approach is effective to extract and evaluate the sum combinational harmonic.

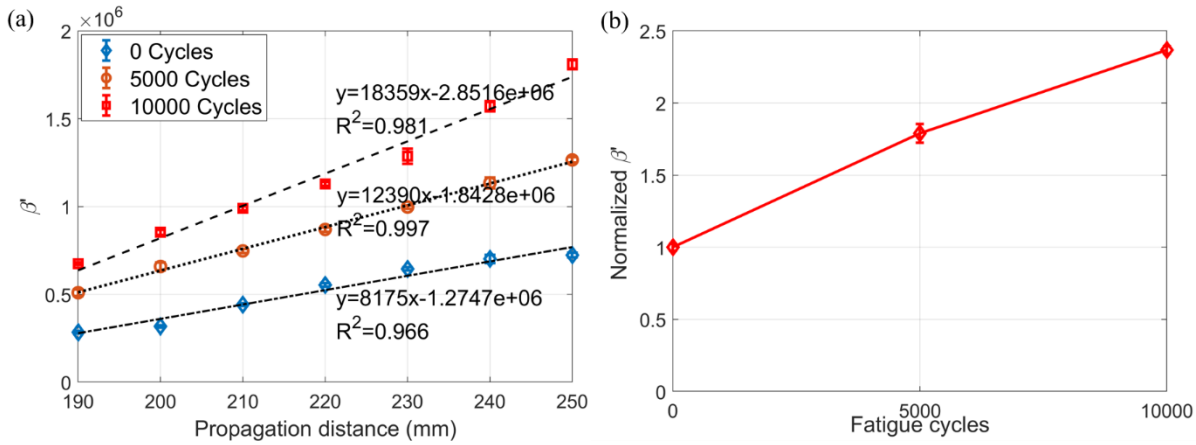

Figure 2.10. (a) Experimentally measured relative nonlinear parameters of sum combinational harmonic using phase-reversal approach with different fatigue cycles against propagation distance, and (b) normalized relative nonlinear parameter at the first measurement point

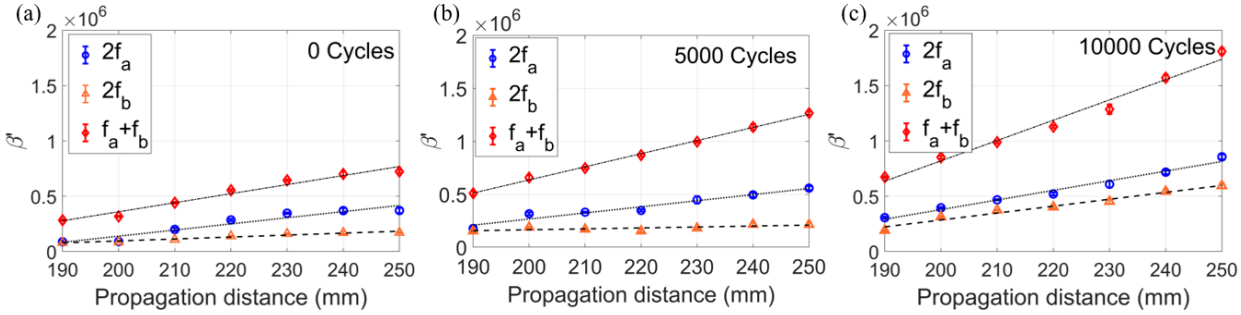

Figure 2.11. Comparison of sum combinational harmonic and second harmonics using phase-reversal approach with different fatigue cycles

The sum combinational harmonic ($f_a + f_b$) and the second harmonics ($2f_a$ and $2f_b$) are compared in Figure 2.11, and the relative nonlinear parameter of fatigue cycles of 0 cycles, 5000 cycles and 10000 cycles are shown for comparing the rate of accumulation of progressive fatigue damage. The slopes of second harmonics ($2f_a$ and $2f_b$) have increasing trend with the number of fatigue cycles. This shows the sensitivity of second harmonics of S_0 waves at low frequency to the progressive fatigue damage, and it is consistent with the previous studies [15, 56, 57]. The sum combinational harmonic ($f_a + f_b$) exhibits a better sensitivity to fatigue damage than the second harmonics ($2f_a$ and $2f_b$), and shows better consistency of linear increasing trend with propagation distance. The results suggest that the S_0 wave mixing using phase-reversal

approach has an excellent performance, and it is effective for the evaluation of progressive fatigue damage in low cycle fatigue regime.

2.5. Conclusion

The wave mixing of two S_0 waves show good sensitivity on the accumulation of fatigue damage. The results of the harmonic generation and accumulation show a better performance for the sum combinational harmonic ($f_a + f_b$) compared with second harmonics (at $2f_a$ and $2f_b$). The progressive fatigue damage can be explicitly determined by the extraction and evaluation of the accumulation rate of the second order harmonics. Overall, the phase-reversal approach combined with the wave mixing method for S_0 waves at low-frequency exhibits a great potential, especially for challenging situations, e.g. when the generation of combinational harmonics is small and overlapped with third order harmonics. The findings of this study can be useful to practical application and development of SHM for continuous evaluation of damage, using the wave mixing method.

Acknowledgement

This work was partially funded by the Australian Research Council (ARC) DP200102300 and DP210103307 grants. The authors are grateful for this support. The authors would like to thank Tingyuan Yin for the discussion of theoretical background. The authors would like to thank Ian Ogier for the support with laboratory work.

References

[1] Lissenden C J 2021 Nonlinear ultrasonic guided waves—Principles for nondestructive evaluation *J. Appl. Phys.* **129** 021101

[2] Soleimanpour R and Ng C-T 2021 Scattering analysis of nonlinear Lamb waves at delaminations in composite laminates *Journal of Vibration and Control* 1077546321990145

[3] Pineda Allen J C and Ng C T 2021 Nonlinear Guided-Wave Mixing for Condition Monitoring of Bolted Joints *Sensors* **21** 5093

[4] Xu L, Wang K, Su Y, He Y, Yang J, Yuan S and Su Z 2022 Surface/sub-surface crack-scattered nonlinear rayleigh waves: A full analytical solution based on elastodynamic reciprocity theorem *Ultrasonics* **118** 106578

[5] Yang Y, Ng C-T and Kotousov A 2019 Second-order harmonic generation of Lamb wave in prestressed plates *J. Sound Vib.* **460** 114903
[6] Wen F, Shan S and Cheng L 2021 Third harmonic shear horizontal waves for material degradation monitoring *Struct. Health Monitor.* **20** 475-83
[7] Hughes J M, Kotousov A and Ng C-T 2020 Generation of higher harmonics with the fundamental edge wave mode *Appl. Phys. Lett.* **116** 101904
[8] Li W, Cho Y and Achenbach J D 2012 Detection of thermal fatigue in composites by second harmonic Lamb waves *Smart. Mater. Struct.* **21** 085019
[9] Pruell C, Kim J-Y, Qu J and Jacobs L J 2009 Evaluation of fatigue damage using nonlinear guided waves *Smart. Mater. Struct.* **18** 035003
[10] Deng M 2003 Analysis of second-harmonic generation of Lamb modes using a modal analysis approach *J. Appl. Phys.* **94** 4152-9
[11] Krishna Chillara V and Lissenden C J 2012 Interaction of guided wave modes in isotropic weakly nonlinear elastic plates: Higher harmonic generation *J. Appl. Phys.* **111** 124909
[12] Matsuda N and Biwa S 2011 Phase and group velocity matching for cumulative harmonic generation in Lamb waves *J. Appl. Phys.* **109** 094903
[13] Hong M, Su Z, Wang Q, Cheng L and Qing X 2014 Modeling nonlinearities of ultrasonic waves for fatigue damage characterization: Theory, simulation, and experimental validation *Ultrasonics* **54** 770-8
[14] Müller M F, Kim J-Y, Qu J and Jacobs L J 2010 Characteristics of second harmonic generation of Lamb waves in nonlinear elastic plates *J. Acoust. Soc. Am.* **127** 2141-52
[15] Wan X, Tse P, Xu G, Tao T and Zhang Q 2016 Analytical and numerical studies of approximate phase velocity matching based nonlinear S0 mode Lamb waves for the detection of evenly distributed microstructural changes *Smart. Mater. Struct.* **25** 045023
[16] Yang Y, Ng C T, Mohabuth M and Kotousov A 2019 Finite element prediction of acoustoelastic effect associated with Lamb wave propagation in pre-stressed plates *Smart. Mater. Struct.* **28** 095007
[17] Jhang K-Y 2009 Nonlinear ultrasonic techniques for nondestructive assessment of micro damage in material: a review *INT J PRECIS ENG MAN* **10** 123-35
[18] He S, Ng C-T and Yeung C 2020 Time-domain spectral finite element method for modeling second harmonic generation of guided waves induced by material, geometric and contact nonlinearities in beams *International Journal of Structural Stability and Dynamics* **20** 2042005
[19] Ishii Y, Biwa S and Adachi T 2018 Non-collinear interaction of guided elastic waves in an isotropic plate *J. Sound Vib.* **419** 390-404
[20] Hasanian M and Lissenden C J 2018 Second order ultrasonic guided wave mutual interactions in plate: Arbitrary angles, internal resonance, and finite interaction region *J. Appl. Phys.* **124** 164904
[21] Jingpin J, Xiangji M, Cunfu H and Bin W 2017 Nonlinear Lamb wave-mixing technique for micro-crack detection in plates *NDT&E Int.* **85** 63-71
[22] Li W, Xu Y, Hu N and Deng M 2020 Numerical and experimental investigations on second-order combined harmonic generation of Lamb wave mixing *AIP Adv.* **10** 045119

[23] Yeung C and Ng C T 2020 Nonlinear guided wave mixing in pipes for detection of material nonlinearity *J. Sound Vib.* **485** 115541
[24] Li W, Deng M, Hu N and Xiang Y 2018 Theoretical analysis and experimental observation of frequency mixing response of ultrasonic Lamb waves *J. Appl. Phys.* **124** 044901
[25] Sun M and Qu J 2020 Analytical and numerical investigations of one-way mixing of Lamb waves in a thin plate *Ultrasonics* **108** 106180
[26] Croxford A J, Wilcox P D, Drinkwater B W and Nagy P B 2009 The use of non-collinear mixing for nonlinear ultrasonic detection of plasticity and fatigue *J. Acoust. Soc. Am.* **126** EL117-EL22
[27] Liu M, Tang G, Jacobs L J and Qu J 2012 Measuring acoustic nonlinearity parameter using collinear wave mixing *J. Appl. Phys.* **112** 024908
[28] Shan S, Hasanian M, Cho H, Lissenden C J and Cheng L 2019 New nonlinear ultrasonic method for material characterization: Codirectional shear horizontal guided wave mixing in plate *Ultrasonics* **96** 64-74
[29] Li W, Lan Z, Hu N and Deng M 2021 Modeling and simulation of backward combined harmonic generation induced by one-way mixing of longitudinal ultrasonic guided waves in a circular pipe *Ultrasonics* **113** 106356
[30] Blanloeuil P, Rose L, Veidt M and Wang C 2021 Nonlinear mixing of non-collinear guided waves at a contact interface *Ultrasonics* **110** 106222
[31] Chen H, Gao G, Hu N, Deng M and Xiang Y 2020 Modeling and simulation of frequency mixing response of two counter-propagating Lamb waves in a two-layered plate *Ultrasonics* **104** 106109
[32] Kim J-Y, Jacobs L J, Qu J and Littles J W 2006 Experimental characterization of fatigue damage in a nickel-base superalloy using nonlinear ultrasonic waves *J. Acoust. Soc. Am.* **120** 1266-73
[33] Viswanath A, Rao B, Mahadevan S, Jayakumar T and Raj B 2010 Microstructural characterization of M250 grade maraging steel using nonlinear ultrasonic technique *J. Mater. Sci.* **45** 6719-26
[34] Ohara Y, Kawashima K, Yamada R and Horio H 2004 Evaluation of amorphous diffusion bonding by nonlinear ultrasonic method. In: *AIP Conf Proc*: American Institute of Physics) pp 944-51
[35] Li W, Jiang C, Qing X, Liu L and Deng M 2020 Assessment of low-velocity impact damage in composites by the measure of second-harmonic guided waves with the phase-reversal approach *Sci. Prog* **103** 0036850419881079
[36] Li W, Hu S and Deng M 2018 Combination of Phase Matching and Phase-Reversal Approaches for Thermal Damage Assessment by Second Harmonic Lamb Waves *Materials* **11** 1961
[37] Shan S, Cheng L and Li P 2016 Adhesive nonlinearity in Lamb-wave-based structural health monitoring systems *Smart. Mater. Struct.* **26** 025019
[38] Jhang K-Y, Lissenden C J, Solodov I, Ohara Y and Gusev V 2020 *Measurement of Nonlinear Ultrasonic Characteristics*: Springer)
[39] Aseem A and Ng C T 2021 Debonding detection in rebar-reinforced concrete structures using second harmonic generation of longitudinal guided wave *NDT&E Int.* **122** 102496

[40] Guan R, Lu Y, Wang K and Su Z 2019 Fatigue crack detection in pipes with multiple mode nonlinear guided waves *Struct. Health Monitor.* **18** 180-92
[41] Pruell C, Kim J-Y, Qu J and Jacobs L 2009 A nonlinear-guided wave technique for evaluating plasticity-driven material damage in a metal plate *NDT&E Int.* **42** 199-203
[42] Liu P, Sohn H, Yang S and Lim H J 2016 Baseline-free fatigue crack detection based on spectral correlation and nonlinear wave modulation *Smart. Mater. Struct.* **25** 125034
[43] De Lima W and Hamilton M 2003 Finite-amplitude waves in isotropic elastic plates *J. Sound Vib.* **265** 819-39
[44] Qu J, Nagy P B and Jacobs L J 2012 Pulse propagation in an elastic medium with quadratic nonlinearity (L) *J. Acoust. Soc. Am.* **131** 1827-30
[45] Mohabuth M, Khanna A, Hughes J, Vidler J, Kotousov A and Ng C-T 2019 On the determination of the third-order elastic constants of homogeneous isotropic materials utilising Rayleigh waves *Ultrasonics* **96** 96-103
[46] Mohabuth M, Kotousov A and Ng C-T 2019 Large acoustoelastic effect for Lamb waves propagating in an incompressible elastic plate *J. Acoust. Soc. Am.* **145** 1221-9
[47] Vidler J, Kotousov A and Ng C-T 2021 Effect of randomly distributed voids on effective linear and nonlinear elastic properties of isotropic materials *International Journal of Solids and Structures* **216** 83-93
[48] Murnaghan F D 1937 Finite deformations of an elastic solid *Am. J. Math.* **59** 235-60
[49] Gandhi N, Michaels J E and Lee S J 2012 Acoustoelastic Lamb wave propagation in biaxially stressed plates *J. Acoust. Soc. Am.* **132** 1284-93
[50] Hu X, Ng C T and Kotousov A 2021 Scattering characteristics of quasi-Scholte waves at blind holes in metallic plates with one side exposed to water *NDT&E Int.* **117** 102379
[51] Kijanka P, Staszewski W J and Packo P 2018 Generalised semi-analytical method for excitability curves calculation and numerical modal amplitude analysis for Lamb waves *Structural Control and Health Monitoring* **25** e2172
[52] Staszewski W, Lee B, Mallet L and Scarpa F 2004 Structural health monitoring using scanning laser vibrometry: I. Lamb wave sensing *Smart. Mater. Struct.* **13** 251
[53] Giurgiutiu V 2007 *Structural health monitoring: with piezoelectric wafer active sensors*: Elsevier)
[54] Vass J, Šmíd R, Randall R, Sovka P, Cristalli C and Torcianti B 2008 Avoidance of speckle noise in laser vibrometry by the use of kurtosis ratio: Application to mechanical fault diagnostics *Mech. Syst. Signal. Process.* **22** 647-71
[55] Pavlakovic B and Lowe M 2003 Disperse Software Manual Version 2.0. 1 6B *Imperial College, London, UK*
[56] Zuo P, Zhou Y and Fan Z 2016 Numerical and experimental investigation of nonlinear ultrasonic Lamb waves at low frequency *Appl. Phys. Lett.* **109** 021902
[57] Zhu W, Xiang Y, Liu C-j, Deng M, Ma C and Xuan F-z 2018 Fatigue damage evaluation using nonlinear Lamb Waves with Quasi phase-velocity matching at low frequency *Materials* **11** 1920

Chapter 3

Frequency selection and time shifting for maximizing the performance of low-frequency guided wave mixing

Publication:

H. Zhu, C.T. Ng, and A. Kotousov, Frequency selection and time shifting for maximizing the performance of low-frequency guided wave mixing, *Ndt & E International*, 133 (2023), 102735.

Statement of Authorship

Title of Paper	Frequency selection and time shifting for maximizing the performance of low-frequency guided wave mixing
Publication Status	☑ Published ☐ Accepted for Publication ☐ Submitted for Publication ☐ Unpublished and Unsubmitted work written in manuscript style
Publication Details	H. Zhu, C.T. Ng, and A. Kotousov, Frequency selection and time shifting for maximizing the performance of low-frequency guided wave mixing, Ndt & E International, 133 (2023), 102735.

Principal Author

Name of Principal Author (Candidate)	Hankai Zhu		
Contribution to the Paper	Conceptualization, Methodology, Experiment, Finite Element simulation, Validation, Formal analysis, Writing – original draft and editing.		
Overall percentage (%)	85%		
Certification:	This paper reports on original research I conducted during the period of my Higher Degree by Research candidature and is not subject to any obligations or contractual agreements with a third party that would constrain its inclusion in this thesis. I am the primary author of this paper.		
Signature		Date	23/10/2023

Co-Author Contributions

By signing the Statement of Authorship, each author certifies that:

i. the candidate's stated contribution to the publication is accurate (as detailed above);

ii. permission is granted for the candidate in include the publication in the thesis; and

iii. the sum of all co-author contributions is equal to 100% less the candidate's stated contribution.

Name of Co-Author	Ching-Tai Ng		
Contribution to the Paper	Supervision, Advising, Writing – review and editing.		
Signature		Date	6 Nov 2023

Name of Co-Author	Andrei Kotousov		
Contribution to the Paper	Supervision, Advising, Writing – review and editing.		
Signature		Date	7 Nov 2023

Chapter 3: Frequency selection and time shifting for maximizing the performance of low-frequency guided wave mixing

Hankai Zhu[1], Ching Tai Ng[1], Andrei Kotousov[2]

[1] School of Civil, Environmental and Mining Engineering, The University of Adelaide, Adelaide, SA 5005, Australia

[2] School of Mechanical Engineering, The University of Adelaide, Adelaide, SA 5005, Australia

Abstract

Evaluation of fatigue damage using nonlinear guided wave mixing has been studied extensively over the past decade. It was found that the combinational harmonics as a result of wave mixing of quasi-synchronized wave modes show attractive features and are sensitive to fatigue damage. However, there were very limited studies on the frequency pair selection and time shifting of the wave mixing signals. In this study, a method is developed and theoretical equations are implemented, which provides a guide on the selection of the wave mixing frequency pair. The proposed frequency pair selection method can advance the trial-and-error method that was generally used for low-frequency wave mixing, which has a large number of possible frequency pairs, and deliberate selection is needed to avoid the overlapping of the generated harmonics. A new time shifting technique is also proposed to enhance the generation of second and combinational harmonics due to the collinear wave mixing. This technique can be very useful when there are various limitations exist on the selection of the excitation frequencies. The efficiency of the proposed method is validated by a series of numerical and experimental studies. Overall, the new findings can be utilized to further advance the development of new damage detection methods using the guided wave mixing method.

Keywords: combinational harmonics generation, frequency selection, fatigue damage, nonlinear guided waves, time shifting, wave mixing method.

3.1. Introduction

Non-destructive evaluation (NDE) is important for maintaining the integrity and structural safety of potentially hazardous engineering structures. Fatigue damage is one of the main concerns as the conventional inspection methods are insensitive to early stage fatigue damage (i.e. before formation of macro-cracks). The latter stage can occupy up to 90% of the total fatigue life. The nonlinear features of guided waves, such as higher order harmonics and combinational harmonics, have been applied to evaluate early stage fatigue damage [1, 2]. In contrast to the linear features of guided waves, the nonlinear features of guided waves have been demonstrated to be more sensitive to the accumulation of fatigue damage [3-5], and are less affected by the change of the environmental and loading conditions [6-8]. Therefore, nonlinear guided waves have attracted significant interest over the past decade [8-11].

3.1.1. Second harmonic and combinational harmonic generation

The previous studies have demonstrated that the second harmonics are sensitive to the presence of fatigue damage. The generation of these harmonics requires to meet two conditions, the synchronism [12, 13] and non-zero power flux [14, 15]. The second harmonics are typically generated using the cross-mode method, in which the generated second harmonic is at a higher order wave mode than the excited wave mode, e.g., from first-order symmetric mode (S_1) to second-order symmetric mode (S_2) of Lamb wave, S_1-S_2 [16-18]. However, the application of the cross-mode method is possible only for specific pairs of frequencies, which satisfy the synchronism conditions (i.e., matching of the phase and group velocities) [19]. These conditions are possible to meet exactly only in the high-frequency excitation in megahertz range. However, the wave excitation in this frequency range generally requires specifically designed angle transducer, and the waves at this frequency range are highly dispersive. These constraints make the signal processing and extraction of nonlinear features become very challenging. They significantly limit practical applications of the cross-mode method.

The quasi-synchronism conditions were proposed by Muller et al. [20]. They demonstrated the possibility of the generation of the cumulative second harmonics using quasi-synchronized wave modes, such as from the fundamental symmetric mode (S_0) to S_0 of Lamb waves, S_0-S_0. Yang et al. [21] investigated the second harmonic generation of S_0 wave in the low frequency range due to the interaction of the incident wave with a contact acoustic

nonlinearity (CAN). Wan et al. [22] and Zuo et al. [23] investigated the second harmonic generation of the S_0 wave in the low frequency range due to material nonlinearities. These studies indicated that the S_0 wave is sensitive to the weakly material nonlinearity, and the amplitude of the second harmonic increases linearly with the propagation distance. The fundamental edge mode (ES_0) waves can also be considered as quasi-synchronized [24], and the generation of second harmonic of ES_0 wave was also investigated [25].

In the wave mixing method, second harmonics and combinational harmonics can be generated simultaneously. This method has attracted significant focus in recent investigations. In particular, it was found that the combinational harmonic at the sum frequency ($f_a + f_b$) and the difference frequency ($f_b - f_a$) are sensitive to both material nonlinearity and the CAN. The utilization of the combinational harmonics for damage characterisation has many advantages compared to the conventional second harmonic generation, especially for avoiding the instrumentation nonlinearity [26, 27]. The latter was one of the challenges reported for the nonlinear guided wave approaches in the literature. There were several studies showed that the combinational harmonic has better performance compared with the second harmonic, especially for the third-order combinational harmonics using three-wave mixing [28, 29]. The phenomena of the third-order harmonic generation due to wave mixing method were also studied theoretically in the literature [13, 30]. However, the current study focuses on the second harmonics and second-order combinational harmonics.

In wave mixing method, there are three approaches were used for the wave excitation in the literature. The wave mixing can be (i) codirectional collinear waves, (ii) counter-propagating collinear waves, and (iii) noncollinear waves. The codirectional collinear wave mixing is analogous to the bulk wave mixing [31], and two incident waves propagate in the same direction. The advantage of this approach is a relatively large wave mixing zone, and the weakly material nonlinearity can be accumulated [5, 32], which is important for the distributed material nonlinearity evaluation. The counter-propagating collinear wave mixing and noncollinear wave mixing have a smaller mixing zone compared to the codirectional collinear wave mixing. A secondary wave can be generated in the wave interaction zone. The noncollinear wave mixing requires a specific wave propagation angle, at which the two incident waves are mixed [33]. The codirectional collinear wave mixing was applied for characterizing the distributed fatigue damage [5, 34, 35], and the fatigue cracks [29, 36, 37]. The counter-propagating collinear wave mixing and noncollinear wave mixing are generally applied to the evaluation of localized damage or defects (e.g. CAN) [38-40]. The collinear wave mixing has

less restrictions than the noncollinear wave mixing [31], and it is more suitable for practical applications. For example, the noncollinear wave mixing requires specific excitation frequencies and wave propagation angle, which are difficult to achieve in practical environment. Therefore, the current study focuses on the collinear wave mixing.

3.1.2. Wave mixing mode pair in the low frequency range

As mentioned above, the nonlinear guided wave mixing method in the low frequency range has many attractive features; e.g. avoidance of the generation of multiple wave modes and less wave dispersion, which can simplify the signal processing [3, 22]. The low frequency excitation can be achieved by using a piezoelectric transducer (PZT) [41]. PZTs are more suitable for in-situ applications and structural health monitoring (SHM) compared to wave generation by wedge transducers, which are normally used for wave excitation in the high-frequency range.

The combinational harmonic generation of S_0 wave in the low frequency range was studied using plate-like structures, and several studies demonstrated that S_0 wave is a viable alternative to the cross-mode method using high-frequency wave mode pairs, e.g. S_1-S_2 pair [36, 42]. Several recent studies investigated the fundamental shear-horizontal mode (SH_0) wave mixing [43] and the longitudinal wave mixing in pipes [44, 45]. As mentioned above, only a limited number of wave mode pairs can meet the synchronism conditions [19, 31]. On the contrary, in the entire low frequency range of quasi-synchronized waves, such as S_0 waves, can be used for the wave mixing. Therefore, there are infinity numbers of quasi-phase matching frequencies can be selected in the low frequency range. However, no systematic studies have been carried out to provide a guide on the selection of the appropriate frequency pair of quasi-synchronized waves for nonlinear guided wave mixing.

If the selection of frequency pair for the wave mixing in the low frequency range is arbitrary, the generation of the sum combinational harmonic ($f_a + f_b$) can overlap with the second harmonics ($2f_a$ and $2f_b$), and the third order harmonics may also interact with both combinational and second harmonics. The coherent coupling and overlapping of the combinational and second harmonics may result in a dramatic increase of the complexity of harmonic analysis and signal processing. The conventional approach for the frequency pair selection for the low frequency wave mixing method has been based on the trial-and-error method [42, 46]. A number of parameters can affect the selection of frequencies for the wave

mixing, such as the dimensions and material properties of the specimen, the wave modes, and the capability of instrumentation. Hence, a significant amount of effort is required for determining a suitable frequency pair in the wave mixing. It is essential to predict the optimal frequency pair selection in wave mixing before numerous of trials. This paper provides a guide for the frequency selection of wave mixing method. The efficiency of this proposed method is validated by a series of numerical and experimental studies.

3.1.3. Time shifting effect on the wave mixing

The time shifting technique has no effect on the fundamental harmonic (at f_a) and second harmonic (at $2f_a$), and therefore, it was rarely studied in the literature. However, the time shifting technique can be very useful for the wave mixing method. In particular, this technique was applied to adjust the wave mixing zone [31, 45, 47]. In the literature, there were only few unsystematic attempts carried out to enhance the performance of wave mixing method using the time shifting [42, 44]. However, these studies were based on the trial-and-error approach, and have not been supported by theoretical equations and were largely focused on a specific pair of frequencies.

In this study, frequency pair selection method in wave mixing has been proposed based on the implemented theoretical equations. In addition, this study presents a new method to maximize the performance of the harmonic generation in wave mixing using the time shifting technique. It enhances the collinear wave mixing of quasi-synchronized waves by minimizing the level of overlap between the second harmonics and the combinational harmonics. The efficiency of the proposed method is investigated by a series of numerical simulations and experimental studies.

This paper is organized as follow. Section 3.2 introduces the theoretical background of frequency pair selection in wave mixing, and then it proposes the time shifting optimization technique for wave mixing. Section 3.3 presents a three-dimensional (3D) finite element (FE) model, which is utilized to simulate the nonlinear wave mixing in a weakly nonlinear material. A series of parametric studies are carried out to illustrate the procedure of the proposed method and demonstrate the effect of frequency pair selection and time shifting on performance of wave mixing. Section 3.4 presents experimental studies, which validates the FE simulations in Section 3.3, and the proposed frequency selection and time shifting method. Finally, conclusions are drawn in Section 3.5.

3.2. Theoretical background

3.2.1. Frequency selection in wave mixing method

In this section, a wave mixing separation index (S) is proposed to characterize the performance of the wave mixing based on the spectral separation of the two harmonics and the level of overlap between the harmonics. It determines the degree of interference that a harmonic suffers due to other harmonics sharing the frequency band. The frequency selection in wave mixing is essential for the generation of combinational harmonics, which may be overlapped with the second harmonics at the adjacent kernels. The sufficient spectral separation between the fundamental harmonics is critical to reduce the overlapping of combinational and second harmonics, and reduce the challenge of extracting the combinational and second harmonics. The overlapping of the combinational and second harmonics significantly increases the complexity of the harmonic analysis and signal processing. As an example, Figure 3.1a shows the overlapping of the sum combinational harmonic and second harmonics, which make the signal processing and extraction of harmonics become very challenging. The spectral separation between the fundamental harmonics is associated with the frequency difference between the fundamental frequencies, and the frequency bandwidth of the incident waves in the frequency spectrum. The frequency bandwidth of a single pulse has an inverse relationship with time duration of the pulse, which is known as Heisenberg uncertainty [48] and defined as

$$T_d \cdot BW = const \tag{3.1}$$

where T_d represents the time duration of the pulse, and BW is the bandwidth in frequency spectrum. The time duration of the single pulse can be further related to the fundamental frequency and number of cycles.

The Hann window is the function most frequently utilized in guided wave studies, and therefore, it is the focus of this study. The minimum separation between two Hann window tone-burst pulses in the frequency spectrum can be determined based on the Hann windowing features since the bandwidth of the pulse is equal to the bandwidth of the windowing function [49]. The Hann windowing features along with other types of windowing functions have been studied in detail by Harris [50]. The 6-dB bandwidth point was considered as critical level, which enables the determination of minimum separation point between two fundamental harmonics [50]. In particular, it was suggested that the crossover point of two kernels needs to achieve the sum of 6-dB bandwidth of two harmonics, and the concept of which is schematically illustrated in Figure 3.1b.

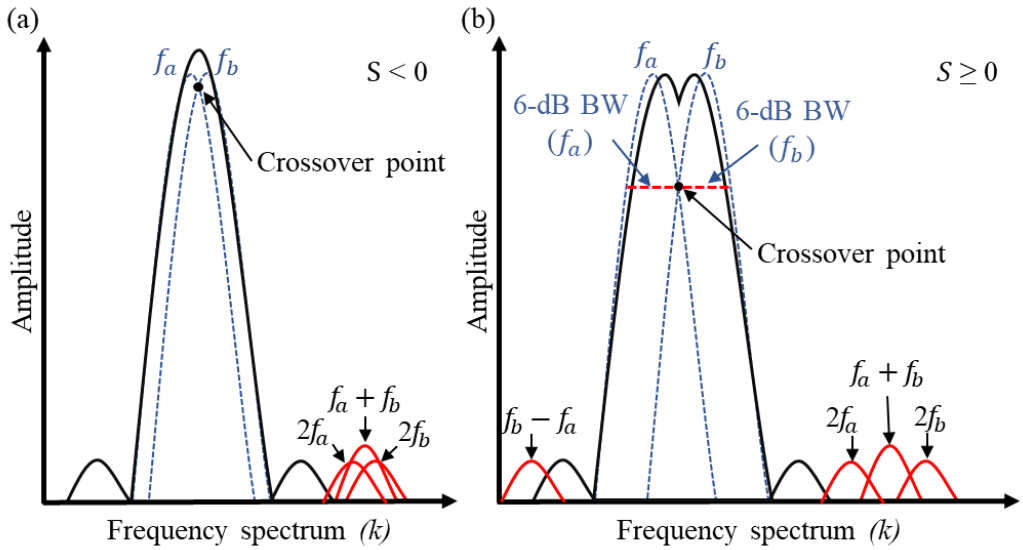

Figure 3.1. Schematic illustration of the crossover point and wave mixing separation index (S) in (a) $S < 0$; (b) $S \geq 0$.

The crossover point is defined as the half-way point between two adjacent kernels (i.e., fundamental harmonics of wave *a* and wave *b*),

$$k_{cr} = \frac{BW_{f_a} + BW_{f_b}}{2} \tag{3.2a}$$

where k_{cr} is the crossover point of fundamental harmonics of wave *a* and wave *b*. BW_{f_a} and BW_{f_b} are the bandwidth of the two fundamental frequencies in frequency spectrum. The 6-dB reduction bandwidth of Hann window is determined as two bins of fundamental frequency Δk [50]. The Equation 3.2a therefore becomes

$$k_{cr}^{H} = \frac{BW_{f_a}^{6dB} + BW_{f_b}^{6dB}}{2} = \Delta k_{f_a} + \Delta k_{f_b} \tag{3.2b}$$

where Δk_{f_a} and Δk_{f_b} are the frequency bins of wave *a* and wave *b*, which can be determined by the corresponding sampling frequency F_s and sampling number n_s, respectively.

$$\Delta k = \frac{F_s}{n_s} \tag{3.3a}$$

$$F_s = \frac{1}{dt} \tag{3.3b}$$

where dt is the time interval. The time duration of the signal pulse can be expressed using the sampling number and time interval

$$T_d = (n_s - 1)dt \tag{3.4a}$$

In addition to the Equation 3.4a, the time duration of Hann window pulse can also be expressed using the number of cycles and fundamental frequency of the incident wave.

$$T_d = \frac{N}{f} \tag{3.4b}$$

where N is the number of cycles and f is the fundamental frequency. Hence, the frequency bin Δk in Equation 3.3a can be expressed in terms of fundamental frequency and number of cycles using Equations 3.4a and 3.4b. As mentioned earlier in this section, the spectral separation between two kernels is correlated with the frequency difference and bandwidth of two fundamental harmonics simultaneously. A wave mixing separation index (S), which can indicate the separation between fundamental harmonics in frequency domain, can be derived using the concept of crossover point of Hann window shown in Equation 2b as

$$S = (f_b - f_a) - \left(\frac{f_a}{N_a + f_a dt} + \frac{f_b}{N_b + f_b dt}\right) \tag{3.5a}$$

S can be used to characterize the separation of the two adjacent kernels of Hann window in arbitrary spectral location. The first term on the right-hand side of Equation 3.5 is the frequency difference ($f_b > f_a$), and the second term in brackets is the bandwidth of two fundamental harmonics. Equation 3.5a can be further simplified by considering that the term of subtraction in the bracket of Equation 3.4a is sufficiently small compared with the large sampling number n_s, and hence, it is negligible for the approximate prediction and the S parameter is simplified as

$$S = (f_b - f_a) - \left(\frac{f_a}{N_a} + \frac{f_b}{N_b}\right) \tag{3.5b}$$

The Equation 3.5b determines the spectral separation between the fundamental harmonics of wave mixing using Hann window, and therefore predicting the level of overlap of fundamental harmonics and the performance of wave mixing. The fundamental harmonics can be significantly overlapped in frequency domain, and become unresolvable in harmonic analysis when wave mixing separation index (S) is a negative value (see Figure 3.1a). In Figure 3.1b, the increased value of wave mixing separation index (S) indicates the increase of the spectral

separation between two kernels of fundamental harmonics, and therefore reducing the overlapping between the sum combinational harmonic ($f_a + f_b$) and the second harmonics ($2f_a$ and $2f_b$). It should be noted that the proposed wave mixing separation index (S) can be used for other types of window, and only slight modification is needed for 6-dB reduction bandwidth in Equation 2b.

Theoretically, the greater value of the wave mixing separation index (S) indicates a better performance of the wave mixing method in terms of the clarity and consistency of the generation of combinational harmonics. The good performance of the wave mixing method can be achieved by increasing the number of cycles of the waves or increasing the frequency difference between two fundamental frequencies. However, in experiments and practical applications, the boundary reflection may occur if too many cycles of the waves are used, especially when the specimen is not sufficiently large. On the other hand, the increase of frequency difference between two fundamental frequencies can also enhance the performance of wave mixing method. However, the frequency selection range of quasi-synchronized waves can be limited by the dispersion relation, generation of multiple wave modes and capability of instrumentation. Hence, it is required to consider the number of cycles and the fundamental frequencies simultaneously. It should be noted that the effect of time shifting between the two incident waves is not taken into the account in the Equation 3.5b, which will be further discussed in Section 3.2.2.

In addition to the overlapping of the combinational and second harmonics, the highest sidelobes generation due to the incident waves may affect the second harmonic of wave *a* ($2f_a$) and the difference combinational harmonic (f_b - f_a). The central locations of the highest sidelobes are [51]

$$f_{La} = f_a - 2.36\Delta k_{f_a} \tag{3.6a}$$

$$f_{Lb} = f_b + 2.36\Delta k_{f_b} \tag{3.6b}$$

where f_L indicates the spectral location of highest sidelobe generation due to the incident waves. The Equations 3.6a and 3.6b can provide an improved insight into the influence of sidelobe generation due to the incident waves on the difference combinational harmonic generation, and the second harmonic generation, respectively. Therefore, additional consideration on frequency selection of wave mixing is needed when the difference combinational harmonic and second harmonic are important for harmonic analysis.

3.2.2. Time shifting in wave mixing method

The wave mixing can be considered as the superposition of two Hann windowed waves with different fundamental frequencies and number of cycles in time-displacement domain. Time shifting of incident waves can be used to optimize the performance of wave mixing provided that the group velocities of two waves are matching. The Hann window tone-burst pulse of a single frequency wave with the consideration of time shifting can be expressed as Equation 7a.

$$u(t) = \begin{cases} 0\,, & 0 \le t \le t_0 \\ \cos(2\pi f t)\left[\frac{1}{2} - \frac{1}{2}cos\left(\frac{2\pi}{T_d}(t - t_0)\right)\right], & t_0 \le t \le T_d + t_0 \end{cases} \quad (3.7a)$$

$$t = 0, dt, \cdots, t_0, \cdots, T_d, \cdots, T_{tot} \quad (3.7b)$$

where t_0 is the time shifting, and $T_{tot} = T_d + t_0$, which is the total time duration of Hann windowing pulse, and the expression of T_d was shown in Equation 3.4b. Equations 3.7a and 3.7b show that effect of time shifting can influence the carrier frequency and the Hann window in frequency spectrum simultaneously. Hence, the effect of time shifting on mixing wave and its generated harmonics are investigated in this section. The mixing wave in displacement field u_m can be considered as the superposition of two incident waves [52] as

$$u_m(t) = u_a(t) + u_b(t) = x_a(t)h_a(t) + x_b(t)h_b(t) \quad (3.7c)$$

where x_a and x_b represent the carrier frequencies. h_a and h_b represent the corresponding Hann window. The effect of time shifting on the frequency spectrum of carrier frequency and Hann window can be analysed using discrete Fourier transform (DFT) [50] as

$$F(k) = \sum_{n=-n_{s/2}}^{n_{s/2}} u(t)\exp(-j2\pi knt) \quad (3.8a)$$

$$k = -\frac{n_s}{2}\Delta k, \cdots, 0, \cdots, \left(\frac{n_s}{2} - 1\right)\Delta k \quad (3.8b)$$

where k is the frequency spectrum as shown in Equation 3.8b with interval of frequency bin Δk as introduced in Equations 3.3a and 3.3b. The linear phase shift term is introduced regardless of the time shifting since the phase of mixing wave in the frequency spectrum is considered, which can be determined as [49]

$$\phi(k) = [\cos(\pi k T_d) - j\sin(\pi k T_d)] \tag{3.9a}$$

The time shifting term could result in the linearly phase shift [49] and can be expressed as

$$t_\phi(k) = [\cos(2\pi k t_0) - j\sin(2\pi k t_0)] \tag{3.9b}$$

The magnitude of a pulse with finite number of samplings can be determined using Dirichlet kernel [53] provided that the sampling number n_s is sufficiently large

$$D_N(k) = \frac{1}{2} + \sum_{n=-n_{s/2}}^{n_{s/2}-1} \cos(\pi k \mathrm{n}) = \frac{\sin(\pi k T_d)}{n_s \sin\left(\frac{\pi k T_d}{n_s}\right)} \tag{3.10}$$

The effect of time shifting on carrier frequency and Hann window can be investigated separately using convolution [52]. Complexity of harmonic analysis can be reduced by using the windowing theorem. The frequency spectrum of the carrier frequency can be determined using modulation property with the implementation of time shifting term as

$$X(k) = t_\phi(k)\frac{1}{2}[\phi(k-f)D_N(k-f) + \phi(k+f)D_N(k+f)] \tag{3.11a}$$

The Hann window in frequency can be expressed in terms of Dirichlet kernel [50], and the linear phase term and the time shifting term are considered simultaneously as

$$W_H(k) = t_\phi(k)\,\phi(k)[\frac{1}{2}D_N(k) + \frac{1}{4}D_N(k-\Delta k) + \frac{1}{4}D_N(k+\Delta k)] \tag{3.11b}$$

The explicit expressions of Equations 3.11a and 3.11b are shown in Equations A1 and A2 of Appendix. Finally, the convolution of carrier frequency in frequency $X(k)$ and Hann window in frequency $W_H(k)$ is

$$F_W(k) = X(k) \circledast W_H(k) \tag{3.12a}$$

which can predict the behaviour of a single frequency wave in frequency spectrum with the implementation of time shifting. The mixing waves follows the linearity property of DFT, which allows the superposition of two kernels in the frequency spectrum. In addition, the mixing wave in time domain can be transformed due to the frequency convolution property as

$$F_{W_m}(k) = X_a(k) \circledast W_a(k) + X_b(k) \circledast W_b(k) \overset{DFT}{\longleftrightarrow} x_a(t)h_a(t) + x_b(t)h_b(t) \tag{3.12b}$$

As shown in Equation 3.12b, it agrees well with the Equation 3.7c, and the equation can provide improved theoretical understanding on the effect of time shifting on wave mixing in the frequency spectrum.

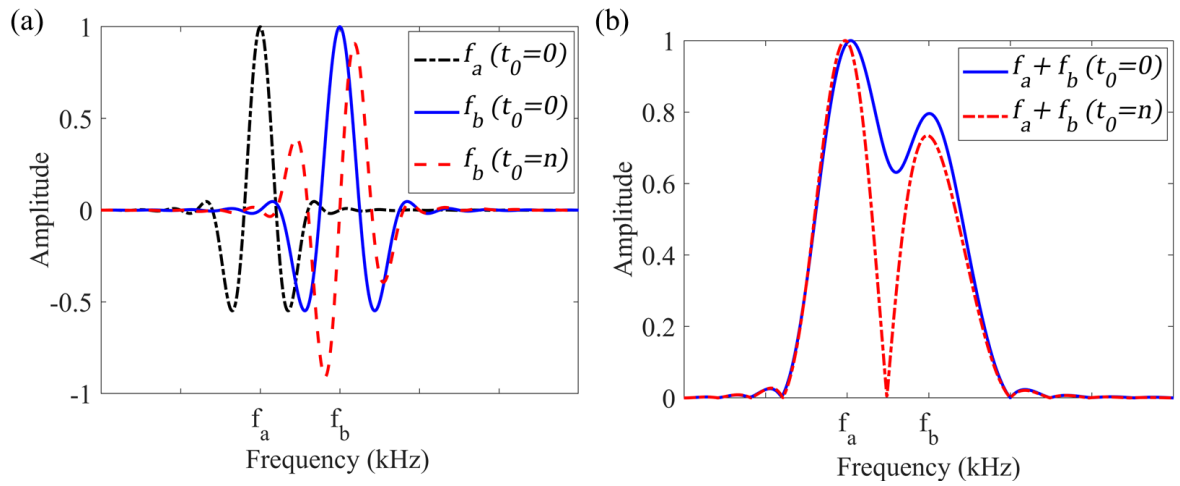

Figure 3.2. Effect of time shifting in frequency spectrum on (a) single frequency waves using Equation 3.12a and (b) the mixing wave using Equation 3.12b

The concept of the time shifting is schematically illustrated in Figure 3.2, and the effect on a single frequency wave and wave mixing are shown separately. In the figure, the wave *a* remains unchanged, and the time shifting is only applied on the wave *b* to provide a better illustration for the effect of time shifting on a single frequency wave. The sidelobes of the incident waves are partially or completely cancelled in frequency domain when the time shifting is applied (see Figure 3.2a). This effect can be used to generate a mixing wave that comprise two closely adjacent fundamental harmonics with an excellent spectral separation, and hence, the performance of the wave mixing in terms the quality and resolution of the harmonic generation can be maximized.

3.3. Numerical simulation and parametric study

3.3.1. Modelling material nonlinearity

The nonlinear governing equations of a structural material, which has weakly material nonlinearity, are briefly discussed in this section. These governing equations were implemented

in ABAQUS/Explicit by VUMAT subroutine for modelling the inherent material nonlinearity. The simulation of material nonlinearities in the finite element (FE) model is based on the infinitesimal theory [54], and the third order elastic constants are incorporated with Murnaghan's strain energy function [55]. The displacement vector $\boldsymbol{u}$ can be expressed in terms of current configuration of material $\boldsymbol{x}$ and reference configuration $\boldsymbol{X}$ as

$$\boldsymbol{u} = \boldsymbol{x} - \boldsymbol{X} \tag{3.13a}$$

The displacement gradient $\boldsymbol{H}$ and displacement gradient tensor $\boldsymbol{F}$ are defined as Equations 13b and 13c.

$$\boldsymbol{H} = \frac{\partial \boldsymbol{u}}{\partial \boldsymbol{X}} \tag{3.13b}$$

$$\boldsymbol{F} = \boldsymbol{I} + \boldsymbol{H} \tag{3.13c}$$

where $\boldsymbol{I}$ donates identity tensor. The Green-Lagrange strain tensor $\boldsymbol{E}$ can be expressed using displacement gradient $\boldsymbol{H}$.

$$\boldsymbol{E} = \frac{1}{2}(\boldsymbol{H} + \boldsymbol{H}^T + \boldsymbol{H}^T\boldsymbol{H}) \tag{3.14}$$

The Murnaghn's strain energy function is given by the Equation 3.15a using principal invariants i_1, i_2 and i_3,

$$\boldsymbol{W}(\boldsymbol{E}) = \frac{1}{2}(\lambda + 2\mu){i_1}^2 + \frac{1}{3}(l + 2m){i_1}^3 - 2\mu i_2 - 2m i_1 i_2 + n i_3 \tag{3.15a}$$

where λ and μ are Lame's elastic constants. l, m and n are third order elastic constants. The principal invariants can be expressed as

$$i_1 = tr(\boldsymbol{E})\,, \qquad i_2 = \frac{1}{2}\left[{i_1}^2 - tr(\boldsymbol{E})^2\right], \qquad i_3 = det(\boldsymbol{E}) \tag{3.15b}$$

The second Piola-Kirchhoff stress of an isotropic medium can be obtained as

$$\boldsymbol{T_{pk2}} = \frac{\partial \boldsymbol{W}(\boldsymbol{E})}{\partial \boldsymbol{E}} \tag{3.16}$$

Hence, the Cauchy stress σ can be obtained in terms of the second Piola-Kirchhoff stress $\boldsymbol{T_{pk2}}$, displacement gradient $\boldsymbol{F}$ and its Jacobian determinant $\boldsymbol{J}^{-1}$, as shown in Equation 3.17.

$$\sigma = \boldsymbol{J}^{-1}\boldsymbol{F}\boldsymbol{T_{pk2}}\boldsymbol{F}^T \tag{3.17}$$

The generated second harmonic and combinational harmonic are analysed in frequency spectrum, using fast Fourier transform (FFT). The relative nonlinear parameters of second

harmonic (β') and combinational harmonics ($\beta_{\pm}{}'$) are defined in Equations 3.18a and 3.18b, respectively.

$$\beta' = \frac{A_{2a}}{{A_a}^2} \tag{3.18a}$$

$$\beta_{\pm}{}' = \frac{A_{b\pm a}}{A_a A_b} \tag{3.18b}$$

where A_a and A_b are the amplitude of the fundamental harmonics, A_{2a} is the amplitude of second harmonics, and $A_{b\pm a}$ represent the amplitude of combinational harmonics.

3.3.2. Finite element model

A 3D FE model was developed to simulate the nonlinear wave behaviour in a 6061-T651 aluminium plate. The wave simulation was solved by ABAQUS/Explicit, and the VUMAT subroutine described in Section 3.3.1 was incorporated to include the weakly material nonlinearity in the simulations. The aluminium plate model as shown in Figure 3.3 is 400 mm × 750 mm and has symmetry boundary conditions at two boundaries. The model is a quarter of the plate used in the experiment. The selected plate dimension can ensure no wave reflection from plate boundaries, while the computational cost can be reduced. The material properties are listed in Table 3.1 [56], which is consistent with the material used in the experiment.

Table 3.1. Material properties of 6061-T651 aluminium at intact condition [56]

ρ (kg·m^{-3})	λ (GPa)	μ (GPa)	l (GPa)	m (GPa)	n (GPa)
2704	54.3	27.2	-281.5	-339.0	-416.0

The thickness of the aluminium plate was 1.6 mm, and eight layers of elements were employed in the thickness direction to ensure the accuracy of phase velocity. In the study, the highest excitation frequency applied on the FE model is 200 kHz, considering the quasi-synchronized phase velocities and group velocities of S_0 waves in the low frequency range. The element size was determined as 0.4 mm, which ensures 20 elements per wavelength [57]. Eight-node linear brick element with reduced integration (C3D8R) was used in the FE model. The symmetrical boundary conditions were applied to the FE model as shown in Figure 3.3,

which can avoid the generation of edge waves, since the edge waves cannot be generated if the PZT is bonded in the centre of the plate. The wave excitation was generated using a circular PZT, and the in-plane displacement with 8.5 μm amplitude was applied on the edge of the quarter of circular PZT. The first measurement point was 400 mm away from the excitation, and normal displacements at 10 measurement points were measured with 10 mm interval of propagation distance.

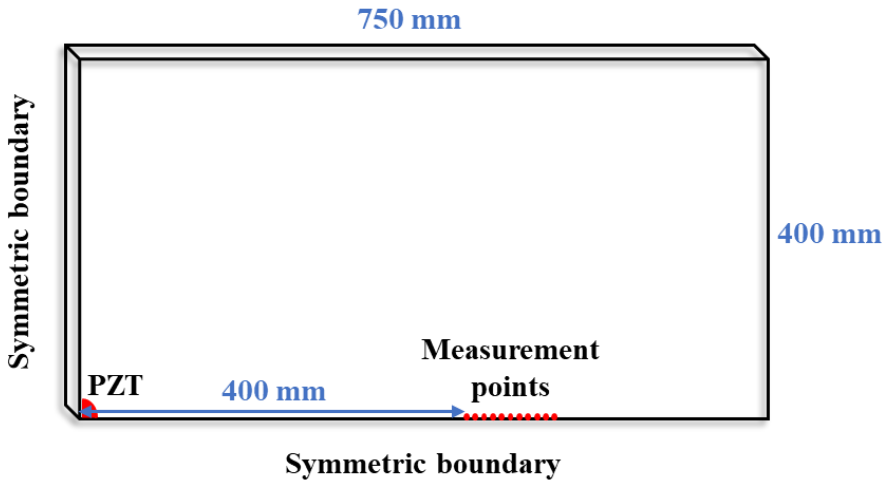

Figure 3.3. Schematic diagram of the 3D FE model

3.3.3. Parametric study

A parametric study is carried out numerically to demonstrate and validate the proposed method through FE simulations. The procedure of frequency pair selection and time shifting optimization for wave mixing method is shown in Figure 3.4. The first step is to determine the fundamental frequency range based on the dispersion curve (see Figure 3.8a in Section 3.4) to achieve the quasi-synchronism. The fundamental frequency f_a can be determined based on the mode tuning curve [58] and the capability of instrumentation, which was carried out experimentally (see Figure 3.8b). After the fundamental frequency f_a is determined, the second step is to apply Equation 3.5b to determine the frequency pair selection of the wave mixing and the selection of number of cycles of the incident waves. A positive value of the wave mixing separation index ($S \geq 0$) needs to be achieved by adjusting the fundamental frequency f_b and the number of cycles of the two incident waves. Finally, the third step is to use the time shifting

optimization to enhance the performance of the wave mixing. The optimization is performed in the frequency spectrum using the implemented theoretical equations, which shows the level of overlap at the crossover frequency of two fundamental harmonics against the time shifting. The expression of crossover frequency is shown in Equation 3.A4 of Appendix, which indicates the frequency of the crossover point of two fundamental harmonics based on the concept of Equation 3.2b. The crossover point is only associated with frequency bin and is not influenced by time shifting. It should be noted that in some special cases the time shifting may have a trivial effect on the selected frequency pair as good separation can already be achieved without optimization. However, it is difficult to find this type of special cases and numerous of trials are needed, which is very time consuming and tedious. On the contrary, a promising frequency pair of wave mixing can be determined using the procedure as shown in Figure 3.4, and the performance of the selected frequency pair can be predicted using the method developed in Section 3.2. The proposed method in the present study is also feasible to be expended for the three-wave mixing with the similar process (i.e., f_a+f_b, then f_b+f_c), and the higher-order combinational harmonics may be overlapped if the frequency selection in the low frequency range is not deliberately designed. Such overlapping of higher-order combinational harmonics is unable to be separated or extracted using the extraction method [35], and the proposed method can provide a guide for the frequency pair selection. In addition, the extraction method can be time-consuming for multiple points measurement of nonlinearities, which requires three-separated measurements for each measurement point. Therefore, the proposed method in the present study can be more efficient for multiple points measurement compared with the extraction method.

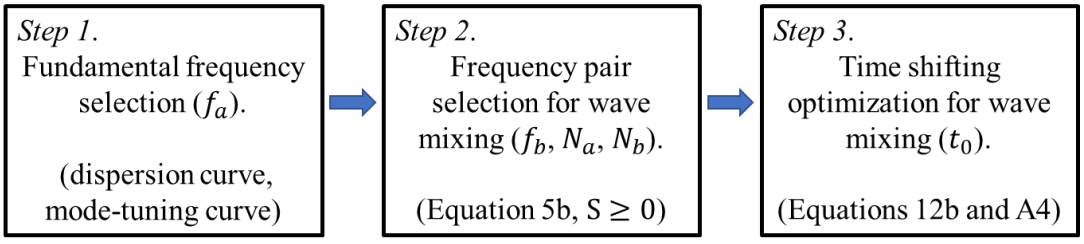

Figure 3.4. Procedure of time shifting optimization

Table 3.2. Different cases of frequency pair for wave mixing

Case	Fundamental frequency (f_a)	Number of cycles (N_a)	Fundamental frequency (f_b)	Number of cycles (N_b)	Time shifting (t_0)	Wave mixing separation index (S)
1a	140 kHz	5 cycles	160 kHz	6 cycles	0 s	-35
2a	140 kHz	7 cycles	185 kHz	8 cycles	0 s	0
3a	140 kHz	9 cycles	185 kHz	10 cycles	0 s	10
4a	140 kHz	9 cycles	195 kHz	10 cycles	0 s	20
1b	140 kHz	5 cycles	160 kHz	6 cycles	0 s	NA
2b	140 kHz	7 cycles	185 kHz	8 cycles	3.4e-6 s	NA
3b	140 kHz	9 cycles	185 kHz	10 cycles	5.1e-6 s	NA
4b	140 kHz	9 cycles	195 kHz	10 cycles	5e-7 s	NA

The fundamental frequency range is limited between 100 kHz and 200 kHz to achieve the quasi-synchronism for the specimen used in this study, and 140 kHz has been determined as the fundamental frequency (f_a) since it has the highest S_0 wave to A_0 wave ratio (as shown by the experimental data in Figure 3.8 of Section 3.4). In Table 3.2, four cases of wave mixing frequency pair are considered (Cases 1a to 4a) to study the effect of the wave mixing separation index (S) on the performance of second harmonics and combinational harmonics generation. In Case 1a, the frequency difference between two fundamental frequencies is very small, and has wide bandwidth of two fundamental harmonics. This case has significant overlapping of two fundamental harmonics by the theoretical prediction. Case 2a can be considered as a baseline case which follows the procedure shown in Figure 3.4. In Case 3a, the fundamental frequencies remain unchanged compared with the Case 2a and the number of cycles are increased, and the reduced overlapping of two fundamental harmonics is predicted by the proposed method. In Case 4a, the frequency difference between two fundamental frequencies is increased compared with Case 3a. It is predicted that Case 4a has better performance than Case 3a.

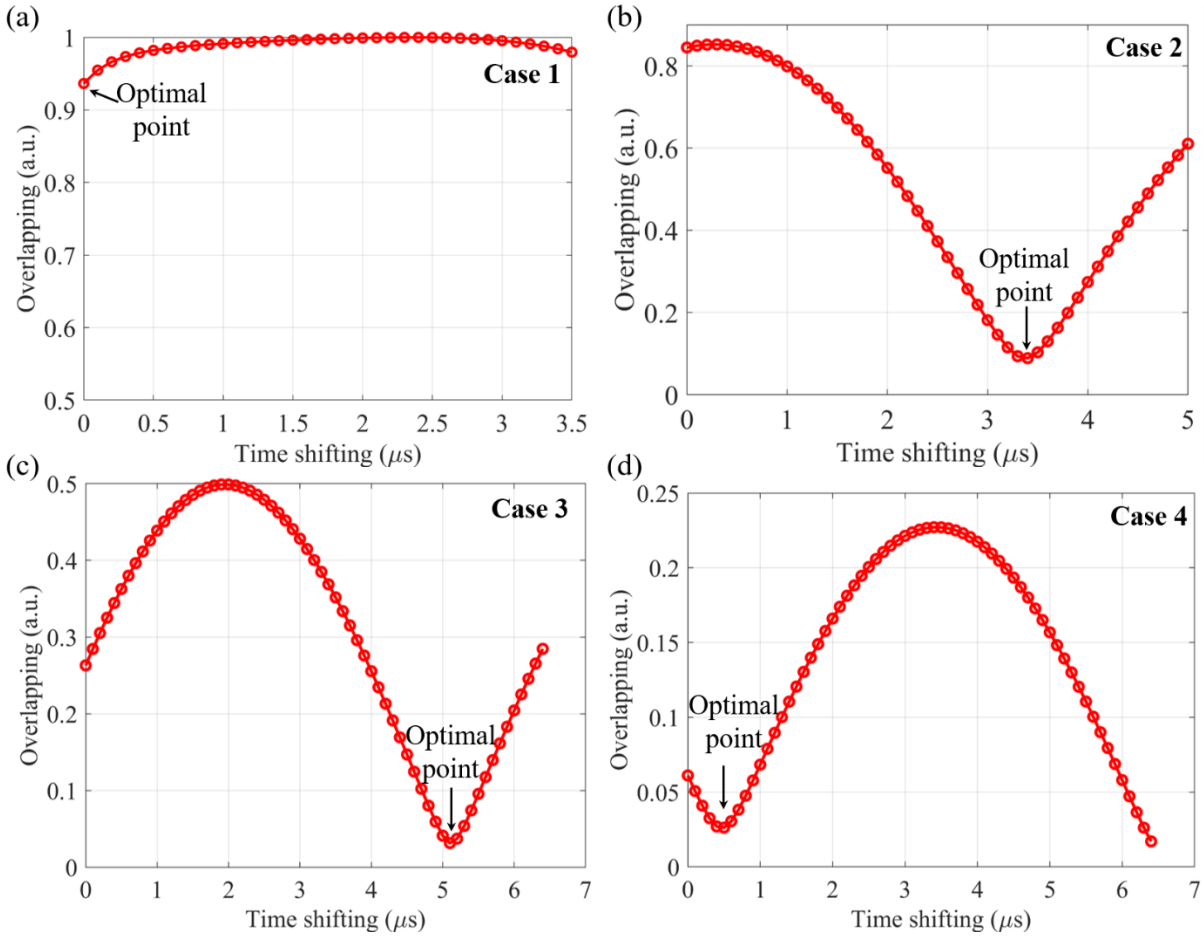

Figure 3.5. Theoretical prediction results of time shifting for (a) Case 1, (b) Case 2, (c) Case 3, and (d) Case 4

The time shifting analysis is performed on the original four cases of wave mixing frequency pair to show the effect of time shifting on wave mixing. In Figure 3.5a, the theoretical prediction indicates that the time shifting is not useful for Case 1, and the overlapping amplitude shows minor change with the increase of time shifting. In addition, the minimum level of overlap is obtained at zero time shifting, and therefore Case 1b can be considered as the identical case as Case 1a. In Cases 2, 3 and 4, the optimized time shifting can be determined at the minimum level of overlap, and the results determined in Figure 3.5 are presented in Table 3.2 (i.e. Cases 2b to 4b). It should be noted that the minimum level of overlap in Case 4 results in boundary reflection, and the second-best point is used. In Figure 3.5, the overlapping amplitude at zero time shifting can be used to verify the prediction in the second step of the proposed approach, which is based on the wave mixing separation index (S). The

results based on the *S* parameter are consistent with the results of time shifting analysis, and the level of overlap at zero time shifting decreases with the increase of the *S* parameter.

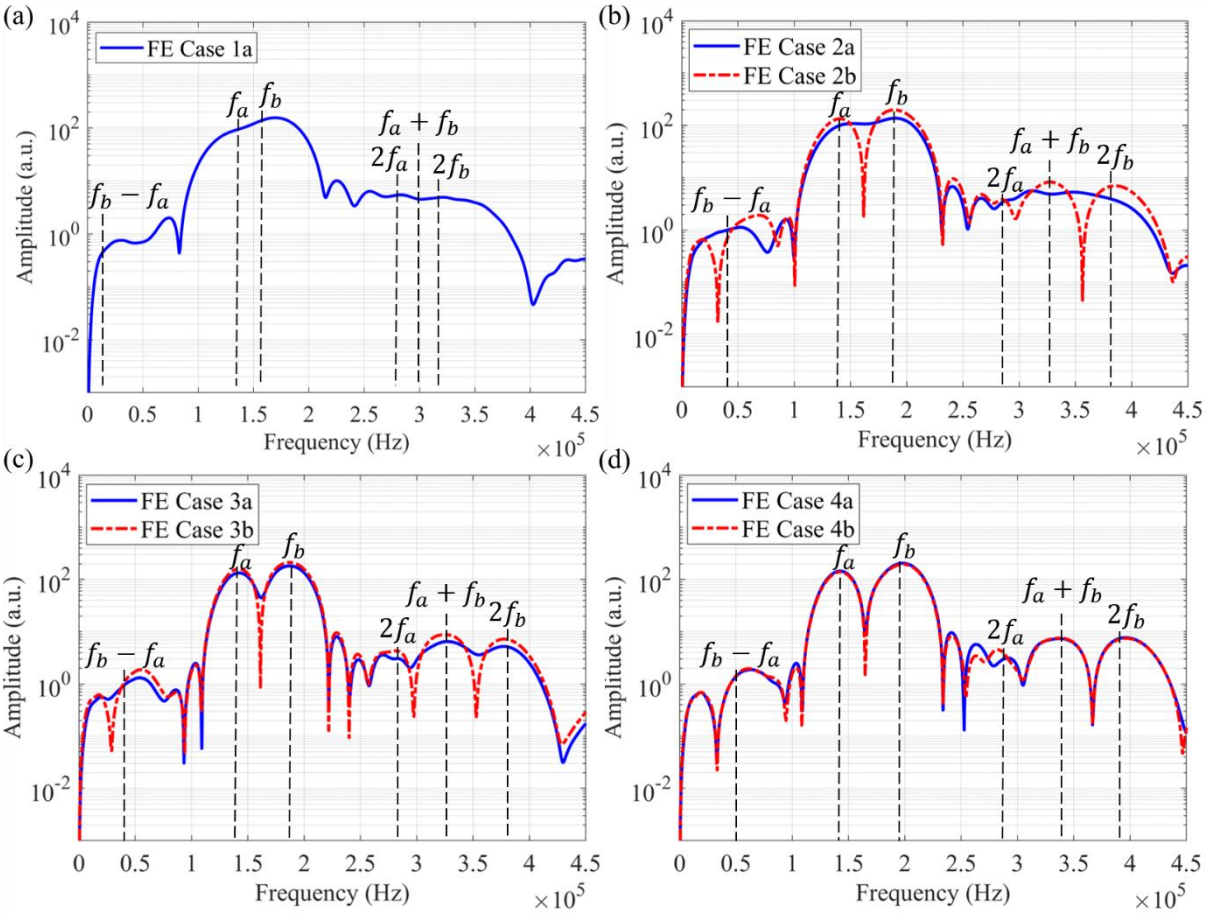

Figure 3.6. Results of numerical simulations for (a) Cases 1a, (b) Cases 2a and 2b, (c) Cases 3a and 3b, and (d) Cases 4a and 4b in frequency spectrum

The outcomes of the numerical simulations are shown in Figure 3.6. The results regarding the overlapping between the two fundamental harmonics in the numerical simulations agree well with the proposed method. The overlapping between the generated second harmonics (at $2f_a$ and $2f_b$) and sum combinational harmonic ($f_a + f_b$) are also consistent with the level of overlap of the fundamental harmonics. In the original cases, *S* parameter can well predict the performance of wave mixing frequency pairs. In Cases 1a and 2a, the sum combinational harmonic and second harmonics show severe overlapping, and results in significant complexity of the harmonic analysis. In Cases 3a and 4a, good separation between the sum combinational and second harmonics can be achieved with the increase of *S* parameter.

The time shifting cases can be compared with the original cases to show the effect of time shifting on wave mixing. Case 2b shows significant improvement of performance of wave mixing compared with the original case, and the harmonic analysis shows good separation of the generated second and combinational harmonics. A better performance of combinational harmonic generation can be achieved in Case 3b compared with Case 2b, which can be predicted with higher value of wave mixing separation index as determined in the original cases and the less overlapping as shown in Figure 3.5. It should be noted that little to no enhancement of performance on wave mixing is shown in Case 4b compared with the original case, which can be considered as the special case as motioned in Section 3.3.3, which can achieve good separation of harmonics without optimization. The difference combinational harmonic is not noticeable in all cases since the specimen only has weakly material nonlinearity [59, 60].

3.4. Experimental studies

3.4.1. Experimental setup

The same cases considered in the numerical simulations (see Table 2) were replicated in the experimental study. Each experimental case was measured four times to determine the uncertainty in the experimental results. The experimental setup is shown in Figure 3.7. The Hann windowing tone-burst was premixed using Equations 3.7a and 3.7c to generate the input signal. The generated signal was input into a NI PXIe-5122 signal generation module, and the input signal was amplified by a CIPRIAN HVA-800A high-voltage power amplifier with 160V peak-to-peak voltage. A circular PZT was used for the source of excitation, which has 0.5 mm thickness and 10 mm diameter. The PZT was bonded to the aluminium plate with conductive epoxy, and the nonlinearity of the bonded layer can be neglected since only a very thin layer of epoxy was used [61]. The specimen was in intact condition and has 1200 mm in both length and width directions with 1.6 mm in thickness direction.

The first measurement point was 400 mm away from the excitation to ensure the full formation of the pure S_0 wave. The vertical displacement measurements at 10 points with 10 mm interval were recorded using 1D laser scanning vibrometer and the PSV-400 acquisition system. Reflective painting was applied on the scanning area to enhance the signal reflection level of 1D laser vibrometer. The recorded signal was averaged 1200 times to improve the signal-to-noise ratio. The acquisition system was connected with a computer to process the experimental data. The acquisition system was synchronized with NI PXIE-5122 signal

generation module. The sampling frequency of acquisition was set as 25.6 MHz with 39.06 nanosecond sampling resolution, and a low-pass filter was applied with upper limit of 1000 kHz. The measured time domain of the S_0 wave signals were used in harmonic analysis.

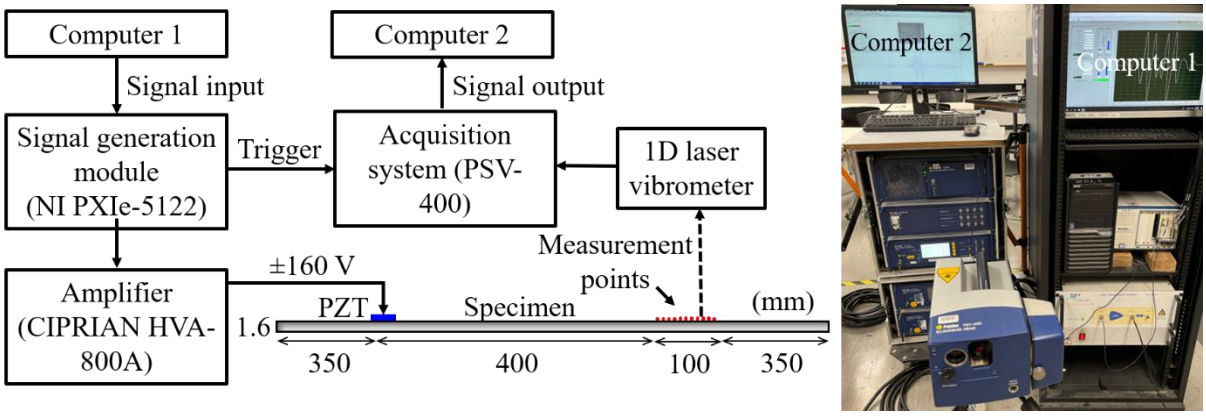

Figure 3.7. Experimental setup

3.4.2. Dispersion curve and mode-tuning curve

The dispersion curve (Figure 3.8a) was obtained using DISPERSE software [62], which is a commercial package using global matrix method to calculate the phase velocity and the group velocity. The Figure 3.8a shows that quasi-synchronism can be achieved in the low frequency range of S_0 wave, and the group velocities of S_0 wave are also quasi-matching in the low frequency range. The mode-tuning curve was measured using the vertical displacement amplitude at the first measurement point. The excitation frequency of mode tuning curve is from 95 kHz to 205 kHz with 5 kHz interval as shown in Figure 3.8b. The results in Figure 3.8b show that the dominance of the A_0 waves over the low frequency range in the vertical displacement direction. The amplitude of S_0 wave increases with the frequency and reaches the maximum amplitude at 185 kHz. The highest S_0 wave to A_0 wave ratio can be observed at 140 kHz.

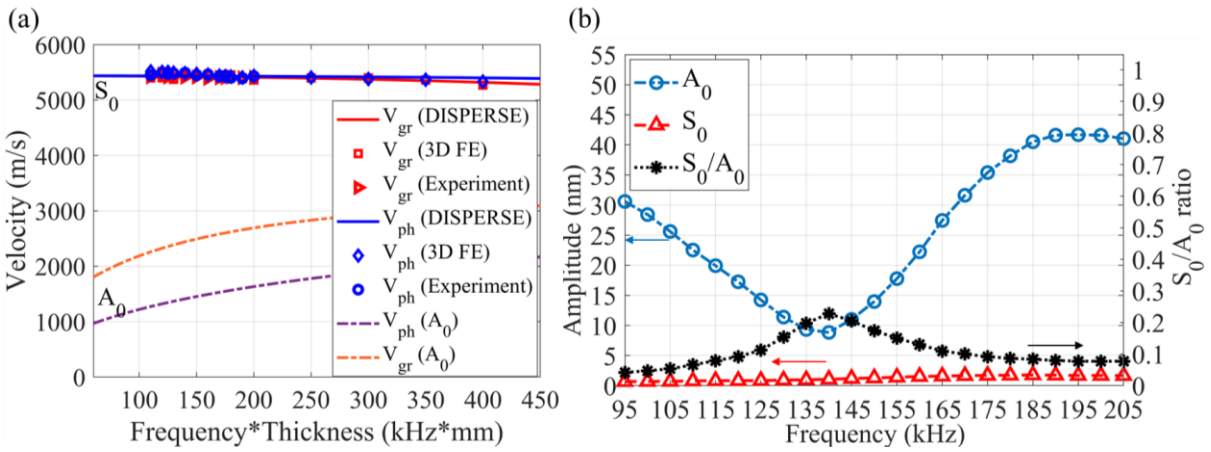

Figure 3.8. (a) Dispersion curve and (b) mode-tuning curve using experimentally measured vertical displacement

3.4.3. Comparison of the finite element simulations

The FE model developed in Section 3.3.1 is validated in this section, using experimental results. The linear features of guided waves are validated in Figure 3.8a in Section 3.4.2. In the experiment, the excitation frequency of dispersion curve is from 100 kHz to 200 kHz with 10 kHz interval. In numerical study, the excitation frequency is validated up to 400 kHz to ensure that the FE model is valid to capture the second harmonic generation of the highest fundamental frequency. The phase velocity and group velocity of S_0 wave of the numerical simulation and experiment have a good agreement, and are consistent with the results obtained from the DISPERSE software.

The nonlinear features of guided waves are validated in Figure 3.9 using the experimental results obtained in the Section 3.4.4. Case 2b can be considered as the baseline case, and the numerical simulation results and experimental results of Case 2b are compared in the frequency spectrum (Figure 3.9a) and in terms of normalized relative nonlinear parameter (Figure 3.9b). The frequency spectrum results of numerical simulations and experiments are normalized about the highest amplitude (at f_b) accordingly. In Figure 3.12a, good matching of second and sum combinational harmonics generation between the experimental result and the numerical simulation is achieved. The small discrepancy of sum combinational harmonic (f_a + f_b) and second harmonic of wave a (at $2f_a$) is due to the small amplitude difference of the fundamental harmonic (f_a). The FE model is limited up to the second order harmonic generation, and therefore, the higher order harmonic generation, e.g. third order harmonics, are not

simulated by the FE model. The Gaussian additive noise in experiment can be observed in the very low frequency range, which is negligible for harmonic analysis because the difference harmonic is not focused in the current study. In Figure 3.9b, the experimental and numerical relative nonlinear parameters are normalized about the first measurement points, accordingly. The normalized relative nonlinear parameter represents the linear increasing trend over wave propagation distance due to the accumulation of material nonlinearity during the wave propagation. There is a good agreement between the numerical simulation and the experimental results. Hence, the linear and nonlinear features of guided waves in the FE model can be validated using the experimental results.

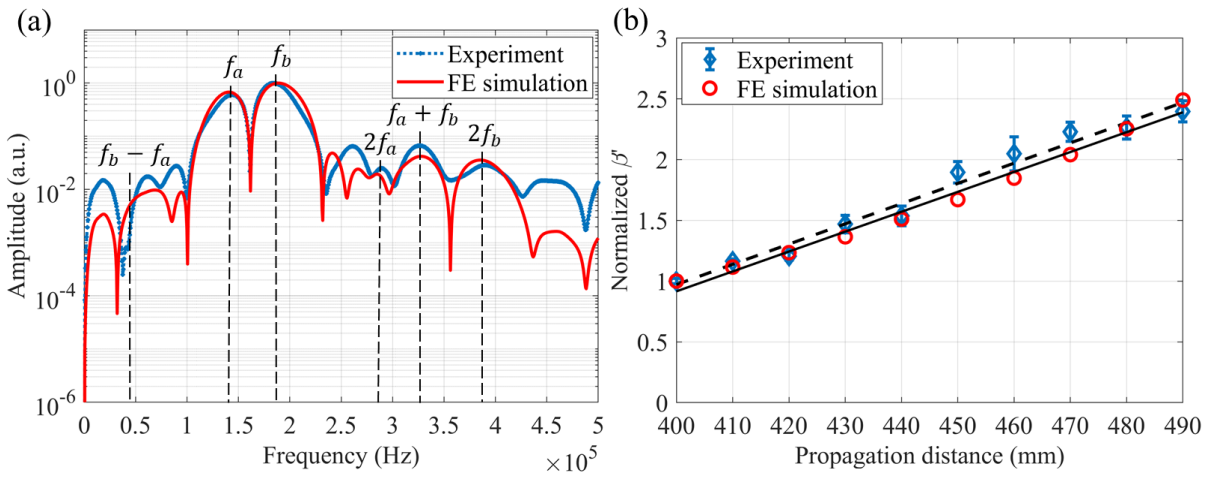

Figure 3.9. FE validation of nonlinear features in Case 2b, (a) in frequency domain, and (b) normalized β' of sum combinational harmonic against wave propagation distance

3.4.4. Experimental results

A relative performance of a frequency pair in the wave mixing method can be characterized based on the R-square value of relative nonlinear parameter of the best fit function. Theoretically, the relative nonlinear parameter of sum combinational harmonic increases linearly with wave propagation distance [20, 22, 25]. The best fit function is performed in the harmonic analysis, and higher value of R-square can indicate better linearity of increasing trend, which means better performance of wave mixing.

3.4.4.1. Effect of the wave mixing separation index on the quality of harmonic generation

Figure 3.10 shows the results of all four cases. A good prediction of the performance can be achieved by using the wave mixing separation index (S). This performance has a noticeable improvement with the increase of S parameter. The fluctuation of relative nonlinear parameter and large error bar in Case 1a can reflect the significant overlapping of second harmonics (at $2f_a$ and $2f_b$) and sum combinational harmonic ($f_a + f_b$). A slight improvement can be observed in Case 2a compared with Case 1a, while the linear increasing trend of relative nonlinear parameter can be observed in Case 3a. In Case 4a, a very good performance of the accumulation of sum combinational harmonic can be achieved with the minimized error bar, and this concludes that the performance of wave mixing frequency pair can be well predicted by S parameter.

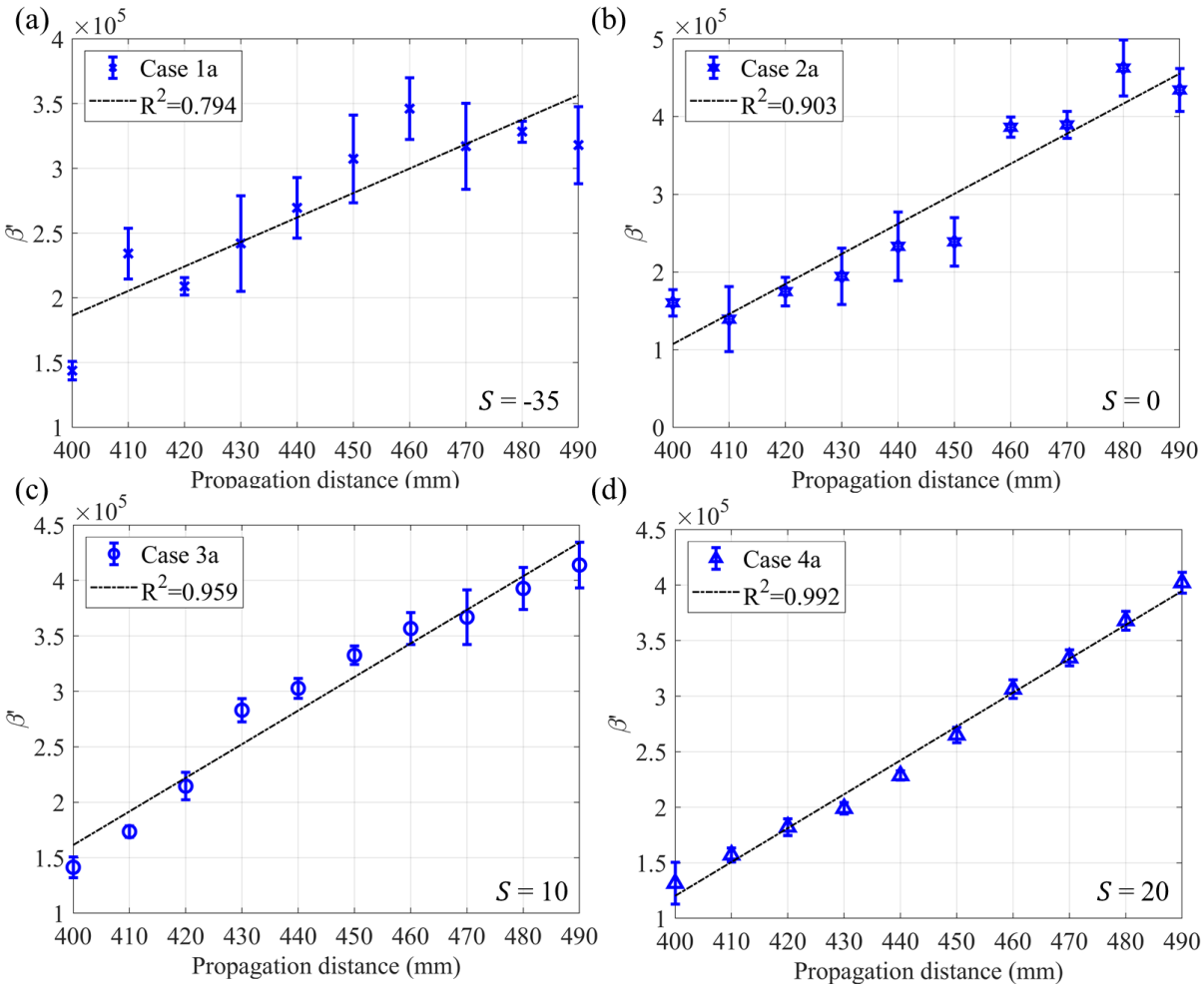

Figure 3.10. Experimental results of β' of sum combinational harmonic ($f_a + f_b$) against propagation distance in (a) Case 1a, (b) Case 2a, (c) Case 3a and (d) Case 4a

3.4.4.2. Effect of the time shifting optimization on the quality of harmonic generation

Figure 3.11 shows the results of cases considered time shifting. In Cases 2b, 3b and 4b, the second harmonics (at $2f_a$ and $2f_b$) and sum combinational harmonic ($f_a + f_b$) have very good separation in frequency spectrum, which agrees well with the results of the numerical simulation in Section 3.3.2. Hence, the harmonic analysis of Cases 2b, 3b and 4b shows that the relative nonlinear parameter increases linearly over wave propagation distance. It should be noted that the generation of higher order harmonics (i.e. third order and fourth order harmonics) become visible in Case 4b. However, the generation of higher order harmonics is out of the scope of this study, and hence, it is not studied in this paper. Therefore, the enhanced performance of the accumulation of sum combinational harmonic can be concluded in comparison with the results of original cases.

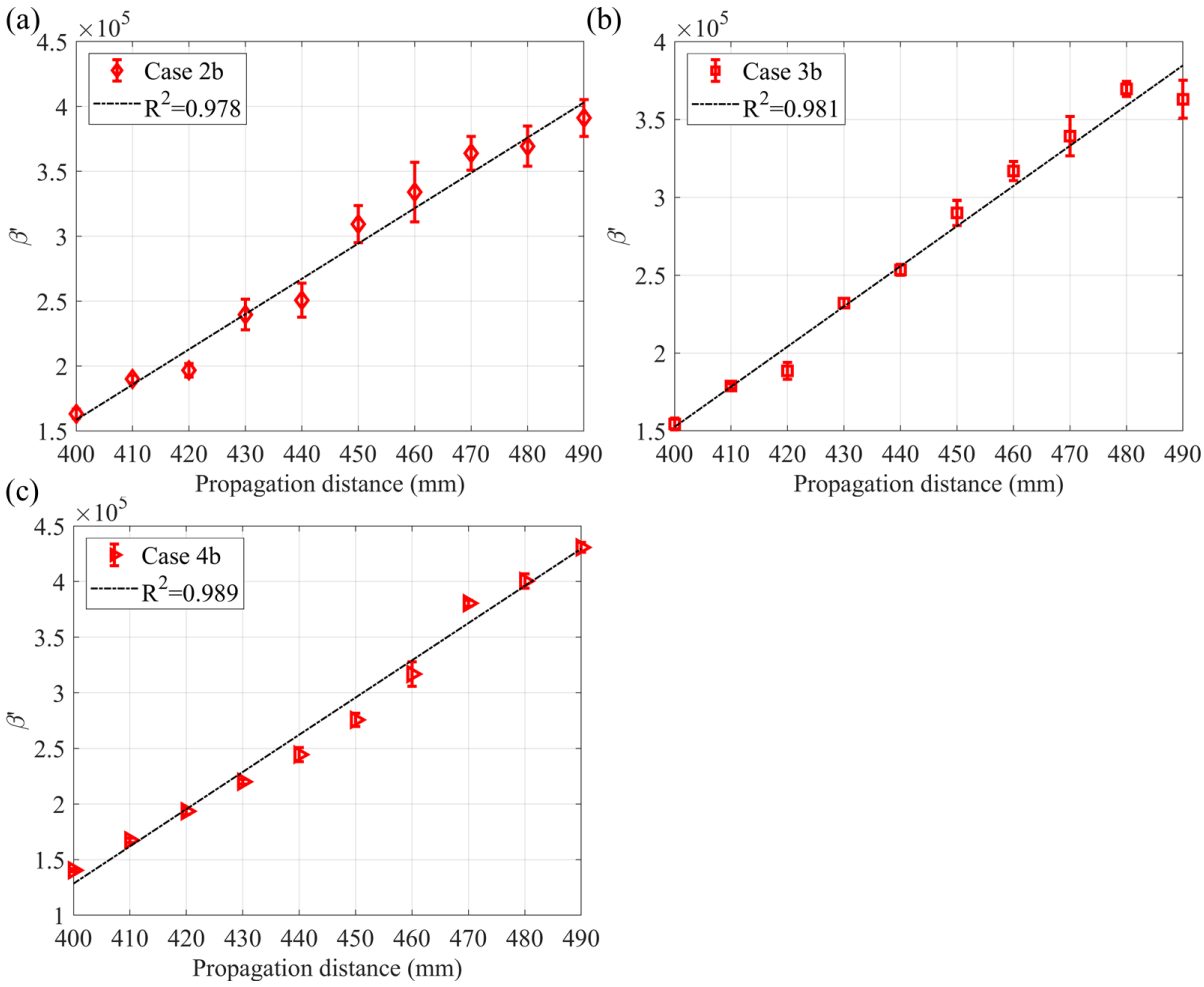

Figure 3.11. Experimental results of β' of sum combinational harmonic ($f_a + f_b$) against propagation distance in (a) Case 2b, (b) Case 3b, and (c) Case 4b

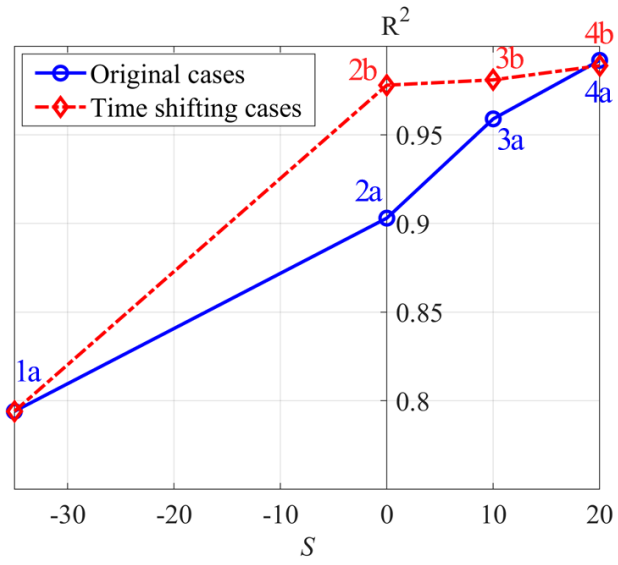

Figure 3.12. R-square value of β' of sum combinational harmonic against wave mixing separation index S

The performance comparison between the original cases and the time shifting cases is shown in Figure 3.12 using the R-square values determined in Figures 3.10 and 3.11. In Case 2b, a significant improvement on the performance of wave mixing can be achieved compared with the original case, and this case can show the efficiency of the time shifting optimization in the wave mixing. Case 3b only slightly enhances the wave mixing performance compared with Cases 3a and 2b since the overlapping of generated harmonics in these two cases are minor. Little to no difference between the original case and the time shifting case can be observed in Cases 4a and 4b. This suggests that the time shifting optimization is not efficient for the special case mentioned in Section 3.3.3, which can achieve good performance without the optimization. It should be noted that Case 4b is predicted to have slightly better performance compared with Case 4a using the proposed method (as shown in Figure 3.5d), and the results shown in Figure 3.12 can be considered as small discrepancy. The small discrepancy is likely due to the Gaussian additive noise of instrumentation and experimental setup (i.e. signal reflection level of 1D laser vibrometer), and it is negligible.

3.5. Conclusion

The frequency pair selection method has been proposed to evaluate the performance of the generation of second and combinational harmonics due to the collinear wave mixing. The

proposed frequency pair selection method can advance the trial-and-error method that was generally used for low-frequency wave mixing, which has a large number of possible frequency pairs, and deliberate selection is needed to avoid the overlapping of the generated harmonics. The time shifting method can be applied to the selected frequency pair to enhance the performance of the wave mixing. The results suggest that the time shifting optimization is applicable to collinear wave mixing when the wave mixing separation index (S) has a positive value. The results also demonstrate the limitation of the time shifting, which is less efficient when the wave mixing separation index (S) is less than zero or when the index is very large. It has demonstrated that the proposed method can be used to enhance the performance of the wave mixing in terms of the clarity and consistency of the combinational and second harmonics generation. The efficiency of the proposed method has been validated by a series of numerical and experimental studies. There is a good agreement between theoretical predictions, numerical simulations and experimental results.

The findings of this study are useful for the selection of frequency pair in collinear wave mixing using two quasi-synchronized waves, especially when the excitation frequencies are limited by various constraints. It should be noted that the findings of the present study are generic and can be applied to the wave mixing of different quasi-synchronized wave modes, such as Rayleigh waves [63], SH0 waves, longitudinal waves in pipes and so on. The findings of this study can help further advance the practical application of fatigue damage evaluation using the guided wave mixing method.

Appendix

Explicit expression of Equations 3.11a and 3.11b,

$$X(k) = [cos(2\pi k t_0) - j\, sin(2\pi k t_0)] \{[cos(\pi(k - f_c)T_d) - j\, sin(\pi(k - f_c)T_d)] \frac{sin(\pi(k - f_c)T_d)}{2N_s \sin\left(\pi(k - f_c)\frac{T_d}{N_s}\right)} + [cos(\pi(k + f_c)T_d) - j\, sin(\pi(k + f_c)T_d)] \frac{sin(\pi(k + f_c)T_d)}{2N_s \sin\left(\pi(k + f_c)\frac{T_d}{N_s}\right)}\} \quad (3.A1)$$

$$W_H(k) = [cos(2\pi k t_0) - j\, sin(2\pi k t_0)]\,[cos(\pi k T_d) - j\, sin(\pi k T_d)] \{\frac{sin(\pi k T_d)}{2N_s \sin\left(\pi k \frac{T_d}{N_s}\right)} + \frac{sin(\pi(k - \Delta k)T_d)}{4N_s \sin\left(\pi(k - \Delta k)\frac{T_d}{N_s}\right)} + \frac{sin(\pi(k + \Delta k)T_d)}{4N_s \sin\left(\pi(k + \Delta k)\frac{T_d}{N_s}\right)}\} \quad (3.A2)$$

Convolution in frequency spectrum,

$$F_W(k) = F(k) \circledast W(k) = \int_{-\infty}^{+\infty} f(\tau) \cdot w(k-\tau)\, d\tau \qquad (3.A3)$$

Crossover frequency of fundamental harmonics with Hann window

$$f_{cr}^{H} = \frac{1}{2}\left[\left(f_a + \Delta k_{f_a}\right) + \left(f_b - \Delta k_{f_b}\right)\right] \qquad (3.A4)$$

Acknowledgement

This work was funded by the Australian Research Council (ARC) DP200102300 and DP210103307 grants. The authors are grateful for the support.

References

[1] Hong M, Mao Z, Todd M D and Su Z 2017 Uncertainty quantification for acoustic nonlinearity parameter in Lamb wave-based prediction of barely visible impact damage in composites *Mech. Syst. Signal. Process.* **82** 448-60

[2] He S, Ng C-T and Yeung C 2020 Time-domain spectral finite element method for modeling second harmonic generation of guided waves induced by material, geometric and contact nonlinearities in beams *International Journal of Structural Stability and Dynamics* **20** 2042005

[3] Lissenden C J 2021 Nonlinear ultrasonic guided waves—Principles for nondestructive evaluation *J. Appl. Phys.* **129** 021101

[4] Marcantonio V, Monarca D, Colantoni A and Cecchini M 2019 Ultrasonic waves for materials evaluation in fatigue, thermal and corrosion damage: A review *Mech. Syst. Signal. Process.* **120** 32-42

[5] Zhu H, Ng C T and Kotousov A 2022 Low-frequency Lamb wave mixing for fatigue damage evaluation using phase-reversal approach *Ultrasonics* 106768

[6] Marzani A and Salamone S 2012 Numerical prediction and experimental verification of temperature effect on plate waves generated and received by piezoceramic sensors *Mech. Syst. Signal. Process.* **30** 204-17

[7] Yang Y, Ng C-T and Kotousov A 2019 Second-order harmonic generation of Lamb wave in prestressed plates *J. Sound Vib.* **460** 114903

[8] Lee Y F and Lu Y 2022 Identification of fatigue crack under vibration by nonlinear guided waves *Mech. Syst. Signal. Process.* **163** 108138

[9] Wang J, Shen Y, Rao D and Xu W 2021 Physical-virtual time reversing of nonlinear Lamb waves for fatigue crack detection and quantification *Mech. Syst. Signal. Process.* **160** 107921

[10] Mandal D D and Banerjee S 2019 Identification of breathing type disbonds in stiffened panels using non-linear lamb waves and built-in circular PWT array *Mech. Syst. Signal. Process.* **117** 33-51
[11] Soleimanpour R and Ng C-T 2021 Scattering analysis of nonlinear Lamb waves at delaminations in composite laminates *Journal of Vibration and Control* 1077546321990145
[12] Deng M 2003 Analysis of second-harmonic generation of Lamb modes using a modal analysis approach *J. Appl. Phys.* **94** 4152-9
[13] Krishna Chillara V and Lissenden C J 2012 Interaction of guided wave modes in isotropic weakly nonlinear elastic plates: Higher harmonic generation *J. Appl. Phys.* **111** 124909
[14] Deng M 1999 Cumulative second-harmonic generation of Lamb-mode propagation in a solid plate *J. Appl. Phys.* **85** 3051-8
[15] Liu Y, Chillara V K, Lissenden C J and Rose J L 2013 Third harmonic shear horizontal and Rayleigh Lamb waves in weakly nonlinear plates *J. Appl. Phys.* **114** 114908
[16] Hong M, Su Z, Wang Q, Cheng L and Qing X 2014 Modeling nonlinearities of ultrasonic waves for fatigue damage characterization: Theory, simulation, and experimental validation *Ultrasonics* **54** 770-8
[17] Li W, Cho Y and Achenbach J D 2012 Detection of thermal fatigue in composites by second harmonic Lamb waves *Smart. Mater. Struct.* **21** 085019
[18] Pruell C, Kim J-Y, Qu J and Jacobs L 2009 A nonlinear-guided wave technique for evaluating plasticity-driven material damage in a metal plate *NDT&E Int.* **42** 199-203
[19] Matsuda N and Biwa S 2011 Phase and group velocity matching for cumulative harmonic generation in Lamb waves *J. Appl. Phys.* **109** 094903
[20] Müller M F, Kim J-Y, Qu J and Jacobs L J 2010 Characteristics of second harmonic generation of Lamb waves in nonlinear elastic plates *J. Acoust. Soc. Am.* **127** 2141-52
[21] Yang Y, Ng C-T and Kotousov A 2019 Second harmonic generation of guided wave at crack-induced debonding in FRP-strengthened metallic plates *International Journal of Structural Stability and Dynamics* **19** 1940006
[22] Wan X, Tse P, Xu G, Tao T and Zhang Q 2016 Analytical and numerical studies of approximate phase velocity matching based nonlinear S0 mode Lamb waves for the detection of evenly distributed microstructural changes *Smart. Mater. Struct.* **25** 045023
[23] Zuo P, Zhou Y and Fan Z 2016 Numerical and experimental investigation of nonlinear ultrasonic Lamb waves at low frequency *Appl. Phys. Lett.* **109** 021902
[24] Hughes J M, Mohabuth M, Kotousov A and Ng C-T 2021 The fundamental ultrasonic edge wave mode: Propagation characteristics and potential for distant damage detection *Ultrasonics* **114** 106369
[25] Hughes J M, Kotousov A and Ng C-T 2020 Generation of higher harmonics with the fundamental edge wave mode *Appl. Phys. Lett.* **116** 101904
[26] Croxford A J, Wilcox P D, Drinkwater B W and Nagy P B 2009 The use of non-collinear mixing for nonlinear ultrasonic detection of plasticity and fatigue *J. Acoust. Soc. Am.* **126** EL117-EL22
[27] Tang G, Liu M, Jacobs L J and Qu J 2014 Detecting localized plastic strain by a scanning collinear wave mixing method *J Nondestr Eval.* **33** 196-204

[28] Sampath S and Sohn H 2022 Cubic nonlinearity parameter measurement and material degradation detection using nonlinear ultrasonic three-wave mixing *Ultrasonics* **121** 106670
[29] Sampath S and Sohn H 2022 Detection and localization of fatigue crack using nonlinear ultrasonic three-wave mixing technique *International Journal of Fatigue* **155** 106582
[30] Li W, Deng M, Hu N and Xiang Y 2018 Theoretical analysis and experimental observation of frequency mixing response of ultrasonic Lamb waves *J. Appl. Phys.* **124** 044901
[31] Hasanian M and Lissenden C J 2018 Second order ultrasonic guided wave mutual interactions in plate: Arbitrary angles, internal resonance, and finite interaction region *J. Appl. Phys.* **124** 164904
[32] Zhu H, Ng C-T and Kotousov A 2022 The performance optimization of combinational harmonic generation for quasi-synchronous Lamb wave mixing. In: *Sensors and Smart Structures Technologies for Civil, Mechanical, and Aerospace Systems 2022*: SPIE) pp 293-300
[33] Ishii Y, Biwa S and Adachi T 2018 Non-collinear interaction of guided elastic waves in an isotropic plate *J. Sound Vib.* **419** 390-404
[34] Liu M, Tang G, Jacobs L J and Qu J 2012 Measuring acoustic nonlinearity parameter using collinear wave mixing *J. Appl. Phys.* **112** 024908
[35] Shan S, Hasanian M, Cho H, Lissenden C J and Cheng L 2019 New nonlinear ultrasonic method for material characterization: Codirectional shear horizontal guided wave mixing in plate *Ultrasonics* **96** 64-74
[36] Jingpin J, Xiangji M, Cunfu H and Bin W 2017 Nonlinear Lamb wave-mixing technique for micro-crack detection in plates *NDT&E Int.* **85** 63-71
[37] Sampath S, Jang J and Sohn H 2022 Ultrasonic Lamb wave mixing based fatigue crack detection using a deep learning model and higher-order spectral analysis *International Journal of Fatigue* 107028
[38] Jiao J, Lv H, He C and Wu B 2017 Fatigue crack evaluation using the non-collinear wave mixing technique *Smart. Mater. Struct.* **26** 065005
[39] Liu P, Sohn H, Yang S and Lim H J 2016 Baseline-free fatigue crack detection based on spectral correlation and nonlinear wave modulation *Smart. Mater. Struct.* **25** 125034
[40] Pineda Allen J C and Ng C T 2021 Nonlinear Guided-Wave Mixing for Condition Monitoring of Bolted Joints *Sensors* **21** 5093
[41] Aseem A and Ng C T 2021 Debonding detection in rebar-reinforced concrete structures using second harmonic generation of longitudinal guided wave *NDT&E Int.* **122** 102496
[42] Aslam M, Bijudas C, Nagarajan P and Remanan M 2020 Numerical and Experimental Investigation of Nonlinear Lamb Wave Mixing at Low Frequency *Journal of Aerospace Engineering* **33** 04020037
[43] Blanloeuil P, Rose L, Veidt M and Wang C 2021 Nonlinear mixing of non-collinear guided waves at a contact interface *Ultrasonics* **110** 106222
[44] Yeung C and Ng C T 2020 Nonlinear guided wave mixing in pipes for detection of material nonlinearity *J. Sound Vib.* **485** 115541
[45] Li W, Lan Z, Hu N and Deng M 2021 Modeling and simulation of backward combined harmonic generation induced by one-way mixing of longitudinal ultrasonic guided waves in a circular pipe *Ultrasonics* **113** 106356

[46] Wang R, Wu Q, Yu F, Okabe Y and Xiong K 2019 Nonlinear ultrasonic detection for evaluating fatigue crack in metal plate *Struct. Health Monitor.* **18** 869-81
[47] Ding X, Xu C, Deng M, Zhao Y, Bi X and Hu N 2021 Experimental investigation of the surface corrosion damage in plates based on nonlinear Lamb wave methods *NDT&E Int.* **121** 102466
[48] Giurgiutiu V 2007 *Structural health monitoring: with piezoelectric wafer active sensors*: Elsevier)
[49] Lathi B P and Green R A 2005 *Linear systems and signals* vol 2: Oxford University Press New York)
[50] Harris F J 1978 On the use of windows for harmonic analysis with the discrete Fourier transform *Proceedings of the IEEE* **66** 51-83
[51] Antoni J and Randall R 2004 Unsupervised noise cancellation for vibration signals: part II—a novel frequency-domain algorithm *Mech. Syst. Signal. Process.* **18** 103-17
[52] Proakis J G 2001 *Digital signal processing: principles algorithms and applications*: Pearson Education India)
[53] Zygmund A 2002 *Trigonometric series* vol 1: Cambridge university press)
[54] Yang Y, Ng C T, Mohabuth M and Kotousov A 2019 Finite element prediction of acoustoelastic effect associated with Lamb wave propagation in pre-stressed plates *Smart. Mater. Struct.* **28** 095007
[55] Murnaghan F D 1937 Finite deformations of an elastic solid *Am. J. Math.* **59** 235-60
[56] Gandhi N, Michaels J E and Lee S J 2012 Acoustoelastic Lamb wave propagation in biaxially stressed plates *J. Acoust. Soc. Am.* **132** 1284-93
[57] Hu X, Ng C T and Kotousov A 2021 Scattering characteristics of quasi-Scholte waves at blind holes in metallic plates with one side exposed to water *NDT&E Int.* **117** 102379
[58] Mei H and Giurgiutiu V 2018 Effect of structural damping on the tuning between piezoelectric wafer active sensors and Lamb waves *Journal of Intelligent Material Systems and Structures* **29** 2177-91
[59] Jhang K-Y 2009 Nonlinear ultrasonic techniques for nondestructive assessment of micro damage in material: a review *INT J PRECIS ENG MAN* **10** 123-35
[60] Jhang K-Y, Lissenden C J, Solodov I, Ohara Y and Gusev V 2020 *Measurement of Nonlinear Ultrasonic Characteristics*: Springer)
[61] Shan S, Cheng L and Li P 2016 Adhesive nonlinearity in Lamb-wave-based structural health monitoring systems *Smart. Mater. Struct.* **26** 025019
[62] Pavlakovic B and Lowe M 2003 Disperse Software Manual Version 2.0. 1 6B *Imperial College, London, UK*
[63] Morlock M B, Kim J-Y, Jacobs L J and Qu J 2015 Mixing of two co-directional Rayleigh surface waves in a nonlinear elastic material *J. Acoust. Soc. Am.* **137** 281-92

Chapter 4

Fatigue crack detection in edges of thin-walled structures with corners using the fundamental mode of edge waves

Publication:

H. Zhu, C.T. Ng, and A. Kotousov, Fatigue crack detection in edges of thin-walled structures with corners using the fundamental mode of edge waves, *Ultrasonics*, 132 (2023), 106995.

Statement of Authorship

Title of Paper	Fatigue crack detection in edges of thin-walled structures with corners using the fundamental mode of edge waves
Publication Status	☑ Published ☐ Accepted for Publication ☐ Submitted for Publication ☐ Unpublished and Unsubmitted work written in manuscript style
Publication Details	H. Zhu, C.T. Ng, and A. Kotousov, Fatigue crack detection in edges of thin-walled structures with corners using the fundamental mode of edge waves, Ultrasonics, 132 (2023), 106995.

Principal Author

Name of Principal Author (Candidate)	Hankai Zhu		
Contribution to the Paper	Conceptualization, Methodology, Experiment, Finite Element simulation, Validation, Formal analysis, Writing – original draft and editing.		
Overall percentage (%)	85%		
Certification:	This paper reports on original research I conducted during the period of my Higher Degree by Research candidature and is not subject to any obligations or contractual agreements with a third party that would constrain its inclusion in this thesis. I am the primary author of this paper.		
Signature		Date	23/10/2023

Co-Author Contributions

By signing the Statement of Authorship, each author certifies that:

i. the candidate's stated contribution to the publication is accurate (as detailed above);

ii. permission is granted for the candidate in include the publication in the thesis; and

iii. the sum of all co-author contributions is equal to 100% less the candidate's stated contribution.

Name of Co-Author	Ching-Tai Ng		
Contribution to the Paper	Supervision, Advising, Writing – review and editing.		
Signature		Date	6 Nov 2023

Name of Co-Author	Andrei Kotousov		
Contribution to the Paper	Supervision, Advising, Writing – review and editing.		
Signature		Date	7 Nov 2023

Chapter 4: Fatigue crack detection in edges of thin-walled structures with corners using the fundamental mode of edge waves

Hankai Zhu[1], Ching Tai Ng[1], Andrei Kotousov[2]

[1] School of Architecture and Civil Engineering, The University of Adelaide, Adelaide, SA 5005, Australia

[2] School of Electrical and Mechanical Engineering, The University of Adelaide, Adelaide, SA 5005, Australia

Abstract

Non-destructive detection and evaluation of fatigue cracks is critical to maintain safety and effective operation of high-value assets working under cyclic loading. However, this can be difficult in the case of the corners of the structural elements, especially at inaccessible locations. In this article, the propagation of the fundamental symmetric mode of edge wave (ES_0) along structural features such as sharp and rounded corners are investigated using experimental and numerical methods. The ultimate aim of this study is to demonstrate that the ES_0 is a promising for defect detection in geometries with corners. The outcomes of this study show that ES_0 wave is able to propagate through sharp and rounded corners and provides a way to inspect difficult-to-reach locations. Further, the numerical simulations indicate that the radius-to-wavelength ratio above 3 has no significant impact on the wave amplitude when the ES_0 propagates through the rounded corner. The results also demonstrate that the presence of fatigue crack leads to generation of the second harmonic of the ES_0 wave mode, and this phenomenon can be utilised in the development of fatigue crack detection and characterization procedures.

Keywords: Sharp corners; Rounded corners; Edge wave; Nonlinear guided wave; Fatigue crack location; NDE

4.1. Introduction

Non-destructive defect evaluation is critical for safety, reliability and effective operation, including for structures subjected to cyclic loading. This type of loading can cause fatigue damage, lead to propagation of fatigue cracks and, finally, cause failures of load bearing structural components. The application of guided ultrasonic waves for fatigue crack detection and evaluation has been studied extensively over the past three decades, specifically, for thin-walled structures [1-3]. The previous research has mainly focused on simple geometries such as the flat plates [4, 5] or circular pipes. Recently, feature guided waves have attracted significant attention of the research community. The propagation of these waves is facilitated by various geometric features such as edges and weld seams, which are commonly exist in most of engineering structures. These features result in wave scattering and reflections making difficult the application of conventional ultrasonic techniques for defect evaluation. However, these features can also serve as waveguides permitting the propagation of so-called feature guided wave modes; and these wave modes can also be utilised for defect detection and evaluation purposes.

Various feature-guided wave modes have been investigated in the past, for example, the one propagating in rail web [6, 7], transverse bends [8-10], fastener hole [11], fuel weep hole [12, 13], and bonded stiffeners [14, 15]. Other studies have focused on defect detection in inaccessible locations such as pipe bend [16, 17], pipe supports [18], steel rebar [19-21], and L-joints [22]. One type of the feature-guided waves called the edge waves is able to propagate along plate edges has attracted a lot of attention over the past decade, and it has been studied both theoretically [23, 24] and experimentally [25, 26]. The edge waves are generally multi-modal and dispersive with exception of the fundamental mode, which is weakly dispersive. The propagation of edge waves is confined near the surface of the edge, so the internal structure has no influence on its behaviour. The dispersion curve of the fundamental symmetric mode of edge wave (ES_0), which is the focus of the current study, was reported in several previous studies [27, 28] and is shown in Figure 4.1a. The results are expressed in terms of the dimensionless value, frequency-thickness value (FTV = $\omega 2h/c_2$), where $2h$ is the thickness of specimen, ω is the angular frequency, and c_2 is the shear wave speed ($c_2 = 3177\ m/s$). It was also demonstrated theoretically and experimentally that the ES_0 wave mode at low frequency-thickness values (FTVs < 6, the definition of FTV is given in the caption to Figure 4.1) has a small amplitude decay and almost no dispersion [29]. At FTVs < 4.5 (the first cut-off frequency) the multi-modes generation can be avoided [26]. It was also demonstrated that the ES_0 wave

mode has a good sensitivity to the corrosion damage and has a great potential for practical applications [30].

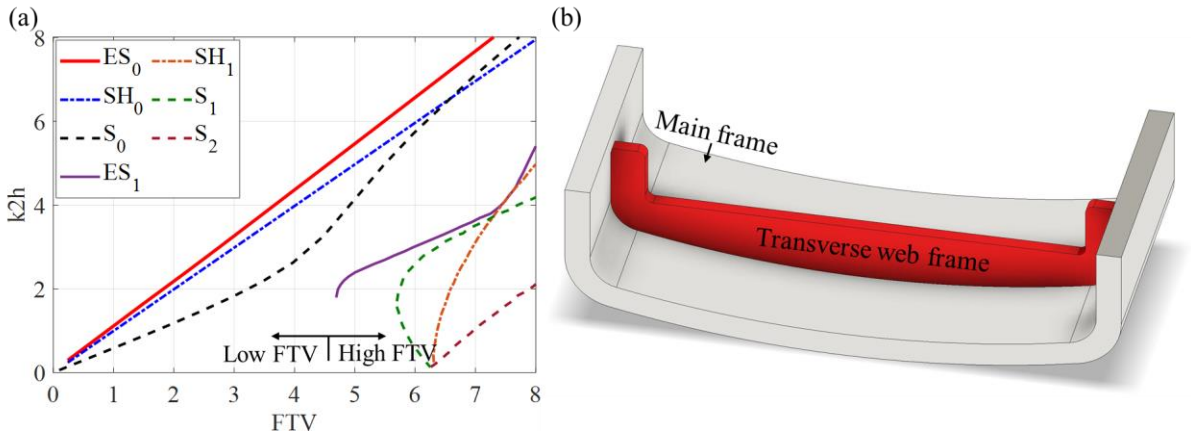

Figure 4.1. (a) Dispersion curve for ES_0 wave against FTVs (k is wavenumber), and (b) Schematic diagram of the transverse web frame of ship structure

The previous studies, which are based on traditional bulk and Rayleigh-Lamb wave modes, often utilise the echo-pulse method. However, this method has its own limitations, and its application can be very challenging due to environmental effects [31], wave scattering and multiple reflections, specifically, if the inspection locations are near the structural edges and geometric features [32]. The conventional way to address the aforementioned issues and improve the sensitivity of defect detection is to apply a 2D sensor array [33, 34], which requires multiple sensors and careful design of the sensor network. However, this can be quite difficult and costly to implement in real situations.

As aforementioned most of the past studies have been focused on ideal geometries, which are rare in many practical situations. Real structural components, such as the one shown in Figure 4.1b, often have corners, which makes the defect inspections difficult. This study is aimed to address these shortcomings as well as investigate the characteristics of guided waves, which are associated with these geometries. This study is limited to detection of a certain type of mechanics damage – fatigue cracks, which are largely associated with cyclic loading. Investigation of detection and characterization of other types of damage will be subject of future studies.

Over the past decade, research efforts directed on the utilisation of various features of nonlinear guided waves have shown a great promise in damage detection. Methods based on the nonlinear features, such as the second-order harmonics generation, demonstrated a much better sensitivity to the presence of fatigue cracks [35, 36] compared with the linear guided waves. It was highlighted in many studies that the generation of second-order harmonics due to presence of a crack is associated with the contact acoustic nonlinearity (CAN). The mechanisms of CAN can be explained as follows. The compressive part of the ultrasonic wave totally transmits through the fatigue crack, while when the fatigue crack is opened as a result of the tensile part of the wave, and the tensile part of the ultrasonic wave is partially scattered and reflected [37, 38] causing nonlinearity and generation of high-order harmonics. Many past studies indicated that this phenomenon (generation of high-order harmonics) can be successfully utilised to detect and evaluate fatigue cracks. Various characteristics, e.g. the group velocity and the arrival time of the second harmonic wave, have been previously utilised for characterizing CFRP debonding [39] and concrete rebar debonding [19] with Rayleigh-Lamb guided waves.

In this study, we first explore the characteristics of ES_0 wave mode in low FTV region propagating along sharp corners and rounded corners. The low FTV region (FTV < 4.5) is of particular interest for the purpose of non-destructive defect evaluation as this avoids energy decay and the generation of multiple edge wave modes. A parametric numerical study is carried out to investigate the effect of the radius-to-wavelength ratio on the ES_0 wave propagation along the rounded corners. The latter represents a typical structural feature as discussed earlier. The finite element (FE) study is verified with experimental results obtaining using Laser Vibrometry. Further, the second harmonic generation at different locations of fatigue cracks is investigated numerically to demonstrate the possibility of fatigue crack detection in thin-walled structures with corners and remote locations, which can be inaccessible with the traditional non-destructive defect detection methods.

This paper is organised as follows. The next section, Section 4.2, briefly presents the theoretical preliminaries of edge waves. The simplified theoretical analysis indicates the possibility for edge waves to propagate through corners. Section 4.3 describes the experimental setups and the outcomes of the experimental study. The three-dimensional (3D) FE model is developed and validated using experimental results, and numerical parametric studies are discussed in detail in Section 4.4. Finally, main conclusions from the numerical and

experimental studies, which are important in practical utilisations of ES_0 wave mode for distant defect detection, are drawn in Section 4.5.

4.2. Theoretical preliminaries

The problem of edge wave propagation along a straight edge of a finite thickness plate can be formulated mathematically using the governing equation of the 3D linear elasticity in terms of the displacement vector $\boldsymbol{u}$ as below. The coordinate system with spatial variables x_1, x_2 and x_3 is shown in Figure 4.2 (in Section 4.3).

$$(\lambda + \mu)\,\mathrm{grad}\,\mathrm{div}\,\boldsymbol{u} + \mu\Delta\boldsymbol{u} = \rho\frac{\partial^2\boldsymbol{u}}{\partial t^2} \tag{4.1}$$

where $\boldsymbol{u} = \{u_1, u_2, u_3\}$ represents the displacement components in the selected reference system, x_1, x_2 and x_3 [23]. λ and μ are Lame's constants, ρ represents mass density, and Δ is the three-dimensional Laplace operator. The edge waves can be assumed to propagate along x_1 direction, and the wavenumber in x_1 direction is denoted as ξ. The propagation factor is $e^{-i(\omega t - \xi x_1)}$ and ω is the angular frequency. The free boundary is assumed at the plate faces, which is perpendicular to x_2-direction, See Figure 4.2.

The Laplace transform and Fourier transform can be applied to simplify the 3D linear elasticity problem with respect to time variable t and spatial variable x_1, respectively [28].

$$\boldsymbol{U}(x_2, x_3, \omega, \xi) = \int_{-\infty}^{\infty}\int_{0}^{\infty}\boldsymbol{u}(x_1, x_2, x_3, t)e^{-i(\omega t - \xi x_1)}\,dt\,dx_1 \tag{4.2}$$

For symmetric wave modes the solution of Equation 4.2 can be decomposed as the superposition of Lamb waves and shear waves [27, 28]:

$$\boldsymbol{U}(x_2, x_3, \omega, \xi) = \sum_{0}^{\infty} C_n^L \boldsymbol{U}_n^L(x_2)e^{-i\xi_n x_3} + \sum_{0}^{\infty} C_n^H \boldsymbol{U}_n^H(x_2)e^{-i\xi_n x_3} \tag{4.3}$$

where C_n^L and C_n^H are the coefficients of Lamb waves and shear waves depending on the boundary conditions at the edge. It should be noted that the displacement components of Lamb waves ($\boldsymbol{U}_n^L$) and shear waves ($\boldsymbol{U}_n^H$) are eigenfunctions and depend on x_2 variable.

The mechanism of edge wave mode propagation through a sharp corner is complex, since a part of the energy will be dissipated in the form of Lamb waves and scattered. The

reflected edge wave mode from a 90-degree sharp corner which propagate along the x_1 direction (in x_1-x_2 plane) has the identical wavenumber component ξ and wave mode as the incident wave mode [23]. At the same time, a new edge wave mode will be generated and propagated along the x_3 direction (in x_3-x_2 plane) with the same wavenumber component ξ and wave mode as the incident wave mode according to the Snell's Law. However, analytical investigations of these wave modes are prohibitively difficult and cumbersome. Therefore, the mechanism of this new edge wave mode generation and propagation will be further analysed and discussed in this paper based on the outcomes of numerical simulations and analysis of numerical results.

4.3. Experimental studies

4.3.1. Experimental setup

The experimental setup is shown in Figure 4.2. The 8-cycle Hann-windowed tone-burst was generated by a signal generation module (NI PXIe-5122), and then the signal was amplified by a high voltage amplifier (CIPRIAN HVA-800A) with 200V peak-to-peak voltage. The ULTRAN GC200 was used as the transducer for the wave excitation generation, and the wedge angle is approximately 52-degree with the wave speed of the wedge material is 2300 m/s [29]. The designed wedge can be suitable for the ES_0 wave generation within a range of FTVs, since the phase velocity and group velocity of ES_0 waves are quasi-synchronous. The wedge transducer was coupled with the specimen and the transducer using high vacuum grease (DOW CORNING), and this coupling method enables stable transmission and generation of ES_0 waves compared with the oil coupling method [29], which can become unsteady over time. The specimen with 700 mm in length, 500 mm in width, and 5mm in the thickness direction was under intact condition. The edges of the specimen were labelled as E1 to E4 based on the transmitting sequence of the wave. The wedge was coupled at edge E1 with an alignment device, and the wedge was 200 mm away from the corner to avoid the interference of reflected waves.

The normal displacement (perpendicular to the x_3 direction) at the midplane was measured using the 1D laser vibrometer and the PSV-400 acquisition system, and the acquisition system was synchronized with the signal generation module. Reflective coating was applied on the edges of the specimen to enhance the signal-to-noise ratio measured. The first measurement point (Point 1) was 100 mm away from the wedge, which is more than three

wavelengths of the excited wave mode, and the distance between two measurement points was 50 mm. There were 39 measurement points in the experiment which are defined as Points 1 to 39. It should be noted that it was infeasible to measure the normal displacement at the corner tips in the experiment, and therefore, only the measurement points at the flat edges were measured. The recorded signal was averaged 800 times, and the sampling acquisition was 25.6 MHz with 39.06 nanosecond sampling resolution, which was sufficient to capture the ES_0 wave propagation. A low-pass filter with upper limit of 1000 kHz was applied to reduce the high frequency noise.

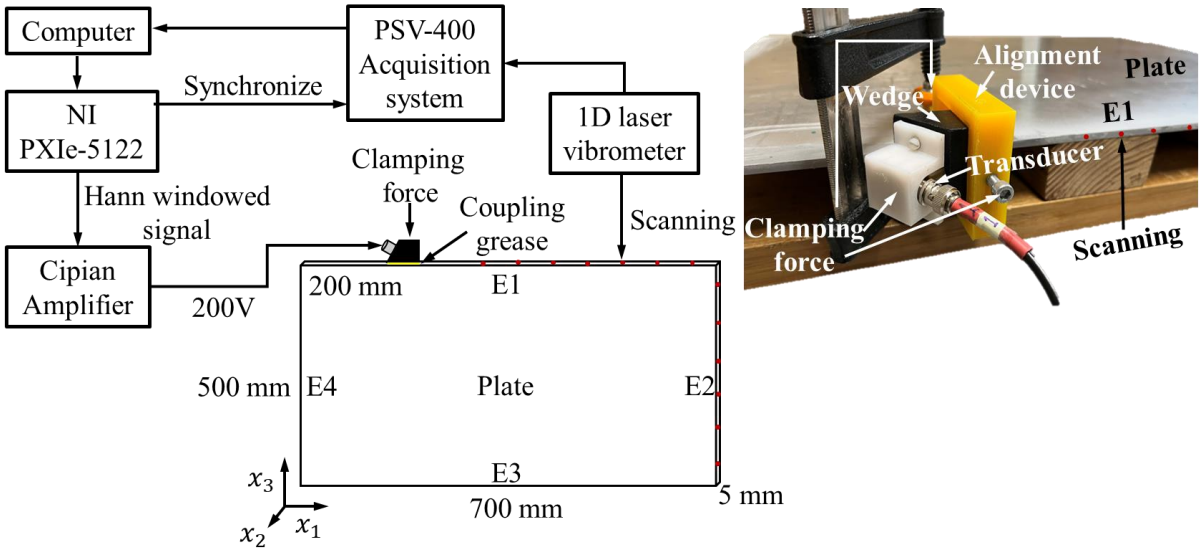

Figure 4.2. Experimental setup

4.3.2. ES_0 wave mode propagation through sharp corners

The time-displacement domain at Point 5 in the first edge (E1) is shown in Figure 4.3, and the envelope of the displacement can be obtained using the Hilbert transform, which was briefly described previously. The result shows that the ES_0 waves with low FTV (at FTV = 2) can propagate over a long distance, and the ES_0 waves can propagate through the sharp corners. The first peak of the envelope (E1E) is the emitted ES_0 wave from wedge and the amplitude is much higher compared with the fundamental symmetric mode (S_0) of Lamb wave. Therefore, the influence of mode coupling of Lamb mode waves with edge mode waves is considered to be negligible. The second peak of envelope (E1R) is the reflected wave generated due to the sharp corner between the edges E1 and E2. The third peak of envelop (E4T) is the transmitted

wave from the edges E4 to E1 after propagating through all four plate edges and all four corners, and the waveform of which can still be distinguished from other scattered waves and wave modes.

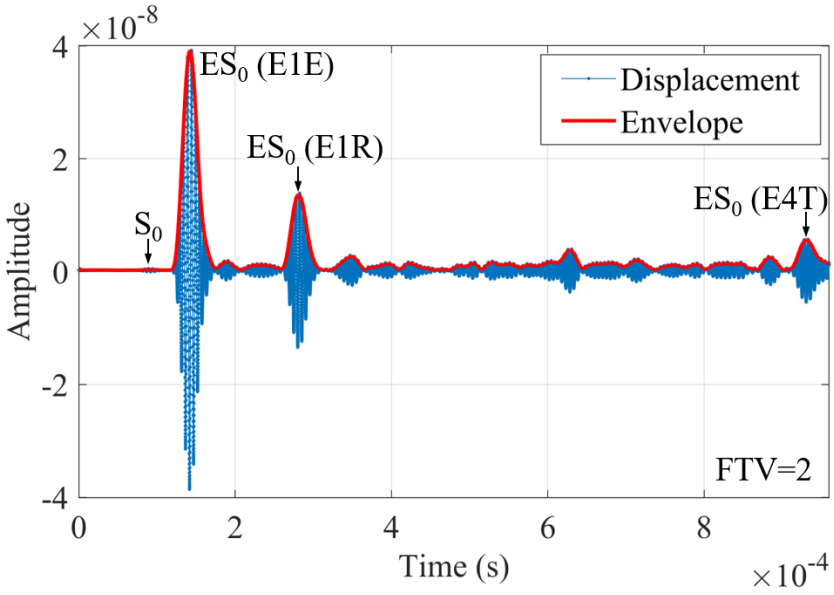

Figure 4.3. Time-displacement domain and the envelope of the measured signal at Point 5

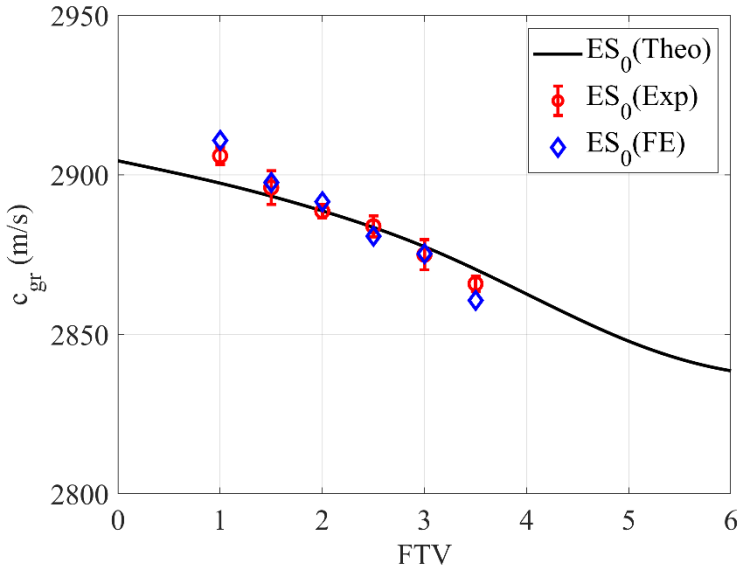

Figure 4.4. Group velocity of ES_0 waves in low FTVs (FTV = $\omega 2h/c_2$) [28, 40]

The group velocities of ES_0 waves were measured over the low FTV range, from 1.5 to 3.5 with 0.5 intervals of FTV, and 0.5 FTVs corresponds to 50 kHz for the current specimen design. The group velocities were measured at the four edges (E1 to E4) for each FTV, Figure 4.4 shows a small group velocity difference between four edges for each FTV used in the experimental study. This indicates that the transmitted waves (i.e., waves after passing corners) have the identical wavenumbers and wave mode as the incident wave, which agrees with the discussion presented in Section 4.2.1. In addition, the group velocities measured with 1D Laser Vibrometer match reasonably well with the theoretical results presented in the earlier study [28]. The minor discrepancy between the group velocities is likely due to the difference in material properties of the specimens, specifically in Poisson's ratios, used in the present and previous studies [41]. As it is follows from the dispersion curve, see Figure 4.1, the phase velocities of ES_0 waves are almost identical to the group velocities due to almost linear dependence of the wavenumber against the frequency of the wave [25].

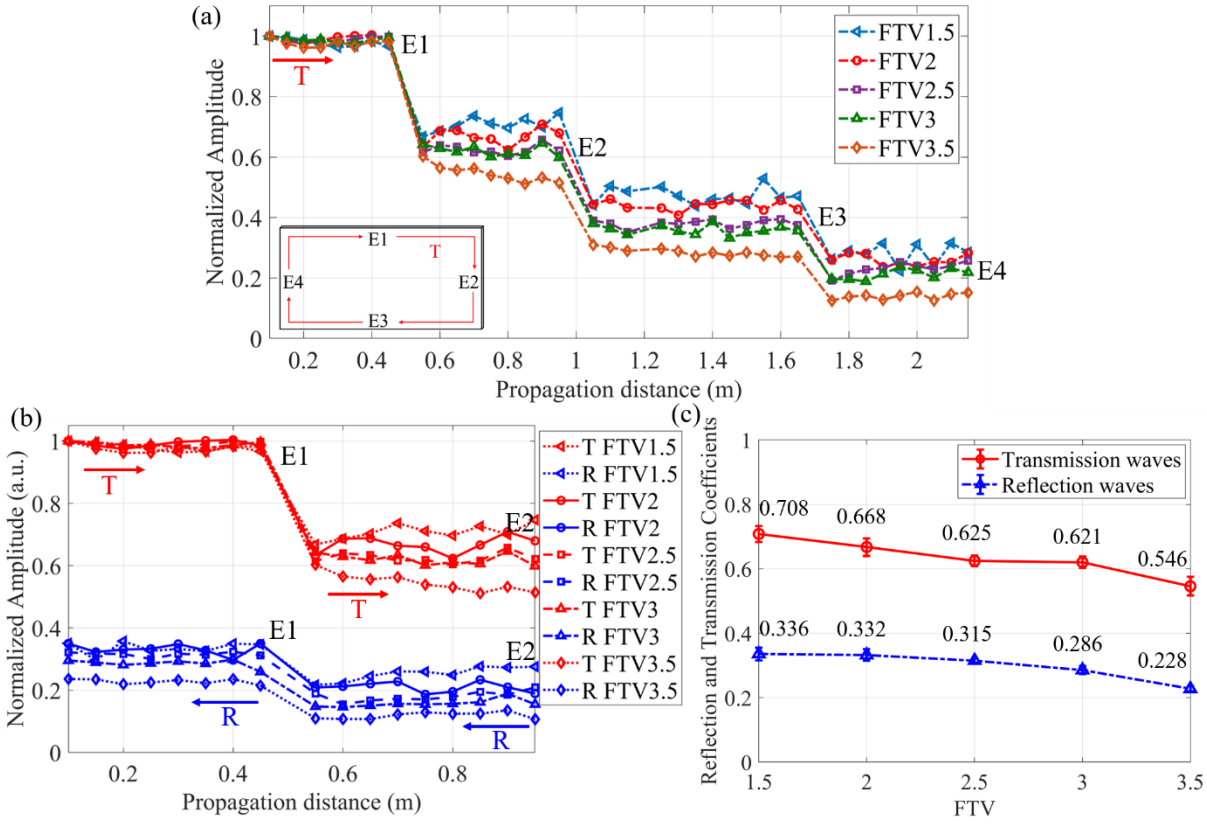

Figure 4.5. (a) Normalized envelope amplitude of transmitted waves from edges E1 to E4, (b) Normalized envelope amplitude of transmitted and reflected waves, (c) coefficients of transmitted and reflected waves against FTVs

Figures 4.5a and 4.5b show the envelope amplitude of the wave pulse, which is normalized by the amplitude of the signal measured at the first measurement point (Point 1) for each FTVs. Different FTVs were excited in the current experimental study to investigate the effect of FTVs on the wave propagation along the edges and corners. The emitted ES_0 wave has negligible amplitude decay when propagating at edge E1, and show steady and consistent amplitude decay at the remaining flat edges (E2, E3 and E4). The transmitted ES_0 wave amplitude shows some fluctuations at FTV = 1.5, which is likely due to the interference of scattering Lamb waves from edges. The mode interference decreases with the increase of FTVs and becomes negligible at FTV = 2.5. The amplitude of the ES_0 wave decreases significantly after propagating through a sharp corner. The results in Figure 4.5a show that approximately 62.5% of the incident ES_0 waves can be transmitted when the wave propagated through edges E1 to E2. This result has a good agreement with the results obtained from the wave analysis related to edges E2 to E3 as well as through edges E3 to E4. This analysis indicates that approximately 62.5% of the transmitted ES_0 wave amplitude remains after propagating through a sharp corner. In Figure 4.5b, the reflected waves are compared with the transmitted waves, and the results show that approximately 33% of emitted ES_0 waves are reflected when interacting with the corner between edges E1 and E2. Similar results can be obtained when comparing the transmitted waves in edge E2 and the reflected waves from edge E3. Different FTVs show small discrepancy in normalized amplitude in Figure 4.5c, which is due to the ES_0 wave mode characteristics, and higher FTV results in higher amplitude decay over wave propagation distance. Therefore, higher FTV has less transmission and reflection of ES_0 wave after interacting with sharp corners, and the transmission and reflection coefficients can be evaluated as approximately 62.5% and 33%, respectively for low FTVs. This means that the dissipated wave energy in the form of Lamb waves is almost negligible for ES_0 wave mode.

4.4. Numerical simulation

4.4.1. Finite element model

The ES_0 wave propagation along the edges and corners was simulated in ABAQUS/Explicit using a three-dimensional (3D) finite element (FE) model. The 3D FE model allows a variety of geometries and different locations of fatigue cracks to be simulated, which can be costly in the experimental investigation. The FE model replicated the specimen and the experimental setup as shown in Figure 4.6. The global and local coordinates are

illustrated, and normal displacement was calculated from the numerical simulation. It should be noted that the plate with the rounded corner is studied in Section 4.4.3, normal direction (x_N), tangential direction (x_T), radius (R), and degree (θ) are defined using the local coordinate system, respectively.

Table 4.1. Material properties

Material	ρ (kg·m^{-3})	E (GPa)	ν
AL5083-H116 [41]	2666	71.3	0.337
Dotmar Polystone [29]	351.4	0.9	0.4

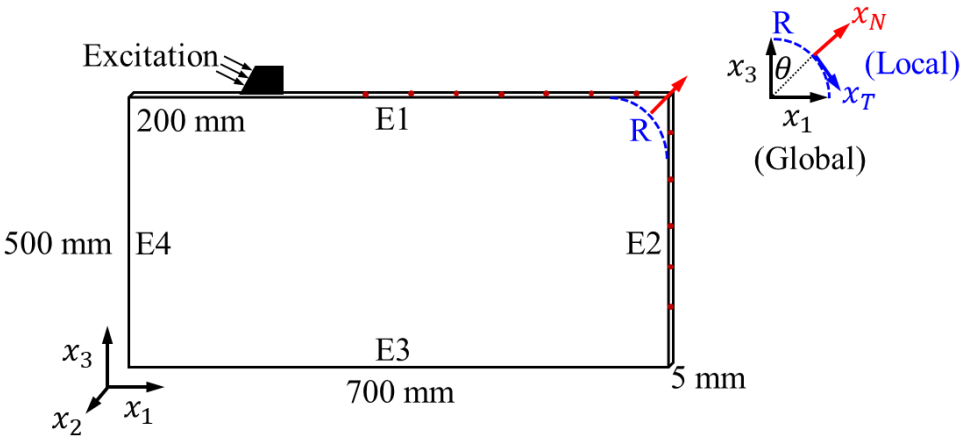

Figure 4.6. 3D FE model with the global and local coordinate systems

The elastic material properties of the specimen and the wedge are shown in Table 4.1. The element size of 0.6 mm was selected to ensure more than 12 elements per wavelength, and eight-node linear brick element with reduce integration (C3D8R) was used in the FE model. The 8-cycle Hann-windowed tone-burst with different FTVs were used as the excitation signal, and the excitation was applied on the inclined wedge surface using normal displacement with 10 μm displacement amplitude. The first measurement point was 100 mm away from the wedge, and the distance interval between the remaining 42 measurement points was 50 mm. A small Rayleigh damping value [42] was used in the FE model to match the amplitude decay of the ES_0 wave over wave propagation distance, which was determined based on the experimental results.

In Figures 4.7a and 4.7b, the contour of displacement magnitude from FE simulation can provide an improved understanding on the edge waves propagation along the edges and the corner. In Figure 4.7c, the edge wave is able to remain confined near the edge without dissipation after interacting with the sharp corner. In addition, the magnitude of scattering Lamb waves is small which should have negligible influence on the edge wave measurement, which has been demonstrated in the experiment (in Figures 4.3 and 4.5).

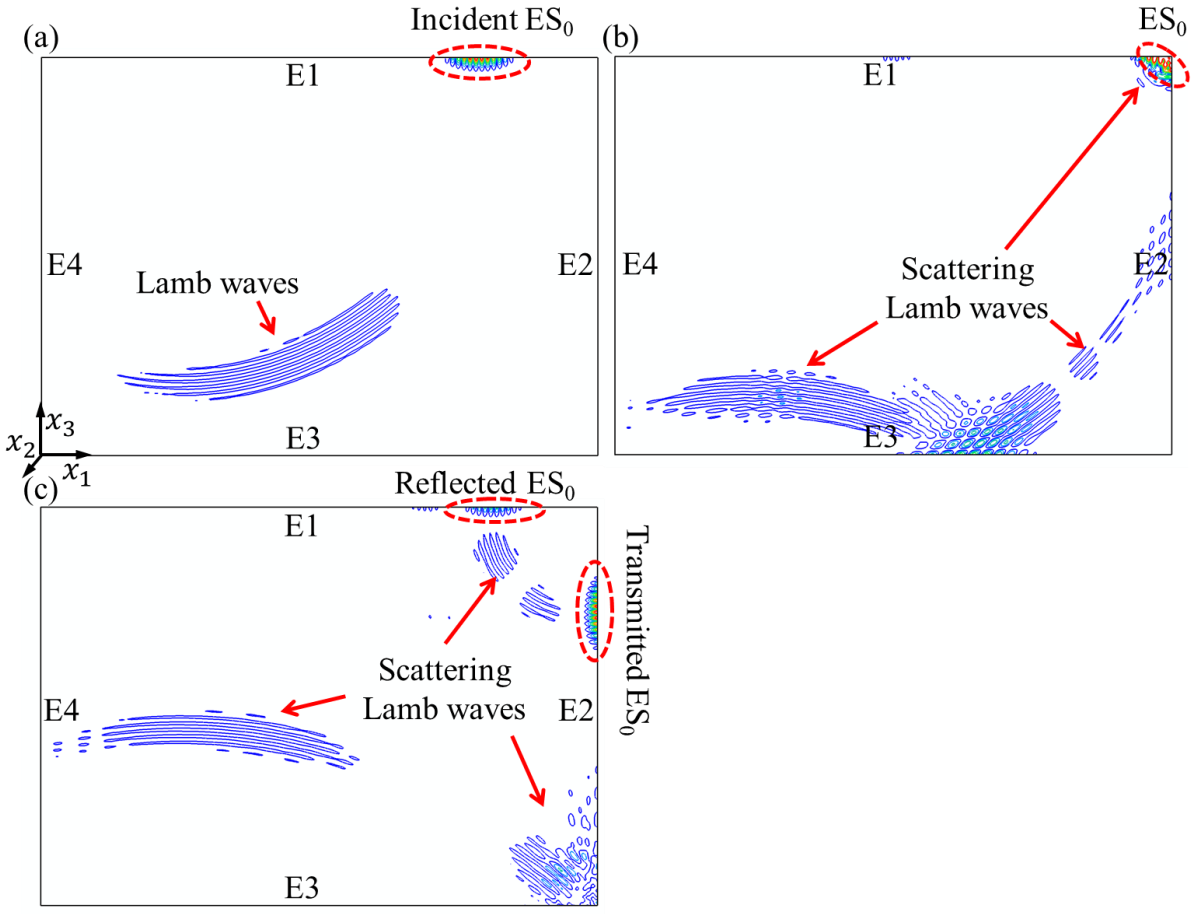

Figure 4.7. Contour of displacement magnitude from FE simulation demonstrating the edge wave propagation (a) before interacting with the sharp corner, (b) interacting with the sharp corner, (c) after interacting with the sharp corner

4.4.2. Finite element model validation

The numerical simulations were carried out following the same conditions of the experimental study, and the envelope amplitudes of wave pulse at the edges and corners of the

specimen were calculated. The results in Figure 4.8a show that there is steady and small amplitude decay when the ES_0 waves propagating along the flat edges. There is significant amplitude decay when the ES_0 wave is transmitted to the adjacent edges. The numerical results have good agreement with the experimental results, and the comparison of results with FTV = 2 is shown in Figure 4.8b. The amplitude of the measurement point that is 1.2 m away from the wedge can be considered as the outliner due to the similar arrival time of two transmitted waves from edges E2 and E4, therefore, it is not shown in numerical simulation and in experimental results. It should be noted that the envelope amplitude at the corners of the specimen can be calculated in the numerical simulations, and the spikes in Figure 4.8a indicate significant energy concentration of the ES_0 wave at the corners. This phenomenon was reported as trapping effect in the literature [9], and the phenomenon is further investigated in Section 4.4.3.

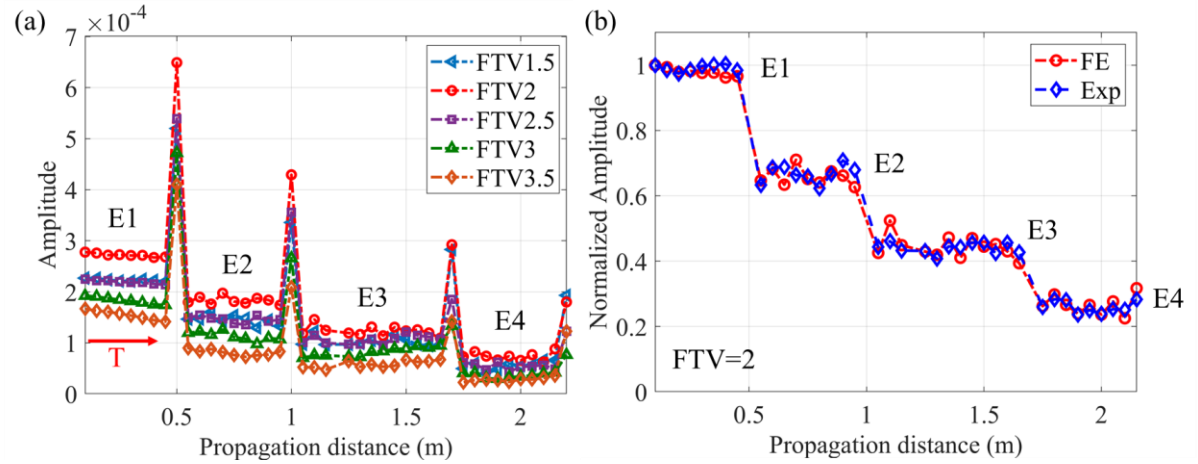

Figure 4.8. (a) Envelop amplitude of transmitted waves from edges E1 to E4, and (b) the FE model validation

4.4.3. Effect of rounded corners on the ES_0 wave mode propagation

The rounded corners are investigated in this section, and the global coordinates can be converted into local coordinates as shown in Figure 4.6. In Figure 4.9a, the corner was rounded with a radius of 2 mm (λ = 14.5 mm), and the results are normalized by the local normal displacement (u_N) at 0-degree. The results show that the displacement that is perpendicular to the free edge (u_3) increases, while the global in-plane displacement (u_1) decreases with the angular coordinate. The local normal displacement (u_N) has significant amplitude change which is symmetric about the 45-degree of the rounded corner, and the highest amplitude is

observed at 45-degree, which agrees well with the wave concentration at the corners as shown in Figure 4.8a. On the other hand, the amplitude of the local tangential displacement (u_T) shows the opposite increasing trend with the angular coordinate compared with the normal displacement, and the amplitude decreases to zero at 45-degree of the rounded corner, which is consistent with the results for the normal displacement.

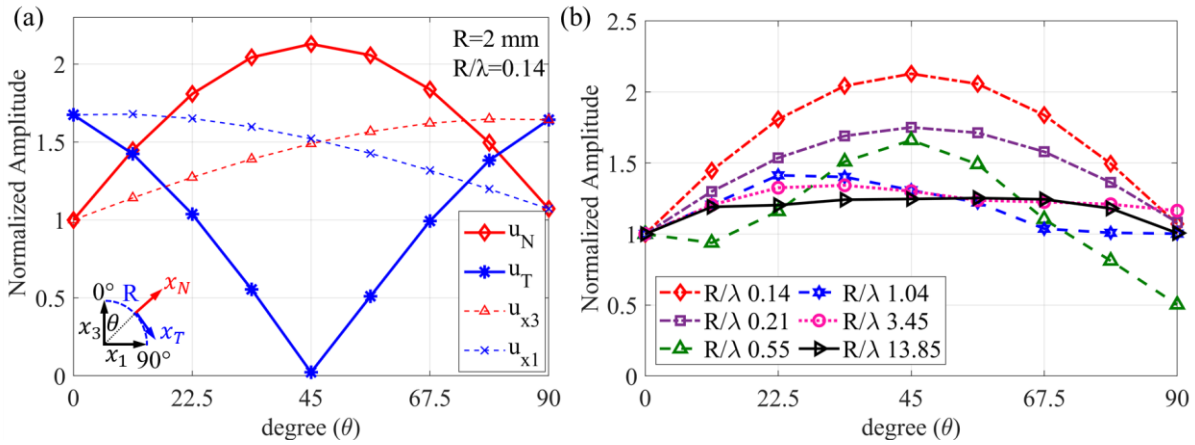

Figure 4.9. (a) Normalized global and local envelope amplitudes at the rounded corner against degrees, and (b) the envelope amplitudes of normal displacement with different R/λ of the rounded corner

A parametric study was carried out to further elucidate the effect of rounded corners on the ES_0 wave propagation. The curvatures of the corner can be categorised as high curvatures (R=1 mm to R=5 mm), medium curvatures (R=8 mm to R=20 mm), and low curvatures (R=50 mm to R=400 mm), according to the radius of corners. In Figure 4.9b, the results are shown with the dimensionless expression in terms of the radius-to-wavelength ratio (R/λ). The results show significant amplitude change in the normal displacement and obvious wave concentration in the corner with small radius-to-wavelength ratio, and the amplitude change is reduced with the increase of radius-to-wavelength ratio, which shows flat trend of amplitude change in the corner with large radius-to-wavelength ratio (i.e. radius of the corner is more than three wavelengths). The results also suggest that the ES_0 waves can propagate on the rounded corner structures and show a great potential for applications to the fatigue crack detection for realistic structures.

4.4.4. Determination of the fatigue crack location

The partially closed fatigue crack is the main focus of the present study, while the material nonlinearity and the micro-defects are not included, and their nonlinearities are relatively small compared with the contact nonlinearity, as demonstrated in the previous studies [43-45]. The length of the seam crack is 8 mm (l = 8 mm), and the width (i.e., interfacial gap) of the seam crack is sufficiently small, which is defined by the build-in function 'seam crack' in the ABAQUS/Explicit (see Figure 4.10a). The previous investigations have shown that the function can simulate the interaction between the Lamb waves and fatigue crack successfully [45-47]. In addition, the displacement amplitude of the edge wave (1.5 μm) is comparable with the interfacial gap (generally in the μm order magnitude) to ensure the generation of CAN [48-50]. The hard contact of normal behaviour and frictional tangential contact with the stiffness coefficient of 1.5 were applied to the assigned seam crack using surface-to-surface contact between the interfaces, which can simulate clapping behaviour due to the interaction of guided waves with fatigue crack. The seam crack can be opened after interacting with the tensile part of edge waves, as demonstrated in Figure 4.10b.

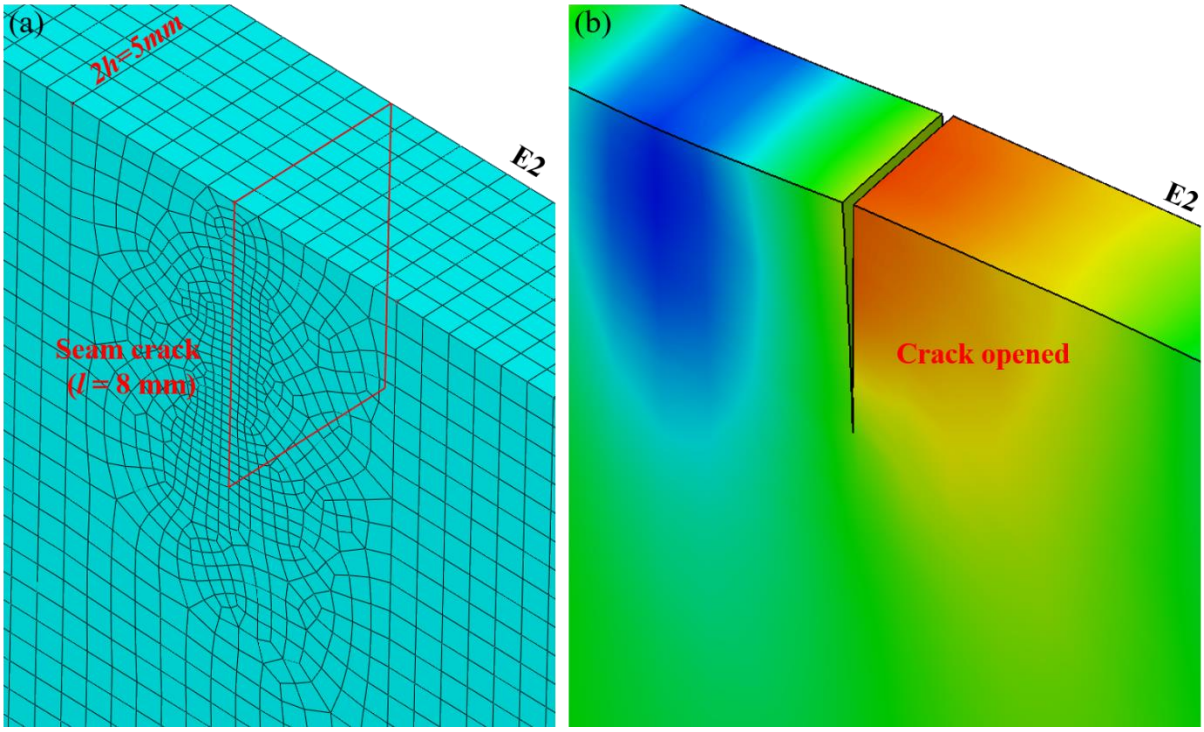

Figure 4.10. (a) Mesh illustration of an 8 mm seam crack at edge E2, and (b) Crack opened due to the tensile part of wave

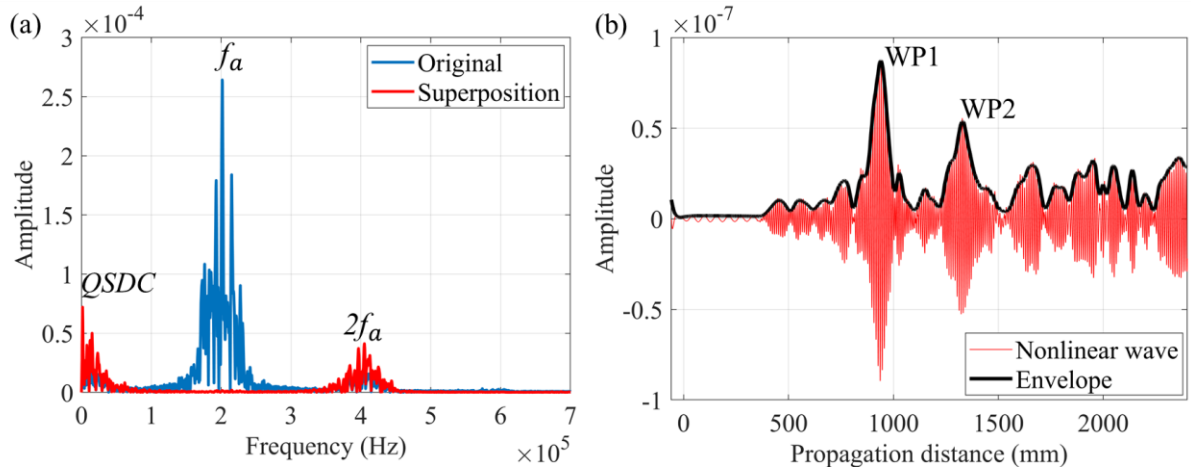

Figure 4.11. (a) Frequency domain of an 8 mm fatigue crack at edge E2, and (b) the compensated time-displacement domain using phase-reversal approach and high-pass filter

The scattering waves are used to determine the location of the fatigue crack using pulse-echo setups [38]. The phase-reversal approach was employed to extract the second harmonic generation due to the interaction of ES_0 mode waves with the fatigue crack [3]. The frequency domain in Figure 4.11a shows that the second harmonic and quasi-static displacement component (QSDC) generation due to the wave-crack interaction can be extracted. However, QSDC is not the focus of the current study, and QSDC can affect the accuracy of determining the fatigue crack location. Therefore, a high-pass filter of 30 kHz is applied on the time-displacement domain to suppress the QSDC. The filtered time-displacement domain is shown in Figure 4.11b, and the half-length of tone-burst pulse was compensated. The envelope of the nonlinear ES_0 wave was used to determine the location of the fatigue crack after the ES_0 wave propagating through the corners. The result shows that the second harmonic generation due to interaction of ES_0 wave with fatigue crack (at E2) is significantly higher than the scattering second harmonic generation of S_0 wave. As shown in Figure 4.11b, the two highest peaks of envelope can be used to determine the location of the fatigue crack based on the second harmonic generation of nonlinear ES_0 wave, one of which is generated by the transmitted ES_0 wave from edges E1 to E2 (WP1), and another is by the reflected ES_0 wave from edges E1 to E4 and then transmitted to edge E2 (WP2). The wave path of the transmitted linear ES_0 wave and the reflected nonlinear ES_0 wave is shown in Table 4.2.

Table 4.2. Wave path of the reflected nonlinear ES_0 wave

Wave path (WP)	Transmitted wave path (linear ES_0 wave)	Fatigue crack location	Reflection wave path (nonlinear ES_0 wave)
WP1	E1→E2	E2	E2→E1
	E1→E2→E3	E3	E3→E2→E1
WP2	E1→E4R→E1→E2	E2	E2→E1
	E1→E4R→E1→E2	E3	E3→E2→E1
WP3	E1→E4	E4	E4→E1
	E1→E4→E3	E3	E3→E4→E1

A parametric study was carried out to investigate the proposed method for determining the fatigue crack location based on the Table 4.2 using MATLAB. The wedge transducer and measurement points (MP) are used for the pulse-echo setups, and the actual fatigue crack location is denoted as 'Crack' in Figure 4.12. In Figure 4.12a, an 8 mm fatigue crack is located perpendicular to edge E2, and the fatigue crack location determined by the proposed method can achieve very good agreement with the actual crack location. The proposed method is supposed to be useful when fatigue crack is located at edge E4, which is similar with the fatigue crack located at edge E2. In Figure 4.12b, the fatigue crack at edge E3 is near the sharp corner. The results of the proposed method show good accuracy compared with the actual crack location. A case considering the similar arrival time of the transmitted and reflected waves using the proposed method is shown in Figure 4.12c, after interacting with the fatigue crack. The transmitted nonlinear ES_0 wave (WP3) is used in the case of Figure 4.12c, which is able to approximate the actual crack location with relatively good accuracy. In the practical application, this issue can be addressed by shifting the location of the actuator. The ES_0 wave can propagate through the rounded corners as shown in Section 4.4.3, and a rounded corner with 3 mm radius is implemented, which is a more realistic case for practical application. The results in Figure 4.12d demonstrate good agreement between the determined location and the actual crack location. The results indicate that the proposed method is applicable for determining the fatigue crack location in practical applications, and the rounded corner of specimen has negligible influence on the proposed method. It should be noted that three measurement points were used as the sensors to verify the consistency of results, however, only

one of the measurement points is needed in the practical application, which makes the proposed method more applicable.

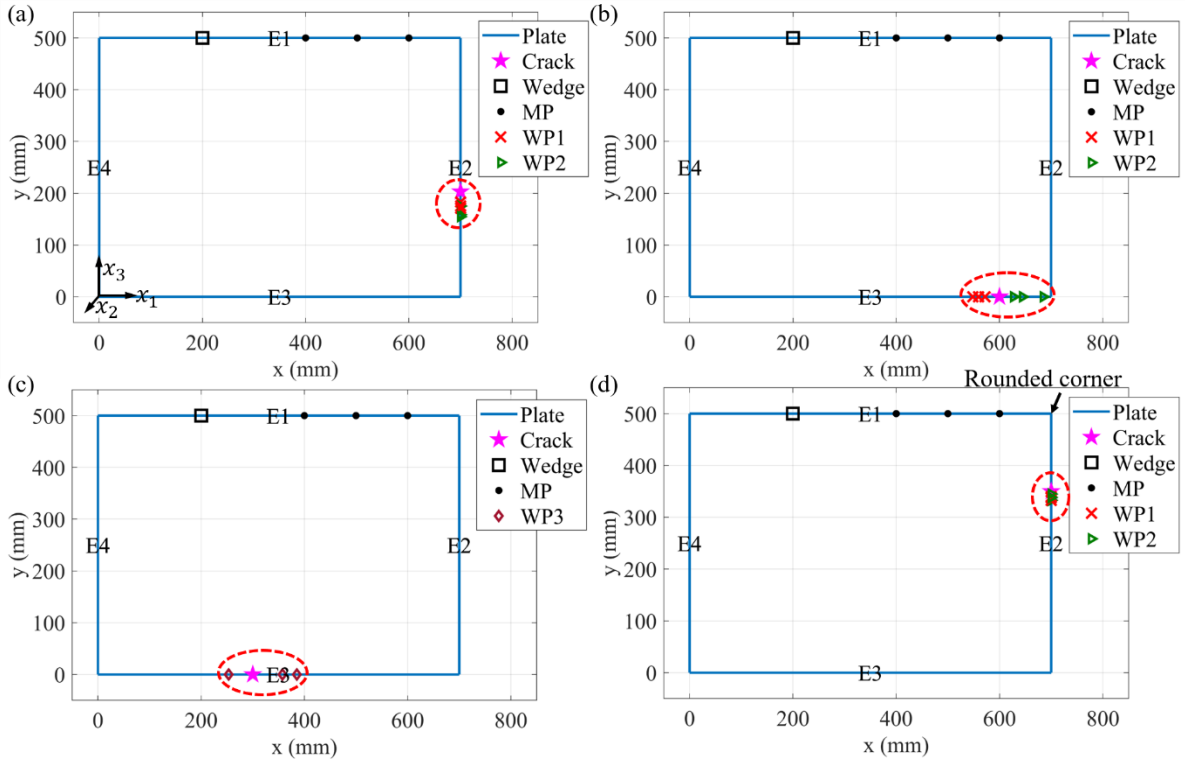

Figure 4.12. Determination of the 8 mm fatigue crack located at (a) edge E2, (b) edge E3, (c) the blind zone of edge E3, and (d) edge E2 with a 3 mm radius of the rounded corner

4.5. Conclusion

The ES_0 wave mode with low FTVs has been explored for fatigue crack detection in a thin-walled structure with corners, and its linear and nonlinear features have been investigated experimentally and numerically. The experimental results show that the ES_0 waves with low FTVs (FTV < 4.5) can propagate along the straight edge without significant decay and is also able to propagate through sharp corners. However, the presence of sharp corners leads to energy loss in the form of scattering Lamb waves, and subsequently the transmission and reflection coefficients are found to be approximately 62.5% and 33%, respectively. These coefficients are almost independent of the FTVs over the considered region of wave excitation frequencies. In addition, the lower FTVs such as FTV = 2 seems to be more suitable for practical applications because the ES_0 wave has the much lower amplitude decay and much

longer propagation distance. The experimental results also suggest that the transmitted ES_0 waves can be measured and distinguished after propagating through all four edges of the plate and all corners. Therefore, fatigue crack detection can still be achieved if only one edge is accessible for placing the excitation wedge and generation of ES_0.

The 3D FE model demonstrated a good agreement with the experimental results and allowed to investigate corners, which are difficult to measure and evaluate in the experimental study. For example, the numerical simulation involving sharp corners show a significant concentration of ES_0 waves, which has been investigated using the validated FE model. However, the amplitude leap of ES_0 wave is significant in the corners with a small radius-to-wavelength ratio (less than 3) while the amplitude leap becomes small when the radius-to-wavelength ratio increases.

The nonlinear features of ES_0 wave mode have been utilised to determine the location of the fatigue crack. Different fatigue crack locations have been considered to justify the proposed method of crack detection. The outcomes of this study have demonstrated that the fatigue crack location determined by the proposed method is in a good agreement with the actual location of the simulated fatigue crack. Further, the numerical results indicate that the proposed method can also be applied to realistic structures which have rounded corners, and the accuracy of determining the fatigue crack location is generally maintained at an acceptable level.

Overall, the present study provided the fundamental understanding of the ES_0 wave mode propagation in edges and the adjust corners. In general, this guided wave mode shows a great potential to be applied in practical environment and challenging applications, especially for the interior structures with complex geometries. The outcomes of this study can serve as a guide for the future developments of new defect detection techniques. Future research can focus on more complex structural features and situations, e.g., involving fluid-structure interfaces, which are typical in pipeline industry and marine applications.

Acknowledgement

This work was funded by the Australian Research Council (ARC) DP200102300 and DP210103307 grants. The authors are grateful for the support.

References

[1] Jingpin J, Xiangji M, Cunfu H and Bin W 2017 Nonlinear Lamb wave-mixing technique for micro-crack detection in plates *NDT&E Int.* **85** 63-71
[2] Yang Y, Ng C-T and Kotousov A 2019 Bolted joint integrity monitoring with second harmonic generated by guided waves *Struct. Health Monitor.* **18** 193-204
[3] Zhu H, Ng C T and Kotousov A 2022 Low-frequency Lamb wave mixing for fatigue damage evaluation using phase-reversal approach *Ultrasonics* 106768
[4] Hu X, Yin T, Zhu H, Ng C-T and Kotousov A 2022 Structural health monitoring of partially immersed metallic plates using nonlinear guided wave mixing *Construction and Building Materials* **346** 128381
[5] Zhu H, Ng C T and Kotousov A 2022 Frequency selection and time shifting for maximizing the performance of low-frequency guided wave mixing *NDT&E Int.* 102735
[6] Ramatlo D A, Wilke D N and Loveday P W 2018 Development of an optimal piezoelectric transducer to excite guided waves in a rail web *NDT&E Int.* **95** 72-81
[7] Hakoda C and Lissenden C J 2020 Application of a general expression for the group velocity vector of elastodynamic guided waves *J. Sound Vib.* **469** 115165
[8] Ramdhas A, Pattanayak R K, Balasubramaniam K and Rajagopal P 2015 Symmetric low-frequency feature-guided ultrasonic waves in thin plates with transverse bends *Ultrasonics* **56** 232-42
[9] Yu X, Manogharan P, Fan Z and Rajagopal P 2016 Shear horizontal feature guided ultrasonic waves in plate structures with 90 transverse bends *Ultrasonics* **65** 370-9
[10] Yu X, Ratassepp M and Fan Z 2017 Damage detection in quasi-isotropic composite bends using ultrasonic feature guided waves *Composites Science and Technology* **141** 120-9
[11] Masserey B and Fromme P 2017 Analysis of high frequency guided wave scattering at a fastener hole with a view to fatigue crack detection *Ultrasonics* **76** 78-86
[12] Vien B S, Rose L R F and Chiu W K 2017 Experimental and Computational Studies on the Scattering of an Edge-Guided Wave by a Hidden Crack on a Racecourse Shaped Hole *Materials* **10** 732
[13] Doherty C C and Chiu W K 2012 Three-dimensional finite element modelling of ultrasonic-guided wave scattering from fuel weep holes *Struct Health Monit* **11** 442-51
[14] Fan Z, Castaings M, Lowe M J, Biateau C and Fromme P 2013 Feature-guided waves for monitoring adhesive shear modulus in bonded stiffeners *NDT&E Int.* **54** 96-102
[15] Yu X, Fan Z, Castaings M and Biateau C 2017 Feature guided wave inspection of bond line defects between a stiffener and a composite plate *NDT&E Int.* **89** 44-55
[16] Heinlein S, Cawley P and Vogt T 2018 Reflection of torsional T (0, 1) guided waves from defects in pipe bends *NDT&E Int.* **93** 57-63
[17] Verma B, Mishra T K, Balasubramaniam K and Rajagopal P 2014 Interaction of low-frequency axisymmetric ultrasonic guided waves with bends in pipes of arbitrary bend angle and general bend radius *Ultrasonics* **54** 801-8

[18] Khalili P and Cawley P 2018 The choice of ultrasonic inspection method for the detection of corrosion at inaccessible locations *NDT&E Int.* **99** 80-92
[19] Aseem A and Ng C T 2021 Debonding detection in rebar-reinforced concrete structures using second harmonic generation of longitudinal guided wave *NDT&E Int.* **122** 102496
[20] Zuo P, Yu X and Fan Z 2017 Numerical modeling of embedded solid waveguides using SAFE-PML approach using a commercially available finite element package *NDT&E Int.* **90** 11-23
[21] Sriramadasu R C, Banerjee S and Lu Y 2019 Detection and assessment of pitting corrosion in rebars using scattering of ultrasonic guided waves *NDT&E Int.* **101** 53-61
[22] Rucka M 2010 Experimental and numerical study on damage detection in an L-joint using guided wave propagation *J. Sound Vib.* **329** 1760-79
[23] Feng F, Shen Z and Shen J 2016 Scattering of obliquely incident waves by straight features in a plate *Wave Motion* **60** 84-94
[24] Kaplunov J, Prikazchikov D and Rogerson G 2005 On three-dimensional edge waves in semi-infinite isotropic plates subject to mixed face boundary conditions *J. Acoust. Soc. Am.* **118** 2975-83
[25] Hughes J M, Kotousov A and Ng C-T 2020 Generation of higher harmonics with the fundamental edge wave mode *Appl. Phys. Lett.* **116** 101904
[26] Wilde M V, Golub M V and Eremin A A 2019 Experimental observation of theoretically predicted spectrum of edge waves in a thick elastic plate with facets *Ultrasonics* **98** 88-93
[27] Feng F, Shen Z and Shen J 2017 Edge waves in a 3D plate: two solutions based on plate mode matching *Mathematics and Mechanics of Solids* **22** 2065-74
[28] Wilde M V, Golub M V and Eremin A A 2019 Experimental and theoretical investigation of transient edge waves excited by a piezoelectric transducer bonded to the edge of a thick elastic plate *J. Sound Vib.* **441** 26-49
[29] Hughes J M, Mohabuth M, Kotousov A and Ng C-T 2021 The fundamental ultrasonic edge wave mode: Propagation characteristics and potential for distant damage detection *Ultrasonics* **114** 106369
[30] Hughes J M, Mohabuth M, Khanna A, Vidler J, Kotousov A and Ng C-T 2021 Damage detection with the fundamental mode of edge waves *Struct. Health Monitor.* **20** 74-83
[31] Aryan P, Kotousov A, Ng C-T and Wildy S 2016 Reconstruction of baseline time-trace under changing environmental and operational conditions *Smart. Mater. Struct.* **25** 035018
[32] Rose L R F, Vien B S and Chiu W K 2020 Analytical solutions for crack-like scatterers and sources in isotropic elastic plates *Wave Motion* **93** 102476
[33] Andreades C, Fierro G P M and Meo M 2020 A nonlinear ultrasonic SHM method for impact damage localisation in composite panels using a sparse array of piezoelectric PZT transducers *Ultrasonics* **108** 106181
[34] Yu L and Giurgiutiu V 2008 In situ 2-D piezoelectric wafer active sensors arrays for guided wave damage detection *Ultrasonics* **48** 117-34
[35] Zhu W, Xu Z, Xiang Y, Liu C, Deng M, Qiu X, Sun D and Xuan F 2021 Nonlinear ultrasonic detection of partially closed cracks in metal plates using static component of lamb waves *NDT&E Int.* **124** 102538
[36] Zhou J, Xiao L, Qu W and Lu Y 2017 Nonlinear Lamb wave based DORT method for detection of fatigue cracks *NDT&E Int.* **92** 22-9
[37] Solodov I Y, Krohn N and Busse G 2002 CAN: an example of nonclassical acoustic nonlinearity in solids *Ultrasonics* **40** 621-5

[38] Xu L, Wang K, Su Y, He Y, Yang J, Yuan S and Su Z 2022 Surface/sub-surface crack-scattered nonlinear rayleigh waves: A full analytical solution based on elastodynamic reciprocity theorem *Ultrasonics* **118** 106578
[39] Ng C-T, Mohseni H and Lam H-F 2019 Debonding detection in CFRP-retrofitted reinforced concrete structures using nonlinear Rayleigh wave *Mech. Syst. Signal. Process.* **125** 245-56
[40] Zernov V and Kaplunov J 2008 Three-dimensional edge waves in plates *Proceedings of the Royal Society A: Mathematical, Physical and Engineering Sciences* **464** 301-18
[41] Whelchel R, Kennedy G, Dwivedi S, Sanders Jr T and Thadhani N 2013 Spall behavior of rolled aluminum 5083-H116 plate *J. Appl. Phys.* **113** 233506
[42] Ramadas C, Balasubramaniam K, Hood A, Joshi M and Krishnamurthy C 2011 Modelling of attenuation of Lamb waves using Rayleigh damping: Numerical and experimental studies *Composite Structures* **93** 2020-5
[43] Li W, Xiao J and Deng M 2022 Micro-defect imaging with an improved resolution using nonlinear ultrasonic Lamb waves *J. Appl. Phys.* **131** 185101
[44] Guan R, Lu Y, Wang K and Su Z 2019 Fatigue crack detection in pipes with multiple mode nonlinear guided waves *Struct. Health Monitor.* **18** 180-92
[45] Wang R, Wu Q, Yu F, Okabe Y and Xiong K 2019 Nonlinear ultrasonic detection for evaluating fatigue crack in metal plate *Struct. Health Monitor.* **18** 869-81
[46] Lee Y F and Lu Y 2022 Identification of fatigue crack under vibration by nonlinear guided waves *Mech. Syst. Signal. Process.* **163** 108138
[47] Yang Y, Ng C-T and Kotousov A 2018 Influence of crack opening and incident wave angle on second harmonic generation of Lamb waves *Smart. Mater. Struct.* **27** 055013
[48] Jhang K-Y, Lissenden C J, Solodov I, Ohara Y and Gusev V 2020 *Measurement of Nonlinear Ultrasonic Characteristics*: Springer)
[49] Van Den Abeele K-A, Johnson P A and Sutin A 2000 Nonlinear elastic wave spectroscopy (NEWS) techniques to discern material damage, part I: nonlinear wave modulation spectroscopy (NWMS) *Journal of Research in Nondestructive Evaluation* **12** 17-30
[50] Broda D, Staszewski W, Martowicz A, Uhl T and Silberschmidt V 2014 Modelling of nonlinear crack–wave interactions for damage detection based on ultrasound—A review *J. Sound Vib.* **333** 1097-118

Chapter 5

Defects evaluation near edges of structural elements using the fundamental mode of edge waves

Publication:

H. Zhu, A. Kotousov, and C.T. Ng, Defects evaluation near edges of structural elements using the fundamental mode of edge waves, *Journal of Sound and Vibration*, 557 (2023), 117753.

Statement of Authorship

Title of Paper	Defects evaluation near edges of structural elements using the fundamental mode of edge wave
Publication Status	☑ Published ☐ Accepted for Publication ☐ Submitted for Publication ☐ Unpublished and Unsubmitted work written in manuscript style
Publication Details	H. Zhu, A. Kotousov, and C.T. Ng, Defects evaluation near edges of structural elements using the fundamental mode of edge waves, Journal of Sound and Vibration, 557 (2023), 117753.

Principal Author

Name of Principal Author (Candidate)	Hankai Zhu		
Contribution to the Paper	Conceptualization, Methodology, Experiment, Finite Element simulation, Validation, Formal analysis, Writing – original draft and editing.		
Overall percentage (%)	85%		
Certification:	This paper reports on original research I conducted during the period of my Higher Degree by Research candidature and is not subject to any obligations or contractual agreements with a third party that would constrain its inclusion in this thesis. I am the primary author of this paper.		
Signature		Date	23/10/2023

Co-Author Contributions

By signing the Statement of Authorship, each author certifies that:

i. the candidate's stated contribution to the publication is accurate (as detailed above);

ii. permission is granted for the candidate in include the publication in the thesis; and

iii. the sum of all co-author contributions is equal to 100% less the candidate's stated contribution.

Name of Co-Author	Andrei Kotousov		
Contribution to the Paper	Supervision, Advising, Writing – review and editing.		
Signature		Date	6 Nov 2023

Name of Co-Author	Ching-Tai Ng		
Contribution to the Paper	Supervision, Advising, Writing – review and editing.		
Signature		Date	7 Nov 2023

Chapter 5: Defects evaluation near edges of structural elements using the fundamental mode of edge waves

Hankai Zhu[1], Andrei Kotousov[2], Ching Tai Ng[1]

[1] School of Architecture and Civil Engineering, The University of Adelaide, Adelaide, SA 5005, Australia

[2] School of Electrical and Mechanical Engineering, The University of Adelaide, Adelaide, SA 5005, Australia

Abstract

Structural elements with edges are widely used across many industries and applications; examples include tapered flange beams and the footing of rail tracks. The distant defect inspection of these structures using the conventional guided wave techniques can be challenging because of multiple wave reflections, dispersion, and wave modes coupling. In this article, the quasi-fundamental antisymmetric mode of edge wave (QEA_0) is proposed for evaluation of defects emanating from curved edges. In the beginning, the dispersion properties and the modal displacement profiles of QEA_0 are studied using Semi-Analytical Finite Element (SAFE) method; and then the results are validated against outcomes of direct numerical simulations and an experimental study. The SAFE method demonstrated the feasibility of calculating the dispersion properties and the modal displacement profiles for the fundamental modes of edge waves propagating along ideal or non-ideal edges. The proposed QEA_0 mode demonstrated several advantages compared with the conventional guided waves as well as its symmetric counterpart, i.e., the quasi-fundamental symmetric mode of edge wave (QES_0). The latter was found to have a limited range of propagation distances along curved edges. In contrast, the QEA_0 mode propagates for much longer distances without significant decay. In addition, the reflected waves due to defects are sensitive to small defects with the characteristic depth of more than 0.1 wavelength, and the defect reflection ratio showed a good correlation with the defect size. The reflected waves also allow to distinguish multiple defects and determine their locations. Overall, the QEA_0 mode shows a great potential for the purpose of non-destructive evaluation (NDE) and structural health monitoring (SHM) of structural edges with complex cross-sectional areas.

Keywords: Curved edges, edge waves, defect detection, SAFE, NDE

5.1. Introduction

Non-destructive evaluation (NDE) and structural health monitoring (SHM) of engineering structures are critical for safe and efficient operation. The evaluation of various defects and damage with guided waves has been the focus of many studies over the past decade. These studies, in particular, demonstrated that guided waves can be utilised for different structures and materials [1-3], and showed a good sensitivity to various types of defects and mechanical damage [4-6]. The early works largely focused on the structures with relatively simple geometries such as plate [7-9] or circular pipe [10, 11]. Recent research efforts considered more realistic structures such as rail tracks [12-14], transverse bends [15, 16], T-joint stiffeners [17, 18], pipe bends [19], I-beams [20-22], and square tubes [23].

Many construction elements have common structural features – edges, which are of particular importance for NDE inspections. Indeed, damage and defects often initiate and/or propagate from free edges, which are prone to manufacturing defects and are often associated with higher stresses than the interior of the structure. However, the areas near edges are very challenging for defect inspections using traditional guided waves such as Lamb-Rayleigh waves due to multiple modes generation, wave reflections and modes coupling. In the same time, structural edges can also serve as waveguides, which allow the propagation of local wave modes such as edge waves [24, 25]. In the limiting case of a sharp wedge, the local wave modes represent so-called wedge wave modes, which propagate near the wedge apex [26, 27]. The wedge waves are non-dispersive and non-decaying, however, are very sensitive to the sharpness of the apex [27]. The attenuation increases dramatically for non-ideal wedge geometries [28], which makes the practical applications of these waves doubtful.

In a plate of finite thickness with ideal (rectangular) edges, two non-decaying local modes of guided waves can propagate, namely, the fundamental symmetric (ES0) and antisymmetric (EA0) modes of edge waves [29]. The analysis of edge waves is more difficult in comparison with traditional plane waves, i.e., Lamb-Rayleigh waves, as it needs solving 3D equilibrium equations instead of using the 2D framework of the plane theory of elasticity [30, 31]. Several analytical and semi-analytical approaches have been developed to analyse 3D edge waves [31, 32], which provided dispersion equations for both fundamental modes of edge waves. It was also demonstrated theoretically that both fundamental modes have no decay [25, 33], however, in practice, the propagation of these modes can be affected by coupling with other modes of

guided waves. The latter is the main challenging in practical applications of these wave modes for NDE purposes.

The edge waves have attracted much attention over the past few years for the purpose of the NDE, including the detection of pitting corrosion [34], hidden crack near the free edge [35] and the corner [36], and the impact damage of composite plates [37]. Recent feasibility studies showed that ES0 mode is particular suitable for distant detection of corrosion damage in flanges of I-beams [38]. However, several studies also reported that similar to the wedge wave mode, the ES_0 mode may become energy decaying in the case of non-ideal geometries [16, 29], which largely restricts the utilisation of this wave mode for many practical applications, e.g. as shown in Fig. 5.1. Therefore, further investigations of the local guided waves are required in order to select the appropriate wave modes and frequency range, which could be utilised effectively for NDE inspections.

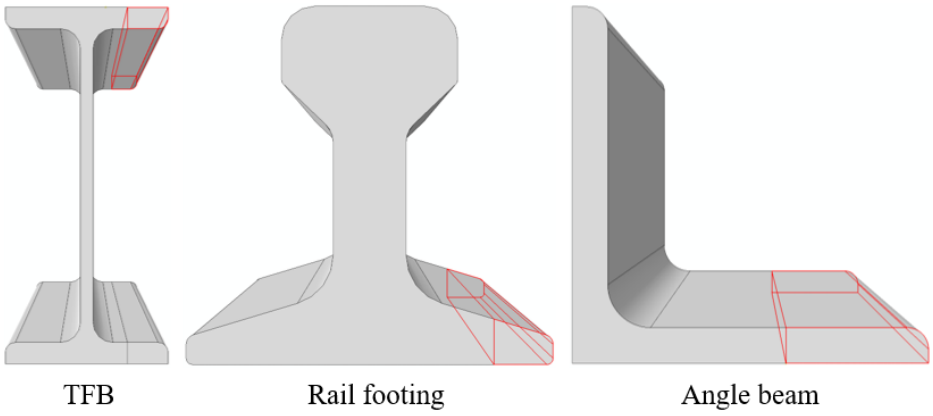

Figure 5.1. Cross-sectional profiles of structural elements with curved edges

Previous studies demonstrated that non-ideal geometries also allow the propagation of various feature guided wave (FGW) modes, which do not exist in ideal geometries. There have been reported at least four types of FGW in different structures: shear-horizontal type [15, 39], torsional type [40], and flexural and longitudinal type [16, 41]. The waveform of the first type is largely confined in an area near the top surface of the non-ideal (i.e., curved) edge or the welding area. The properties of the flexural and longitudinal type of FGWs depend significantly on the local geometry of the waveguide. The practical utilisation of these types of FGW modes could be restricted to specific local geometries, and the wave energy localisation

can be affected if the geometry of the waveguide is slightly changed. On the other hand, the torsional type of FGW has similar wave characteristics (i.e., modal solution and dispersion relation) with some higher order edge wave modes.

The FGW, classical edge waves, quasi-edge waves (i.e., edge waves in non-ideal edge), wedge waves, Raleigh waves, and plate waves are discussed below to provide some physical insights as well as relations between different modes and geometries. The edge waves and other types of FGWs have many common features. In the certain frequency range, strong trapping effect may occur, which restricts the energy leakage to the adjacent material. The edge waves and quasi-edge waves can be considered as types of FGWs, which propagate along the traction-free edge, and have some special wave propagation properties. These waves are guided by sharp and rounded edges (classic and quasi-edge waves), as well as weld seams/stiffeners (SH-type FGW). As mentioned above, the wave energy of FGW can only be trapped in the waveguide within the certain frequency range, and a local maximum of the power flow can be calculated using approach developed in [40, 42]. The local maximum of the power flow corresponds to the minimum wave leakage into surrounding material. In contrast, the fundamental modes of classical edge waves can be confined in the waveguide (plate apex) in a very wide frequency range. In addition, the wave leakage of the fundamental modes of classical edge waves is generally much smaller than that of the FGWs. The propagation properties of the fundamental modes of edge waves at higher frequency thickness values (FTVs > 8) tend to converge to the corresponding properties of wedge waves, as explained in [32]. In the long-wavelength limit (FTV << 1), the wave speeds of the fundamental edge waves asymptotic approach to the Rayleigh wave speed and the Rayleigh-type of flexural wave speed [31, 43]. The fundamental edge wave mode (EA_0) at some frequencies has the similar dispersion relationships as the fundamental mode of Lamb waves (A_0) and the wedge waves, see Fig. 5.2 in Section 2 and the reference [32].

In this study, we proposed to utilise the quasi-antisymmetric fundamental mode of edge wave (QEA_0) for damage detection of the structural elements with non-ideal edges. In the beginning, the Semi-Analytical Finite Element (SAFE) method was applied to investigate the dispersion properties and modal displacement profiles of the edge wave modes for different local geometries of waveguides. The obtained dispersion curve and modal displacement profile of QEA_0 modes were verified using an experimental study. It was demonstrated that the QEA_0 mode has a very low decay, which is specifically promising for distant and long-range NDE inspections. Further, a 3D numerical model was developed based on the geometry and

outcomes of the experimental studies to further investigate the feasibility of defect detections using the proposed QEA_0 mode.

This paper is organised as follow. Section 5.2 provides the theoretical background for analysis of the edge waves, and the methodology for the SAFE method has been briefly provided. Section 5.3 presents the outcomes of the parametric SAFE analysis including the wave velocities, modal displacement profiles and waveforms of QEA_0 mode for non-ideal edge geometries. The transient 3D finite element (FE) model is outlined in Section 5.4, which is used to investigate the feasibility of defect detection with QEA_0 mode. The outcomes of experimental study as well as comparison against SAFE and transient 3D FE results are presented in Section 5.5. Finally, the general conclusions from the present study along with directions for future work are briefly drawn in Section 5.6.

5.2. Methodology

5.2.1 Fundamentals of edge waves

The governing equation for the problem of edge wave propagating along the ideal edge with finite thickness can be formulated mathematically by equation of the 3D linear elasticity [44], in the Cartesian coordinates $\boldsymbol{x} = \{x_1, x_2, x_3\}$ as

$$(\lambda + \mu)\,\text{grad}\,\text{div}\,\boldsymbol{u} + \mu\Delta\boldsymbol{u} = \rho\frac{\partial^2\boldsymbol{u}}{\partial t^2} \tag{5.1}$$

where $\boldsymbol{u} = \{u_1, u_2, u_3\}^T$ is the displacement vector, which represents the displacement components in the Cartesian coordinates. Δ is the three-dimensional Laplace operator. λ and μ are Lame's constants, and ρ is mass density. The propagation factor is $e^{-i(\omega t - \xi x_3)}$, which can be determined by the angular frequency ω and the complex wavenumber ξ in the wave propagation direction (i.e., x_3-direction). The thickness of the plate is $2h$. The plate faces $S = \{0 < x_1 < \infty, x_2 = \pm h, x_3 < \infty\}$, which are perpendicular to x_2-direction, are assumed to have stress-free boundaries.

The displacement vector $\boldsymbol{u}$ can be transformed by the Laplace transform and the Fourier transform to simplify the 3D linear elasticity problem with respect to time variable t and spatial variable x_3, respectively [25].

$$\boldsymbol{U}(x_1, x_2) = \int_{-\infty}^{\infty} \int_{0}^{\infty} \boldsymbol{u}(x_1, x_2, x_3, t) e^{-i(\omega t - \xi x_3)}\, dt\, dx_3 \tag{5.2}$$

The previous studies [25, 30] have demonstrated that the wave-field of edge wave can be decomposed as Lamb wave and shear-horizontal waves with the form

$$\boldsymbol{U}(\omega, \xi) = \sum_{n=0}^{\infty} C_n^L \boldsymbol{U}_n^L(x_2) e^{-i\xi_n x_1} + \sum_{n=0}^{\infty} C_n^H \boldsymbol{U}_n^H(x_2) e^{-i\xi_n x_1} \tag{5.3}$$

where C_n^L and C_n^H are the coefficients of Lamb waves and shear waves depending on the boundary conditions at the edge, and the displacement components of Lamb waves ($\boldsymbol{U}_n^L$) and shear waves ($\boldsymbol{U}_n^H$) are eigenfunctions.

The dispersion curves [30, 31, 45] and the modal displacement profiles [25, 32] have been investigated based on the mode decomposition, Eq. 5.3, for fundamental as well as higher order modes of edge waves. It was found that the eigenvalues of the fundamental modes are real in the theoretical investigation [32], and these modes are slightly dispersive. In contrast, the higher order modes of edge waves are strongly dispersive and the attenuation of these wave modes is significantly affected by Poisson's ratio, ν; higher values of ν leads to a stronger attenuation [31]. However, the higher-order modes are beyond the scope of the current study.

The frequency thickness values (FTV) are defined as FTV = $\omega 2h/c_2$ for the dispersion curves and the calculation of wave properties, where ω is the angular frequency, $2h$ is the thickness, and c_2 is the shear wave speed. From practical point of view, the generation of edge waves over the whole range of FTVs may be a challenging task because of the wave modes coupling and multi-modes generation, particularly, at the higher FTV range (i.e., FTV > 8), see Fig. 5.2. It was demonstrated that in the low ($1 < \text{FTV} \leq 4$) and medium ($4 < \text{FTV} < 8$) FTV ranges, the edge waves can be reliably generated using the wedge excitation method [24]. Thus, the focus of current study is on the fundamental edge wave modes in the low and medium ranges of FTVs.

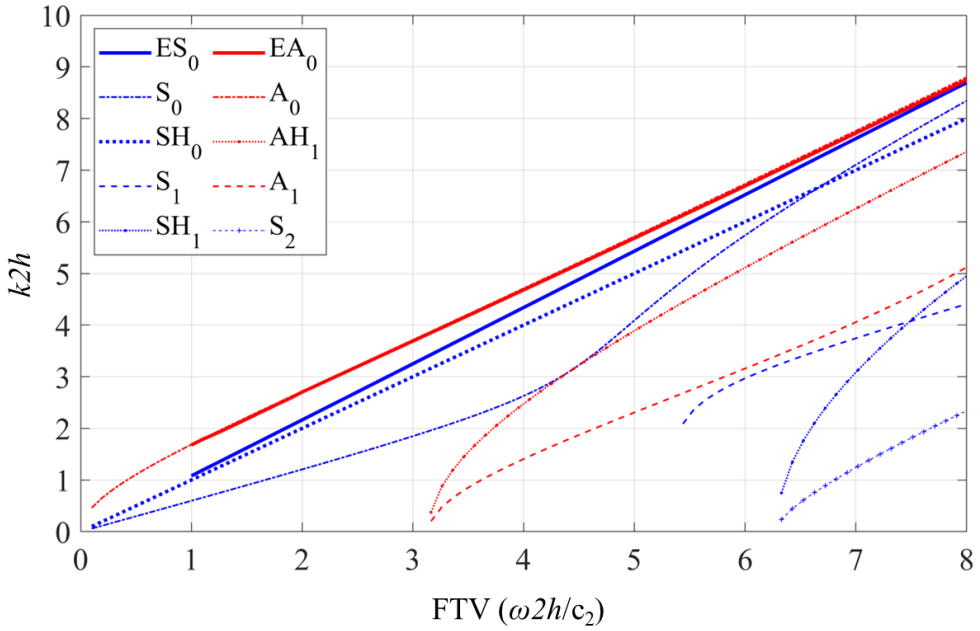

Figure 5.2. Dispersion curves of edge wave modes (ES_0 and EA_0) [25, 30] along with other wave modes (i.e., Lamb wave modes S_i, A_i, and shear-horizonal wave modes SH_i, AH_i, i=0,1,2…) as calculated using software package DISPERSE [46], k is angular wavenumber, $2h$ is thickness

5.2.2. SAFE method

The analytical and semi-analytical approaches for analysis of edge waves were based on the mode decomposition (Eq. 5.3) as described in the previous section. The eigenvalues and corresponding wave modes are normally obtained from this equation by enforcing the boundary conditions and applying the boundary collocation method [25, 30] or reciprocity theorem [32]. However, these analytical approaches are not very amendable to an non-ideal edge geometries [47]; and its application to non-symmetric cross-sections of waveguides can be particularly challenging.

The alternative to the analytical approaches is the Semi-Analytical Finite Element (SAFE) method. The SAFE method has developed for decades, and it has been proven to be a powerful tool for analysis of guided waves propagating in waveguides with arbitrary geometry and cross-sectional area. The idea behind this method is to model the cross-sectional area using finite elements and apply harmonic waves in the form of $e^{-i(\omega t-\xi x_3)}$ along the wave propagation direction. This method has been successfully applied to calculate the modal properties of guided waves in a wide range of waveguides [48].

A modification of the SAFE method, so called the SAFE-PML (Semi-Analytical Finite Element with Perfectly Matched Layer) method, is utilised in this work to calculate the dispersion properties and the modal displacement profiles of edge waves propagating along waveguides with ideal and non-ideal cross-sectional geometries. The SAFE-PML allows to more efficiently determine the both real and imaginary parts of the eigenvalues as a function of the excitation frequency; and the PML essentially serves as an absorbing layer. The most detailed description of the method and the discussion on the PML length were presented in [49, 50]. In a general case, the SAFE-PML provides infinite number of eigenvalues for a certain excitation frequency [48], however, the wave modes have to be filtered separately for each eigenvalue [49]. The identification of the dispersion curve for a specific wave mode can be very challenging, specifically, if the eigenvalues are complex. The latter implies analysis of a large number of eigenvalues and the corresponding wave modes for each excitation frequency. A wave mode filtering algorithm [50] is needed to determine the corresponding wave modes for the complex eigenvalues. However, in the case of the fundamental edge wave modes, which are not energy decaying in the low and medium FTV ranges [32, 51], the calculation of the dispersive relationship is much simpler as the imaginary part of the eigenvalues is very small, and it can be neglected in the calculation procedure.

5.3. Parametric SAFE analysis

5.3.1. Ideal Geometry of waveguide

The purpose of this section is to investigate the effect of non-ideal edges on dispersions curves and modal displacement profiles (wave modes). In the beginning, the ideal geometry with rectangular edges is analysed using the SAFE-PML method and the results are compared with outcomes of past analytical studies. The ideal geometry and modelled finite element (FE) mesh are shown in Fig. 5.3. The analysis was conducted using SAFE-PML method implemented in COMSOL Multiphysics 5.6 software package. The thickness of the ideal edge was 5 mm ($2h$ = 5 mm). The PML with a depth of $8h$ was added to the internal region that is sufficiently far away from the free edge surface. The interior region has a depth of $20h$ to ensure that the fundamental mode of edge waves is not affected by the finite geometry. The mesh size was selected to be 0.5 mm. The free-quadratic elements were used to model the ideal geometry (rectangular edges), while the free-triangular elements were utilised for non-ideal geometries (curved edges).

The stress-free boundaries were enforced on all faces of the waveguide ($S = \{0 < x_1 < \infty, x_2 = \pm h\}$). The initial conditions for the displacement and velocity components were set at zero. The model was solved for excitation frequencies from 100 kHz to 800 kHz (corresponding to the FTV from 1 to 8), with the 10 kHz frequency step (or ΔFTV = 0.1). For each frequency, a large number of eigenvalues, typically 1500, were calculated to make sure that the eigenvalues of the fundamental modes of edge waves are among the calculated values.

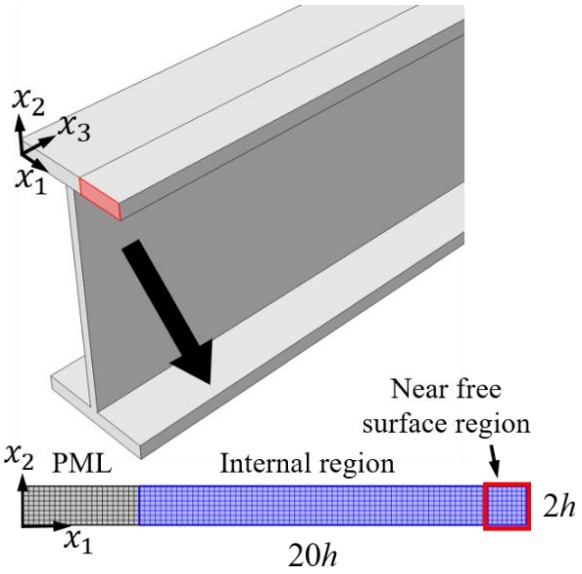

Figure 5.3. Schematic illustration of the SAFE-PML model for edge waves propagation along a waveguide with ideal edges

Typical results of calculations using SAFE-PML are shown in Fig. 5.4a (for the ideal edge). In this figure, the red and blue lines belong to the real plane and represent the fundamental modes of edge waves as explained earlier. Based on these calculations, the phase velocity as a function of FTVs is presented in Fig. 5.4b. In addition, the outcomes of SAFE-PML calculations are identical, or indistinguishable, to the dispersion curves as shown in Fig. 5.2.

The present results are compared with the outcomes of theoretical studies [25, 30, 52, 53]. In Fig. 5.4b, the calculated phase velocities of ES_0 and EA_0 modes are plotted along with the theoretical results [25, 30] demonstrating an excellent agreement. Figs. 5.5a and 5.5b show the in-plane displacement (u_1, see Fig. 5.3 for the reference system) component of the

waveforms of symmetric and antisymmetric modes of edge waves, respectively. The arrow in the figures is the complex Poynting vector along the x_3-direction (i.e., wave propagation direction), which represents the axial power flow density. These figures present the displacement amplitude of the fundamental edge waves, which demonstrate that the waveform of edge wave modes is localised near the edge typically within roughly three wavelengths; and there is almost no energy leak to the interior of the waveguide. These outcomes are consistent with previous analytical studies [32].

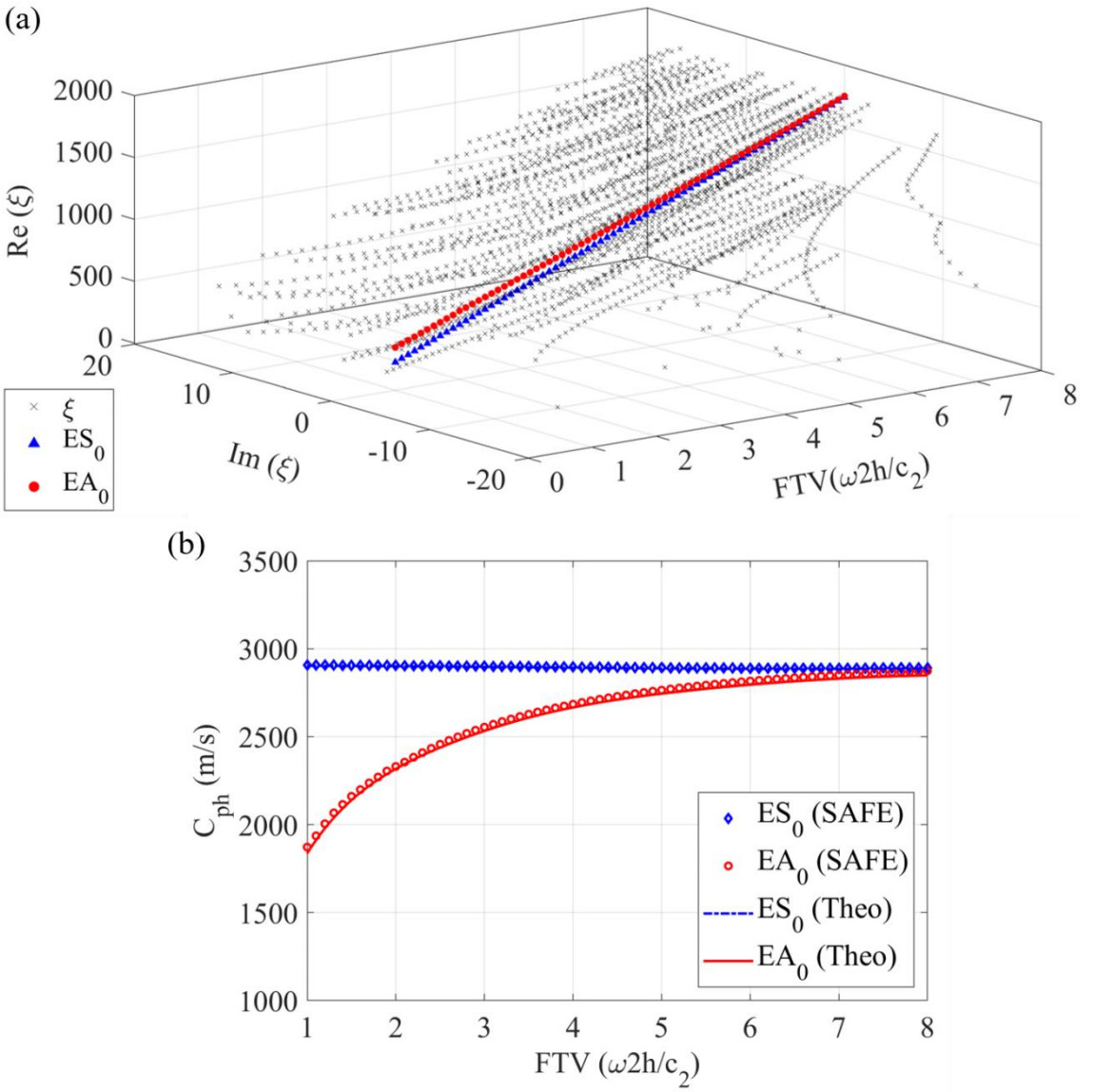

Figure 5.4. (a) Eigenvalues calculated by SAFE-PML method for the waveguide with ideal edge against FTVs and attenuation, and (b) phase velocity validation

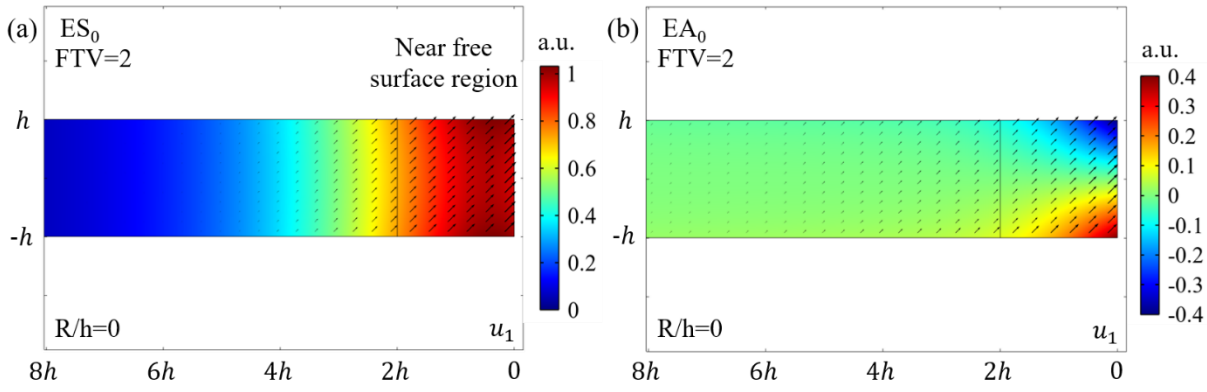

Figure 5.5. The waveforms of (a) ES_0 and (b) EA_0 calculated by SAFE-PML method, with displacement contour (u_1) and complex Poynting vector (in x_3-direction)

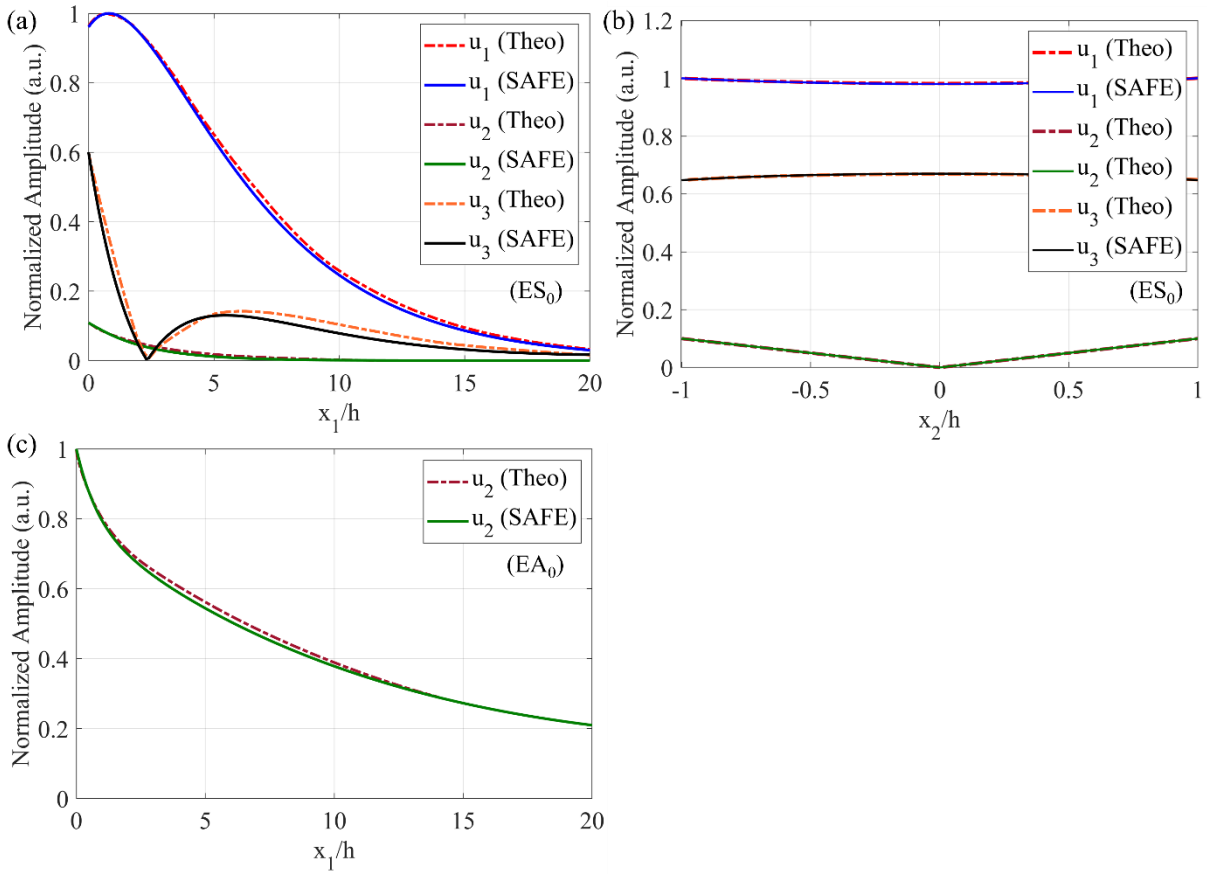

Figure 5.6. Validation on the modal displacement profiles of the waveguide with ideal edges (a) ES_0 mode in x_1-direction, (b) ES_0 mode in x_2-direction, and (c) EA_0 mode in x_1-direction

The comparison of the modal displacement profiles of the ES_0 mode against analytical results presented in [25] are shown in Figs. 5.6a and 5.6b, along x_1-direction, and x_2-direction,

respectively. The small deviation in Fig 5.6a between the SAFE outcomes and the analytical findings is negligible. Fig. 5.6c shows the calculation outcomes based on SAFE-PML method for the EA_0 mode along with analytical results [53]. Overall, the present results show an excellent agreement with the theoretical results. Therefore, this agreement provides a confidence in the further results for non-ideal geometries obtained by the same method, which will be considered next.

5.3.2. Non-ideal geometries of waveguides

The convergence of the classical edge waves to the quasi-edge waves in waveguides with rounded edges over the range of $0 \leqslant R/h \leqslant 2$ is investigated in this Section with respect to the modal displacement profiles and wave speeds. The waveguides with rounded edges and different radius-to-thickness (R/h) ratios are analysed with the adopted method. The computational results demonstrate that a wave mode similar to the fundamental antisymmetric edge wave (EA_0) mode, which is the quasi-fundamental antisymmetric edge wave (QEA_0) mode, can propagate in this case. Figs. 5.7a – 5.7c present the normal displacement component of the waveforms corresponding to the QEA_0 mode for different FTVs in the waveguide with rounded edge. The results indicate that the wave energy becomes more localised near the sharp edge region with the increase of FTV.

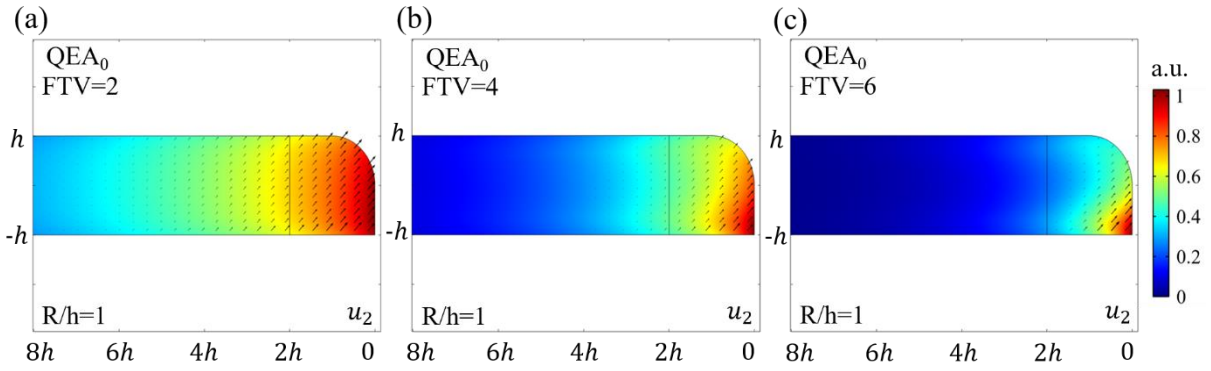

Figure 5.7. SAFE contour of the normal displacement waveform of QEA_0 in a waveguide with non-ideal edge (R/h =1) for (a) FTV=2, (b) FTV=4, and (c) FTV=6, with displacement contour (u_2) and complex Poynting vector (in x_3-direction)

The modal displacement profiles along the depth and thickness directions are shown in Figs. 5.8a-5.8d. Fig. 5.8a and Fig. 5.8b demonstrate the effect of different FTVs at the same

R/h ratio on the displacement profiles, in depth direction, and in thickness direction, respectively. In Fig. 5.8c and Fig. 5.8d, the FTV is kept the same and the R/h ratios varied from 0 to 2. The ideal geometry of the edge corresponds to R/h = 0, which is the classical edge waves, while the edge is completely rounded when the R/h = 2. The results are consistent with the previous findings (Fig. 5.7). It can be concluded from Fig. 5.8 that the level of the wave energy localisation of the QEA_0 mode depends on both FTV and R/h ratio.

The confinement of the edge waves due to the increase of R/h ratio may be explained by the stronger trapping effect near the sharp edge compared with the flat edge surface and the rounded edges. This confinement in classical edge waves (i.e., with ideal edges and flat edge surface) as a function of the FTVs was investigated before, see [32, 52]; and the classical edge waves were found to be localised near the sharp edges and converges to the wedge waves at high FTVs (at FTVs > 8). In the case of the quasi-edge waves in the waveguide with rounded edges (see Fig. 5.7 and Figs. 5.8a-5.8b), the wave confinement also occurs with the increase of the FTVs and the displacement profiles are localised near the sharp edge. When increasing the R/h ratio, the quasi-edge waves become more confined at the opposite sharp edge, see Fig. 5.7. In addition, in the case of the wedge waves, the attenuation associated with the wave leakage increases significantly when the R/h ratio increases [28]. Similarly, the presence of the rounded edge may also increase the wave energy leakage for quasi-edge waves, and localises the edge wave energy near the sharp edge, specifically at high R/h ratios, see Fig. 5.8.

The dispersion properties of the ES_0 mode propagating along the non-ideal edges (the QES_0 mode) are very sensitive to local geometry, i.e., the R/h ratios (see Fig. 5.9a). Moreover, this mode demonstrates a large attenuation, in particular, for high FTVs and/or large R/h ratios. The attenuation for completely rounded edge decreases at higher FTVs and converges to FGW at FTV = 7.8. This behaviour has many similarities with the shear-horizontal type of FGW, which was investigated in [15]. Overall, this mode is not very suitable for practical utilisations for the purposes of NDE due to large attenuation, especially if the geometry of the waveguide is far from the ideal.

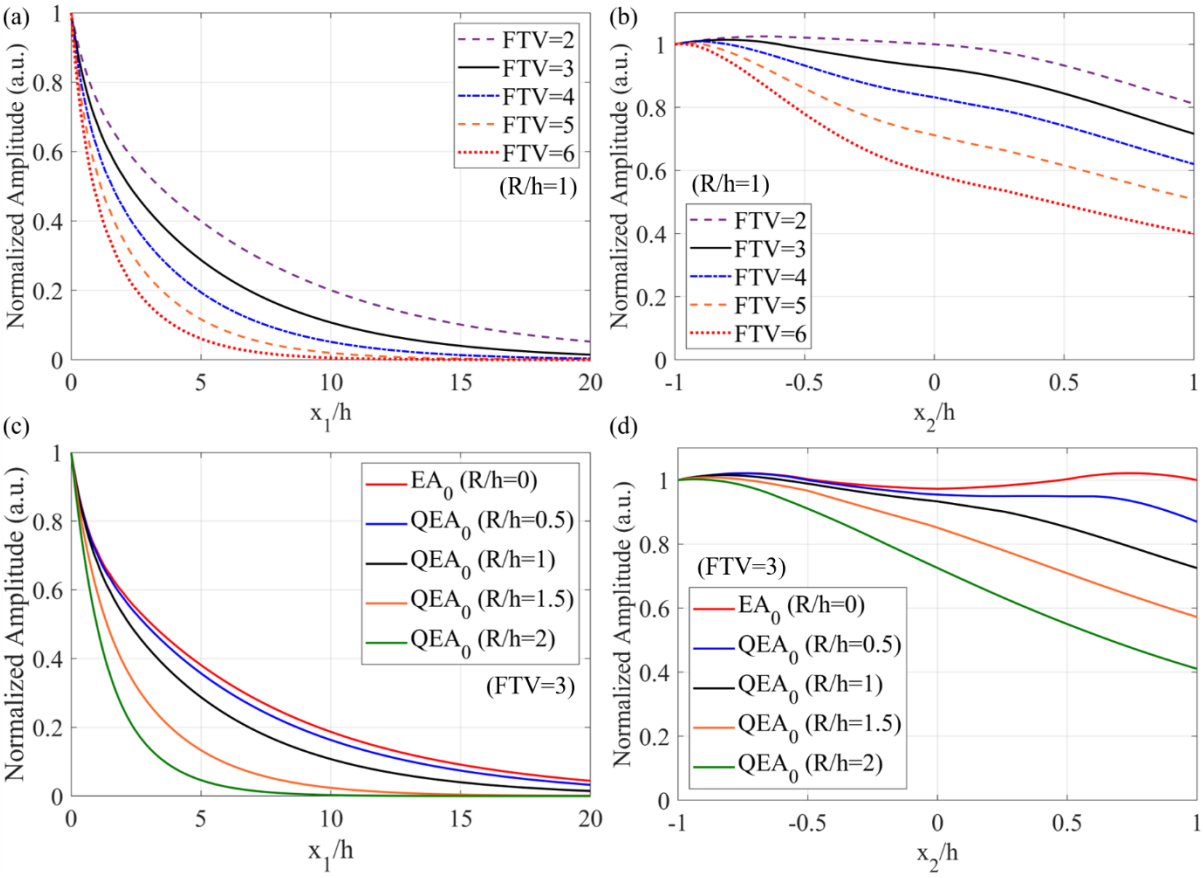

Figure 5.8. SAFE calculation of the normal displacement profiles of QEA_0 for the waveguide with non-ideal edges in the (a) x_1-direction with different FTVs, (b) x_2-direction with different FTVs, (c) x_1-direction with different R/h ratios, and (d) x_2-direction with different R/h ratios

In contrast, the QEA0 mode demonstrates a very limited leakage and the attenuation (almost undetectable computationally) over all considered R/h ratios and within the investigated FTV range, which mathematically corresponds to a very small imaginary part of the corresponding eigenvalue. This wave characteristic simplifies the mode and frequency selection for practical applications, signal processing, and make this wave mode very attractive for distant inspections. However, the QEA_0 mode is dispersive and Fig. 5.9b, shows the dependencies of the phase velocities of this mode as a function of FTVs at different R/h ratios. Nevertheless, the effect of the R/h ratio on phase velocities is relatively small.

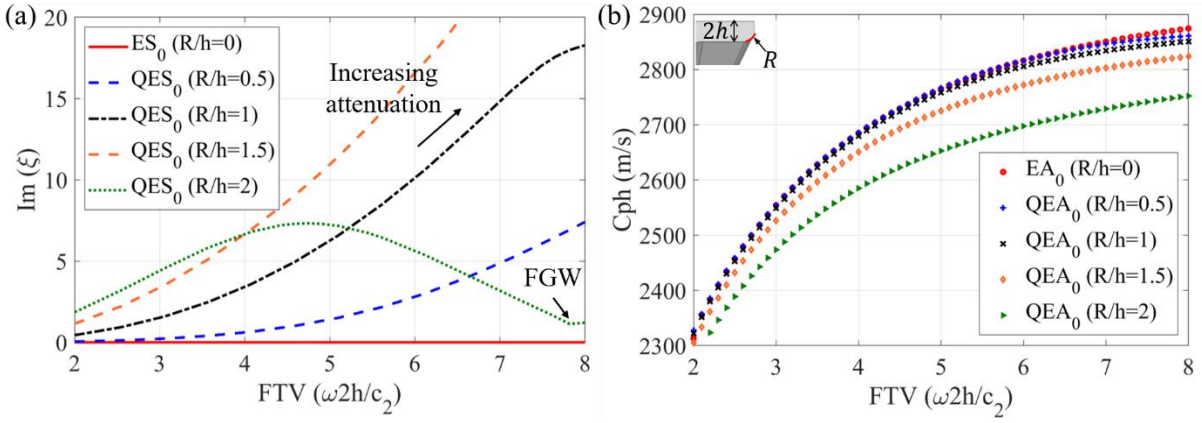

Figure 5.9. SAFE prediction of the fundamental mode of edge waves against FTVs in a waveguide with arbitrary curves (a) attenuation of QES_0 mode, and (b) phase velocities of QEA_0 mode

5.4. Numerical simulations

5.4.1. 3D Finite Element model

A 3D FE model was developed in ABAQUS/Explicit to simulate the wave propagation behaviour. The material properties are listed in Table 5.1; and these properties and the geometry are the same as utilised in the experimental study, which will be described in the next section. The FE geometry represents a tapered flange beam (TFB) with R/h ratio of 1. The cross-section geometry of the beam is shown in Fig. 5.14b in Section 5.5 ahead. The edge waves can only propagate along the feature region (i.e., near the free edge), where the traction-free condition could be applied [40]. Therefore, the internal structure of the waveguide has no influence on the propagation of the highly-localised edge wave modes; thus only half of the beam structure has been modelled to reduce the computational time. The excitation wedge was modelled with the same finite element type as the beam; and the perfect coupling between the wedge and beam was modelled using the tie constraint. It should be noted that the orientation of the excitation wedge was different for the generation of QEA_0 and QES_0 modes, which is similar to the experimental studies. The displacement boundary conditions were applied orthogonal to the inclined face of the wedge, with displacement amplitude of 8 μm. The maximum size of 0.5 mm was selected for all finite elements of the FE model to ensure more than 15 elements per wavelength in the considered FTV range. Eight-node linear brick element with reduced integration (C3D8R) was used in the FE model. The Rayleigh damping α was implemented [54] to simulate the wave amplitude attenuation due to the material damping [55].

Table 5.1. Material properties

Material	ρ (kg·m^{-3})	E (GPa)	ν	α damping
125TFB (1018 steel) [20]	7870	205	0.29	90
Excitation wedge (Dotmar Polystone) [24]	351.4	0.9	0.4	28783.3

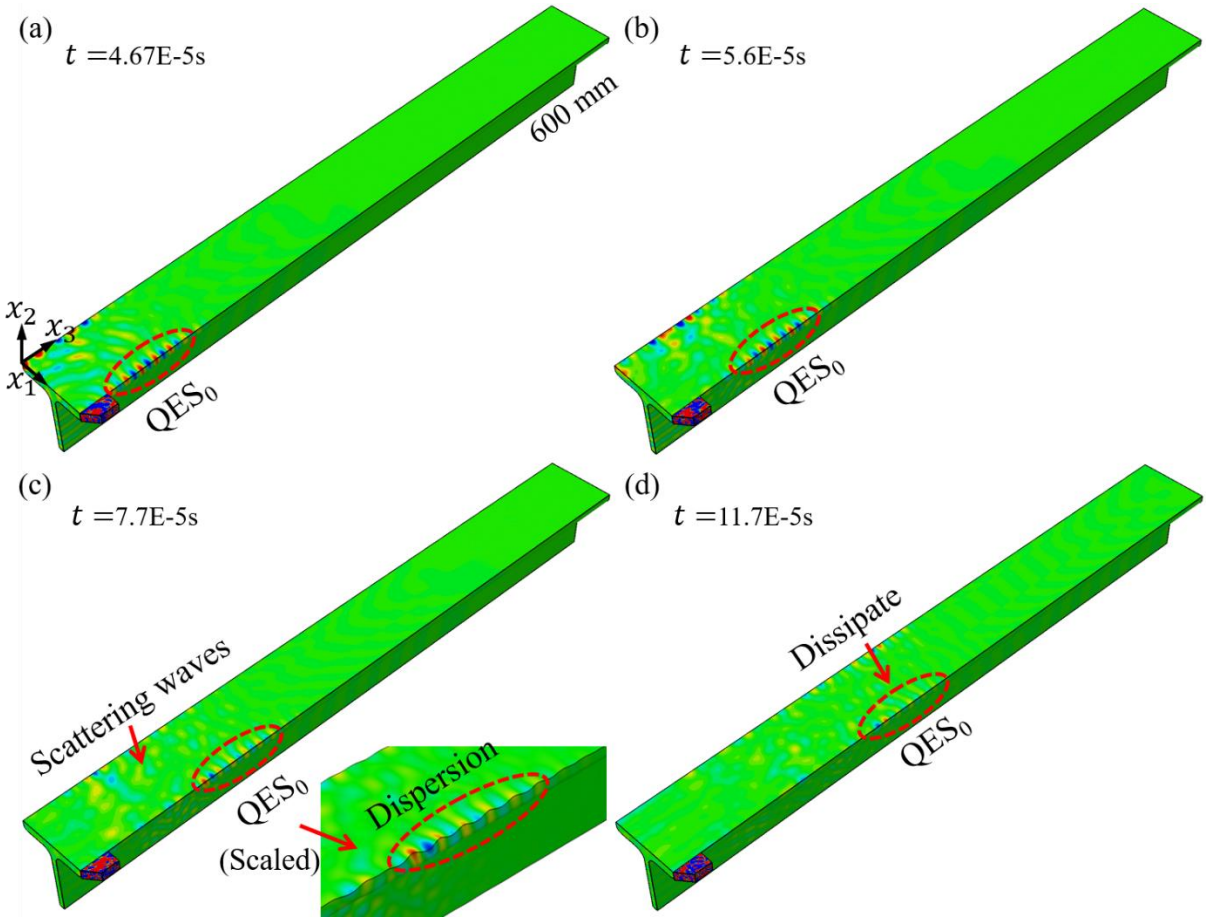

Figure 5.10. 3D FE model contour of in-plane displacement (u_1) wavefield with QES$_0$ mode (FTV=2) at different time steps

In Fig. 5.10, the waveform of the QES$_0$ mode with low FTV shows significant dispersion after limited wave propagation distances, and the QES$_0$ mode shows significant coupling with other propagating plate wave modes (i.e., Lamb and shear-horizontal wave modes). In contrast, in Fig. 5.11, the QEA$_0$ mode shows negligible dispersion over long wave propagation distances, and the waveform can still be confined near the free surface region. It should be noted that Lamb waves can also be generated by the wedge as shown in Fig. 5.10a,

which disperses rapidly and shows negligible influence on the propagation of the QEA_0 mode, since its displacement magnitude is significantly smaller compared with the QEA_0 mode. The detailed numerical studies are presented and discussed in the next Session.

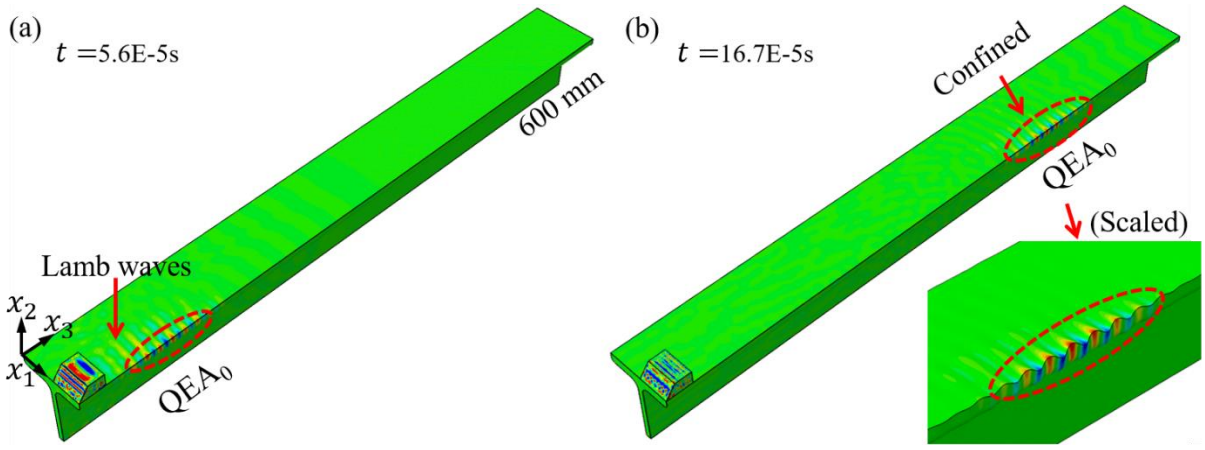

Figure 5.11. 3D FE model contour of normal displacement (u_2) wavefield with QEA_0 mode (FTV=2) at different time steps

5.4.2. Effect of the curved edge on the QEA_0 propagation

The experimental measurement of the displacement profile of the QEA_0 mode in the case of a curved edge surface can be challenging, since it is very difficult to perfectly align the 1D laser vibrometer perpendicular to the curved surface. This is not the case for the 3D FE simulation, and any displacement components along the curved edge can be easily evaluated. The displacement amplitude along the curved flange was compared with that of the flat flange as illustrated in Fig. 5.12. The results show a relatively rapid decrease of the displacement amplitude along the curved edge with the measurement distance. The difference in the amplitudes along flat and curved edges was small, approximately 10%.

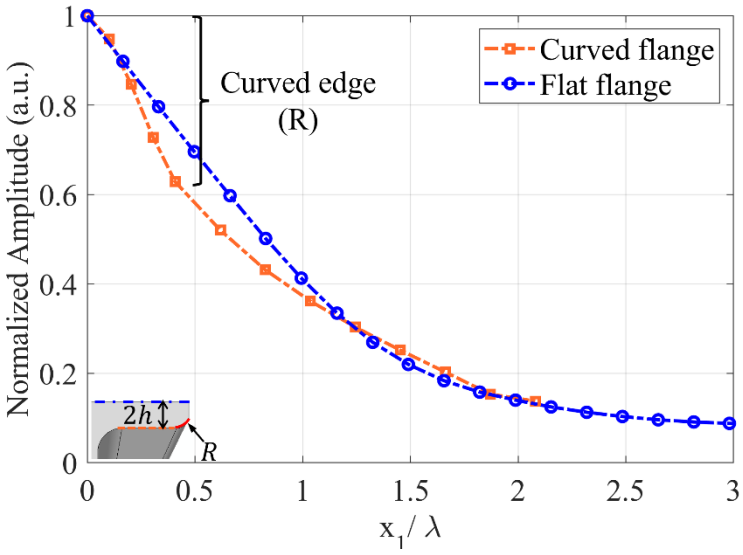

Figure 5.12. Numerical simulation of QEA_0 mode displacement amplitude along the flat and curved flanges against the distance-to-wavelength ratio

5.4.3. Sensitivity of QEA_0 to partially through-thickness defects

The 3D FE model allows different defects to be simulated and analysed, which can be costly if investigated experimentally. The focus of the present section is to analyse the sensitivity of the QEA_0 mode to partially through-thickness edge defects, which represent a corner crack and a corrosion spot as illustrated in Fig. 5.13a. The defect depths for these defects (*d*) are defined as shown in Fig. 5.13a. All defects had 1 mm width. The defects were modelled by removing the mesh elements assigned to the considered defect geometries as detailed in Fig. 5.13a. A low FTV (FTV = 3) was utilised for the simulation of the defect detection using the QEA_0 mode. In Fig. 5.13b shows the defect reflection ratios which is the ratio of the displacement amplitude of the incident and reflected waves, due of the different type of defects and their depths. The outcomes of numerical studies demonstrate that QEA_0 is sensitive to the considered types of edge defects. The noise level was determined based on the experimental results presented in Section 5.5.3; and the reflected waves due to the defects usually show a higher amplitude than the noise level. This indicates that the numerical results can also be reproduced experimentally.

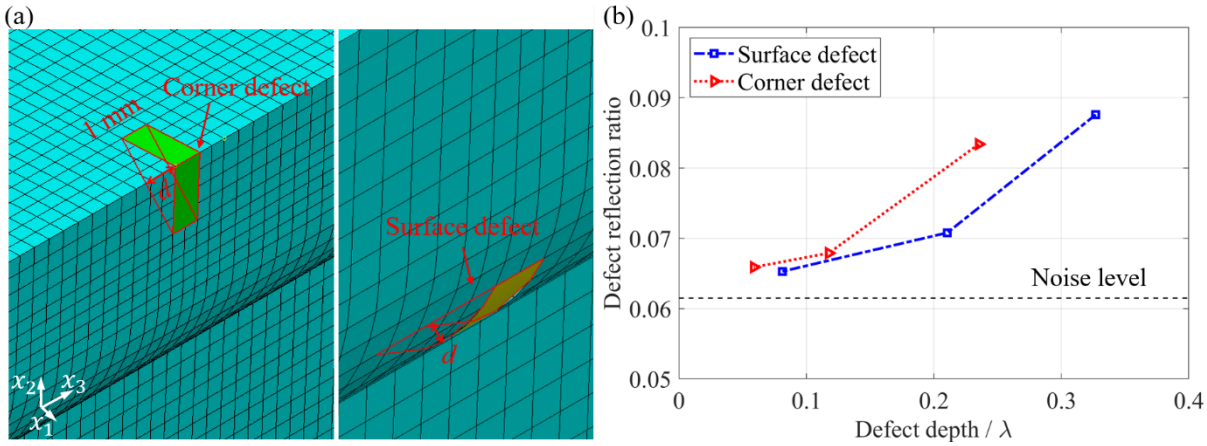

Figure 5.13. (a) Schematic illustration of defects with FE mesh, and (b) defect reflection ratio against defect depth-to-wavelength ratio

5.5. Experimental studies

5.5.1. Experimental setup

The experimental setup is shown in Fig. 5.14a. A specimen of 1000 mm in length and the cross-section as shown in Fig. 5.12b was initially free from defects. A signal generation module (NI PXIe-5122) was used to generate the 12-cycle Hann-windowed tone-burst. The generated input signal was amplified by 200V peak-to-peak voltage using a high voltage amplifier (CIPIAN HVA-800A), and then the input signal was transmitted to the transducer (ULTRAN-GC200) for the wave excitation. The transducer was glued to an excitation wedge, and the wedge angle was 31-degree, which is calculated based on the Snell's law (the wave speed of the wedge material c_w=1336.37 m/s) to maximise the energy transfer to the QEA_0 [56]. The excitation wedge is suitable to generate the QEA_0 mode within a range of FTVs as shown in Fig. 5.15a (i.e., FTV=2.5~6). The high vacuum grease (DOW CORNING) was used for bonding the transducer and the excitation wedge, and also the excitation wedge and the specimen to ensure the stable transmission of the generated edge waves. The excitation wedge was clamped to the specimen in x_2-direction for the generation of QEA_0 mode as shown in Fig. 5.14c. The normal displacements near the free surface region adjacent to the flat edge were measured using the 1D laser vibrometer.

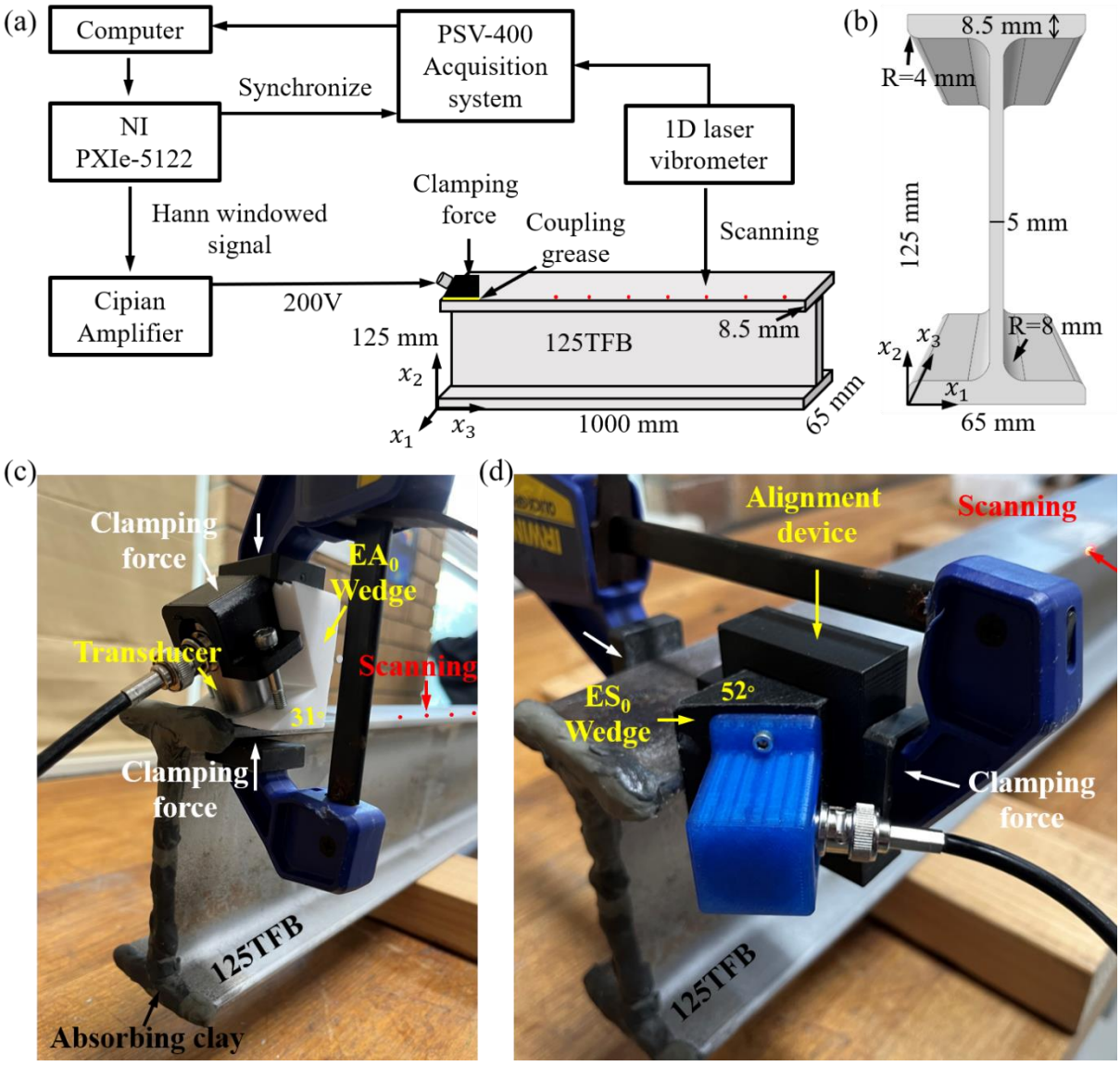

Figure 5.14. Experimental setup (a) Laser acquisition setup, (b) 125TFB cross-section profile, (c) details of QEA_0 mode generation, and (d) details of QES_0 mode generation

The first measurement point was 200 mm away from the excitation wedge, and the remaining 12 measurement points were placed at 50 mm distance interval. The reflective coating was applied to the specimen to improve the signal-to-noise ratio. The absorbing clay was attached to the beam ends to reduce the boundary reflections. The generation of the QES_0 mode used the similar experimental setups as shown in Fig. 5.14d, with a different orientation of the excitation wedge, which was clamped to the specimen in x_1-direction. The in-plane displacement was measured normal to the x_1-direction to characterise the QES_0 mode. The

wedge material for the generation of QES_0 mode was different (c_w=2300 m/s), and the wedge angle was selected at 52-degree, reflecting the different wave speed of this material [24].

The PSV-400 acquisition system was synchronized with the signal generation module. The signal recording of the acquisition was averaged 600 times, with is sufficient to capture the linear features of edge waves with fundamental modes. The sampling rate of the acquisition was 25.6 MHz with the 39.06 nanoseconds time step, and a low-pass filter with 1000 kHz was applied to reduce the high-frequency noise.

Displacement results obtained from the experiment were consistent and repeatable, and the fundamental modes of edge waves had significantly larger displacement amplitude compared with other wave modes. This can be considered as an advantage for the in-situ application, which indicates lower requirement on instrumentation compared with the generation of other wave modes (e.g., Lamb and shear-horizontal wave modes). In Fig. 5.15b, the group velocity of QEA_0 mode was measured in the low and medium FTV ranges, from 2 to 6, corresponding to 120 kHz and 360 kHz with a step of 30 kHz (i.e., 0.5 FTV). The experimental results show a good agreement with the SAFE results, with only exception of FTV = 2, which demonstrates a slight deviation compared with the SAFE calculations due to the mismatch of the designed wedge angle with the Snell's condition (see Fig. 5.15a).

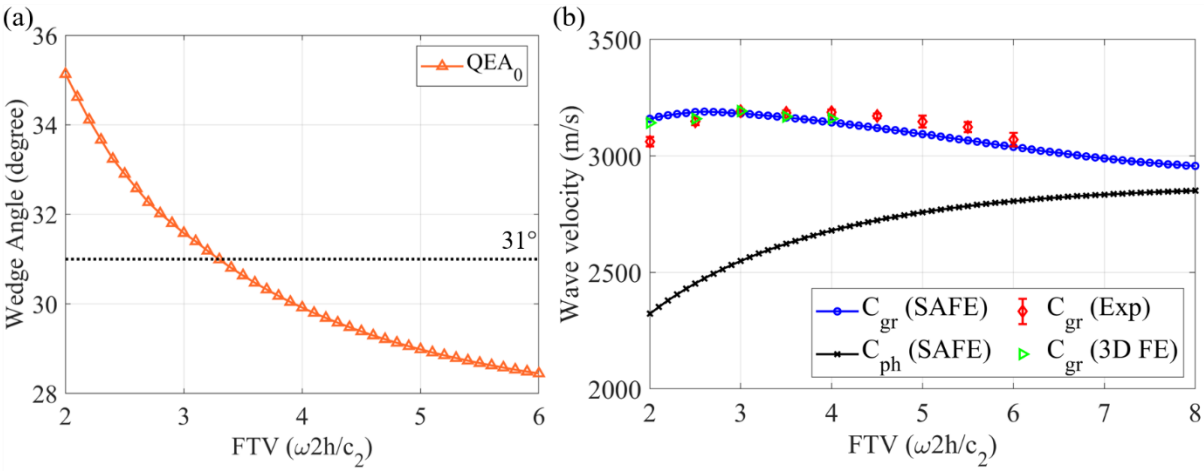

Figure 5.15. (a) Wedge angle, and (b) wave velocity of the QEA_0 mode

5.5.2. Comparison of the QEA_0 and QES_0 modes

The generated QEA_0 and QES_0 modes are investigated in the low and medium FTV ranges to demonstrate the effects of FTVs on the wave propagation behaviour. In Figs. 5.16a and 5.16b, the QEA_0 mode shows significantly long wave propagation distances with a negligible decrease of the displacement amplitude, especially in the low FTV range (see Fig. 5.16a). It means this mode had almost no attenuation within the specimen length. Hence, the QEA_0 mode in the low FTV range is suitable for most practical applications, in which the typical length of structures can reach 10 to 20 meters. It should be noted that the higher order modes can also be generated in the medium FTV range, which are observed in Fig. 5.16b, however, the amplitude of these modes disperse rapidly with the propagation distance. This indicates that the higher order modes are not suitable for the distant inspection of the non-ideal edges, and the interference with the QEA_0 mode reduces significantly after approximately 500 mm from the excitation wedge. Within this distance the higher order modes and the fundamental modes can interfere resulting in some amplitude decay of the QEA_0 mode. However, this interference is very small in the medium FTV range (i.e., less than 5% deviation over 800 mm propagation distance).

In contrast, the QES_0 mode has a significant displacement amplitude decay over relatively short wave propagation distances, see Figs. 5.16c and 5.16d. In the low FTV range (Fig. 5.16c), the waveforms of QES_0 reveals a clear distortion and dispersion, which are likely due to the wave mode coupling between the edge wave modes and the other propagating plate wave modes (i.e., Lamb and shear-horizontal wave modes). This phenomenon can be also observed from the direct numerical simulation results, Fig. 5.10 in Section 5.4. In general, the wave modes coupling between edge wave modes and other wave modes decreases with the increase of the FTVs, and the distortion of the waveforms becomes less severe. However, the higher order modes can be generated in the medium and high FTV range, and the attenuation increases significantly as presented in Fig. 5.16d. The trend presented in this figure agrees with the SAFE results presented in Fig. 5.9a in Section 5.3. In addition, the wave energy of the QES_0 mode in the higher FTVs is also largely localised near the sharp corner of non-ideal edges. Overall, based on general requirements to distant defect detection of non-ideal waveguides, the QEA_0 mode is more advantageous if compared with the propagation behaviour of the QES_0 mode.

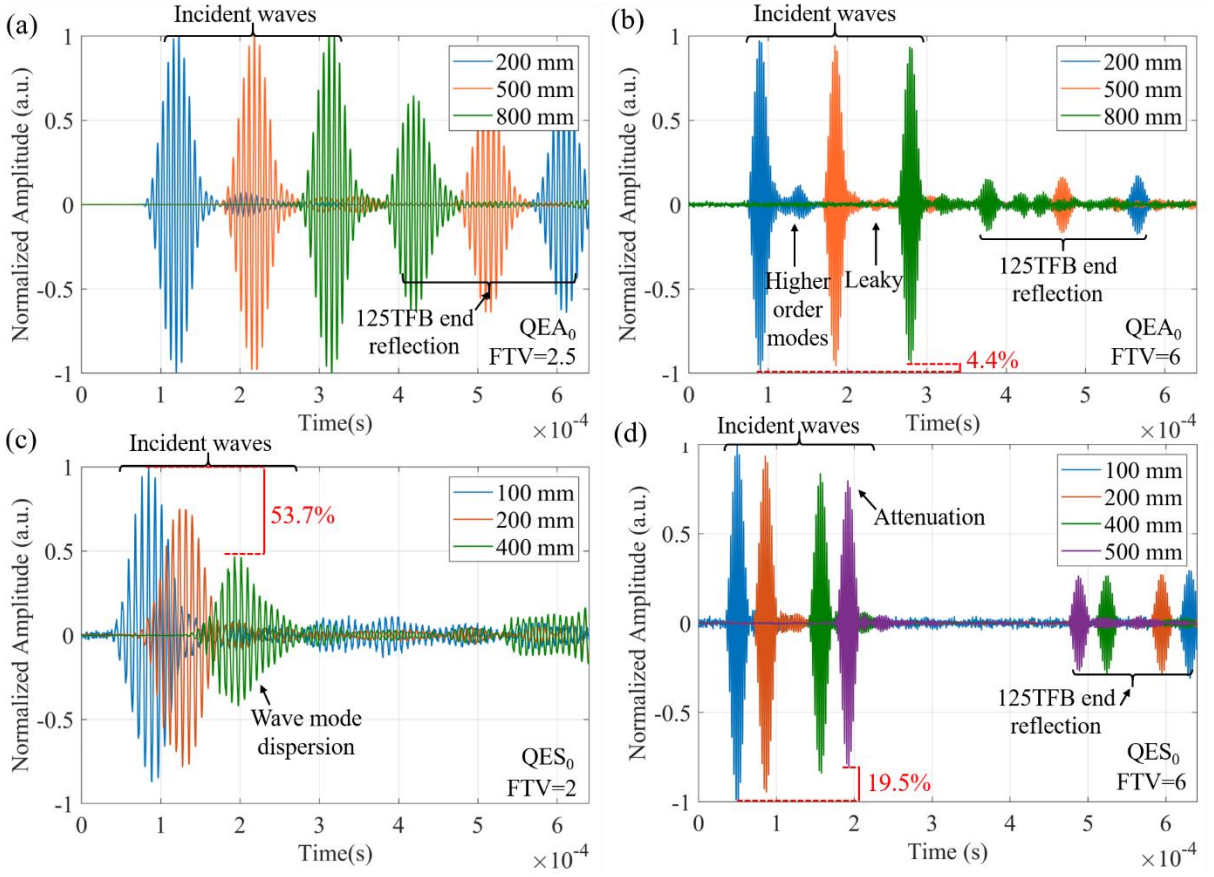

Figure 5.16. Comparison between the QEA_0 and QES_0 modes in time domain, (a) low FTV (FTV=2.5, 150 kHz) QEA_0 mode, (b) medium FTV (FTV=6, 360 kHz) QEA_0 mode, (c) low FTV (FTV=2, 120 kHz) QES_0 mode, and (d) medium FTV (FTV=6, 360 kHz) QES_0 mode

5.5.3. Further characterisation of the QEA_0 mode

The normal displacement amplitude of the QEA_0 mode was also investigated in the depth direction (x_1-direction) at the flat flange, and the displacement profiles of the QEA_0 mode are presented in Fig. 5.17a. The locations of the measurement points are 300 mm away from the wedge transducer. The results for each FTV are normalized against the first measurement point, x_1 = 0, see Fig. 5.17a. The results indicate that the internal structure (i.e., the web) has no influence on the propagation of the QEA_0 mode, and the edge waves only exist in the feature region (i.e., near the free edge) [40]. The normalised amplitude drops below approximately 6% the QEA_0 mode becomes indistinguishable from the noise, which is largely associated with equipment and the scattering effects of Lamb and shear-horizontal wave modes. The waveforms are more localised near the edge surface with the increase of FTVs. The latter is consistent with the simplified SAFE-PML model discussed in Section 5.3. If the results are

normalised by the wavelength λ, as shown in Fig. 5.17b, the QEA_0 mode is localised within three wavelengths for all considered FTVs. This result also provides a general guideline for NDE inspections using the QEA_0 mode, i.e., the effective inspection depth is roughly corresponding to the wavelength.

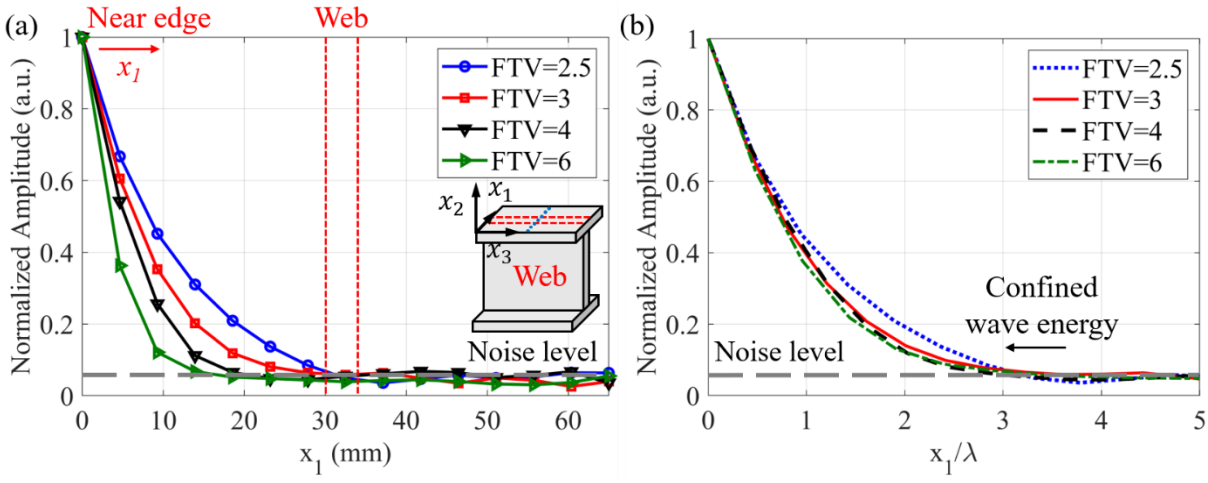

Figure 5.17. QEA_0 displacement amplitude along the flat flange in the x_1-direction (a) against the distance away from the edge, and (b) against the distance-to-wavelength ratio

5.5.4. Defect evaluation with QEA_0 mode

Two through-thickness notches have been fabricated to investigate the sensitivity of QEA_0 mode to crack-like defects. The dimensions of the first notch were 1.2 mm in depth (x_1-direction) and 1.1 mm in width (x_3-direction). There was also a surface squat located near the beam end, which was used to investigate the possibility of a multiple defect evaluation with this fundamental mode. Another defect was located at another edge, which had 7.7 mm depth and 7.2 mm width. The eco-pulse method was utilised for defect detection and the Hilbert transform was applied to simplify the analysis by calculating the waveform envelopes.

In Fig. 5.18a, a reflection from the first 1.2 mm depth notch is clearly observed, and the wave propagation distance were calculated based on the group velocity presented earlier in Fig. 5.15b in Section 5.5.1. The calculated notch location (i.e. 265.8 mm) was in an excellent agreement with the actual notch location (i.e., 265.0 mm away from the measurement point) with a difference of less than 0.2%. In addition, the reflection due to the surface squat was also revealed despite multiple reflection signals from the beam end reflection or the notch. The

calculated squat location also agreed well with the actual location of the squat symmetry line resulting in only 2.9% difference.

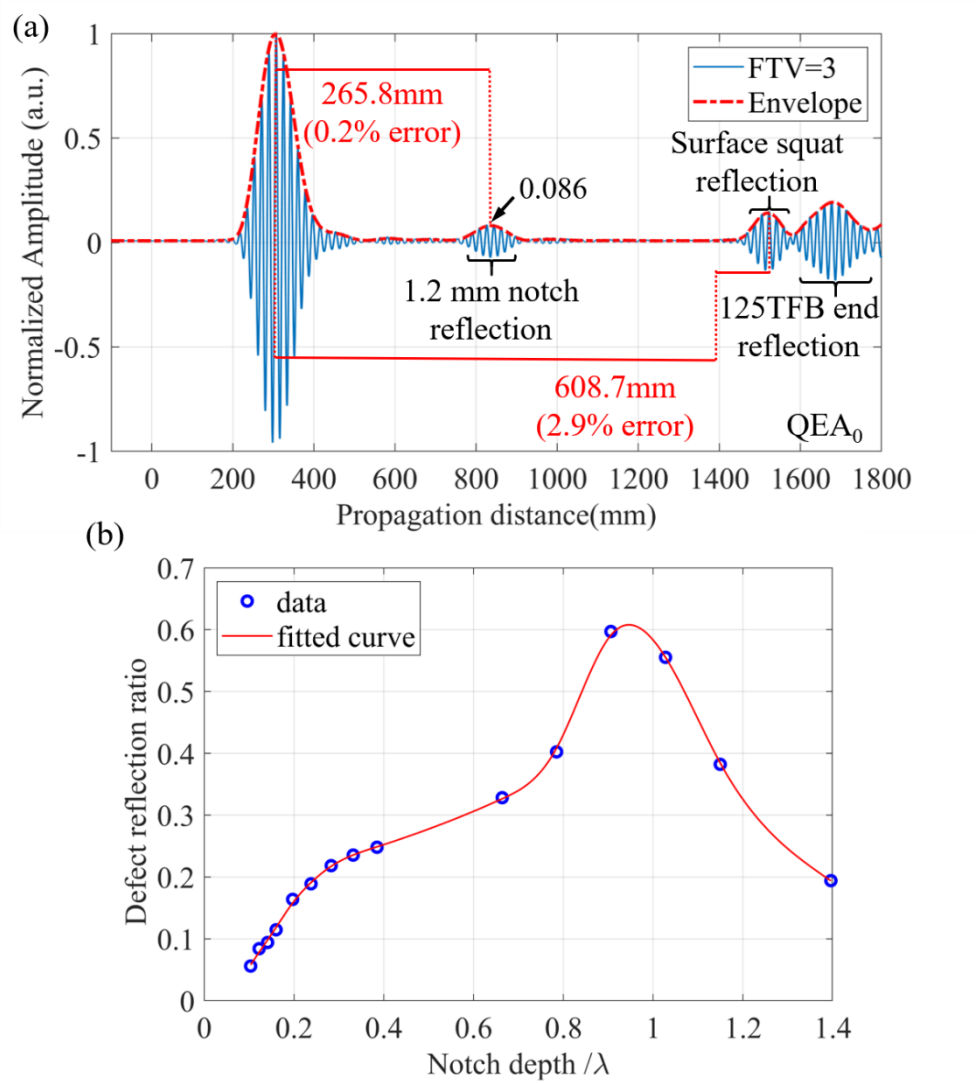

Figure 5.18. (a) 1.2 mm notch reflection with FTV=3 (180 kHz), and (b) defect reflection ratio against notch depth-to-wavelength ratio

In Fig. 5.18b, the defect reflection ratio (the ratio of the displacement amplitude of the incident and reflected waves) is calculated for different notch depth-to-wavelength ratios. The two different notches were evaluated tuning the different FTVs (i.e., different frequencies). The small notch with 1.2 mm depth was used to investigate the small notch by wavelength ratio (depth/$\lambda < 0.4$), while the large notch with 7.7 mm depth was used to determine the large notch by wavelength ratio (depth/$\lambda > 0.4$). In the beginning, the defect reflection ratio increases with

an increase of the notch depth-to-wavelength ratio and reaches the maximum at 1. Then, this ratio decreases with further increase of the notch depth-to-wavelength ratio as shown in Fig. 5.18b. Therefore, the optimum wavelength for detection of crack-like defects would be roughly corresponding to the depth of the defect. This conclusion is also consistent with the outcomes of the SAFE calculation, which demonstrate that high FTVs can only provide a high amplitude of the reflected signal in the case of shallow surface defects.

5.5.5. Experimental validation of FE model

The 3D FE model has been validated using the experimental results described in the previous Section. This Section will be focused on the linear features of QEA_0 mode, including the waveforms, displacement profiles, and the wave velocity of this mode. The waveform in the time domain (in Fig. 5.19a) shows a good agreement between the experimental and numerical results. A small discrepancy between the results is due to the boundary reflections in 3D FE model, which are associated with the inclusion of the absorbing layer in experimental studies and modelling of the excitation wedge. In Fig. 5.19b, the numerical displacement profile along the flat flange in the x_1-direction matches well with the both, the SAFE and experimental results. The group velocity in the low FTV range has been compared with all other results (SAFE and experimental) earlier and this comparison is shown in Fig. 5.15b, Section 5.5.1. The numerical results were only calculated from FTV = 2 to FTV = 4, since the focus of the present study is only the low FTVs, and the simulation of edge waves with higher FTVs requires smaller element size. The well-matched numerical and experimental results suggest that the developed 3D FE model can provide a good prediction of the linear wave behaviour of QEA_0 mode, and the validated 3D FE model can be applied for the further investigations of the QEA_0 mode.

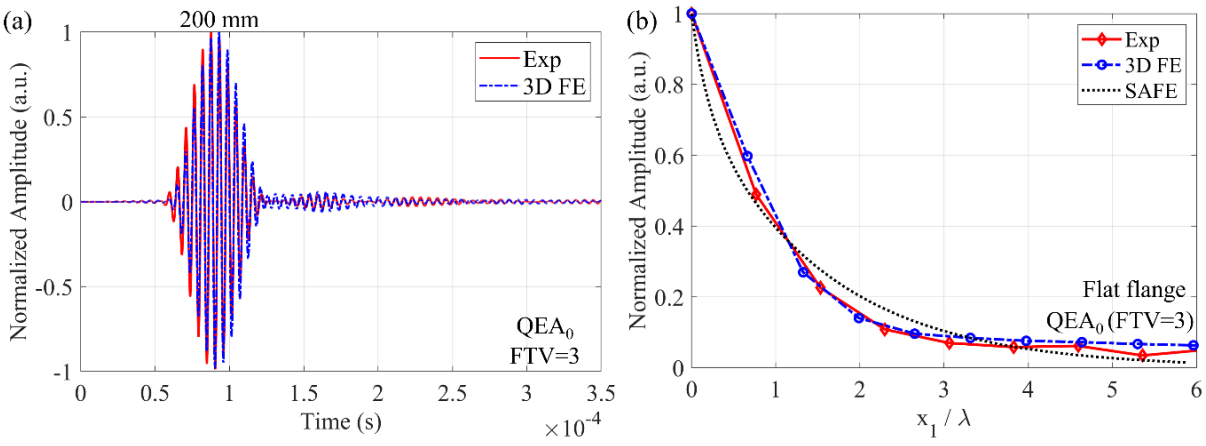

Figure 5.19. 3D FE model validation (a) waveform in time domain, and (b) displacement profile along the flat flange

5.6. Conclusion

In this work, the SAFE-PML method has been applied to the calculation of the dispersion properties and the modal displacement profiles of the fundamental modes of edge waves, which was previously studied using analytical methods. The propagation of QEA_0 mode along ideal and non-ideal edges of structural elements has been investigated based using the SAFE-PML method, and the dispersion properties and modal displacement profiles have been determined. The result agrees very well with the theoretical findings in the classical edge waves problem with ideal edges. The QEA_0 mode shows significant advantages for its utilisation for near edge defect evaluation compared with other guided wave modes, especially in the low FTV range. The QEA_0 mode can propagate over very long distances along non-ideal edges; and it demonstrates a great potential for the distant defect evaluation. In contrast, other guided wave modes are very sensitive to the cross-sectional profile of the waveguide; and may non-exist for certain shapes or disperse rapidly. In addition, the outcomes of this study have demonstrated that the modal displacement profile of the QEA_0 mode is localised near the free edge surface; and it is confined within three wavelengths from the free edge surface. The interior structure has a negligible influence on the QEA_0 mode propagation. The QEA_0 mode has a larger displacement amplitude at the sharp edge ($x_2 \approx -h$) compared with the curved edge ($x_2 \approx h$). Nevertheless, the displacement amplitude at the curved edge is still comparable with the flat edge for all considered geometries. Therefore, the QEA_0 mode in the low FTV range ($1 < \text{FTV} \leq 4$) can be used for inspections of larger cross-sectional areas compared with

the higher FTV range. In contrast, the medium FTV range (4 < FTV < 8) can be used for the structures with smaller cross-sections. In this case, the boundary reflections from the interior of the structure are almost negligible for the propagation of the QEA_0 mode.

The experimental and numerical studies have demonstrated that the QEA_0 mode is applicable to detection of small defects with the characteristic depth of more than 0.1 wavelength. The defect size correlates well with the defect reflection ratio. The multiple defects can be used resolved and evaluated separately using the echo-pulse method and Hilbert transform. The conducted experimental studies indicated that the locations of multiple defects can be determined very accurately with error less than 3%. Using the validated 3D FE model, we also demonstrated that the QEA_0 mode is very promising for detection of corner and surface defects, which are most common in practice.

Overall, the present study provides a comprehensive and fundamental understanding on the evaluation and localisation of defects with the QEA_0 mode near the free edges of structural elements, which have non-ideal edges. The findings of the present study show a great potential of this guided wave mode for the purpose of NDE and SHM of many structures, especially for the edges of structures with complex cross-sectional profiles. Future investigations can also focus on the nonlinear features of the QEA_0 mode to advance the distant defect evaluation techniques for more challenging applications.

Acknowledgement

This work was funded by the Australian Research Council (ARC) DP200102300 and DP210103307 grants. The authors are grateful for the support. The authors would like to thank Chang Jiang for the support with SAFE model. The authors would like to thank Ian Ogier for the support with laboratory work.

References

[1] Wu J, Ng C T and Fang H 2022 Internal damages detection for structural timber members using low-frequency anti-symmetric guided wave *Construction and Building Materials* **322** 126355

[2] Hu X, Yin T, Zhu H, Ng C-T and Kotousov A 2022 Structural health monitoring of partially immersed metallic plates using nonlinear guided wave mixing *Construction and Building Materials* **346** 128381

[3] Zhu H, Ng C T and Kotousov A 2022 Low-frequency Lamb wave mixing for fatigue damage evaluation using phase-reversal approach *Ultrasonics* **124** 106768
[4] Mohseni H and Ng C-T 2019 Rayleigh wave propagation and scattering characteristics at debondings in fibre-reinforced polymer-retrofitted concrete structures *Struct. Health Monitor.* **18** 303-17
[5] Jiang C, Zhang C, Li W, Deng M, Ng C-T J S M and Structures 2022 Assessment of damage in composites using static component generation of ultrasonic guided waves **31** 045025
[6] Sampath S and Sohn H 2022 Cubic nonlinearity parameter measurement and material degradation detection using nonlinear ultrasonic three-wave mixing *Ultrasonics* **121** 106670
[7] Sampath S and Sohn H 2022 Detection and localization of fatigue crack using nonlinear ultrasonic three-wave mixing technique *International Journal of Fatigue* **155** 106582
[8] Jiang C, Li W, Deng M and Ng C-T 2022 Quasistatic pulse generation of ultrasonic guided waves propagation in composites *J. Sound Vib.* 116764
[9] Zhu H, Ng C T and Kotousov A 2023 Frequency selection and time shifting for maximizing the performance of low-frequency guided wave mixing *NDT&E Int.* **133** 102735
[10] Guan R, Lu Y, Wang K and Su Z 2019 Fatigue crack detection in pipes with multiple mode nonlinear guided waves *Struct. Health Monitor.* **18** 180-92
[11] Li W, Lan Z, Hu N and Deng M 2021 Modeling and simulation of backward combined harmonic generation induced by one-way mixing of longitudinal ultrasonic guided waves in a circular pipe *Ultrasonics* **113** 106356
[12] Evans M, Lucas A and Ingram I 2018 The inspection of level crossing rails using guided waves *Construction and Building Materials* **179** 614-8
[13] Hakoda C and Lissenden C J 2020 Application of a general expression for the group velocity vector of elastodynamic guided waves *J. Sound Vib.* **469** 115165
[14] Chen R, Hu C, Xu J, Gong Z, Liu L, Wang P and Chen X 2021 Research on guided wave propagation characteristics in turnout rails with variable cross-section *J. Sound Vib.* **494** 115853
[15] Yu X, Manogharan P, Fan Z and Rajagopal P 2016 Shear horizontal feature guided ultrasonic waves in plate structures with 90 transverse bends *Ultrasonics* **65** 370-9
[16] Ramdhas A, Pattanayak R K, Balasubramaniam K and Rajagopal P 2015 Symmetric low-frequency feature-guided ultrasonic waves in thin plates with transverse bends *Ultrasonics* **56** 232-42
[17] Yu X, Fan Z, Castaings M and Biateau C 2017 Feature guided wave inspection of bond line defects between a stiffener and a composite plate *NDT&E Int.* **89** 44-55
[18] Doherty C and Chiu W K 2012 Scattering of ultrasonic-guided waves for health monitoring of fuel weep holes *Struct Health Monit* **11** 27-42
[19] Heinlein S, Cawley P and Vogt T 2018 Reflection of torsional T (0, 1) guided waves from defects in pipe bends *NDT&E Int.* **93** 57-63
[20] Masurkar F and Tse P 2020 Theoretical and experimental evaluation of the health status of a 1018 steel I-beam using nonlinear Rayleigh waves: Application to evaluating localized plastic damage due to impact loading *Ultrasonics* **108** 106036
[21] Zhu H, Ng C-T and Kotousov A 2022 The performance optimization of combinational harmonic generation for quasi-synchronous Lamb wave mixing. In: *Sensors and Smart Structures Technologies for Civil, Mechanical, and Aerospace Systems 2022*: SPIE) pp 293-300

[22] Cheng L, Xin H, Groves R M and Veljkovic M 2021 Acoustic emission source location using Lamb wave propagation simulation and artificial neural network for I-shaped steel girder *Construction and Building Materials* **273** 121706
[23] Wan X, Liu M, Zhang X, Fan H, Tse P W, Dong M, Wang X, Wei H, Xu C and Ma H 2021 The use of ultrasonic guided waves for the inspection of square tube structures: Dispersion analysis and numerical and experimental studies *Struct. Health Monitor.* **20** 58-73
[24] Hughes J M, Mohabuth M, Kotousov A and Ng C-T 2021 The fundamental ultrasonic edge wave mode: Propagation characteristics and potential for distant damage detection *Ultrasonics* **114** 106369
[25] Wilde M V, Golub M V and Eremin A A 2019 Experimental and theoretical investigation of transient edge waves excited by a piezoelectric transducer bonded to the edge of a thick elastic plate *J. Sound Vib.* **441** 26-49
[26] Chen M-I, Tesng S-P, Lo P-Y and Yang C-H 2018 Characterization of wedge waves propagating along wedge tips with defects *Ultrasonics* **82** 289-97
[27] De Billy M and Hladky-Hennion A 1999 The effect of imperfections on acoustic wave propagation along a wedge waveguide *Ultrasonics* **37** 413-6
[28] Osipov A and Norris A 1999 The Malyuzhinets theory for scattering from wedge boundaries: a review *Wave motion* **29** 313-40
[29] Lawrie J B and Kaplunov J 2012 Edge waves and resonance on elastic structures: an overview *Mathematics and Mechanics of solids* **17** 4-16
[30] Feng F, Shen Z and Shen J 2017 Edge waves in a 3D plate: two solutions based on plate mode matching *Mathematics and Mechanics of Solids* **22** 2065-74
[31] Zernov V and Kaplunov J 2008 Three-dimensional edge waves in plates *Proceedings of the Royal Society A: Mathematical, Physical and Engineering Sciences* **464** 301-18
[32] Wilde M V, Golub M V and Eremin A A 2019 Experimental observation of theoretically predicted spectrum of edge waves in a thick elastic plate with facets *Ultrasonics* **98** 88-93
[33] Hughes J M, Kotousov A and Ng C-T 2020 Generation of higher harmonics with the fundamental edge wave mode *Appl. Phys. Lett.* **116** 101904
[34] Hughes J M, Mohabuth M, Khanna A, Vidler J, Kotousov A and Ng C-T 2021 Damage detection with the fundamental mode of edge waves *Struct. Health Monitor.* **20** 74-83
[35] Cerniglia D, Pantano A and Vento M 2012 Guided wave propagation in a plate edge and application to NDI of rail base *J Nondestr Eval.* **31** 245-52
[36] Vien B S, Rose L R F and Chiu W K 2017 Experimental and Computational Studies on the Scattering of an Edge-Guided Wave by a Hidden Crack on a Racecourse Shaped Hole *Materials* **10** 732
[37] Zhu H, Ng C T and Kotousov A 2023 Fatigue crack detection in edges of thin-walled structures with corners using the fundamental mode of edge waves *Ultrasonics* **132** 106995
[38] Chu J Y H and Courtney C R 2021 The Detection of Impact Damage to the Edges of CFRP Plates Using Extensional Ultrasonic Edge Waves *J Nondestr Eval.* **40** 1-12
[39] Yu X, Zuo P, Xiao J and Fan Z 2019 Detection of damage in welded joints using high order feature guided ultrasonic waves *Mech. Syst. Signal. Process.* **126** 176-92
[40] Yu X, Qin R and Deng M 2021 New insights into topographically feature guided waves (FGW) propagation in non-uniform elastic waveguides *Wave Motion* 102866
[41] Ramdhas A, Pattanayak R K, Balasubramaniam K and Rajagopal P 2013 Antisymmetric feature-guided ultrasonic waves in thin plates with small radius transverse bends from low-frequency symmetric axial excitation *J. Acoust. Soc. Am.* **134** 1886-98

[42] Nie G, Dai B, Liu J and Zhang L 2021 Bending waves in a semi-infinite piezoelectric plate with edge coated by a metal strip plate *Wave Motion* **103** 102731
[43] Norris A, Krylov V and Abrahams I 2000 Flexural edge waves and Comments on "A new bending wave solution for the classical plate equation"[J. Acoust. Soc. Am. 104, 2220–2222 (1998)] *J. Acoust. Soc. Am.* **107** 1781-4
[44] Feng F, Shen Z and Shen J 2016 Scattering of obliquely incident waves by straight features in a plate *Wave Motion* **60** 84-94
[45] Kaplunov J, Pichugin A and Zernov V 2009 Extensional edge modes in elastic plates and shells *J. Acoust. Soc. Am.* **125** 621-3
[46] Pavlakovic B and Lowe M 2003 Disperse Software Manual Version 2.0. 1 6B *Imperial College, London, UK*
[47] Cherednichenko K 2007 An asymptotic expansion of the boundary-layer type for flexural waves along the curved edge of a Kirchhoff-Love elastic plate *Journal of Mathematical Sciences* **142** 2682-8
[48] Predoi M V, Castaings M, Hosten B and Bacon C 2007 Wave propagation along transversely periodic structures *J. Acoust. Soc. Am.* **121** 1935-44
[49] Zuo P, Yu X and Fan Z 2017 Numerical modeling of embedded solid waveguides using SAFE-PML approach using a commercially available finite element package *NDT&E Int.* **90** 11-23
[50] Zuo P and Fan Z 2017 SAFE-PML approach for modal study of waveguides with arbitrary cross sections immersed in inviscid fluid *J. Sound Vib.* **406** 181-96
[51] Kaplunov J and Nobili A 2017 The edge waves on a Kirchhoff plate bilaterally supported by a two-parameter elastic foundation *Journal of Vibration and Control* **23** 2014-22
[52] Pichugin A and Rogerson G 2012 Extensional edge waves in pre-stressed incompressible plates *Mathematics and mechanics of solids* **17** 27-42
[53] Krushynska A 2011 Flexural edge waves in semi-infinite elastic plates *J. Sound Vib.* **330** 1964-76
[54] Soleimanpour R, Ng C-T and Wang C H 2017 Higher harmonic generation of guided waves at delaminations in laminated composite beams *Struct. Health Monitor*. **16** 400-17
[55] Mei H and Giurgiutiu V 2019 Guided wave excitation and propagation in damped composite plates *Struct. Health Monitor*. **18** 690-714
[56] Allen J C P and Ng C T 2022 Debonding detection at adhesive joints using nonlinear Lamb waves mixing *NDT&E Int.* **125** 102552

Chapter 6

Investigation of fatigue crack closure effects on the evaluation of edge cracks with the fundamental mode of edge waves

Manuscript (Submitted)

Statement of Authorship

Title of Paper	Evaluation of fatigue cracks using the fundamental mode of edge waves
Publication Status	☐ Published ☐ Accepted for Publication ☑ Submitted for Publication ☐ Unpublished and Unsubmitted work written in manuscript style
Publication Details	

Principal Author

Name of Principal Author (Candidate)	Hankai Zhu		
Contribution to the Paper	Conceptualization, Methodology, Experiment, Finite Element simulation, Validation, Formal analysis, Writing – original draft and editing.		
Overall percentage (%)	85%		
Certification:	This paper reports on original research I conducted during the period of my Higher Degree by Research candidature and is not subject to any obligations or contractual agreements with a third party that would constrain its inclusion in this thesis. I am the primary author of this paper.		
Signature		Date	23/10/2023

Co-Author Contributions

By signing the Statement of Authorship, each author certifies that:

i. the candidate's stated contribution to the publication is accurate (as detailed above);

ii. permission is granted for the candidate in include the publication in the thesis; and

iii. the sum of all co-author contributions is equal to 100% less the candidate's stated contribution.

Name of Co-Author	Andrei Kotousov		
Contribution to the Paper	Supervision, Advising, Writing – review and editing.		
Signature		Date	7 Nov 2023

Name of Co-Author	Ching-Tai Ng		
Contribution to the Paper	Supervision, Advising, Writing – review and editing.		
Signature		Date	6 Nov 2023

Chapter 6: Investigation of fatigue crack closure effects on the evaluation of edge cracks with the fundamental mode of edge waves

Hankai Zhu[1], Andrei Kotousov[2,*], Ching Tai Ng[1]

[1] School of Architecture and Civil Engineering, The University of Adelaide, Adelaide, SA 5005, Australia

[2] School of Electrical and Mechanical Engineering, The University of Adelaide, Adelaide, SA 5005, Australia

Abstract

Fatigue cracks often initiate and propagate from edges of structural components. Detection and evaluation of edge fatigue cracks could be very challenging, specifically, due to the crack closure phenomenon, which makes fatigue cracks to be partially closed when the applied loading is removed. The latter condition usually corresponds to maintenance and defect inspections. Despite that fatigue crack closure is well investigated, past experimental and theoretical studies related to guided wave-based NDEs largely ignored this phenomenon. In this article, the fundamental symmetric mode of edge waves (ES_0) is used to evaluate crack closure effects on the evaluation of fatigue cracks with ES_0 wave mode. The experimental studies have demonstrated that the reflected and transmitted signals at different frequencies correlate very well with the length of the open region of fatigue cracks. However, an accurate evaluation of the total crack length can only be conducted under applied load, which fully separates the crack faces. Finally, a new FE model has been proposed to simulate the fatigue crack closure and its effects on propagation of guided waves. The outcomes of FE modelling and experimental study were found in a good agreement.

Keywords: Edge waves, fatigue cracks, crack closure phenomenon, FE modelling, NDE

6.1. Introduction

Non-destructive fatigue crack detection and evaluation is critical for the efficient and safe operation of hazard structures, in particular, the structures working under cyclic loading. Non-destructive evaluation (NDE) of fatigue cracks may be very challenging due to many reasons. One of these reasons is the crack closure phenomenon, which results that only a part of the fatigue crack, say about fifty percent, is open and free from contact stress when the applied load is removed [1-6]. The latter condition usually corresponds to maintenance and non-destructive inspection conditions across many structural components.

Recently, nonlinear ultrasonic guided waves have attracted significant attention for non-destructive defect evaluation (NDE) purposes due to their good sensitivity to small-scale fatigue damage [7-10]. The wave-crack interactions can lead to, so-called, contact acoustic nonlinearity (CAN) resulting in a nonlinear response to a harmonic excitation. Various non-linear effects associated with the CAN have been utilised in order to develop baseline-free NDE techniques for different types of structures, including thin-walled plates or shells [11-13] and pipes [14]. The past studies showed that the interaction between fatigue cracks and different ultrasonic guided wave modes is very complex [15-17], and also indicated that fatigue cracks can generate both linear [18-20] and nonlinear [15, 16] characteristic response signatures for each of these guided wave modes. These signatures have been investigated for Lamb and shear waves (i.e., S_0 and SH_0 wave modes). In particular, it was found that the nonlinear signatures are much more sensitive to the presence and severity of fatigue cracks than the linear counterparts [17, 21, 22]. Two common parameters are often used in NDE based on nonlinear guided wave signatures, which are the relative nonlinear parameter and the nonlinear index. However, it was difficult to relate these parameters to the severity of fatigue cracks i.e., the fatigue crack length in the case of plate or shell components [21-24].

The nonlinear wave response of fatigue cracks due to the CAN is influenced by the amplitude of the excitation and crack orientation with respect to the incident wave. In addition to the above factors, the wave response can also be affected by the partial crack closure; this will be explained next. Due to the high stress concentration the propagating fatigue crack generates wake of plasticity behind its tip leading to the crack closure phenomenon. The formation of the plastic wake and the level of closure are both affected by the cyclic loading conditions, e.g., load ratio or amplitude of the cyclic loading, as well as material and fatigue properties. Crack closure, in particular, implies that a significant part of the fatigue crack

remains closed when the applied load is removed and a certain load needs to be applied to fully separate the crack faces or open the crack. This phenomenon was first discovered by Wolf Elber in 1970 during his PhD candidature at the University of New South Wales [1]. Since this discovery, it was extensively investigated over the past fifty years because of the very important role that this phenomenon plays in fatigue life of structural components [2, 3, 6]. However, the fact that fatigue cracks are partially closed during NDEs was largely ignored in non-liner guided wave research. Although, this phenomenon has been pointed as a main contributing factor to the failure to detect or correctly evaluate the severity of fatigue damage during traditional ultrasonic inspections [23, 25, 26]. Subsequently, the current paper is aimed to experimentally and numerically investigate the effects of the partial crack closure on the evaluation of fatigue cracks with nonlinear guide waves.

Free edges and surfaces of engineering structures are of particular concern from the structural integrity point of view as fatigue failures often initiate from edges or manufacturing defects associated with the fabrication of these edges. Detection and evaluation of edge cracks are difficult with conventional guided wave modes e.g., Lamb and shear waves due to reflections and scattering from the edge. In particular, the reflections and wave scattering may result in the mode conversion, which can significantly complicate the interpretation of the acquired wave signals. However, free edges of the plate and shell structural components can also serve as waveguides, which permit the propagation of feature-guided waves, such as edge waves [13, 27-29]. The fundamental symmetric mode of edge waves (ES_0) has demonstrated several advantages compared to the conventional Lamb and shear waves. These advantages include long propagation distances with almost no energy decay, and no or little influence of the interior structures on the wave propagation as the edge waves are largely concentrated near the free surface. In addition, the ES_0 mode is non-dispersive, which significantly simplifies the signal processing as well as interpretation. These advantages make the ES_0 mode promising for the purpose of NDEs, especially for structures with complex geometries and having inaccessible locations. The ES_0 mode has been applied to detect corrosion damage in I-beams [30], cracks [31, 32], and early-fatigue damage [33]. These studies have demonstrated that the ES_0 mode is quite sensitive to all considered types of structural damage. This guided wave mode will be utilised in the current study.

Together with extensive experimental studies on the interactions of guided waves with fatigue cracks, Finite Element (FE) simulations of linear and nonlinear guided wave phenomena have been conducted by many researchers to assist with the development of

experimental methods and NDE techniques. The previous studies usually idealised a fatigue crack as a straight seam crack and its interaction with the incident waves by the clapping (breathing) behaviour. The latter implies that the crack is fully opened in the tensile part of the incident wave and fully closed in the compressive part [34-36]. Meanwhile, several articles considered more realistic scenarios and fatigue crack behaviour, e.g., curved cracks [37], 3D cracks [16, 17], and cracks subjected to vibration excitations [38]. However, it seems there were no computational studies addressing one of the one of the most important features of actual fatigue cracks, which is its partial closure. The shortcomings of the previous studies and a limited progress so far in modelling this phenomenon warrant for further investigations of nonlinear wave phenomena associated with more realistic representations of fatigue cracks in numerical simulations.

The present paper is organised as follows. Section 2 presents the overview of the fundamental mode of edge waves, or the ES_0 mode, providing the dispersion curves, modal displacement profiles, as well as penetration depths as a function of the excitation frequency. The details and outcomes of the experimental studies are described in Section 3. In Section 4, a new FE model, which is the one of main outcomes of this article, is developed to simulate the behaviour of a partially closed fatigue crack. The new model is validated against the experimental studies. Finally, the conclusions are drawn in Section 5.

6.2. Fundamentals of edge waves

The purpose of this section is to present the fundamentals and wave characteristics of ES_0 mode, the fundamental symmetric mode of edge waves. This wave mode is concentrated near the free edge, and therefore it can be utilised for the evaluation of the fatigue cracks near the free edge. The dispersion curve and the modal displacement profiles were investigated by the previous articles [27, 39, 40] using semi-analytical methods. The outcomes are normally presented in terms of the frequency thickness values (FTV = $\omega 2h/c_2$), where ω is the angular frequency, $2h$ is the thickness of the plate, and c_2 is the shear wave speed. The dispersion curves are shown in Fig. 6.1a. It can be noted that the ES_0 mode is slightly dispersive over the entire FTV range, which indicates that the quasi-synchronism (phase velocity matching needed for the second harmonic generation) can be achieved [41]. The wave speed of the ES_0 mode approaches the Rayleigh wave at the very low values of FTV (FTV << 1, e.g., for very thin plates), while the wave properties (wave speeds and displacement profiles) of the fundamental

edge wave approach to those of the wedge wave in the high FTV range (i.e., FTV > 8). Experimental studies [13, 33] also indicate that the generation of the ES_0 mode is always coupled with other wave modes, i.e., coupling with SH_0 and S_0 in the low FTV range (FTV < 4), and coupling with higher order Lamb wave modes when FTV > 6. It was also found that the fundamental edge wave in the high FTV range has a large decay due to the coupling with the higher order Lamb wave modes and energy leak to these modes. These characteristics of the fundamental edge waves make the FTV selection quite critical for practical applications. Subsequently, based on the previous research, the FTV range in the present study was selected as follows: 1 < FTV < 4.

In this work, a Semi-Analytical Finite Element (SAFE) model with a perfectly matched layer (PML) was developed to investigate the wave characteristics of the ES_0 mode. The detail of the SAFE model is not presented here for the sake of brevity, and the details could be found in our previous article [32]. The SAFE calculations showed an excellent agreement with the semi-analytical results [27, 39] (see Fig. 6.1b). The effect of FTV variations on the modal displacement profiles is further investigated based on the SAFE model. The coordinate system is shown in Fig. 6.4 in Section 3 ahead, where the x_1-coordinate is along the depth direction of the plate and perpendicular to its free surface.

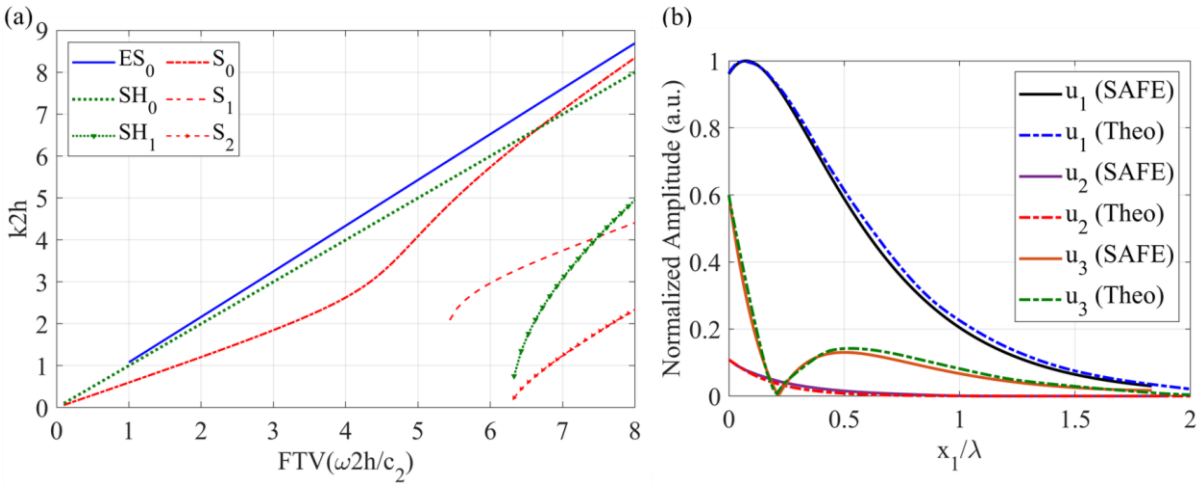

Figure 6.1. (a) Dispersion curves of edge wave modes [27, 39] along with other wave modes as calculated using software package DISPERSE [42], and (b) modal displacement profile of ES_0 mode, at FTV=1

In Fig. 6.2a, the wavelength of ES_0 mode for a plate ($2h$ = 3 mm) as a function of the FTV is plotted. The modal displacement profiles calculated using the SAFE model were normalized by the corresponding wavelengths (see Fig. 6.2b). Fig. 6.2b shows that the ES_0 mode is concentrated near the free surface and decays within one wavelength in the depth direction (x_1). It can be also noted that the FTV values have no effect on the wave decay. Because of this feature, the interior region has almost negligible influence on the propagation of the ES_0 mode.

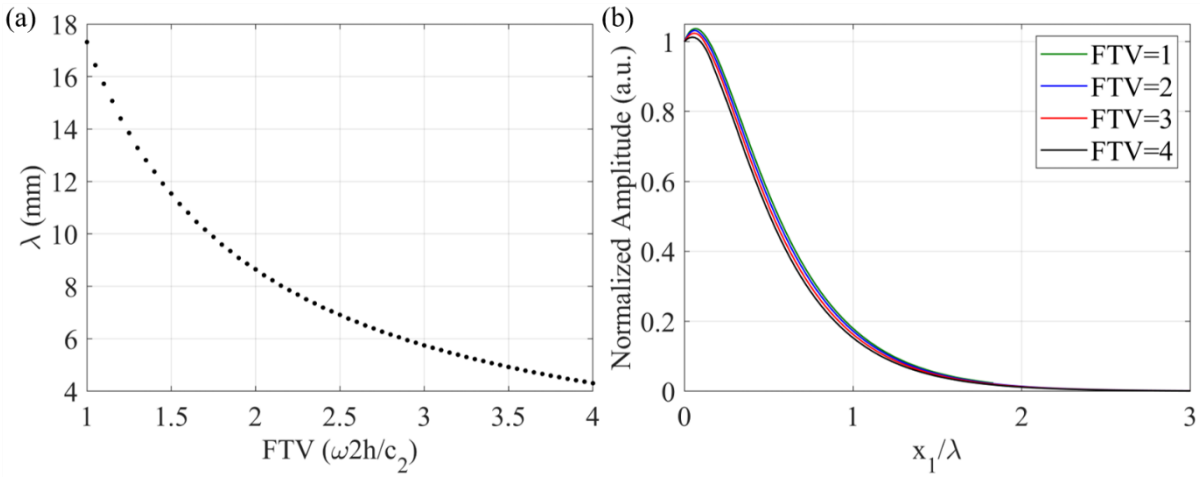

Figure 6.2. ES_0 mode wave properties (a) wavelength against FTVs and (b) modal displacement profiles in x_1-direction with different FTVs

6.3. Experimental studies

In Section 3.1, the fabrication of the test specimen with a high-cycle fatigue crack is described. The details of the experimental setup for guided wave testing are provided in Section 3.2, and the experimental results are presented in Section 3.3.

6.3.1. Test specimens

The fabrication of the sample weakened by high-cycle fatigue cracks is briefly presented in this sub-section. Two specimens were cut from an airspace grade aluminium alloy plate of 3mm thickness for further testing. Specimen 1 has a 5 mm diameter circular hole, and two starter notches of 0.35 mm width and length, see Fig. 6.3. The sinusoidal cyclic tensile loading with 10 Hz frequency was applied to the specimen using INSTRON 1432 to initiate fatigue cracks from the starter notches. The maximum tensile stress was 50 MPa, which is

approximately 45% of the yield stress. The stress ratio, R (the ratio of the minimum to maximum stresses in the load cycle), was 0.1. The specimen was subjected to one million fatigue cycles. The final fatigue crack length (l) was approximately 25 mm. The starter notch and the hole were removed after the cyclic loading to form the edge crack as shown in Fig. 6.3.

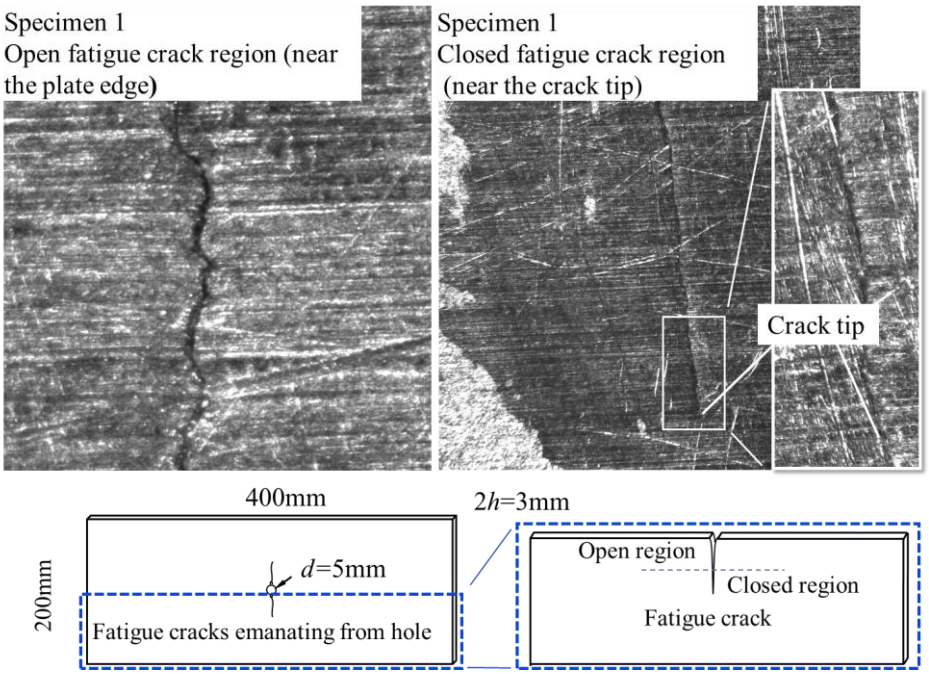

Figure 6.3. Microscope images of the fatigue crack in Specimen 1 at different locations along the crack

A micro-examination revealed two characteristic regions along the fatigue crack: one is near the free surface (free edge), which is open; and the second, which is closed spreading all way to the crack tip. As mentioned in the Introduction, this experimental observation is well-known in fatigue area and associated with the plasticity-induced crack closure, the phenomenon first discovered by Elber [1]. The faces of the crack in the closed region are in contact and slightly separated due to the surface roughness; while the separation in the first region is much larger and the crack faces seem to be not in contact. Specimen 2 and its loading conditions were identical to Specimen 1. However, the cyclic loading was interrupted at 0.67 million fatigue cycles when the crack length reached 5 mm.

6.3.2. *Experimental setup for guided wave testing*

The experimental setup for the guided wave testing is shown in Fig. 6.4. A 12-cycle Hann-windowed tone-burst was generated using a signal generation module (NI PXIe-5122), and the generated signal was amplified by an amplifier (CIPIAN HVA-800A) with 100V peak-to-peak voltage. The input was transmitted to the transducer (ULTRAN-GC500) to generate the wave excitation, and the transducer was coupled with a pixel wedge to maximize the generation of ES_0 mode. The wedge angle was 52-degree considering the wave speed of the wedge material (c_w = 2300 m/s) and Snell's law. The acoustic coupling (high vacuum grease) was applied between the transducer and the specimen to ensure the stable excitation of the guided edge waves. The 3D-printed alignment device was used to apply a clamping force on the pixel wedge. The first measurement point (P_1) was located 50 mm away from the excitation wedge, and the distance interval between the remaining measurement points was approximately 50 mm. The displacement (i.e., normal to the x_2-x_3 plane) was measured using a 1D laser vibrometer, which was synchronized with the acquisition system (PSV-400) and the signal generation module. The received signal was averaged 1000 times, and a low-pass filter with 1200 kHz was enforced to mitigate the high-frequency noise and improve the sign-to-noise ratio. The time step of the signal was 39.06 ns, and the sampling rate was 25.6 MHz.

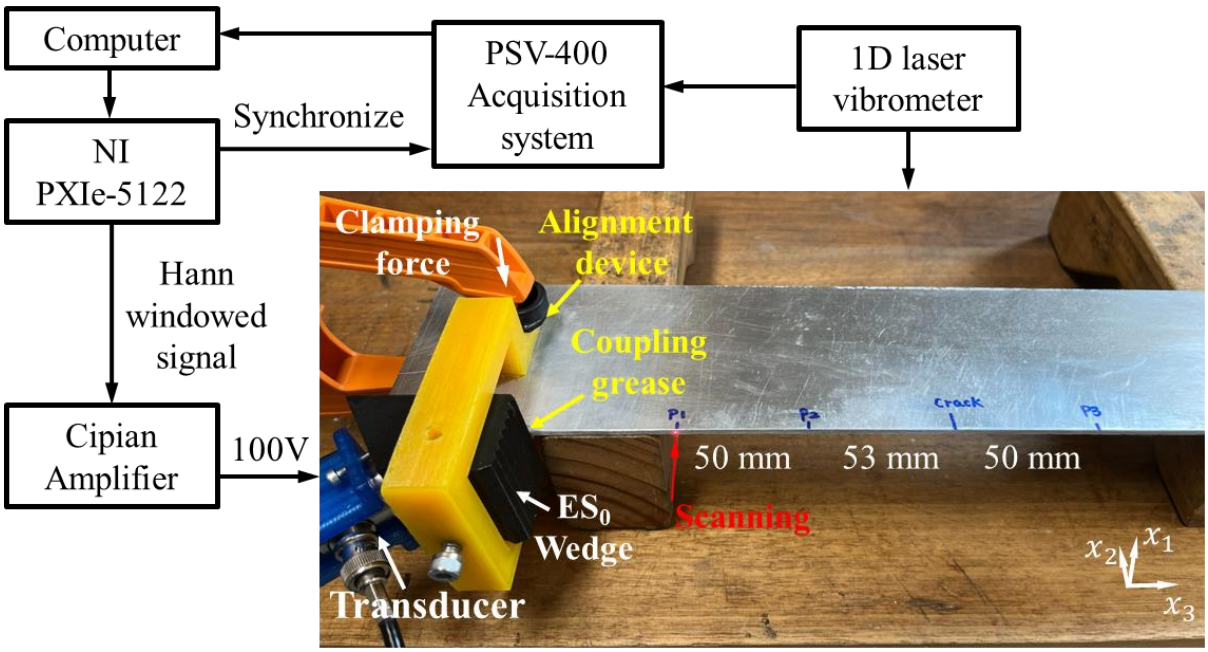

Figure 6.4. Experimental setup

6.3.3. Experimental results

A non-damaged plate with sharp edges was used to validate the experimental method of the generation of the fundamental edge waves. In Fig. 6.5, the group velocities of the ES_0 mode with different FTV values were calculated, and these experimental values show a good agreement with the theoretical predictions [27, 28, 43] reported previously. This agreement provided confidence in the experimental method, which was used for further investigations.

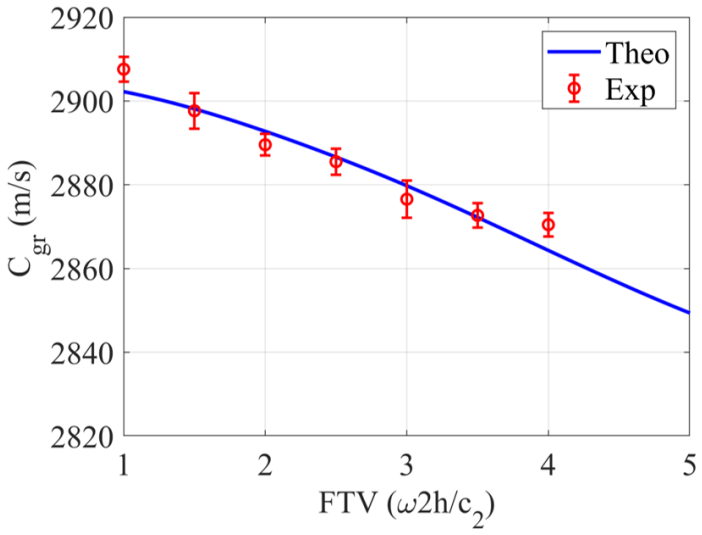

Figure 6.5. Wave velocity of the ES_0 mode against FTVs

In the case of Specimen 1, the length of the fatigue crack (l = 25 mm) was more than three wavelengths for the selected range of FTV values. Because of the localisation of the ES_0 mode within one wavelength near the free edge, the fatigue crack blocks the direct transmission of the edge wave signal.

Figs. 6.6a – 6.6c show the time domain of the reflected and transmitted signals at different measurement points as specified in Fig. 6.4 as well as the transmission and reflection wave ratios as a function of the FTVs shown in Fig. 6.6d. Fig. 6.6a also shows the non-linear component of the signal obtained using the phase reversal approach [10], where u_0 and u_{180} correspond to the phase signal shifted by 180 degrees. This approach has been widely utilised in past studies to enhance the characterisation of weak material nonlinearities using the second-order harmonic, while the influence of the fundamental and the third-order harmonics is suppressed by the signal substruction.

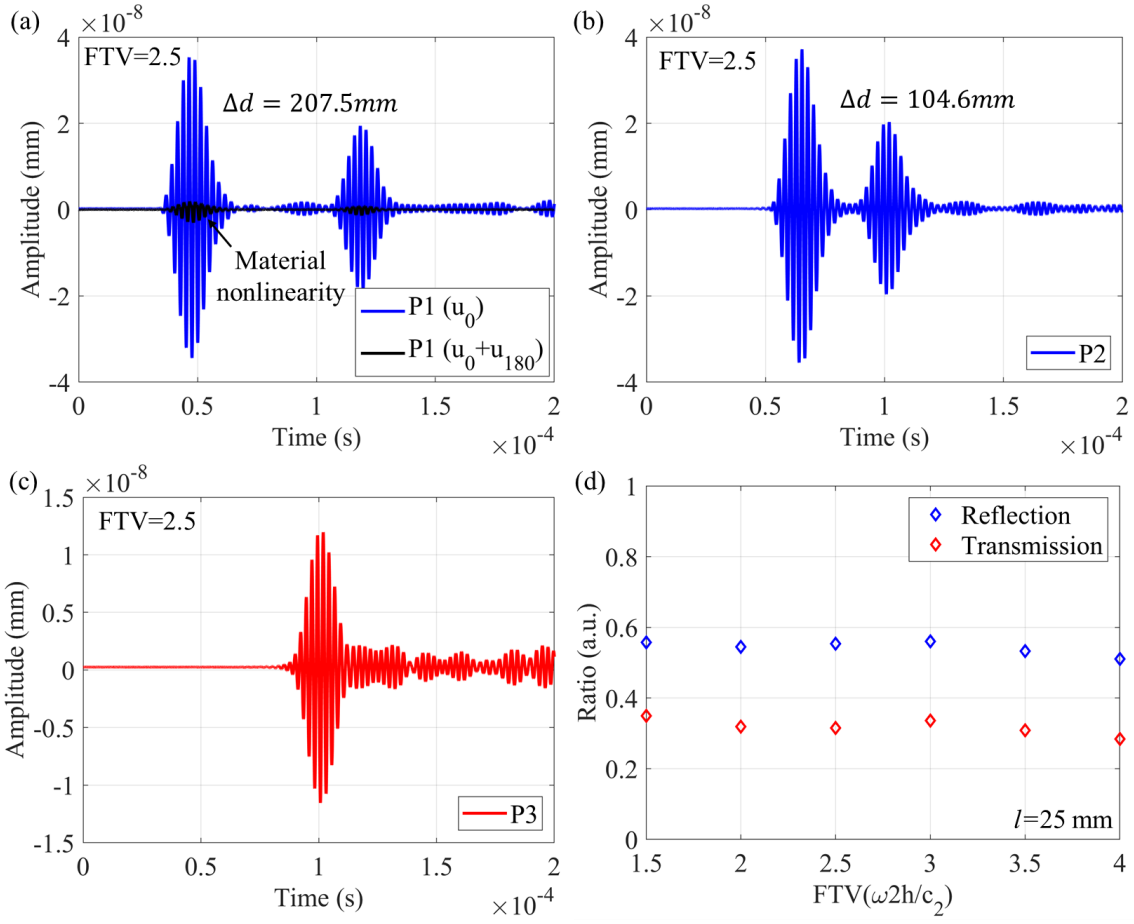

Figure 6.6. Time domain signal for fatigue crack of 25 mm length, at points (a) - 1, (b) - 2, (c) - 3, see Fig. 6.4 for location of these points and (d) transmission and reflection wave ratios as a function of the FTVs.

The results presented in Fig. 6.6 indicate that fatigue cracks have much stronger effects on the propagation of the ES_0 mode than the conventional Rayleigh-Lamb waves [16, 44]. Therefore, fatigue cracks can be detected and evaluated using the linear wave features of the reflected and transmitted signals generated by the incident ES_0 mode. For example, the distance between the measurement points and the fatigue crack location can be calculated using the reflection signal shown in Figs. 6.6a and 6.6b, which are 103.75 mm (between the crack and P1), and 52.3 mm (for P2), respectively. The evaluated distances match very well with the actual fatigue crack location. Results presented in Fig. 6.6c indicate that the edge waves can propagate through the fatigue crack. Different FTVs were applied in testing, and the results show a very limited difference in the reflection and transmission ratios as shown in Fig. 6.6d, with approximately 55% of the incident waves composes of the reflected signal. The possible explanation for the relatively large transmission ratio at small wavelengths is the ability of edge

waves to propagate through sharp edges and corners, which was demonstrated in our previous study [13].

The linear response of the ES_0 mode was then utilised for the quantitative evaluation of the fatigue crack length. The edge of the plate with fatigue crack was gradually machined to change the crack length and further investigate the sensitivity of propagation of ES_0 mode at different crack lengths. The ES_0 mode depth penetration is related to the wavelength and for large cracks, the incident signal is fully blocked by the crack and the edge wave travels along the open crack faces to form the transmission signal. The reflection ratio decreases if the wavelength is more than the fatigue crack length. This is because the crack can reflect only a proportion of the incident waves and the rest of the wave can propagate further without being blocked by the crack. For non-dispersive waves, one would expect that the reflection ratio reaches the maximum when the wavelength approaches the crack length, and this maximum ratio should remain the same when the wavelength further decreases (see Fig. 6.6d). The experimental results indicate that the transmission ratio increases with the increase of the wavelength, when the wavelength is larger than the crack length. These phenomena can be explained by a slight dispersion of the ES_0 mode at FTVs > 3.5. The dispersion can slightly influence the results of the transmission and reflection ratios evaluation in the higher range of FTV values.

In Figs. 6.7a and 6.7b show results for Specimen 1, which was machined to reduce the length of the crack to 10 mm. The reflected waves reached the maximum ratio at FTV = 2.25, and this ratio was maintained the same with the further increase of the FTVs. The wavelength corresponding to the maximum reflection ratio (or FTV = 2.25) is 7.69 mm, which is very close to the actual fatigue crack length (10mm). Therefore, the crack length can be evaluated using FTVs at which the transmission ratio reaches maximum or at the point where the growth of the transmission ratio changes to plateau.

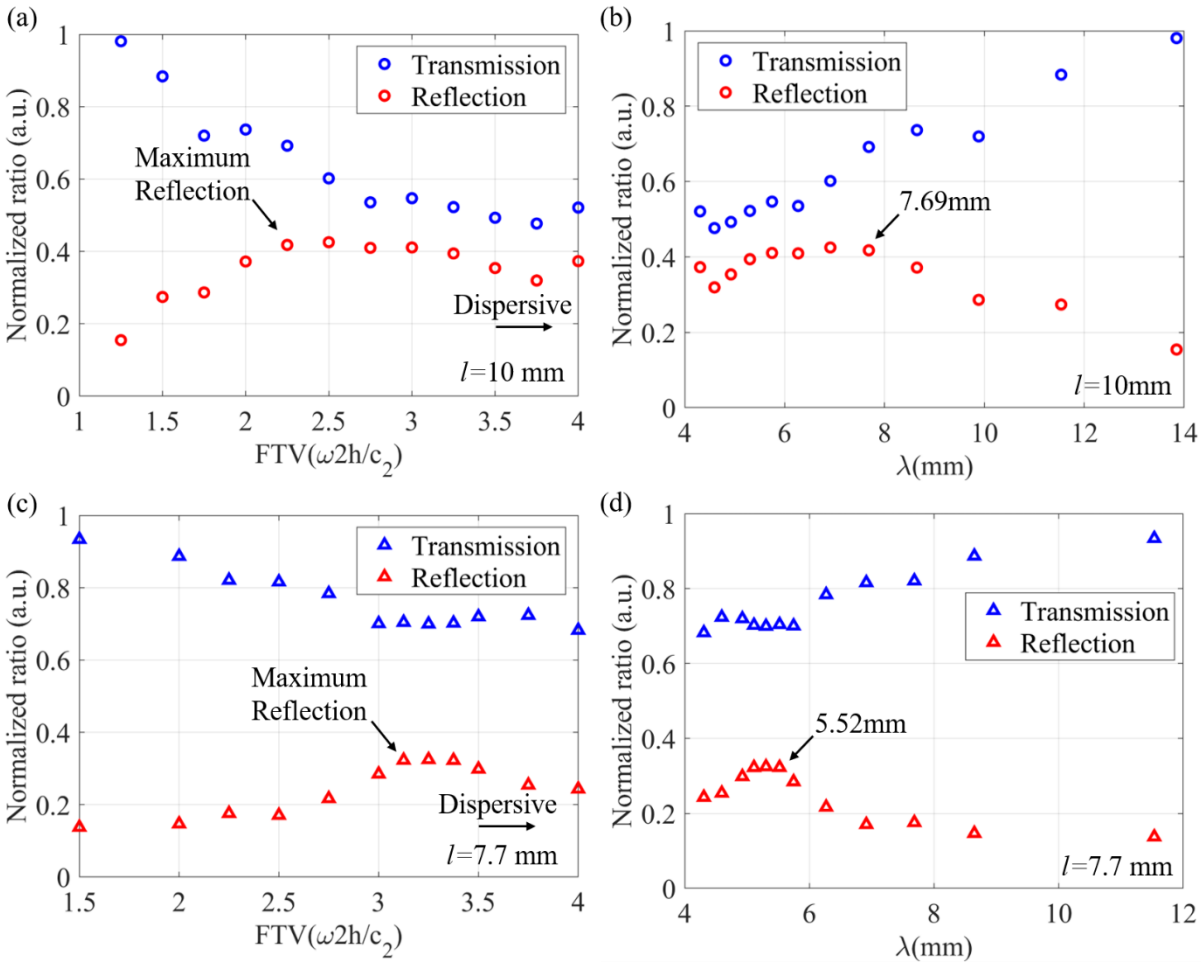

Figure 6.7. Transmission and reflection wave ratio (normalized by the incident wave) with different fatigue crack lengths, (a) and (c) against FTVs, and (b) and (d) against wavelengths

Specimen 1 was further machined to further reduce the crack length to 7.7 mm. The results in Figs. 6.7c and 6.7d show that the maximum reflection ratio corresponds to FTV = 3.125, and the corresponding wavelength is 5.52 mm. These values are in agreement with the results shown in Fig. 6.7b, while the actual crack length is larger by 2.2 mm, very similar to the previous case of 10 mm crack. The presented results along with the previous studies [20, 21], which utilised a nonlinear approach, indicate that the length of the fatigue cracks are likely to be underestimated due to the crack closure phenomenon as described in the Introduction.

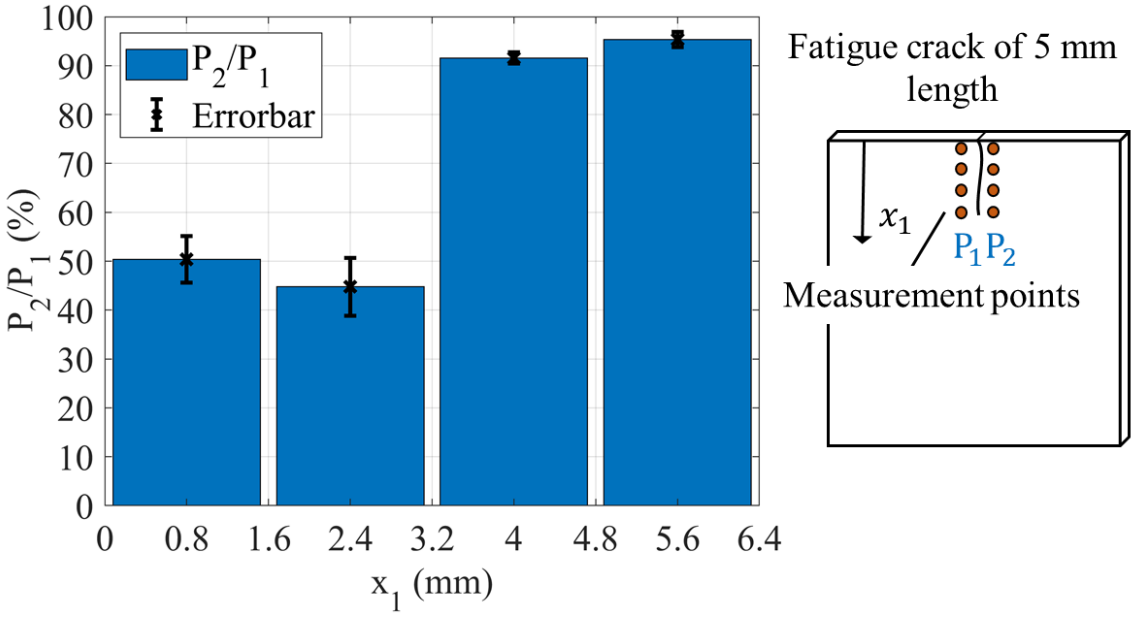

Figure 6.8. Transmitting wave displacement normalized by emitting wave displacement at different measurement points of Specimen 2, using FTV=2

Specimen 2 was used to further investigate the effect of the opening and closure of the fatigue crack and its interaction with the edge waves. The out-of-plane displacement (x_2-direction, see Fig. 6.4) was measured on both sides of the fatigue crack as illustrated in Fig. 6.8. The distance between the two measurement points on the opposite sides is approximately 3.5 mm, which is smaller than the half of the wavelength (λ = 8.65 mm) to ensure that the corresponding measurements are in the same phase of the incident wave. The vertical distance between points is approximately 1.6 mm. This represents the minimum distance that can be used due to the limitations associated with the radius of the laser beam of the Scanning Laser Vibrometer, which was utilised for experimental measurements. The results in Fig. 6.8 show that the opposite points display significant differences in the displacements near the free surface (or x_1 < 3.2 mm); while quite consistent displacements below 3.2 mm in depth direction (or near the tip of the crack). This indicates that the fatigue crack near the tip is tightly closed, and the incident edge wave is unable to open the closed part of the crack. This finding agrees well with the results as presented in Fig. 6.7, which underestimate the length of fatigue crack due to the crack closure phenomenon. The fundamental outcome of these experimental study is a demonstration of the effect of the crack closure on the evaluation of the size of fatigue crack

using guided waves and the deficiency of the breathing crack assumption, which is often utilised in numerical studies on guided wave interactions with fatigue cracks.

6.4. Finite Element simulation

To support and validate the outcomes of the experimental studies a new FE model, which incorporates the partial crack closure effects, was developed and discussed in this Section. This Section also presents the outcomes of the simulations of more realistic crack behaviour, which takes into account the crack closure phenomenon as well as the outcomes of the conventional (or breathing crack) modelling [26, 36, 38]. The results are also obtained for different levels of pre-stresses, which change the crack opening.

6.4.1. FE model

A 2D FE model was developed in ABAQUS/Explicit to simulate the wave interaction with the partially closed crack. The material properties are listed in Table 6.1. The plate model as shown in Fig. 6.9 has 300 mm length and 150 mm width. A seam crack with a length of 5 mm (l = 5 mm) is simulated with the build-in function 'seam crack', and the surface-to-surface contact between the interfaces is applied. The hard contact of normal behaviour and frictional tangential contact with a stiffness coefficient of 1.5 were assigned to the seam crack. The previous studies [26, 36, 38] have shown that the seam crack can successfully simulate the interaction between the Lamb waves and fatigue crack. The element size of 0.1 mm was selected to ensure more than 15 elements per wavelength, and the seam crack area is refined with the mesh size of 0.01 mm. Four-node bilinear plane strain quadrilateral with reduced integration (CPE4R) was used in the FE model.

Table 6.1. Material properties

Material	ρ (kg·m^{-3})	E (GPa)	ν	Expansion Coefficient
Al-6061	2704	72	0.333	2.34E-005

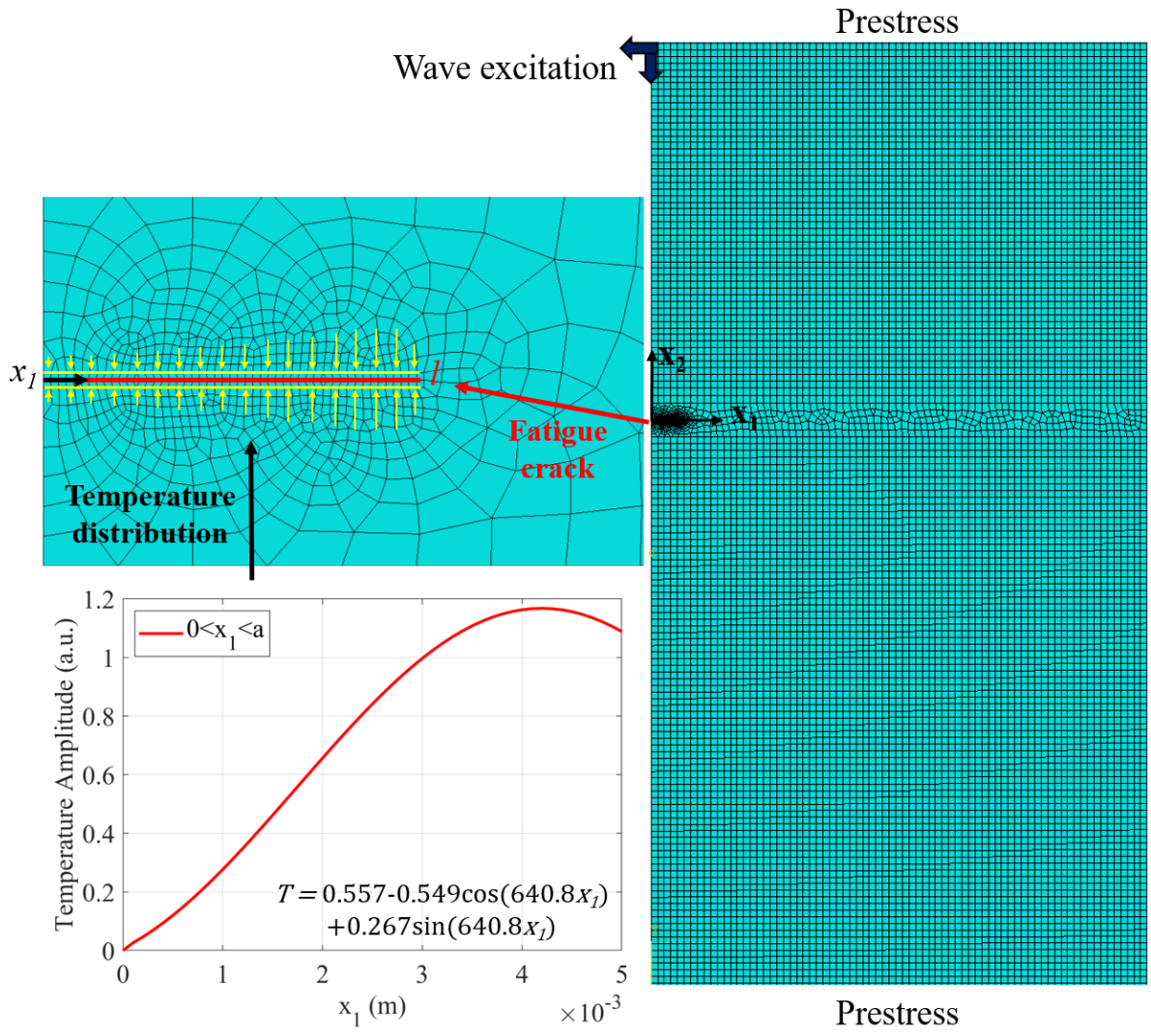

Figure 6.9. FE model with mesh and the temperature distribution profile.

A fictitious temperature distribution, which results in a local thermal expansion, was applied to the adjacent area of the seam crack (0.01 mm distance interval as shown in Fig. 6.9). This temperature distribution is used to simulate the plastic wake and partial closure of fatigue cracks. The temperature distribution was prescribed in the predefined field at the initial stage of FE simulations before the next wave excitation stage. The analytical field of temperature distribution used for the proposed seam crack is shown in Fig. 6.9 with an amplitude of 1000 Kelvins. The analytical field was determined using the trial-and-error method based on the experimental results and the quasi-static response of fatigue cracks to the applied loading. The displacement amplitude of the wave excitation is 10 μm in the x_1-direction and 6 μm in the x_2-direction, which are based on the edge wave characteristics as shown in Fig. 6.1b. The pre-

stress can be applied on the plate and will be further investigated in the next section, and the pre-stress is applied in the initial stage if needed.

6.4.2. Partially closed crack

In Fig. 6.10, the numerical results are validated against the experimental results, which show a good agreement, and partially validate the proposed fatigue crack modelling approach. The comparison between the newly developed FE model and the conventional model is presented in Fig. 6.11. The fatigue crack is partially closed under the tensile part of the incident waves in the new model (see Fig. 6.11a), while the seam crack is fully opened in the conventional model (see Fig. 6.11c). In contrast, under the compressive part of waves, the fatigue crack is partially opened in the new model (see Fig. 6.11b), while the seam crack is fully closed in the conventional (breathing crack) model (see Fig. 6.11d). The developed FE model can better describe the realistic fatigue crack behaviour when interacting with the guided waves, which is consistent with the previous theoretical and experimental studies [20, 45].

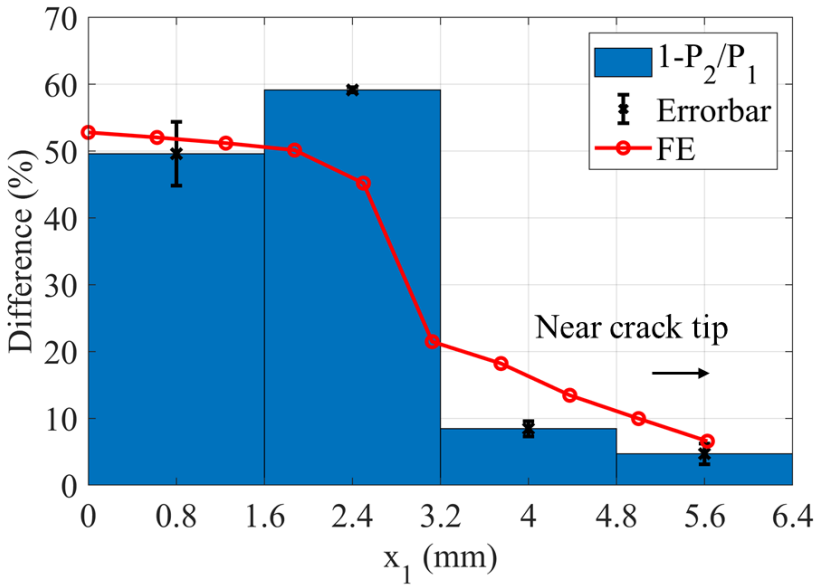

Figure 6.10. FE model validation, with fatigue crack length of 5 mm, using FTV=2

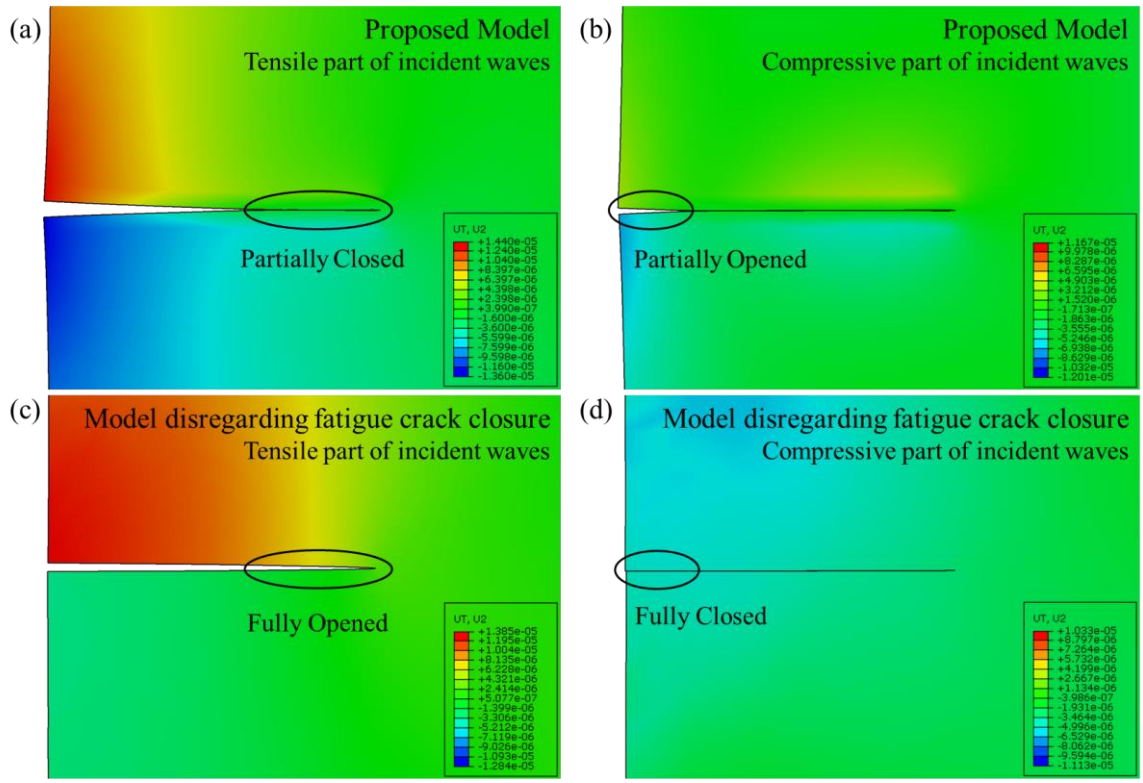

Figure 6.11. Comparison of the crack profile under tensile/compressive part of incident waves between the new FE model and the conventional FE model, which disregards fatigue crack closure effects.

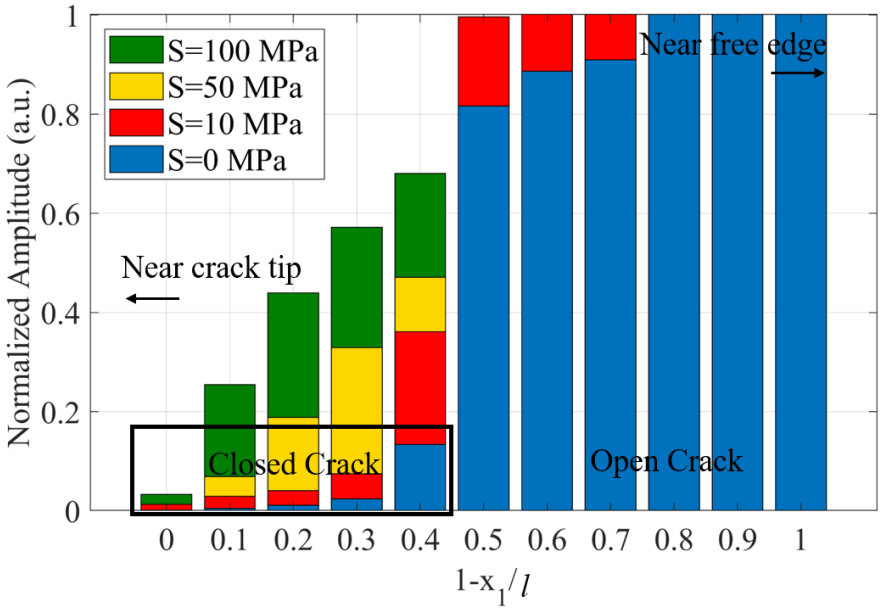

Figure 6.12. Effect of pre-stress on the partially closed crack

The different tensile pre-stress levels are applied to the developed FE model, from 0 MPa to 100 MPa, to investigate the effect of tensile pre-stress on the opening and closure of the fatigue crack. The difference between the two groups of measurement points ($1-P_2/P_1$) defined in the previous Section, Fig. 6.8, is shown in Fig. 6.12, the pre-stress level significantly affects the crack opening and closure as well as the wave interactions. The increase of tensile pre-stress leads to a larger opening area of the crack near the crack tip area (i.e., less crack closure length), and this result agrees well with the previous investigations [36, 45]. The results indicate that the applied loading is necessary for the accurate evaluation of the length of fatigue cracks. However, in practice it may be quite difficult to apply this loading during NDE inspections.

6.5. Conclusion

In conclusion, the developed experimental method, which is based on the maximum/minimum transmission/reflection ratios, is suitable for the quantitative evaluation of the fatigue crack length. The results show that the ES_0 mode is very sensitive to the fatigue cracks, and the linear responses of ES_0 mode due to the interaction between edge waves and the fatigue crack is significantly larger than the conventional Lamb and shear waves. The fatigue crack length can be estimated by sweeping the different FTVs, and the fatigue crack length is directly associated with the wavelengths. However, the present study also demonstrates that the fatigue crack length may be underestimated using the linear wave approach, similar to other published outcomes [20, 21], which utilised a nonlinear approach. Further investigation shows that the fatigue crack near the tip has negligible interaction with the ES_0 mode. In contrast, the part of the fatigue crack near the free edge shows a significant influence on the both transmission and reflection ratios.

It is also demonstrated that to accurately simulate the linear wave responses of fatigue cracks the modelling approaches must take into account the crack closure phenomenon. The clapping mechanism and breathing crack idealisations seem to be not appropriate assumptions for the simulation of the response of fatigue cracks to waves or vibrations. The developed FE model offers a simple method to simulate a crack closer using a thermal expansion, which has the same effect on the crack behaviour. The developed model demonstrated a good agreement with the experimental results, which support the significance of the crack closure phenomenon. In addition, the numerical results show that the increase of tensile pre-stress levels leads to a smaller closure length near the crack tip, which allows the fatigue crack length to be evaluated

more accurately. The finding of the present study can be considered as initial step to improved understanding of the wave-crack interaction involving crack closure effects, and can help further develop fatigue crack NDE procedures using guided wave modes.

Acknowledgement

This work was funded by the Australian Research Council (ARC) DP200102300 and DP210103307 grants. The authors are grateful for the support.

References

[1] W. Elber, Fatigue crack closure under cyclic tension, Engineering Fracture Mechanics, 2 (1970) 37-45.
[2] J. Codrington, A. Kotousov, The distributed dislocation technique for calculating plasticity-induced crack closure in plates of finite thickness, International Journal of Fracture, 144 (2007) 285-295.
[3] J. Codrington, A. Kotousov, A crack closure model of fatigue crack growth in plates of finite thickness under small-scale yielding conditions, Mechanics of Materials, 41 (2009) 165-173.
[4] A. Kotousov, L. Bortolan Neto, S.S. Rahman, Theoretical model for roughness induced opening of cracks subjected to compression and shear loading, International Journal of Fracture, 172 (2011) 9-18.
[5] J. Vidler, A. Kotousov, C.-T. Ng, Residual opening of fatigue cracks due to the wake of plasticity, Procedia Structural Integrity, 45 (2023) 82-87.
[6] J. Vidler, A. Kotousov, C.-T. Ng, Analysis of crack closure and wake of plasticity with the distributed dislocation technique, Theoretical and Applied Fracture Mechanics, 127 (2023) 104034.
[7] X. Hu, T. Yin, H. Zhu, C.-T. Ng, A. Kotousov, Structural health monitoring of partially immersed metallic plates using nonlinear guided wave mixing, Construction and Building Materials, 346 (2022) 128381.
[8] M. Sun, Y. Xiang, M. Deng, B. Tang, W. Zhu, F.-Z. Xuan, Experimental and numerical investigations of nonlinear interaction of counter-propagating Lamb waves, Applied Physics Letters, 114 (2019) 011902.
[9] H. Zhu, C.T. Ng, A. Kotousov, Frequency selection and time shifting for maximizing the performance of low-frequency guided wave mixing, NDT & E International, 133 (2023) 102735.
[10] H. Zhu, C.T. Ng, A. Kotousov, Low-frequency Lamb wave mixing for fatigue damage evaluation using phase-reversal approach, Ultrasonics, 124 (2022) 106768.
[11] S. Sampath, H. Sohn, Detection and localization of fatigue crack using nonlinear ultrasonic three-wave mixing technique, International Journal of Fatigue, 155 (2022) 106582.
[12] Y. Yang, C.-T. Ng, A. Kotousov, H. Sohn, H.J. Lim, Second harmonic generation at fatigue cracks by low-frequency Lamb waves: Experimental and numerical studies, Mechanical Systems and Signal Processing, 99 (2018) 760-773.

[13] H. Zhu, C.T. Ng, A. Kotousov, Fatigue crack detection in edges of thin-walled structures with corners using the fundamental mode of edge waves, Ultrasonics, 132 (2023) 106995.
[14] R. Guan, Y. Lu, K. Wang, Z. Su, Fatigue crack detection in pipes with multiple mode nonlinear guided waves, Structural Health Monitoring, 18 (2019) 180-192.
[15] K. Wang, Z. Fan, Z. Su, Orienting fatigue cracks using contact acoustic nonlinearity in scattered plate waves, Smart Materials and Structures, 27 (2018) 09LT01.
[16] L. Xu, Y. Su, K. Wang, X. Yang, S. Yuan, Z. Su, An elastodynamic reciprocity theorem-based closed-form solution to second harmonic generation of lamb waves by a fatigue crack: Theory & experimental validation, Journal of Sound and Vibration, 509 (2021) 116226.
[17] L. Xu, K. Wang, X. Yang, Y. Su, J. Yang, Y. Liao, P. Zhou, Z. Su, Model-driven fatigue crack characterization and growth prediction: a two-step, 3-D fatigue damage modeling framework for structural health monitoring, International Journal of Mechanical Sciences, 195 (2021) 106226.
[18] J. Cheng, J.N. Potter, A.J. Croxford, B.W. Drinkwater, Monitoring fatigue crack growth using nonlinear ultrasonic phased array imaging, Smart Materials and Structures, 26 (2017) 055006.
[19] A. Hosoi, T. Kishi, Y. Ju, Healing of fatigue crack by high-density electropulsing in austenitic stainless steel treated with the surface-activated pre-coating, Materials, 6 (2013) 4213-4225.
[20] K. Wang, Y. Li, Z. Su, R. Guan, Y. Lu, S. Yuan, Nonlinear aspects of "breathing" crack-disturbed plate waves: 3-D analytical modeling with experimental validation, International Journal of Mechanical Sciences, 159 (2019) 140-150.
[21] K. Wang, M. Liu, Z. Su, S. Yuan, Z. Fan, Analytical insight into "breathing" crack-induced acoustic nonlinearity with an application to quantitative evaluation of contact cracks, Ultrasonics, 88 (2018) 157-167.
[22] S. Sampath, J. Jang, H. Sohn, Ultrasonic Lamb wave mixing based fatigue crack detection using a deep learning model and higher-order spectral analysis, International Journal of Fatigue, 163 (2022) 107028.
[23] Y. Kim, H.J. Lim, H. Sohn, Nonlinear ultrasonic modulation based failure warning for aluminum plates subject to fatigue loading, International Journal of Fatigue, 114 (2018) 130-137.
[24] Y.F. Lee, Y. Lu, R. Guan, Nonlinear guided waves for fatigue crack evaluation in steel joints with digital image correlation validation, Smart Materials and Structures, 29 (2020) 035031.
[25] C. Harding, G. Hugo, S.J.N.-D.T.-A. Bowles, Automated ultrasonic inspection for crack detection at F-111 lower wing skin fastener holes, 44 (2007) 80-85.
[26] R. Wang, Q. Wu, F. Yu, Y. Okabe, K. Xiong, Nonlinear ultrasonic detection for evaluating fatigue crack in metal plate, Structural Health Monitoring, 18 (2019) 869-881.
[27] M.V. Wilde, M.V. Golub, A.A. Eremin, Experimental and theoretical investigation of transient edge waves excited by a piezoelectric transducer bonded to the edge of a thick elastic plate, Journal of Sound and Vibration, 441 (2019) 26-49.
[28] V. Zernov, J. Kaplunov, Three-dimensional edge waves in plates, Proceedings of the Royal Society A: Mathematical, Physical and Engineering Sciences, 464 (2008) 301-318.
[29] X. Yu, R. Qin, M. Deng, New insights into topographically feature guided waves (FGW) propagation in non-uniform elastic waveguides, Wave Motion, (2021) 102866.
[30] J.M. Hughes, M. Mohabuth, A. Khanna, J. Vidler, A. Kotousov, C.-T. Ng, Damage detection with the fundamental mode of edge waves, Structural Health Monitoring, 20 (2021) 74-83.

[31] B.S. Vien, L.R.F. Rose, W.K. Chiu, Experimental and Computational Studies on the Scattering of an Edge-Guided Wave by a Hidden Crack on a Racecourse Shaped Hole, Materials, 10 (2017) 732.
[32] H. Zhu, A. Kotousov, C.T. Ng, Defects evaluation near edges of structural elements using the fundamental mode of edge waves, Journal of Sound and Vibration, 557 (2023) 117753.
[33] J.M. Hughes, A. Kotousov, C.-T. Ng, Generation of higher harmonics with the fundamental edge wave mode, Applied Physics Letters, 116 (2020) 101904.
[34] M. Hong, Z. Su, Q. Wang, L. Cheng, X. Qing, Modeling nonlinearities of ultrasonic waves for fatigue damage characterization: Theory, simulation, and experimental validation, Ultrasonics, 54 (2014) 770-778.
[35] J. Jingpin, M. Xiangji, H. Cunfu, W. Bin, Nonlinear Lamb wave-mixing technique for micro-crack detection in plates, Ndt & E International, 85 (2017) 63-71.
[36] Y. Yang, C.-T. Ng, A. Kotousov, Influence of crack opening and incident wave angle on second harmonic generation of Lamb waves, Smart Materials and Structures, 27 (2018) 055013.
[37] Y.F. Lee, Y. Lu, Advanced numerical simulations considering crack orientation for fatigue damage quantification using nonlinear guided waves, Ultrasonics, 124 (2022) 106738.
[38] Y.F. Lee, Y. Lu, Identification of fatigue crack under vibration by nonlinear guided waves, Mechanical Systems and Signal Processing, 163 (2022) 108138.
[39] F. Feng, Z. Shen, J. Shen, Edge waves in a 3D plate: two solutions based on plate mode matching, Mathematics and Mechanics of Solids, 22 (2017) 2065-2074.
[40] M.V. Wilde, M.V. Golub, A.A. Eremin, Experimental observation of theoretically predicted spectrum of edge waves in a thick elastic plate with facets, Ultrasonics, 98 (2019) 88-93.
[41] H. Jin Lim, H. Sohn, P. Liu, Binding conditions for nonlinear ultrasonic generation unifying wave propagation and vibration, Applied Physics Letters, 104 (2014) 214103.
[42] B. Pavlakovic, M. Lowe, D. Alleyne, P. Cawley, Disperse: A general purpose program for creating dispersion curves, Review of Progress in Quantitative Nondestructive Evaluation: Volume 16A, (1997) 185-192.
[43] J.M. Hughes, M. Mohabuth, A. Kotousov, C.-T. Ng, The fundamental ultrasonic edge wave mode: Propagation characteristics and potential for distant damage detection, Ultrasonics, 114 (2021) 106369.
[44] D. Sun, W. Zhu, X. Qiu, L. Liu, Y. Xiang, F.-Z. Xuan, Nonlinear ultrasonic detection of closed cracks in metal plates with phase-velocity mismatching, NDT & E International, (2023) 102788.
[45] R. Pippan, A. Hohenwarter, Fatigue crack closure: a review of the physical phenomena, Fatigue & fracture of engineering materials & structures, 40 (2017) 471-495.

Chapter 7

Conclusions

Chapter 7: Conclusions

7.1. Summary

This PhD thesis is concerned with the development of new techniques for fatigue damage evaluation in thin-walled structures using the fundamental modes of guided waves.

The distributed fatigue damage (or material degradation) has been evaluated with the wave mixing, in the first part of the thesis (Chapters 2 and 3). The outcomes of these chapters show that the generation of combinational harmonics is sensitive to the material nonlinearity manifesting the material degradation due to progressive low-cycle fatigue damage. In addition, the generation of combinational harmonics has exhibited a higher sensitivity to the distributed fatigue damage than the second-order harmonics. The developed techniques based on wave mixing have improved the quality of the experiments and significantly enhanced the efficiency of the combinational harmonic generation.

It is well known that fatigue cracks are often initiate and propagate from free edges in thin-walled structures. In Chapters 4, 5, and 6, the fundamental modes of edge waves have been studied, which can propagate near the free edges, and wave properties of these wave modes have been investigated for the purpose of NDE of fatigue edge cracks. The outcomes of these chapters have demonstrated that the fundamental edge waves can propagate in different thin-walled structural with different cross-sectional geometries, and the edge waves are very sensitive to crack-like defects, thus these feature guided waves are very promising candidates for the development of new NDE techniques.

In Chapter 2, the phase-reversal approach has been incorporated into the wave mixing to evaluate the accumulated fatigue damage. The generated combinational harmonic using two S_0 mode waves has shown a good sensitivity to the accumulated fatigue damage and correlates well with the progressive fatigue damage. The phase-reversal approach combined with the wave mixing of the fundamental mode of Lamb waves has exhibited a great potential, especially for challenging situations, e.g., when the generation of combinational harmonics is small and overlapped with third order harmonics. In addition, the generation of the combinational harmonics has shown better performance compared with the second harmonics. The findings of this study can be critical for practical application and development of NDE, which utilise the wave mixing method.

Chapter 3 has focused on the effects of frequency pair and time shifting on the wave mixing using quasi-synchronized guided wave modes. Previously, the frequency pair selection of fundamental wave modes has generally been based on the trial-and-error method, however, avoiding overlapping of the generated harmonics requires the certainty in the selection of the frequency pairs. A new method based on theoretical modelling has been developed. This method provides a guide for the selection of the wave mixing frequency pair. Moreover, a time shifting method has been developed and applied to enhance the generation of the combinational harmonics using the collinear wave mixing. This method can be particularly useful when the frequency pair selection is constrained due to various limitations, which are very common in the practical applications. The efficiency of the proposed methods has been validated numerically and experimentally in several case studies. Overall, the developed methods can be utilised to further advance the application of fatigue damage evaluation techniques based on wave mixing method.

The propagation of the fundamental mode of edge waves (ES_0) along the corners of the thin-walled structures has been investigated in Chapter 4. It has been found that this wave mode can be utilised to inspect the fatigue crack at the plate structures with corners, and it can be particularly advantageous for NDE of damage and defects in inaccessible locations. The experimental studies have revealed that the ES_0 can propagate through sharp corners, and a new edge wave can be generated after the interaction with the corner. This new wave has the identical wavenumber with the incident wave. The careful numerical studies have shown that a rounded corner has insignificant effect on the edge wave propagation when the radius-to-wavelength ratio is above 3. In addition, the second harmonic generated due to presence of a fatigue crack can also propagate through the corners, and this finding is especially important for the development of NDE techniques to detect fatigue cracks in inaccessible locations.

Chapter 5 is concerned with the propagation of the fundamental mode of edge waves in non-ideal geometries i.e., thin plates with curved edges. Analytical approaches developed over the past fifty years are very complex for the case of non-ideal edges of the waveguide. Therefore, a SAFE model has been developed for the purpose of the evaluation of wave properties. The comparison between the SAFE calculations and the analytical results for the ideal geometries has shown that the developed SAFE method can achieve an excellent agreement with the analytical results. This agreement provides the confidence in the developed SAFE method and obtained results for the case of non-ideal edges. Further investigation has shown that the quasi-fundamental antisymmetric mode of edge wave (QEA_0) has almost no

decay and can propagate for long distances, while its symmetric counterpart has strong wave mode dispersion in the non-ideal edges. In addition, the QEA_0 has demonstrated a good sensitive to the defect with the characteristic length less than the 0.1 wavelength. The outcomes of Chapter 5 have provided a new approach for detail investigations of edge waves, especially for the wave properties calculation for edges with complex shapes. The findings can be applied to many practical situations, which require fatigue damage evaluation with NDE techniques.

Chapter 6 has investigated the evaluation of the fatigue crack length using ES_0 mode. The experimental studies have demonstrated that the reflected and transmitted signals at different frequencies of ES_0 waves correlate very well with the length of the opened region of fatigue cracks. A new advanced FE model has been developed to simulate the wave phenomena associated with plasticity-induced closure of fatigue cracks. The numerical and experimental results have been found in a good agreement. However, an accurate evaluation of the total crack length can be conducted under the applied tensile load, when the crack is fully opened. This conclusion is in-line with past studies, which concluded that the plasticity-induced closure phenomenon is one of the main reasons behind a possible underestimation of the severity of fatigue damage with different NDE techniques.

In summary, this study has investigated the fatigue damage in thin-walled structures, and the methods developed in this study are applicable for practical applications. Early fatigue damage (or damage before formation of a micro-crack) in such structures can be evaluated using fundamental mode of Lamb waves, and the further progressive damage or fatigue cracks, which normally initiate at free edges, can be evaluated using the fundamental modes of edge waves. The findings of the present study can help to further develop fatigue damage/crack evaluation techniques using guided wave based NDE methods, and provide an improved understanding of the wave propagation phenomenon associated with the more realistic structural geometries and fatigue crack closure behaviour.

7.2. Future work recommendations

The current work has laid a foundation for many new developments in the area of NDE. For example, in the case of the damage evaluation in thin-walled structures, the present results could be extended as follow.

1. The further application of the developed wave mixing method in Chapters 2 and 3, using the fundamental wave modes, such as wave mixing of edge waves, and three-wave mixing, for the purpose of early-stage evaluation of fatigue damage.
2. The further investigation of the edge waves propagation along the non-ideal edges for the purpose of the fatigue crack evaluation, using the proposed SAFE mode in Chapter 5. The edge fatigue crack with partially through thickness is of particular interest, and the local wave interaction using edge waves may be sensitive to this type of the early-stage fatigue crack as well.
3. The investigation of edge waves propagation in composite materials for the purpose of delamination damage inspections. The dispersion curves of edge wave can be calculated using the developed SAFE model, which provides a powerful tool for the dispersion curve calculation of anisotropic materials, e.g. fibre-reinforced composites.
4. The influence of environmental conditions (i.e., soil and water) on the propagation of edge waves needs to be investigated, since there are many thin-walled infrastructure components are either buried underground or immersed in the water. This could be achieved based on further development and modifications of the aforementioned SAFE model.
5. The feasibility of edge wave propagating on the free edges with thickness variation, for the purpose of damage evaluation in more realistic structures. The edge wave properties are directly associate with the frequency and thickness, and the gradual change of the thickness may also result in the phenomena so call ‘acoustic blackhole’. Therefore, the wave properties of edge waves may change accordingly considering the combined effects.
6. The further development of a more realistic model considering the fatigue crack closure behaviour. Chapter 6 has demonstrated that the closure behaviour of fatigue crack can be simulated using the thermal expansion analogy with plastic wake behind the crack tip. The further investigations could be carried out based on the aforementioned FE model and incorporated with the nonlinear features of the guided waves.